

# **INTEGRATED REACTIVE CO<sub>2</sub> CAPTURE AND CONVERSION TO PRODUCE CALCIUM AND MAGNESIUM CARBONATES**

A Thesis

Presented to the Faculty of the Graduate School

of Cornell University

In Partial Fulfillment of the Requirements for the Degree of

Doctor of Philosophy of Engineering

by

Meishen Liu

May 2021

© 2021

Meishen Liu

All Rights Reserved

## ABSTRACT

# INTEGRATED REACTIVE CO<sub>2</sub> CAPTURE AND CONVERSION TO PRODUCE CALCIUM AND MAGNESIUM CARBONATES

Meishen Liu

More than 82% of our energy needs are being met by fossil-based energy resources, which contribute to about 79% of global CO<sub>2</sub> emissions. Designing novel integrated chemical pathways for the capture, conversion, and storage of CO<sub>2</sub> is a crucial need for advancing sustainable energy conversion. The accelerated capture, conversion and storage of CO<sub>2</sub> as water-insoluble and stable calcium and magnesium carbonates, also known as carbon mineralization, is a promising thermodynamically downhill route. One of the knowledge gaps is a limited understanding of the dynamic chemical and morphological transformation in alkaline calcium and magnesium bearing materials as they are reacted in far-from-equilibrium environments. To address this challenge, synchrotron cross-scale X-ray scattering measurements are harnessed to elucidate simultaneously probe the chemical and morphological evolution of materials in a chemical or thermal reaction environment.

Another constraint of carbon mineralization is the slow kinetics at low CO<sub>2</sub> concentrations. As a result, there is a significant interest in environmentally benign approaches to capture CO<sub>2</sub>. One of the less explored but highly transformative approaches to capture CO<sub>2</sub> is via coupled absorption-crystallization approaches. This approach addresses the challenge of low solubility of CO<sub>2</sub> by using aqueous solvents with high affinity to bind CO<sub>2</sub>. The resulting carbamate, bicarbonate or carbonate species react with alkaline sources to produce inorganic carbonates while regenerating the solvent. Thermodynamic models are constructed to predict and evaluate the

performance of different solvents. Experiments are designed to determine the optimal experimental configurations for integrated reactive CO<sub>2</sub> capture and conversion, reaction time, reaction temperature, solvent concentration, and temperature. Our results show that aqueous solvents such as sodium glycinate, MEA, AMP, and DBU are effective in capturing and delivering CO<sub>2</sub> to produce calcium or magnesium carbonates at 50-75°C with inherent solvent regeneration. These findings inform the development of intensified approaches to capture and convert CO<sub>2</sub> into inorganic carbonates, and represent alternative strategies to regenerate solvents chemically at low temperatures, as an alternative to high temperature thermal regeneration.

# TABLE OF CONTENTS

<b>ABSTRACT</b> .....	i
<b>TABLE OF CONTENTS</b> .....	iii
<b>LIST OF FIGURES</b> .....	viii
<b>LIST OF TABLES</b> .....	xx
<b>ACKNOWLEDGEMENT</b> .....	xxi
<b>CHAPTER 1 INTRODUCTION</b> .....	1
<b>CHAPTER 2 BACKGROUND</b> .....	8
2.1 CO <sub>2</sub> Hydration .....	8
2.1.1 Inorganic Carbon Speciation in the Absence of CO <sub>2</sub> Capture Solvents .....	8
2.1.2 Inorganic Carbon Speciation in the Presence of CO <sub>2</sub> Capture Solvents in the Open System .....	11
2.2 Mineral Dissolution and Carbonate Formation .....	16
2.3 Research Objectives .....	17
2.3.1 Problem Statement .....	17
2.3.2 Scientific Questions .....	17
2.3.3 Research Goals .....	18

**CHAPTER 3 CHEMO-MORPHOLOGICAL COUPLING DURING SERPENTINE HEAT  
TREATMENT FOR CARBON MINERALIZATION ..... 23**

3.1 Introduction ..... 23

3.2 Materials and Their Characterization ..... 25

3.3 Results and Discussion ..... 26

    3.3.1 Structural Changes in Lizardite on Thermal Treatment ..... 26

    3.3.2 Morphological Changes in Lizardite on Thermal Treatment ..... 28

3.4 Conclusions ..... 32

**CHAPTER 4 PHASE EVOLUTION AND TEXTURAL CHANGES DURING THE  
DIRECT CONVERSION AND STORAGE OF CO<sub>2</sub> TO PRODUCE  
CALCIUM CARBONATE FROM CALCIUM HYDROXIDE ..... 44**

4.1 Introduction ..... 44

4.2 Experimental Methods ..... 47

    4.2.1 Materials and Methods ..... 47

    4.2.2 USAXS/SAXS/WAXS Measurements ..... 47

4.3 Results and Discussion ..... 48

    4.3.1 Phase transformations during the carbon mineralization of calcium hydroxide..... 48

    4.3.2 Evolution of the pore-solid interface during the carbon mineralization of calcium  
    hydroxide ..... 49

4.4 Conclusions ..... 51

**CHAPTER 5 INTEGRATED CO<sub>2</sub> CAPTURE, CONVERSION AND STORAGE TO  
PRODUCE CALCIUM CARBONATE USING AN AMINE LOOPING  
STRATEGY..... 60**

5.1 Introduction ..... 60

5.2 Experimental Methods ..... 64

    5.2.1 Integrated carbon mineralization with in-situ amine looping ..... 65

    5.2.2 Characterization of the reactants and products in the carbon mineralization process.  
    ..... 66

    5.2.3 X-ray reflectivity measurements ..... 67

    5.2.4 Wide Angle X-ray Scattering (WAXS) measurement..... 68

5.3 Results and Discussion ..... 68

    5.3.1 Effect of MEA concentration..... 68

    5.3.2 Effect of reaction temperature..... 71

    5.3.3 Characterization of the bulk phases and surface structure of calcium carbonate .... 73

5.4 Conclusions ..... 76

**CHAPTER 6 NOVEL AQUEOUS AMINE LOOPING APPROACH FOR THE DIRECT  
CAPTURE, CONVERSION AND STORAGE OF CO<sub>2</sub> TO PRODUCE  
MAGNESIUM CARBONATE..... 90**

6.1 Introduction ..... 90

6.2 Experimental Materials and Methods ..... 94

    6.2.1 Aqueous alkaline amine looping process for accelerated carbon mineralization .... 95

6.2.2	Characterization of chemical and morphological properties .....	95
6.3	Results and Discussion .....	98
6.3.1	Effect of temperature and MEA concentration .....	98
6.3.2	Morphological characterization of magnesium carbonates .....	100
6.4	Conclusions .....	105
<b>CHAPTER 7 SINGLE-STEP, LOW TEMPERATURE AND INTEGRATED CO<sub>2</sub></b>		
<b>CAPTURE AND CONVERSION USING SODIUM GLYCINATE TO</b>		
<b>PRODUCE CALCIUM CARBONATE.....</b>		
		115
7.1	Introduction .....	115
7.2	Experimental Materials and Methods .....	119
7.2.1	. Aqueous alkaline amino acid looping process for accelerated carbon mineralization .....	119
7.2.2	Quantification of Carbonate Formation and the Corresponding Morphological Features .....	120
7.3	Results and Discussions .....	121
7.3.1	CO <sub>2</sub> reaction with sodium glycinate.....	121
7.3.2	Effect of temperature .....	123
7.3.3	Effect of amino acid salt concentration.....	124
7.3.4	Reaction Time .....	125
7.3.5	Structural and morphological characterization of recovered materials .....	126
7.4	Conclusion.....	127

<b>CHAPTER 8 INTEGRATED CO<sub>2</sub> CAPTURE AND REMOVAL VIA CARBON MINERALIZATION WITH INHERENT REGENERATION OF AQUEOUS SOLVENTS</b> .....	140
8.1 Introduction .....	140
8.2 Experimental Materials and Methods .....	145
8.2.1 Experimental Approach for Integrated CO <sub>2</sub> Capture and Carbonate Formation...	145
8.2.2 Characterization of chemical and morphological properties .....	146
8.3 Results and Discussion .....	147
8.3.1 Effect of the solvent concentration on carbon mineralization .....	147
8.3.2 Compositions of the Carbonate-Bearing Products .....	151
8.4 Conclusion.....	152
<b>CHAPTER 9 CONCLUSION AND FUTURE WORK</b> .....	177
9.1 Conclusion.....	177
9.2 Future Work .....	179
<b>REFERENCE</b> .....	181

## LIST OF FIGURES

- Figure 2.1 Carbon speciation in open and closed systems without any additives. The concentration of  $\text{H}_2\text{CO}_3^*_{(\text{aq})}$ ,  $\text{HCO}_3^-_{(\text{aq})}$ , and  $\text{CO}_3^{2-}_{(\text{aq})}$  as a function of pH in an open system exposed to the atmosphere with a  $\text{CO}_2$  concentration of 400 ppm and  $\text{pCO}_2$  of 1 atm are shown in Figure 2.1 (a) and Figure 2.1 (b), respectively. The concentration of  $\text{H}_2\text{CO}_3^*_{(\text{aq})}$ ,  $\text{HCO}_3^-_{(\text{aq})}$ , and  $\text{CO}_3^{2-}_{(\text{aq})}$  as a function of pH in a closed system at  $\text{CO}_2$  concentration of 400 ppm and  $\text{CO}_2$  partial pressure of 1 atm are shown in Figure 2.1 (c) and Figure 2.1 (d), respectively. The total carbon concentration at the equilibrium pH of 5.55 in a closed system with  $\text{CO}_2$  concentration of 400 ppm is  $1.59 \times 10^{-5}$  M (Figure 2.1 (c)). The total carbon concentration at the equilibrium pH of 3.85 in a closed system with  $\text{pCO}_2$  of 1 atm is 0.035 M (Figure 2.1 (d))..... 19
- Figure 2.2 Inorganic and organic carbon speciation in open system with MEA sodium glycinate, AMP, and DBU. The concentration of organic solvent speciation and  $\text{H}_2\text{CO}_3^*_{(\text{aq})}$ ,  $\text{HCO}_3^-_{(\text{aq})}$ , and  $\text{CO}_3^{2-}_{(\text{aq})}$  as a function of pH in an open system with MEA sodium glycinate, AMP, and DBU exposed to 1 atm  $\text{CO}_2$  are shown in Figure 2.2 (a), Figure 2.2 (b), Figure 2.2 (c), and Figure 2.2 (d), respectively..... 21
- Figure 2.3 Inorganic and organic carbon speciation in open system with MEA sodium glycinate, AMP, and DBU. The concentration of organic solvent speciation, pH and  $\text{H}_2\text{CO}_3^*_{(\text{aq})}$ ,  $\text{HCO}_3^-_{(\text{aq})}$ , and  $\text{CO}_3^{2-}_{(\text{aq})}$  as a function of organic concentration in an open system with MEA sodium glycinate, AMP, and DBU exposed to 1 atm  $\text{CO}_2$  are shown in Figure 2.3 (a), Figure 2.3 (b), Figure 2.3 (c), and Figure 2.3 (d), respectively. .... 22
- Figure 3.1 Changes in (a) the characteristic lizardite peak ( $q = 0.85 \text{ \AA}^{-1}$ ,  $d = 7.39 \text{ \AA}$ , h k l: (0 0 1) (Mellini, 1982)) and (b) the integrated peak intensity in the temperature range of 40 °C to 1150 °C. The relative integrated intensity represented in (b) is the integrated intensity of the

characteristic lizardite peak at a given temperature normalized to the integrated intensity at 40 °C. Vertical bars in (b) represent estimated 5% standard deviation uncertainties.....	35
Figure 3.2 Changes in the weight of lizardite heat-treated to 350°C, 650°C, and 900°C with respect to untreated lizardite at 25°C determined using thermogravimetric analysis. ....	36
Figure 3.3 Changes in the characteristic peaks of mullite ( $d = 3.84 \text{ \AA}$ , $q = 1.59 \text{ \AA}^{-1}$ , h k l: (0 2 0)(Angel & Prewitt, 1986)) (a-1), cristobalite ( $d = 1.64 \text{ \AA}$ , $q = 3.83 \text{ \AA}^{-1}$ , h k l: (3 3 1)(Dove et al., 2000)) (b-1), forsterite ( $d = 1.37 \text{ \AA}$ , $q = 4.60 \text{ \AA}^{-1}$ , h k l: (3 0 4)(Hazen, 1976)) (c-1), and enstatite ( $d = 1.37 \text{ \AA}$ , $q = 4.60 \text{ \AA}^{-1}$ , h k l: (3 0 4)(Smith, 1959)) (d-1) on heating from 30 °C to 1150 °C. The corresponding integrated intensities of mullite (a-2), cristobalite (b-2), forsterite (c-2), and enstatite (d-2) show the onset of these phases in the range of 725 °C and 750 °C. The relative integrated intensities represented in the right panel correspond to the integrated intensity of the characteristic peak at a given temperature normalized to the integrated intensity at 30 °C. Vertical bars in (a-2), (b-2), (c-2), and (d-2) represent estimated 5% standard deviation uncertainties. ....	38
Figure 3.4 Changes in the cumulative pore volume (a) and pore volume distributions (b) in lizardite heat treated at 350 °C, 650 °C, and 900 °C with respect to untreated lizardite at 25 °C.....	39
Figure 3.5 Changes in the particle size distributions of lizardite heat treated at 350 °C, 650 °C, and 900 °C with respect to untreated lizardite at 25 °C. ....	40
Figure 3.6 Comparison of morphological changes of untreated lizardite at 25 °C (a) with lizardite heat-treated at 900 °C (b) and 1150 °C (c) using scanning electron microscopy images. The particles within the white square correspond to the crystalline phases formed at elevated temperatures. ....	41

Figure 3.7 Changes in the combined slit-smearred USAXS/SAXS data on heating lizardite to a nominal temperature of 1150 °C. An increase in the scattering intensity is noted on heating to 700 °C at  $q$  larger than  $0.03 \text{ \AA}^{-1}$ . This transformation corresponds to the change in the lamellar morphology of lizardite at ambient temperature to a pseudo-amorphous structure. Further heating to 1150 °C results in the formation of crystalline phases (see Figure 3.3) and is accompanied by a reduction in the scattering intensity at  $q$  larger than  $0.03 \text{ \AA}^{-1}$ . ..... 42

Figure 3.8 Changes in Porod slopes for  $q$  in the range of  $0.02 \text{ \AA}^{-1}$  to  $0.4 \text{ \AA}^{-1}$ . The slopes are determined after desmearing the USAXS/SAXS data shown in Figure 7. The roughness of the pore-solid interfaces increases on serpentine dehydroxylation. Interfaces become smoother on the formation of high temperature phases such as  $\text{Al}_{2.35}\text{Si}_{0.64}\text{O}_{4.82}$  (mullite),  $\text{SiO}_2$  (cristobalite),  $\text{Mg}_2\text{SiO}_4$  (forsterite),  $\text{Fe}_{0.3}\text{Mg}_{0.7}(\text{SiO}_3)$  (enstatite). ..... 43

Figure 4.1 The cumulative pore volume (a) and pore volume distribution (b) of unreacted calcium hydroxide using BET measurements. .... 53

Figure 4.2 Changes in the characteristic peak of calcium hydroxide ( $d = 3.105 \text{ \AA}$ ,  $q = 2.024 \text{ \AA}^{-1}$ , h k l: (1 0 0)) and the integrated peak intensity are represented in (a) and (b) respectively (Petch, 1961b). The relative integrated intensity of calcium hydroxide represented in (b) is the integrated intensity of the characteristic peak at a given temperature normalized to the integrated intensity at 30 °C. Vertical bars in (b) represent estimated 5% standard deviation uncertainties. .... 54

Figure 4.3 Changes in the characteristic carbonates peaks: calcite ( $d = 3.85 \text{ \AA}$ ,  $q = 1.63 \text{ \AA}^{-1}$ , h k l: (0 1 2)) (Chessin et al., 1965) in (a-1), vaterite ( $d = 2,08 \text{ \AA}$ ,  $q = 3.02 \text{ \AA}^{-1}$ , h k l: (1 1 0)) (Kamhi, 1963) in (b-1), and aragonite ( $d = 2.48 \text{ \AA}$ ,  $q = 2.53 \text{ \AA}^{-1}$ , h k l: (2 1 0)) (Dal Negro & Ungaretti, 1971) in (c-1) as calcium hydroxide is reacted with  $\text{CO}_2$  at reaction temperatures in the range

of 30 °C to 500 °C. The integrated peak intensities of calcite, vaterite, and aragonite are shown in Figures (a-2), (b-2), and (c-2) respectively. Vertical bars represent estimated 5% standard deviation uncertainties in Figures (a-2), (b-2), and (c-2)..... 55

Figure 4.4 Identification of the characteristic peaks in unreacted and reacted calcium hydroxide at 30 °C and 497 °C, respectively, using Wide Angle X-Ray Scattering (WAXS) measurements. Peak identification is based on the crystallographic data reported for calcium hydroxide (Petch, 1961b), calcite (Chessin et al., 1965; Maslen, Streltsov, & Streltsova, 1993), vaterite (Christy, 2017; Kamhi, 1963), and aragonite (Dal Negro & Ungaretti, 1971). ..... 57

Figure 4.5 Changes in the combined slit-smearred USAXS/SAXS data as calcium hydroxide is reacted with CO<sub>2</sub> where (a) and (b) represent temperatures in the range of 29 °C to 300 °C and 325 °C to 502 °C, respectively..... 58

Figure 4.6 Porod slopes as calcium hydroxide is reacted with calcium carbonate are represented. Low  $q$  and high  $q$  ranges represent 0.001-0.01 Å<sup>-1</sup> and 0.01-0.1 Å<sup>-1</sup>, respectively. The data was obtained after desmearing the USAXS/SAXS data shown in Figure 5. Porod slope of 1 and 4 indicated scattering from rigid rods and smooth surfaces, respectively. Porod slopes in the range of 2-3 and 3-4 are indicative of branched systems or networks also known as mass fractals and rough interfaces with a fractal dimension,  $D$  where  $n = 6 - D$  represents a surface fractal. .... 59

Figure 5.1 Schematic representation of integrated carbon mineralization with *in-situ* amine looping with (a) a continuous supply of CO<sub>2</sub> as flue gas with *in-situ* capture and release of carbon-bearing species, and (b) CO<sub>2</sub>-loaded amine-bearing solvents for *in-situ* release of carbon-bearing species for accelerated mineralization..... 77

Figure 5.2 (a) Extent of carbonation of CaO and CaSiO<sub>3</sub> reacted with water and 10 wt%, 30 wt%, and 50 wt% MEA at 50 °C for 3 hr at P<sub>CO<sub>2</sub></sub> = 1 atm and a stirring rate 300 rpm. Particle size distribution of CaO (b-1) and CaSiO<sub>3</sub> (c-1) reacted with water and 50 wt% MEA at 50 °C in Mode 1 for 3 hr at P<sub>CO<sub>2</sub></sub> = 1 atm and a stirring rate 300 rpm. Particle size distribution of CaO (b-2) and CaSiO<sub>3</sub> (c-2) reacted with 50 wt% CO<sub>2</sub> loaded-MEA at 50 °C in Mode 2 for 3 hr and a stirring rate 300 rpm. .... 79

Figure 5.3 (a) Extent of carbonation of CaO and CaSiO<sub>3</sub> with water and 50 wt% MEA at 25 °C, 50 °C, 75 °C, and 90 °C in Mode 1 for 3 hr at P<sub>CO<sub>2</sub></sub> = 1 atm and a stirring rate 300 rpm. Particle size distribution of CaO reacted with water (b-1) and 50 wt% MEA (b-2) at 90 °C in Mode 1 for 3 hr at P<sub>CO<sub>2</sub></sub> = 1 atm and a stirring rate 300 rpm. (c-1) Particle size distribution of CaSiO<sub>3</sub> reacted with water (c-1) and 50 wt% MEA (c-2) at 90 °C in Mode 1 for 3 hr at P<sub>CO<sub>2</sub></sub> = 1 atm and a stirring rate 300 rpm. .... 81

Figure 5.4 Determination of the phases present in calcium oxide and calcium silicate using thermogravimetric analyses (TGA). Modes 1 and 2 represent continuous CO<sub>2</sub> flow (P<sub>CO<sub>2</sub></sub> = 1 atm) through a slurry containing MEA and MEA pre-loaded with CO<sub>2</sub> without a continuous supply of CO<sub>2</sub> gas. The effect of water and 10 wt%, 30 wt%, and 50 wt% MEA at 50 °C when reacted for 3 hr and a stirring rate of 300 rpm with calcium oxide (a-1) and calcium silicate (b-1) are shown. The effect of temperature (25 °C, 50 °C, 75 °C, and 90 °C) in water and 50 wt% MEA when reacted for 3 hr and a stirring rate of 300 rpm with calcium oxide (a-2) and calcium silicate (b-2) are shown. .... 83

Figure 5.5 Changes in the phases present in the reacted and unreacted calcium oxide (a) and calcium silicate (b) materials are represented by ATR-FTIR spectra. Spectra in black represents the unreacted calcium-bearing materials. Spectra in red and blue represents

calcium oxide and calcium silicate reacted in water and MEA at 50 °C with continuous CO <sub>2</sub> flow (P <sub>CO<sub>2</sub></sub> = 1 atm) for 3 hours and a stirring rate of 300 rpm. ....	85
Figure 5.6 Comparison of the morphological changes in unreacted calcium oxide (a-1) and calcium silicate (b-1) with calcium oxide (a-2) and calcium silicate (b-2) reacted with 50 wt% MEA at 50 °C when reacted for 3 hours and a stirring rate of 300 rpm. ....	86
Figure 5.7 Identification of unreacted CaO, CaO reacted with H <sub>2</sub> O and 50 wt % MEA at 50 °C in Mode 1. Peak identification is based on the crystallographic data reported for CaO, Ca(OH) <sub>2</sub> , calcite, vaterite, and aragonite. ....	87
Figure 5.8 Cumulative pore volume of unreacted CaO and CaSiO <sub>3</sub> and reacted with 50 wt% MEA at 50 °C when reacted for 3 hours and a stirring rate of 300 rpm. ....	88
Figure 5.9 X-ray reflectivity data representing changes in the calcite surface when exposed to air, solutions with a pH of 7, 5, and 3. Larger error bars in the data at pH 3 condition correspond to the increasing surface roughness of the calcite surface. ....	89
Figure 6.1 Schematic representation of the alkaline aqueous amine looping process for the carbon mineralization of magnesium oxide to produce magnesium carbonate. ....	106
Figure 6.2 Extent of carbon mineralization of MgO reacted with water, 10 wt%, 20 wt%, 30 wt%, and 50 wt% at 25 °C, 50 °C, 75 °C, and 90 °C at P <sub>CO<sub>2</sub></sub> = 1 atm for 3 hrs and stirring rate of 300 rpm ± 5 rpm. Estimated error is based on 5% uncertainty. Experiments were performed in duplicate. ....	107
Figure 6.3 Identification of the functional groups present in the (a) reacted solid and (b) fluid obtained from reacting MgO with 30 wt% MEA at 50 °C with P <sub>CO<sub>2</sub></sub> = 1 atm atm for 3 hours and stirring rate of 300 rpm ± 5 rpm, using ATR-FTIR measurements. ....	109

Figure 6.4 Comparison of the morphological changes in (a) unreacted magnesium oxide and (b) MgO reacted with 30 wt% MEA at 50 °C with  $P_{CO_2} = 1$  atm for 3 hours and stirring rate of  $300 \text{ rpm} \pm 5 \text{ rpm}$ . The needle-shaped particles in (b) correspond to nesquehonite particles. .... 110

Figure 6.5 Changes in the combined slit-smear USAXS/SAXS data as MgO is reacted with CO<sub>2</sub>-loaded MEA to produce magnesium carbonate as shown in (a). The characteristic peak of lansfordite at  $q = 0.5 \text{ \AA}^{-1}$  is shown in (b) and the integrated intensity of the characteristic peak of lansfordite at  $q = 0.5 \text{ \AA}^{-1}$  is shown in (c). .... 111

Figure 6.6 (a) Power law slope and radius of gyration ( $R_g$ ) values obtained from the fitting of experimental USAXS/SAXS curves in the  $q$ -range of  $0.02 - 0.8 \text{ \AA}^{-1}$ . (b-1) and (b-3) pore size distribution and cumulative pore volume for unreacted MgO and MgO reacted with 30 wt% MEA for 3 hours, respectively. The curves were obtained by using the BJH method on N<sub>2</sub> desorption isotherm. (b-2) early stage emergence of (001) lansfordite (Giester et al., 2000; Ming & Franklin, 2010) peak during carbonation of MgO to MgCO<sub>3</sub>. .... 113

Figure 6.7 The *in-situ* cell for Grazing Incidence – Small Angle X-Ray Scattering (GI-SAXS) measurements is shown in (a). A representative scattering image (b) and the scattering curve (c) that correspond to the nucleation of magnesium carbonate particles on quartz (0 0 1) surface are shown. The size distribution obtained from fitting the scattering curve using the Guinier-Porod slope is shown in (d). The experiments were performed at 25 °C. 0.1988 mL 30 wt% CO<sub>2</sub>-loaded MEA solution was injected into 5 mL 0.1 M Mg(NO<sub>3</sub>)<sub>2</sub> solution, which marked the beginning of the *in-situ* measurement. .... 114

Figure 7.1 Schematic representation of the alkaline aqueous amino acid salt looping process for the single step, low temperature and integrated CO<sub>2</sub> capture and conversion using sodium

glycinate to produce calcium carbonate. Reactions representing CO<sub>2</sub> hydration, CO<sub>2</sub> capture using amino acid salts, amino acid salt regeneration, cation recovery from Ca- and Mg-bearing solids, and carbonate formation are shown here. .... 130

Figure 7.2 Changes of aqueous species during CO<sub>2</sub> capture using Na-glycinate determined using ATR-FTIR analyses. HCO<sub>3</sub><sup>-</sup> at 1005 cm<sup>-1</sup>, 1300 cm<sup>-1</sup>, and 1365 cm<sup>-1</sup> (Milella & Mazzotti, 2019). CO<sub>3</sub><sup>2-</sup> at 1395 cm<sup>-1</sup> (Davis & Oliver, 1972). NH<sub>2</sub>COO<sup>-</sup> at 1120 cm<sup>-1</sup>, 1413 cm<sup>-1</sup>, and 1545 cm<sup>-1</sup> (Hisatsune, 1984; Milella & Mazzotti, 2019; Pretsch et al., 2009). .... 131

Figure 7.3 Extent of carbon mineralization of CaO (red) and CaSiO<sub>3</sub> (blue) with 1 M sodium glycinate at temperatures of 25, 50, 75, and 90 °C for 3 hours in (a), with different concentration of 0, 0.5, 1, and 3 M sodium glycinate at 75 °C for 3 hours in (b), with 1 M sodium glycinate at 75 °C for different reaction times of 1, 3, and 5 hours in (c). All the experiments are performed at P<sub>CO2</sub> = 1 atm and a stirring rate of 300 rpm. .... 132

Figure 7.4 Changes in the species present in the aqueous phase recovered after the carbon mineralization of CaO using ATR-FTIR analyses. Figures (a), (b) and (c) represent experiments performed to investigate the influence of temperature, amino acid salt concentration, and reaction time, respectively (Ahmed et al., 2013; Doki et al., 2004; Ramachandran et al., 2007). .... 134

Figure 7.5 Changes in the species present in the aqueous phase recovered after the carbon mineralization of CaSiO<sub>3</sub> using ATR-FTIR analyses. Figures (a), (b) and (c) represent experiments performed to investigate the influence of temperature, amino acid salt concentration, and reaction time, respectively (Ahmed et al., 2013; Doki et al., 2004; Ramachandran et al., 2007). .... 135

Figure 7.6 Changes in the phases present in calcium oxide on carbon mineralization in the presence of 1 M sodium glycinate at 25, 50, 75, and 90 °C reacted for 3 hours in (a), with different concentration of 0, 0.5, 1, and 3 M sodium glycinate at 75 °C for 3 hours in (b), with 1 M sodium glycinate at 75 °C for different reaction time of 1, 3, and 5 hours in (c). All the experiments are performed at  $P_{CO_2} = 1$  atm and a stirring rate of 300 rpm. Peaks are identified based on the crystallographic data reported for calcium oxide, calcite, vaterite, and aragonite. Crystallographic phases are identified based on the data presented in references (Chessin et al., 1965; Dal Negro & Ungaretti, 1971; Müller, 2010; Petch, 1961; Primak et al., 1948; J. Wang & Becker, 2009). The morphological changes of the CaO samples on carbonation are probed by SEM with (d) representing the unreacted CaO, (e) representing the reaction with H<sub>2</sub>O at 75 °C for 3 hours, and (f) representing CaO after the reaction with 1 M sodium glycinate at 75 °C for 3 hr (Chessin et al., 1965; Negro & Ungaretti, 1971; Maslen et al., 1993; Müller, 2010; Wang & Becker, 2009). ..... 136

Figure 7.7 Changes in the phases present in calcium silicate on carbon mineralization in the presence of 1 M sodium glycinate at 25, 50, 75, and 90 °C reacted for 3 hours in (a), with different concentration of 0, 0.5, 1, and 3 M sodium glycinate at 75 °C for 3 hours in (b), with 1 M sodium glycinate at 75 °C for different reaction time of 1, 3, and 5 hours in (c). All the experiments are performed at  $P_{CO_2} = 1$  atm and a stirring rate of 300 rpm. Peaks are identified based on the crystallographic data reported for calcium silicate (or wollastonite), calcite, vaterite, and aragonite. Crystallographic phases are identified based on the data presented in references (Chessin et al., 1965; Negro & Ungaretti, 1971; Müller, 2010; Petch, 1961; Primak et al., 1948; Wang & Becker, 2009). The morphological changes of the CaSiO<sub>3</sub> samples on carbonation are probed by SEM with (d) representing the unreacted CaSiO<sub>3</sub>, (e) representing

the reaction with H <sub>2</sub> O at 75 °C for 3 hours, and (f) representing CaSiO <sub>3</sub> after the reaction with 1 M sodium glycinate at 75 °C for 3 hr (Chessin et al., 1965; Negro & Ungaretti, 1971; Maslen et al., 1993; Müller, 2010; Wang & Becker, 2009).	138
Figure 8.1 Schematic representation of using regenerable solvents to capture and remove CO <sub>2</sub> via carbon mineralization.	160
Figure 8.2 Total carbon (TC), Organic carbon (OC), and Inorganic Carbon (OC) concentrations in the aqueous phase as a function of the concentration of MEA (a-1) and sodium glycinate (b-1) are shown. pH as a function of MEA concentration (a-2) and sodium glycinate concentration (b-2) are also shown.	161
Figure 8.3 Extent of carbon mineralization of CaO (a), CaSiO <sub>3</sub> (b), and MgO (c) reacted in the presence of 0 eq mol/L, 0.5 eq mol/L, 1.0 eq mol/L, and 2.5 eq mol/L monoethanolamine (MEA, black square), sodium glycinate (NaGly, red circle), 2-amino-2-methylpropanol (AMP, blue upward facing triangle), and 1,8-diazabicyclo [5.4.0] undec-7-ene (DBU, green downfacing triangle). All the experiments are performed at 75 °C, pCO <sub>2</sub> = 1 atm, reaction time of 3 hours and a stirring rate of 300 rpm.	162
Figure 8.4 Identification of the species in the aqueous phase obtained after the carbon mineralization of (a) CaO, (b) CaSiO <sub>3</sub> , and (c) MgO reacted in monoethanolamine (MEA) using ATR-FTIR analyses. Species are identified based on spectra reported in reference.	164
Figure 8.5 Identification of the species in the aqueous phase obtained after the carbon mineralization of (a) CaO, (b) CaSiO <sub>3</sub> , and (c) MgO reacted in sodium glycinate (NaGly) using ATR-FTIR analyses. Species are identified based on spectra reported in references (Ahmed et al., 2013; Doki et al., 2004; Ramachandran et al., 2007).	166

Figure 8.6 Identification of the species in the aqueous phase obtained after the carbon mineralization of (a) CaO, (b) CaSiO<sub>3</sub>, and (c) MgO reacted in 2-amino-2-methylpropanol (AMP) using ATR-FTIR analyses. Species are identified based on spectra reported in references (Ahmed et al., 2013; Doki et al., 2004; Ramachandran et al., 2007)..... 168

Figure 8.7 Identification of the species in the aqueous phase obtained after the carbon mineralization of (a) CaO, (b) CaSiO<sub>3</sub>, and (c) MgO reacted in 1,8-diazabicyclo [5.4.0] undec-7-ene (DBU) using ATR-FTIR analyses. Species are identified based on spectra reported in references (Ahmed et al., 2013; Doki et al., 2004; Ramachandran et al., 2007). ..... 170

Figure 8.8 Identification of the species in the solid product obtained after the carbon mineralization of CaO in (a) monoethanolamine (MEA), (b) sodium glycinate (NaGly), (c) 2-amino-2-methylpropanol (AMP), and (d) 1,8-diazabicyclo [5.4.0] undec-7-ene (DBU) using ATR-FTIR analyses. Species are identified based on spectra reported in references (Al-Hosney & Grassian, 2005; Böke et al., 2004; Plav et al., 1999)..... 171

Figure 8.9 Identification of the species in the solid product obtained after the carbon mineralization of CaSiO<sub>3</sub> in (a) monoethanolamine (MEA), (b) sodium glycinate (NaGly), (c) 2-amino-2-methylpropanol (AMP), and (d) 1,8-diazabicyclo [5.4.0] undec-7-ene (DBU) using ATR-FTIR analyses. Species are identified based on spectra reported in references (Al-Hosney & Grassian, 2005; Basavaraj et al., 2019; Böke et al., 2004; Plav et al., 1999; Thompson et al., 2012). ..... 172

Figure 8.10 Identification of the species in the solid product obtained after the carbon mineralization of MgO in (a) monoethanolamine (MEA), (b) sodium glycinate (NaGly), (c) 2-amino-2-methylpropanol (AMP), and (d) 1,8-diazabicyclo [5.4.0] undec-7-ene (DBU)

using ATR-FTIR analyses. Species are identified based on spectra reported in references (Hopkinson et al., 2012; Morgan et al., 2015)..... 173

Figure 8.11 Identification of the crystalline species in the solid product obtained after the carbon mineralization of CaO in (a) monoethanolamine (MEA), (b) sodium glycinate (NaGly), (c) 2-amino-2-methylpropanol (AMP), and (d) 1,8-diazabicyclo [5.4.0] undec-7-ene (DBU) using XRD analyses. Crystallographic phases are identified based on the data presented in references (Chessin et al., 1965; Dal Negro & Ungaretti, 1971; Maslen et al., 1993; Müller, 2010; Petch, 1961; Primak et al., 1948; J. Wang & Becker, 2009)..... 174

Figure 8.12 Identification of the crystalline species in the solid product obtained after the carbon mineralization of CaSiO<sub>3</sub> in (a) monoethanolamine (MEA), (b) sodium glycinate (NaGly), (c) 2-amino-2-methylpropanol (AMP), and (d) 1,8-diazabicyclo [5.4.0] undec-7-ene (DBU) using XRD analyses. Crystallographic phases are identified based on the data presented in references (Chessin et al., 1965; Dal Negro & Ungaretti, 1971; Maslen et al., 1993; Müller, 2010; Petch, 1961; Primak et al., 1948; Wang & Becker, 2009). ..... 175

Figure 8.13 Identification of the crystalline species in the solid product obtained after the carbon mineralization of MgO in (a) monoethanolamine (MEA), (b) sodium glycinate (NaGly), (c) 2-amino-2-methylpropanol (AMP), and (d) 1,8-diazabicyclo [5.4.0] undec-7-ene (DBU) using XRD analyses. Crystallographic phases are identified based on the data presented in references (Ballirano et al., 2013; Davies & Bubela, 1973; Ming & Franklin, 2010; Y. Wang et al., 2020)..... 176

## LIST OF TABLES

Table 3.1 Composition of lizardite.....	33
Table 3.2 Summary of the surface area, cumulative pore volume, and mean particle size of untreated serpentine at 25 °C and heat-treated at 350 °C, 650 °C, and 900 °C. ....	34
Table 7.1 Main infrared band assignments of the species present in the CO <sub>2</sub> –Na-glycinate–H <sub>2</sub> O system. The symbols $\nu$ , $\nu_a$ and $\delta$ indicate the stretching mode, the asymmetric stretching mode, and the bending mode of the relevant molecules, respectively (Davis & Oliver, 1972; Frasco, 1964; Hisatsune, 1984; Milella & Mazzotti, 2019; Pretsch, et al., 2009).....	129
Table 8.1 Physical and chemical properties of the solvents used for integrated CO <sub>2</sub> capture and carbon mineralization.....	154
Table 8.2 Summary of the reactions representing CO <sub>2</sub> hydration, CO <sub>2</sub> capture and speciation associated with various solvents including monoethanolamine (MEA), sodium glycinate (NaGly), 2-amino-2-methylpropanol (AMP), and 1,8-diazabicyclo [5.4.0] undec-7-ene (DBU).....	155
Table 8.3 Summary of extents of carbonation of CaO, CaSiO <sub>3</sub> , and MgO at 75°C, CO <sub>2</sub> partial pressure of 1 atm, reaction time of 3 hours, 15 wt% solid, and a stirring rate of 300 rpm. The carbonate content used to obtain the extent of carbon mineralization is based on Thermogravimetric Analysis (TGA).....	158

## ACKNOWLEDGEMENTS

I would like to thank my advisor Prof Greeshma Gadikota at Cornell University for patiently guiding my research, supporting my experiments, and the countless hours helping me with writing and editing. Dr. Gadikota has great passion for science and research in service of the scientific and broader community. I will always see her as a leader.

I would also like to thank my Ph.D. committee members: Prof. Qi Li and Prof. Matthew Reid in the School of Civil and Environmental Engineering at Cornell University. I really appreciate their guidance. I am very grateful for the support of several collaborators at national labs including Dr. Radu Custelcean at Oak Ridge National Laboratory for his guidance on CO<sub>2</sub> capture and Dr. Yun Liu at National Institution of Standard and Technology for his guidance and help on neutron scattering measurements. A warm thank you to Dr. Soenke Seifert, Dr. Ivan Kuzmenko, Dr. Jan Ilavksy, Dr. Suresh Narayan and Dr. Qingteng Zhang for supporting synchrotron experiments at the Advanced Photon Source at Argonne National Laboratory.

I am grateful for the timely help and encouragement of all the members from Gadikota Research Group: Sohaib Mohammed, Hassnain Asgar, Tianhe Yin, Xun Gao, Prince Ochonma, Shufan Yin, Allison Hohenshil, Erin Huang, and Nurhilya Damiri. I would also like to thank all my classmates in the school of civil and environmental engineering at Cornell for their help and support. The support of our administrative staff in the School of Civil and Environmental Engineering has been essential in helping me conduct my experiments and work towards my thesis in a timely manner.

Last but the most important, I am very grateful for the support and encouragement of my parents. I am appreciative of the happiness that my cat, Schrodinger brings to my life. I would like

to thank all my friends at Cornell University for their enthusiastic support and unconditional kindness.

*To my beloved parents*

# CHAPTER 1

## INTRODUCTION

Fossil-based energy resources from subsurface environments provide more than 82% of our energy needs. The consumption of these resources contributes to about 79% of global CO<sub>2</sub> emissions (Mission Innovation, 2018). Atmospheric CO<sub>2</sub> concentrations have increased from about 280 ppmv before the industrial age to over 400 ppmv now, which contributes to adverse environmental impacts. Thus, meeting our growing need for energy and resources while managing CO<sub>2</sub> emissions more effectively is one of our grand societal challenges (Mission Innovation, 2018; National Academies of Sciences Engineering and Medicine, 2019). In order to reduce the environmental impacts arising from CO<sub>2</sub> emissions, carbon emissions into air have to be reduced at the rate of 1 GtC/year by 2025 and 4 GtC/year by 2050 (Reichle et al., 1999).

In the recent decades, various approaches to remove CO<sub>2</sub> including ocean disposal and biological fixation have been considered (Park et al., 2003; Reichle et al., 1999). One of the approaches that has high transformation potential and can be integrated with engineered processes and with natural environment is carbon mineralization. Carbon mineralization involves converting CO<sub>2</sub> into solid inorganic carbonates. Carbon mineralization is a versatile pathway that can be adapted for CO<sub>2</sub> capture, utilization, storage, and removal. The thermodynamically downhill or exothermic features and environmentally benign features are unique to carbon mineralization (Fauth et al., 2000; Lackner, 2002; Seifritz, 1990).

Carbon mineralization can be engineered *in-situ* in subsurface environments and in engineered or *ex-situ* processes (Oelkers et al., 2008; Sanna et al., 2014). In *in situ* carbon mineralization, the CO<sub>2</sub>-bearing fluids are introduced into calcium or magnesium-bearing rocks

and minerals and the earth is harnessed as a reactor system to convert CO<sub>2</sub> into Ca- or Mg-bearing carbonates. In contrast, *ex-situ* carbon mineralization pathways can be engineered for specific compositions of the alkaline reactants, aqueous compositions, and partial pressures of the gases to direct well-controlled reactions (Gadikota, 2020). While *in-situ* carbon mineralization harnesses the geothermal gradient of earth, the physico-chemical parameters associated with *ex-situ* mineralization reactions can be tuned to specific kinetics of carbon mineralization. The advantage of *ex-situ* mineralization is that value-added products can be produced without monitoring (Azdarpour et al., 2015; Chiang & Pan, 2017; Hopkins, 2008; Oelkers et al., 2008; Power et al., 2013; Sanna et al., 2014).

The key technological challenge in scaling up carbon mineralization processes has been the slow kinetics, formation of metastable by-products, and a limited understanding of how the feedbacks associated with the chemical and morphological evolution of the reactants influence the kinetics. If carbon mineralization pathways can be engineered to capture and store CO<sub>2</sub> in flue gas streams, they present a viable and scalable alternative to the conventional carbon capture, utilization, and storage (CCUS) approaches where CO<sub>2</sub> is captured from flue gas streams, compressed, and transported to be stored in subsurface geologic environments (Mission Innovation, 2018; Gadikota et al., 2015; Gadikota & Park, 2015; Lackner, 2002; Park & Fan, 2004; Reichle et al., 1999).

Various fluid-solid reaction configurations have been explored to accelerate engineered carbon mineralization. Direct gas-solid carbon mineralization pathways require temperatures as high as 300 °C and CO<sub>2</sub> partial pressures of 150 atm to convert serpentine into carbonates (Lackner, 2002; Huijgen & Comans, 2003; Lackner et al., 1997). As an alternative, gas-liquid-solid reactions pathways that facilitate the dissolution of alkaline minerals and ease mass transfer

for carbon mineralization were developed as lower temperature alternatives to high temperature gas-solid reaction pathways (Gerdemann et al., 2007; Park et al., 2008). To accelerate the dissolution of minerals at low pH independently from carbonate formation which occurs at high pH, pH swing approaches were proposed (Park et al., 2003; Park & Fan, 2004; Sanna et al., 2014; Sanna et al., 2012). Alternatively, accelerated carbon mineralization is achieved in a single-step at elevated temperatures and CO<sub>2</sub> partial pressures, which is analogous to in-situ carbon mineralization during carbon storage (Gadikota et al., 2014; Gadikota & Park, 2015; Gerdemann et al., 2007; O'Connor et al., 2005).

To accelerate the kinetics of these carbon mineralization reactions, feedstock activation, addition of chemicals, biological enhancement, and reactor integration have been proposed (Park et al., 2003; Park & Fan, 2004; Sanna et al., 2014; Sanna et al., 2012). Common methods for feedstock activation involve thermal treatment and grinding, which increase the reactive surface area. Chemical and biological routes for enhancing carbon mineralization have been extensively explored. For example, inorganic and organic acids have been proposed to accelerate the dissolution of minerals, bicarbonates have been utilized to buffer the pH of these reacting systems, and carbonic anhydrase, a biomimetic enzyme has been suggested for CO<sub>2</sub> capture (Gadikota and Park, 2015). Further, the use of abundant brine solutions for carbon mineralization has been explored (Gadikota et al., 2014). This approach is a cost effective and environmentally benign approach as an alternative to harnessing fresh water with low levels of salinity. One of the challenges associated with enhancing carbon mineralization lies in the low solubility of CO<sub>2</sub> in water, which challenges the use of dilute CO<sub>2</sub>-bearing flue gas streams. While carbonic anhydrase has been proposed to enhance CO<sub>2</sub> hydration to produce bicarbonate ions, challenges associated with scalability and energy efficient regeneration remain. To address these challenges, integrated

CO<sub>2</sub> capture and carbon mineralization pathways with inherent regeneration of the solvents for capturing CO<sub>2</sub> need to be developed. Additionally, the temporal evolution of structure of the alkaline materials and the associated reactivity needs to be delineated to develop mechanistic insights with the intent of intervening in these reaction pathways to accelerate the kinetics. Therefore, the development of *in-operando* characterization methods is essential to provide comprehensive mechanistic insights into carbon mineralization reactions.

Given the scientific challenges in accelerating the conversion of CO<sub>2</sub> to carbonates, the research objectives of this study are four-fold: **(i)** design novel integrated reaction pathways for integrated CO<sub>2</sub> capture and carbon mineralization with the inherent regeneration of the CO<sub>2</sub> capture solvent and **(ii)** advance mechanistic insights into carbon mineralization by harnessing *in-operando* X-ray scattering and spectroscopic measurements. Thus, the chapters in this thesis are organized to address these objectives as discussed below.

Chapter 2 provides a detailed thermodynamic analysis of the carbon mineralization process, including the inorganic carbon (carbonate ions, bicarbonate ions, and carbonic acid) speciation and organic carbon speciation when using regenerable solvents. Based on this background, the research objectives of this study are described in this chapter.

Chapter 3 discusses the structural and morphological basis underlying enhancements in the reactivity of less reactive minerals (e.g., lizardite) using *in-operando* cross-scale X-ray scattering measurements. Latest advancements in ultra-small angle X-ray scattering (USAXS), small angle X-ray scattering (SAXS), wide angle X-ray scattering (WAXS) are harnessed to simultaneously provide insights into the changes in the crystal structure and the nano-scale morphology of earth abundant and hydrated magnesium silicate minerals as they are heated to enhance their reactivity.

These results are further validated using morphological analyses including porosity, particle size and surface area. The detailed transformations of lamellar serpentine to a pseudo-amorphous state on heating and the subsequent conversion to denser crystalline phases are elucidated. The transformation of lamellar lizardite to its pseudo-amorphous state corresponded to an increase in the porosity and surface area, while the formation of crystalline phases reduced the porosity and surface area while increasing the particle size. An overview of the solid reaction experimental set-up for USAXS/SAXS/WAXS measurements are discussed. These findings were published in *Fuel* (Liu and Gadikota, 2018).

Chapter 4 discusses the use of in-operando cross-scale characterization operations to prove the phase evolution and the corresponding textural changes as calcium hydroxide is converted to calcium carbonate under the continuous flow of CO<sub>2</sub> at an ambient pressure of 1 atm and on heating continuously from 30 °C to 500 °C. The feasibility of probing structural and microstructural evolution of reactive alkaline solids in gaseous environments is demonstrated using cross-scale X-ray scattering measurements for the first time. These findings were published in *Geosciences* (Liu and Gadikota, 2018).

Chapter 5 reports the effectiveness of single-step and two-step integrated reactive CO<sub>2</sub> capture and carbon mineralization approaches with inherent chemical regeneration of the solvents such as monoethanolamide (MEA) via hybrid absorption-reactive crystallization pathways. The carbonate conversions of calcium oxide and calcium silicates and the corresponding morphologies of these materials are discussed. These studies were published in *Energy and Fuels* (Liu and Gadikota, 2018).

Chapter 6 investigates single-step reactive CO<sub>2</sub> capture and carbon mineralization of magnesium oxide (MgO) using MEA as the solvent. The enhancement in carbon mineralization with inherent looping of the CO<sub>2</sub> capture solvents via CO<sub>2</sub> capture and release states is reported. The structural and morphological evolution as magnesium oxide is reacted to produce magnesium carbonates are reported using cross-scale X-ray scattering approaches. These studies were published in *Sustainable Energy and Fuels* (Liu and Gadikota, 2020).

Chapter 7 explores the usage of amino acid salts such as sodium glycinate as an alternative to primary amines such as MEA for integrated reactive CO<sub>2</sub> capture and mineralization using alkaline solids such as CaO and CaSiO<sub>3</sub>. The influence of sodium glycinate concentration, temperature, and reactive time on integrated CO<sub>2</sub> capture and carbon mineralization are reported. Na-glycinate undergoes multiple CO<sub>2</sub> capture and regeneration cycles in the aqueous phase facilitating greater availability of aqueous carbon species for carbonate precipitation. These results are reported in *Fuel* (Liu and Gadikota, 2020).

Chapter 8 contrasts the effectiveness of various solvents such as monoethanolamine (MEA, primary amine), sodium glycinate (amino acid salt), 2-amino-2-methylpropanol (AMP, hindered amine), and 1,8-diazabicyclo [5.4.0] undec-7-ene (DBU, cyclical amine) on the carbon mineralization of CaO, CaSiO<sub>3</sub>, and MgO in integrated single-step CO<sub>2</sub> capture and reactive crystallization. Thermodynamic analyses of CO<sub>2</sub> capture in MEA and sodium glycinate are discussed to provide fundamental insights into the pH and temperature conditions that aid accelerated carbon mineralization. These outcomes from these studies were reported in *Energy and Fuels* (2021).

Finally, the key findings, conclusions and recommendations for future work based on the findings reported in this thesis are summarized in Chapter 9.

## CHAPTER 2

### BACKGROUND

*Some of the contents of this chapter have been adapted from the paper published at Liu, M., Hohenshil, A., & Gadikota, G. “Integrated CO<sub>2</sub> Capture and Removal Via Carbon Mineralization with Inherent Regeneration of Aqueous Solvents.” *Energy & Fuels* (2021).*

One of the key rate-limiting steps in accelerating CO<sub>2</sub> capture and carbon mineralization is CO<sub>2</sub> hydration in the aqueous phase. Increasing the solubility or hydration of CO<sub>2</sub> in water is crucial for increasing the concentrations of bicarbonate and carbonate ions necessary for producing solid inorganic carbonates. Therefore, the thermodynamics underlying CO<sub>2</sub> capture and the reactions of interest are summarized in this chapter as background for the subsequent chapters.

#### 2.1 CO<sub>2</sub> Hydration

##### 2.1.1 Inorganic Carbon Speciation in the Absence of CO<sub>2</sub> Capture Solvents

There are three steps in mineralization: CO<sub>2</sub> hydration, dissolution of the minerals, and carbonates precipitation. Each step could become the rate limiting step based on the conditions.

When it comes to CO<sub>2</sub> hydration, carbonate and bicarbonate, carbonic acid species could form in the aqueous phase (**Reactions 2.2-2.4**). In case of an “open system” in which the CO<sub>2</sub> pressure is held constant, the concentration of the carbonic acid remains the same at different pH at equilibrium. Higher dissolved inorganic carbon concentrations are noted at higher pH conditions in an open system. Carbonate concentrations that are needed for carbon mineralization increase with pH, which favors the formation of solid inorganic carbonates.





In the open system, the partial pressure of  $\text{CO}_2$  denoted by  $P_{\text{CO}_2}$  is constant. The concentration of the carbonic acid (**Equation 2.1**), bicarbonate (**Equation 2.2**), and carbonate (**Equation 2.3**) species in the open system at different pH conditions is calculated using the equilibrium constants listed above.

According to Reaction 2.2:

$$[\text{H}_2\text{CO}_3^*_{(aq)}] = K_h P_{\text{CO}_2} \quad \text{Eq 2.1}$$

According to Reaction 2.3:

$$[\text{HCO}_3^-_{(aq)}] = \frac{[\text{H}_2\text{CO}_3^*_{(aq)}] {}^aK_{a1}}{[\text{H}^+_{(aq)}]} = \frac{K_h P_{\text{CO}_2} {}^aK_{a1}}{[\text{H}^+_{(aq)}]} \quad \text{Eq 2.2}$$

According to Reaction 2.4:

$$[\text{CO}_3^{2-}_{(aq)}] = \frac{[\text{HCO}_3^-_{(aq)}] {}^aK_{a2}}{[\text{H}^+_{(aq)}]} = \frac{K_h P_{\text{CO}_2} {}^aK_{a1} {}^aK_{a2}}{[\text{H}^+_{(aq)}]^2} \quad \text{Eq 2.3}$$

The concentrations of carbonic acid, bicarbonate ( $\text{HCO}_3^-$ ), and carbonate ( $\text{CO}_3^{2-}$ ) species at  $\text{CO}_2$  concentrations of 400 ppm and 1 atm are shown in **Figures 2.1 (a)** and **2.1 (b)**. It is important to note that the concentrations of carbonic acid, bicarbonate ( $\text{HCO}_3^-$ ), and carbonate ( $\text{CO}_3^{2-}$ ) species are several orders of magnitude higher in open systems where the  $p\text{CO}_2$  is 1 atm, compared to the system where ambient air with a  $p\text{CO}_2$  of 400 ppm. These speciation calculations

provide the thermodynamic basis for enhanced carbon mineralization at higher partial pressures of CO<sub>2</sub> as opposed to lower concentrations.

Unlike in open systems where the concentrations of dissolved inorganic species increase with pH, the total carbon content is constant in closed systems. Thus, the total concentration of carbonic acid, bicarbonate and carbonate species is the same since there is no additional carbon source. In this case, the total inorganic carbon concentration would follow **Equation 2.4** The concentrations of carbonic acid, bicarbonate and carbonate species are calculated using **Equations 2.2 -2.4**. The total inorganic carbon content in the aqueous phase is determined using the following expressions. The concentration of the carbonic acid (**Equation 2.5**), bicarbonate (**Equation 2.6**), and carbonate (**Equation 2.7**) species in the close system at different pH could be calculated using the equilibrium constants listed above.

$$C_{TOT} = [H_2CO_3^*(aq)] + [HCO_3^-(aq)] + [CO_3^{2-}(aq)] = [H_2CO_3^*(aq)] + \frac{[H_2CO_3^*(aq)]^a K_{a1}}{[H^+(aq)]} + \frac{[H_2CO_3^*(aq)]^a K_{a1}^a K_{a2}}{[H^+(aq)]^2} = [H_2CO_3^*(aq)] \left\{ 1 + \frac{^a K_{a1}}{[H^+(aq)]} + \frac{^a K_{a1}^a K_{a2}}{[H^+(aq)]^2} \right\} \quad \text{Eq 2.4}$$

$$[H_2CO_3^*(aq)] = \frac{C_{TOT}}{1 + \frac{^a K_{a1}}{[H^+(aq)]} + \frac{^a K_{a1}^a K_{a2}}{[H^+(aq)]^2}} \quad \text{Eq 2.5}$$

$$[HCO_3^-(aq)] = \frac{[H_2CO_3^*(aq)]^a K_{a1}}{[H^+(aq)]} = \frac{C_{TOT}^a K_{a1}}{[H^+(aq)] + ^a K_{a1} + \frac{^a K_{a1}^a K_{a2}}{[H^+(aq)]}} \quad \text{Eq 2.6}$$

$$[CO_3^{2-}(aq)] = \frac{[HCO_3^-(aq)]^a K_{a2}}{[H^+(aq)]} = \frac{C_{TOT}^a K_{a1}^a K_{a2}}{[H^+(aq)]^2 + ^a K_{a1}[H^+(aq)] + ^a K_{a1}^a K_{a2}} \quad \text{Eq 2.7}$$

Using these expressions, the total dissolved inorganic carbon at pCO<sub>2</sub> of 400 ppm is determined to be 1.6 x 10<sup>-5</sup> M at pH = 5.55. At pCO<sub>2</sub> of 1 atm, the total dissolved inorganic carbon

is 0.035 M at pH = 3.85. The concentrations of carbonic acid, bicarbonate, and carbonate species at different pH conditions at pCO<sub>2</sub> of 400 ppm and 1 atm are shown in **Figure 2.1 (c)** and **Figure 2.1 (d)**, respectively. In closed systems, carbonate species are dominant at pH greater than 10. The inorganic carbon species in closed and open systems in the absence of CO<sub>2</sub> capture solvents is the benchmark for contrasting the enhancements in inorganic carbon that can be achieved using CO<sub>2</sub> capture solvents.

### **2.1.2 Inorganic Carbon Speciation in the Presence of CO<sub>2</sub> Capture Solvents in the Open System**

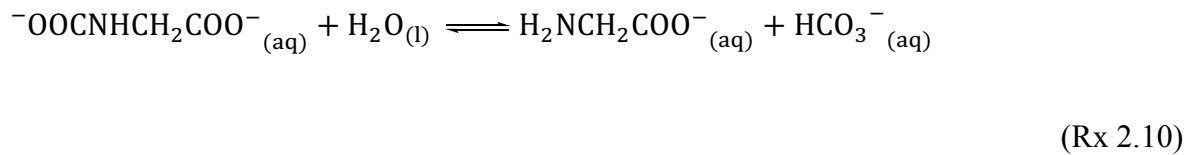
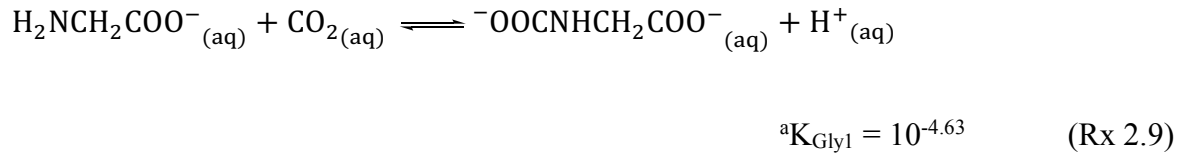
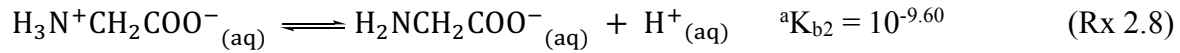
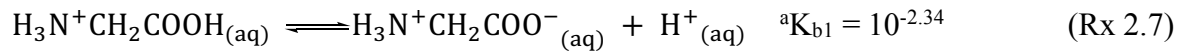
One approach to accelerate carbon mineralization is by increasing the concentration of dissolved carbonate species. This objective can be achieved by using CO<sub>2</sub> capture solvents. Coupling carbon mineralization with the regeneration of the CO<sub>2</sub> capture solvents is exothermically favorable and eliminates the need for high temperatures needed for conventional solvent regeneration. Based on the structure of the solvent, CO<sub>2</sub> capture using aqueous amines proceeds through mainly two different mechanisms: amines that capture CO<sub>2</sub> via the formation of carbamates such as primary (e.g. MEA) and secondary (e.g. DEA) amines, and amines that capture CO<sub>2</sub> via the formation of bicarbonates such as sterically hindered (e.g. AMP) and tertiary (e.g. MDEA) amines. (Ji et al., 2018) For example, CO<sub>2</sub> capture in primary amines such as monoethanolamine (MEA) proceeds via the reaction of two molecules of MEA with one molecule of CO<sub>2</sub> to produce a carbamate ion (**Reactions 2.5** and **2.6**) (Ji et al., 2018). Alternatively, CO<sub>2</sub> capture in amino acid salts such as sodium glycinate solvents (**Reaction 2.7-2.10**), (Caplow, 1968; Guo et al., 2013; Vaidya et al., 2010) sterically hindered amines such as 2-amino-2-methylpropanol (AMP) (**Reaction 2.11** and **2.12**), (Barzagli et al., 2013; Caplow, 1968; Mandal et al., 2003; Zhang et al., 2008) and cyclical amines such as 1,8-diazabicyclo [5.4.0] undec-7-ene

(DBU) (Reaction 2.13) (Heldebrant et al., 2005; Kaupmees et al., 2014) proceed via the formation of bicarbonate ions. Unlike with primary amines such as MEA, one molecule of sodium glycinate or DBU captures one molecule of CO<sub>2</sub>.

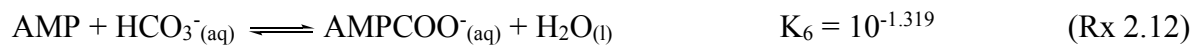
### *CO<sub>2</sub> Capture Using MEA*



Sodium glycinate



### *CO<sub>2</sub> Capture Using AMP*



### *CO<sub>2</sub> Capture Using DBU*



Combining with the reactions of CO<sub>2</sub> hydration in water in the last section, the concentrations of inorganic and organic carbon species could be calculated using the following equations and plotted in **Figure 2.2 (a)**. The change of pH, concentration of different carbon sources with different MEA concentration is plotted in **Figure 2.3 (a)**.

According to the Reaction 2.5

$$[\text{MEA}\text{H}^+_{(\text{aq})}] = \frac{[\text{MEA}_{(\text{aq})}][\text{H}^+_{(\text{aq})}]}{K_5} \quad \text{Eq 2.8}$$

According to Reaction 2.6:

$$[\text{MEACOO}^-_{(\text{aq})}] = [\text{MEA}_{(\text{aq})}] [\text{HCO}_3^-_{(\text{aq})}] K_6 \quad \text{Eq 2.9}$$

The starting MEA concentration is known, so the MEA<sub>TOT</sub> is constant during the reaction.

$$\text{MEA}_{\text{TOT}} = [\text{MEA}_{(\text{aq})}] + [\text{MEA}\text{H}^+_{(\text{aq})}] + [\text{MEACOO}^-_{(\text{aq})}] \quad \text{Eq 2.10}$$

In this case, the concentration of MEA could be calculated as:

$$[\text{MEA}_{(\text{aq})}] = \frac{\text{MEA}_{\text{TOT}}}{1 + \frac{[\text{H}^+_{(\text{aq})}]}{K_5} + \frac{K_{\text{h}} P_{\text{CO}_2} {}^a K_{\text{a1}} K_6}{[\text{H}^+_{(\text{aq})}]}} \quad \text{Eq 2.11}$$

The concentration of MEAH<sup>+</sup> is

$$[\text{MEA}\text{H}^+_{(\text{aq})}] = \frac{[\text{MEA}_{(\text{aq})}][\text{H}^+_{(\text{aq})}]}{K_5} = \frac{\text{MEA}_{\text{TOT}}[\text{H}^+_{(\text{aq})}]^2}{K_5[\text{H}^+_{(\text{aq})}] + [\text{H}^+_{(\text{aq})}]^2 + K_{\text{h}} P_{\text{CO}_2} {}^a K_{\text{a1}} K_5 K_6} \quad \text{Eq 2.12}$$

The concentration of organic carbon MEACOO<sup>-</sup> is

$$[\text{MEACOO}^-_{(\text{aq})}] = [\text{MEA}_{(\text{aq})}] [\text{HCO}_3^-_{(\text{aq})}] K_6 = \frac{\text{MEA}_{\text{TOT}} K_h P_{\text{CO}_2} {}^aK_{a1} {}^aK_{a2} K_5 K_6}{K_5 [\text{H}^+_{(\text{aq})}]^2 + [\text{H}^+_{(\text{aq})}]^3 + K_h P_{\text{CO}_2} {}^aK_{a1} K_5 K_6 [\text{H}^+_{(\text{aq})}]} \quad \text{Eq 2.13}$$

Similarly, the speciation of sodium glycinate could be calculated in the similar ways and the concentrations of inorganic and organic carbon species are plotted in **Figure 2.2 (b)**. The change of pH, concentration of different carbon sources with different sodium glycinate concentration is plotted in **Figure 2.3 (b)**.

$$[\text{H}_3\text{N}^+\text{CH}_2\text{COO}^-_{(\text{aq})}] = \frac{[\text{H}_2\text{NCH}_2\text{COO}^-_{(\text{aq})}][\text{H}^+_{(\text{aq})}]}{{}^aK_{b2}} \quad \text{Eq 2.14}$$

$$[\text{H}_3\text{N}^+\text{CH}_2\text{COOH}_{(\text{aq})}] = \frac{[\text{H}_3\text{N}^+\text{CH}_2\text{COO}^-_{(\text{aq})}][\text{H}^+_{(\text{aq})}]}{{}^aK_{b1}} = \frac{[\text{H}_2\text{NCH}_2\text{COO}^-_{(\text{aq})}][\text{H}^+_{(\text{aq})}]^2}{{}^aK_{b1} {}^aK_{b2}} \quad \text{Eq 2.15}$$

$$[\text{}^- \text{OOCNHCH}_2\text{COO}^-_{(\text{aq})}] = \frac{[\text{H}_2\text{NCH}_2\text{COO}^-_{(\text{aq})}][\text{CO}_2_{(\text{aq})}] {}^aK_{\text{Gly1}}}{[\text{H}^+_{(\text{aq})}]} \quad \text{Eq 2.16}$$

$$\text{Gly}_{\text{TOT}} = [\text{H}_3\text{N}^+\text{CH}_2\text{COOH}_{(\text{aq})}] + [\text{H}_3\text{N}^+\text{CH}_2\text{COO}^-] + [\text{H}_2\text{NCH}_2\text{COO}^-_{(\text{aq})}] + [\text{}^- \text{OOCNHCH}_2\text{COO}^-_{(\text{aq})}] \quad \text{Eq 2.17}$$

$$[\text{H}_2\text{NCH}_2\text{COO}^-_{(\text{aq})}] = \frac{\text{Gly}_{\text{TOT}}}{\left\{ \frac{[\text{H}^+_{(\text{aq})}]^2}{{}^aK_{b1} {}^aK_{b2}} + \frac{[\text{H}^+_{(\text{aq})}]}{{}^aK_{b2}} + 1 + \frac{[\text{CO}_2_{(\text{aq})}] {}^aK_{\text{Gly1}}}{[\text{H}^+_{(\text{aq})}]} \right\}} \quad \text{Eq 2.18}$$

The speciation of AMP could be calculated in the similar ways and the concentrations of inorganic and organic carbon species are plotted in **Figure 2.2 (c)**. The change of pH, concentration of different carbon sources with different AMP concentration is plotted in **Figure 2.3 (c)**.

$$[\text{AMPCOO}^-_{(\text{aq})}] = [\text{AMP}_{(\text{aq})}] [\text{HCO}_3^-_{(\text{aq})}] K_6 \quad \text{Eq 2.19}$$

$$\text{AMP}_{\text{TOT}} = [\text{AMP}_{(\text{aq})}] + [\text{AMPH}^+_{(\text{aq})}] + [\text{AMPCOO}^-_{(\text{aq})}] \quad \text{Eq 2.20}$$

$$[\text{AMP}_{(\text{aq})}] = \frac{\text{AMP}_{\text{TOT}}}{1 + \frac{[\text{H}^+_{(\text{aq})}]}{K_5} + \frac{K_h \text{PCO}_2 {}^a K_{a1} K_6}{[\text{H}^+_{(\text{aq})}]}} \quad \text{Eq 2.21}$$

$$[\text{AMPH}^+_{(\text{aq})}] = \frac{[\text{AMP}_{(\text{aq})}] [\text{H}^+_{(\text{aq})}]}{K_5} = \frac{\text{AMP}_{\text{TOT}} [\text{H}^+_{(\text{aq})}]^2}{K_5 [\text{H}^+_{(\text{aq})}] + [\text{H}^+_{(\text{aq})}]^2 + K_h \text{PCO}_2 {}^a K_{a1} K_5 K_6} \quad \text{Eq 2.22}$$

$$[\text{AMPCOO}^-_{(\text{aq})}] = [\text{AMP}_{(\text{aq})}] [\text{HCO}_3^-_{(\text{aq})}] K_6 = \frac{\text{AMP}_{\text{TOT}} K_h \text{PCO}_2 {}^a K_{a1} {}^a K_{a2} K_5 K_6}{K_5 [\text{H}^+_{(\text{aq})}]^2 + [\text{H}^+_{(\text{aq})}]^3 + K_h \text{PCO}_2 {}^a K_{a1} K_5 K_6 [\text{H}^+_{(\text{aq})}]} \quad \text{Eq 2.23}$$

The speciation of DBU could be calculated in the similar ways and the concentrations of inorganic and organic carbon species are plotted in **Figure 2.2 (d)**. The change of pH, concentration of different carbon sources with different MEA concentration is plotted in **Figure 2.3 (d)**.

$$[\text{DBUH}^+_{(\text{aq})}] = \frac{[\text{DBU}_{(\text{aq})}] [\text{H}^+_{(\text{aq})}]}{K_5} \quad \text{Eq 2.24}$$

$$\text{DBU}_{\text{TOT}} = [\text{DBU}_{(\text{aq})}] + [\text{DBUH}^+_{(\text{aq})}]$$

Eq 2.25

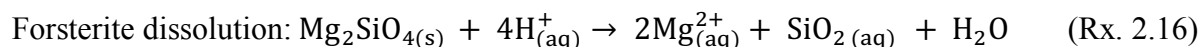
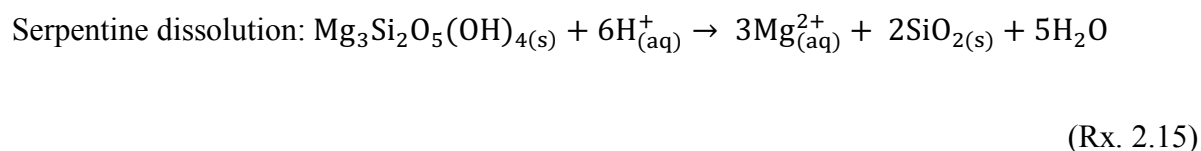
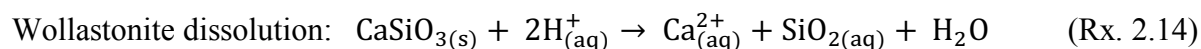
$$[\text{DBU}_{(\text{aq})}] = \frac{\text{DBU}_{\text{TOT}}}{1 + \frac{[\text{H}^+_{(\text{aq})}]}{K_5}}$$

Eq 2.26

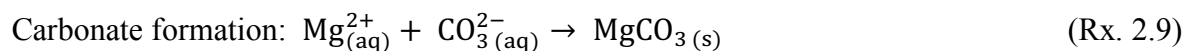
$$[\text{DBUH}^+_{(\text{aq})}] = \frac{[\text{DBU}_{(\text{aq})}] [\text{H}^+_{(\text{aq})}]}{K_5} = \frac{[\text{H}^+_{(\text{aq})}] \text{DBU}_{\text{TOT}}}{K_5 + [\text{H}^+_{(\text{aq})}]} \quad \text{Eq 2.27}$$

## 2.2 Mineral Dissolution and Carbonate Formation

Mineral dissolution, as one of the carbon mineralization steps, may be the rate limiting step depending on the condition of pH, temperature, aqueous environment (Marini, 2007; Oelkers & Schott, 1995; Oelkers, 1996). The composition and the crystal structure of the precursors determine the rate and the mechanism of the mineral dissolution process (Marini, 2007; Oelkers & Schott, 1995; Oelkers, 1996). Here are some dissolution reactions of some earth abundant minerals from **Reaction 2.14** to **2.16**.



Calcium and magnesium ions are formed during the mineral dissolution process. The calcium and magnesium ions react with the carbonate ions in the aqueous phase to precipitate calcium and magnesium carbonates. The reactions are listed as **Reaction 2.9** and **2.10**.



In this thesis, we elucidate hybrid absorption – carbonate crystallization approaches with inherent solvent regeneration by harnessing these thermodynamic concepts. The solvents enhance CO<sub>2</sub> capture as discussed and are regenerated as solid inorganic carbonates are formed. However,

complex chemical and morphological coupling phenomena underlie these interactions and the associated kinetics. To address this challenge, the research objectives are discussed below.

## **2.3 Research Objectives**

### **2.3.1 Problem Statement**

The limited understanding of the chemo-morphological coupling for the reactive CO<sub>2</sub> capture and conversion of CO<sub>2</sub> limits the development of integrated and scalable processes. Ca- and Mg-bearing silicate minerals are abundant in natural rocks and alkaline industrial residues, such as steel slag, and coal fly ash. The resource base for carbon mineralization needs to be increased. While carbon mineralization of Ca- and Mg-bearing industrial residues has been studied at elevated CO<sub>2</sub> partial pressures and temperatures, the direct use of flue gas streams and temperatures lower than 90°C to capture and mineralize carbon remain less explored. Achieving predictive controls over these processes requires *in-operando* characterization of the fluid-solid interactions underlying reactive CO<sub>2</sub> capture and carbon mineralization pathways. To address these challenges, the specific research questions that are addressed are articulated in the following section.

### **2.3.2 Scientific Questions**

The scientific questions that form the basis for this research are:

- How do we enhance the resource base for carbon mineralization to incorporate less reactive hydrated magnesium silicates and to make them more reactive?
- What are the different approaches for designing reactive CO<sub>2</sub> capture and carbon mineralization pathways with inherent solvent regeneration?

- What is the effectiveness of reactive CO<sub>2</sub> capture and carbon mineralization pathways in single-step CO<sub>2</sub>-solvent-alkaline solid reactions and two step CO<sub>2</sub>-solvent and CO<sub>2</sub>-loaded solvent-alkaline solid reactions?
- What is the influence of the physico-chemical parameter space including the effects of temperature, solvent concentration, and reactive time on integrated CO<sub>2</sub> capture and carbon mineralization?
- What is the chemo-morphological evolution of the reacting solids and the dynamic speciation of the fluidic environments as CO<sub>2</sub> capture and carbon mineralization occurs?
- What is the influence of the chemical structure of the solvent, solvent concentration on the inorganic carbon content available to react with calcium or magnesium minerals to produce the respective inorganic carbonates?
- What are the extents of carbon mineralization achieved using calcium oxide, magnesium oxide, and calcium silicate which are abundant in alkaline residues using various solvents?
- What are the carbonate phases formed and what are the key features of the solvent as it is regenerated during carbonate formation?

### 2.3.3 Research Goals

The key research goals of this project are outlined below:

- Design novel reaction pathways with low energy penalty for accelerating carbon mineralization
- Advance a fundamental understanding of the chemo-morphological behavior in fluid-solid interactions using *in-operando* characterization approaches

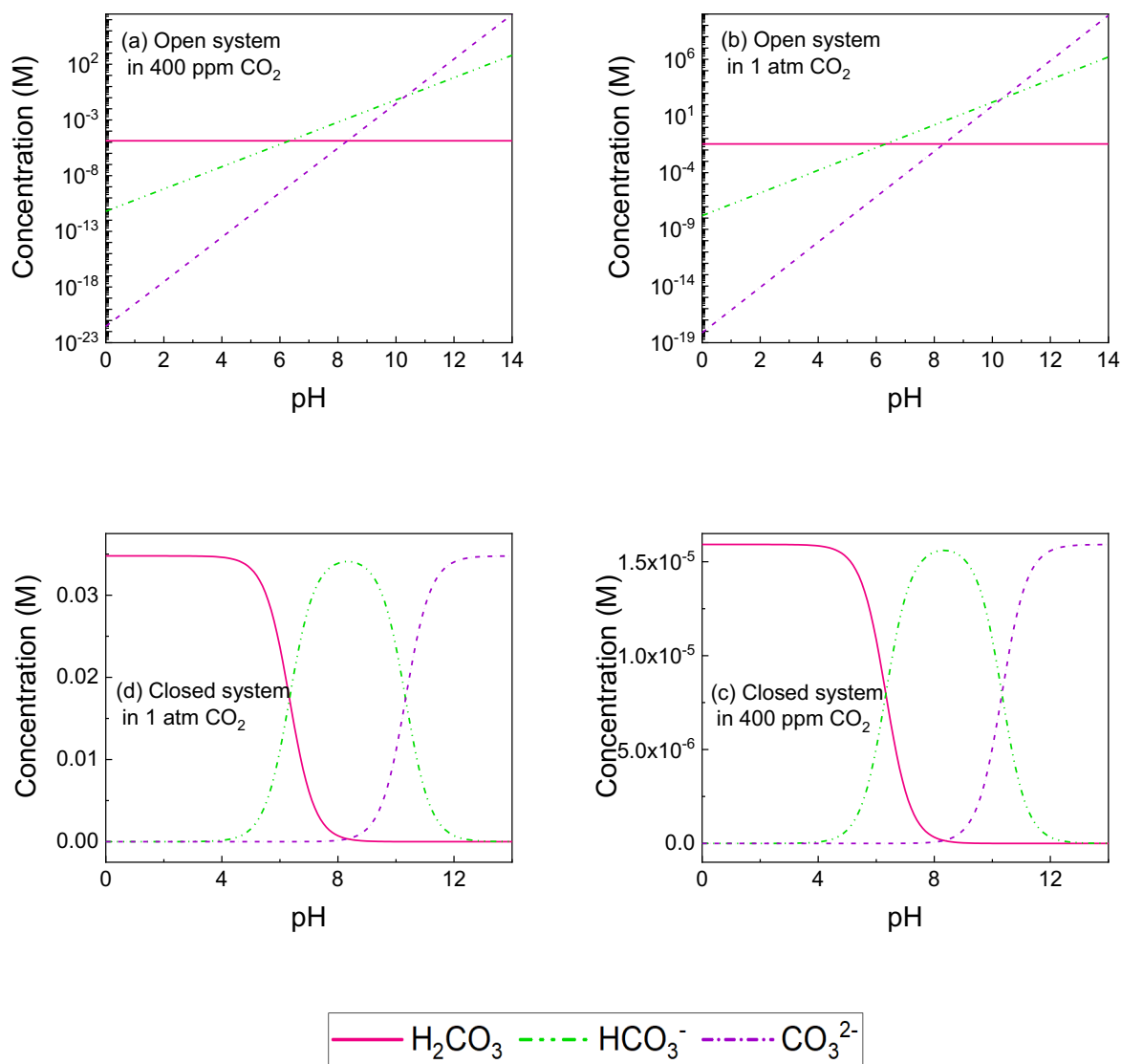


**Figure 2.1** Carbon speciation in open and closed systems without any additives. The concentration of  $[\text{H}_2\text{CO}_3^*_{(\text{aq})}]$ ,  $[\text{HCO}_3^-_{(\text{aq})}]$ , and  $[\text{CO}_3^{2-}_{(\text{aq})}]$  as a function of pH in an open system exposed to the atmosphere with a  $\text{CO}_2$  concentration of 400 ppm and  $p\text{CO}_2$  of 1 atm are shown in **Figure 2.1 (a)** and **Figure 2.1 (b)**, respectively. The concentration of  $[\text{H}_2\text{CO}_3^*_{(\text{aq})}]$ ,  $[\text{HCO}_3^-_{(\text{aq})}]$ , and  $[\text{CO}_3^{2-}_{(\text{aq})}]$  as a function of pH in a closed system at  $\text{CO}_2$  concentration of 400 ppm and  $\text{CO}_2$  partial pressure of 1 atm are shown in **Figure 2.1 (c)** and **Figure 2.1 (d)**, respectively. The total

carbon concentration at the equilibrium pH of 5.55 in a closed system with CO<sub>2</sub> concentration of 400 ppm is  $1.59 \times 10^{-5}$  M (Figure 2.1 (c)). The total carbon concentration at the equilibrium pH of 3.85 in a closed system with pCO<sub>2</sub> of 1 atm is 0.035 M (**Figure 2.1 (d)**).

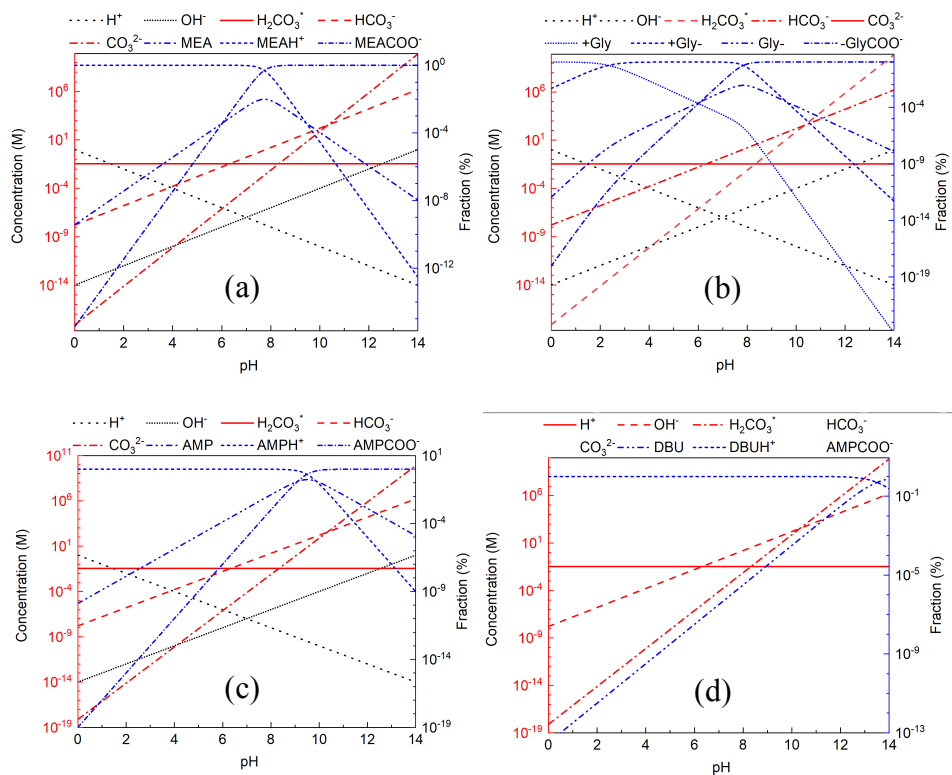


**Figure 2.2** Inorganic and organic carbon speciation in open system with MEA sodium glycinate, AMP, and DBU. The concentration of organic solvent speciation and  $[H_2CO_3^*_{(aq)}]$ ,  $[HCO_3^-_{(aq)}]$ , and  $[CO_3^{2-}_{(aq)}]$  as a function of pH in an open system with MEA sodium glycinate, AMP, and DBU exposed to 1 atm  $CO_2$  are shown in **Figure 2.2 (a)**, **Figure 2.2 (b)**, **Figure 2.2 (c)**, and **Figure 2.2 (d)**, respectively.

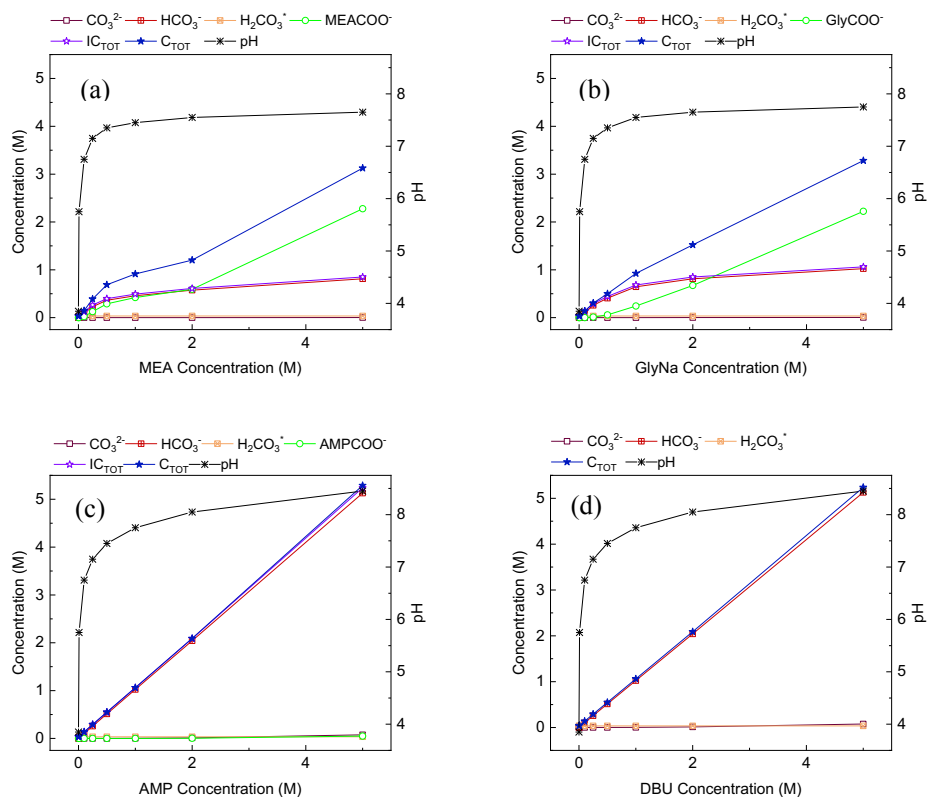


**Figure 2.3** Inorganic and organic carbon speciation in open system with MEA sodium glycinate, AMP, and DBU. The concentration of organic solvent speciation, pH and  $[\text{H}_2\text{CO}_3^*_{(\text{aq})}]$ ,  $[\text{HCO}_3^-_{(\text{aq})}]$ , and  $[\text{CO}_3^{2-}_{(\text{aq})}]$  as a function of organic concentration in an open system with MEA sodium glycinate, AMP, and DBU exposed to 1 atm  $\text{CO}_2$  are shown in **Figure 2.3 (a)**, **Figure 2.3 (b)**, **Figure 2.3 (c)**, and **Figure 2.3 (d)**, respectively.

## CHAPTER 3

# CHEMO-MORPHOLOGICAL COUPLING DURING SERPENTINE HEAT TREATMENT FOR CARBON MINERALIZATION

*The contents of this chapter have been published as a scientific peer-reviewed journal at Liu, M., & Gadikota, G. “Chemo-morphological Coupling during Serpentine Heat Treatment for Carbon Mineralization.” *Fuel* 227 (2018): 379-385.*

### 3.1 Introduction

One of the challenges at the forefront of sustainable energy production is the safe and permanent storage of CO<sub>2</sub>. One option is to capture and convert CO<sub>2</sub> into calcium and magnesium carbonates using earth-abundant calcium and magnesium-bearing silicates as the sources of alkalinity (Chizmeshya et al., 2007; Béarat et al., 2006; Gadikota et al., 2014; Gadikota & Park, 2014; Lackner, 2002; Li & Hitch, 2017; Park & Fan, 2004; Power et al., 2013). Serpentine (Mg<sub>3</sub>Si<sub>2</sub>O<sub>5</sub>(OH)<sub>4</sub>) is one example of an earth-abundant hydrated magnesium silicate mineral that has been extensively studied for carbon mineralization (Farhang et al., 2016; Gadikota et al., 2014; Highfield et al., 2012; Park et al., 2008; Park & Fan, 2004; Ryu et al., 2016; Werner et al., 2014; Wilson et al., 2006). Various routes for serpentine carbonation have been explored including the conversion of CO<sub>2</sub> and serpentine into magnesium carbonate via direct gas-liquid-solid routes (Gadikota et al., 2014), or accelerated extraction of Mg followed by magnesium carbonate precipitation (Park et al., 2008; Park & Fan, 2004).

To accelerate the kinetics of CO<sub>2</sub> conversion to magnesium carbonate, the thermal activation of serpentine was proposed. Thermal activation of serpentine to temperatures up to 700 °C dehydroxylates the crystal lattice resulting in a more reactive amorphous material (Barnes et

al., 1950). Previous studies reported carbonate conversions of heat-treated serpentine as high as 73.5% at 185 °C,  $P_{\text{CO}_2}$  of 150 atm in 1.0 M NaCl + 0.64 M NaHCO<sub>3</sub> on reaction for 1 hour (Gerdemann et al., 2007). More recent studies reported using flue gas concentrations for successfully converting heat-treated serpentine to magnesium carbonate (Farhang et al., 2016; Werner et al., 2014). Despite significant research efforts directed towards converting heat-treated serpentine to magnesium carbonate, there is a limited fundamental understanding of the structural and morphological changes that occur in serpentine on heating and the influence of these changes on the reactivity of the mineral.

While McKelvy and co-workers evaluated the changes in the structure of heat-treated serpentine using X-ray diffraction (XRD) and fourier transform infrared spectroscopy (FTIR) analyses (McKelvy et al., 2004), the corresponding morphological changes such as the porosity, pore-solid interfacial structure, and the surface area were not reported. Recent advances in synchrotron radiation have now allowed us to probe the changes in the morphologies and structures of porous materials from the angstrom to the micrometer-scale using Ultra small, small, and wide angle X-ray scattering (USAXS/SAXS/WAXS) measurements (Gadikota, 2017; Gadikota et al., 2017; Gadikota & Allen, 2018; Gadikota et al., 2017). In the case of serpentine, the changes in the structure and the interlayer basal spacing were determined using wide angle X-ray scattering (WAXS) and small angle X-ray scattering (SAXS) measurements. Ultra small angle X-ray scattering (USAXS) measurements in conjunction with Brunauer–Emmett–Teller (BET) porosity measurements and particle size analyses were used to determine the morphological changes in serpentine on thermal treatment.

### 3.2 Materials and Their Characterization

The serpentine morph used in this study was lizardite. The chemical composition of the unreacted lizardite listed in **Table 1** was determined using Wavelength Dispersion X-Ray Fluorescence (WD-XRF, Pananalytical Axios, The Netherlands). The mean particle size, surface area and cumulative pore volume of the ground unreacted serpentine were found to be 10.80  $\mu\text{m}$ , 36.3  $\text{m}^2/\text{g}$  and 0.115  $\text{ml}/\text{g}$ , respectively. In addition to lizardite, the other major phase present was identified as quartz.

To determine the *in-operando* structural and morphological changes in serpentine on heat treatment, USAXS/SAXS/WAXS measurements were performed at Sector 9-ID at Advanced Photon Source (APS) in Argonne National Laboratory (ANL), Argonne, IL. Lizardite was prepared by grinding the material to a size smaller than 100  $\mu\text{m}$  followed by compaction into pellets. The thickness of the pellet used in this experiment was 1 mm ( $\pm 0.2$  mm). The heat treatment of the lizardite-bearing serpentine was performed by placing the pellet in a Linkam TS1500 heating stage (Linkam Scientific Instruments Ltd., Tadworth, UK) with temperature control of  $\pm 0.1$   $^{\circ}\text{C}$ . The temperature ramp rate was set at 3.3  $^{\circ}\text{C}/\text{min}$  and the temperature range was from 30  $^{\circ}\text{C}$  to 1150  $^{\circ}\text{C}$ . The heater was then aligned with the USAXS/SAXS/WAXS instrument at Sector 9-ID.

The USAXS/SAXS instruments are based on the original Bonse-Hart double-crystal configuration, which used multiple dispersive reflections from perfect crystals to reach a region of scattering vector  $q$ , where  $q = (4\pi/\lambda) \sin \theta$ ,  $\lambda$  is the wavelength of the X-ray, and  $2\theta$  is the scattering angle (Bonse & Hart, 1965; Ilavsky et al., 2009). All measurements (USAXS/SAXS/WAXS) could be made within about 3 minutes, reducing uncertainties bringing by the change of sample configuration within the beam (Ilavsky et al., 2009). The total X-ray flux

of the measurement was  $10^{-13}$  photon  $s^{-1}$ . The wavelength of the X-ray used in the experiment was 0.59 Å, which corresponded to the energy of 21.0 keV. Calibrations were made using silver behenate and the NIST standard reference material, SRM 640d (Si). Collected data were reduced and analyzed by the Irena and Nika software packages embedded in IgorPro (Wavemetrics, Lake Oswego, OR) (Ilavsky, 2012; Ilavsky et al., 2009; Ilavsky & Jemian, 2009).

Several complementary measurements were performed to complement the scattering measurements. Powdered lizardite was thermally treated to 350 °C, 650 °C, 900 °C, and 1150 °C in an oven for 3 hours for determining the changes in the porosity, surface area, surface morphology and particle size on heating. The changes in the porosity and the specific surface area of the powdered lizardite on heating were determined using the BET technique (Quantachrome Autosorb1 Analyzer), while particle size distributions were determined via a laser diffraction method (Beckman Coulter, Inc., LS 13 320 MW). The surface morphological features were determined using a scanning electron microscopy (SEM, Hitachi High Technologies America, Hitachi S3400-N). The changes in the weight of the sample on heating was determined using thermogravimetric analysis (TGA, TA Instruments TGA550).

### **3.3 Results and Discussion**

#### **3.3.1 Structural Changes in Lizardite on Thermal Treatment**

Heating lamellar structures such as lizardite produced several changes across the material hierarchy. One of the characteristic features of hierarchical materials is the interlayer basal spacing which was observed in the SAXS regime. The interlayer space is the distance between the silicate layers in case of lizardite. One measure of the interlayer space is the basal reflection or the  $d(001)$  peak corresponding to the scattering from one hydrated magnesium silicate nanosheet and the

interlayer space. The position and the intensity of the characteristic interlayer peak indicate the distance corresponding to the interlayer space and the nanosheet, and the quantity of interlayer nanopores, respectively. The interlayer basal reflection is a characteristic of other hierarchical natural materials such as clays.

In swelling clays such as Na- or Ca-montmorillonite, the interlayer basal spacing changes with the layers of intercalated water in these regions, unlike in non-swelling clays such as kaolinite (Gadikota et al., 2017). In swelling clays bearing intercalated water, a reduction in the interlayer basal spacing is noted on heating to 150 °C. Unlike swelling clays, phyllosilicates such as lizardite do not contain intercalated water. On heating to 150 °C, no significant changes in the positions of the  $d(001)$  or  $d(002)$  peaks or their intensities were noted. This observation is attributed to the absence of the characteristic ability to shrink or swell due to the loss or gain of water, and no structural changes in the hydrated magnesium silicate nanosheet.

Further heating above 550 °C reduced the intensity of the interlayer basal reflection with the peak disappearing on heating to 825 °C. This observation is consistent with previous studies reporting changes in the lamellar structure of lizardite to an amorphous form due to the removal of -OH groups (Barnes et al., 1950; McKelvy et al., 2004; Trittschack & Grob ty, 2012). Thermogravimetric analyses of untreated lizardite showed the onset of weight loss around 500 °C with near complete loss achieved on heating to 825 °C which corresponds to lizardite dehydroxylation (**Figure 3.2**). Various lizardite samples were also heat-treated at 350 °C, 650 °C and 900 °C in an *ex-situ* environment prior to thermogravimetric analyses. Heat treatment of lizardite at 350 °C did not change the weight of the sample significantly compared to the untreated serpentine. On heating to 650 °C, a weight loss of 2.25% was observed suggesting that the presence of residual -OH groups. No significant changes in the weight of the sample were noted on heating

to 900 °C suggesting the complete removal of -OH groups at those conditions. The observations of the changes in the weight of serpentine due to dehydroxylation in **Figure 3.2** are consistent with the loss in the crystalline structure of serpentine in **Figures 3.1**. In the context of carbon mineralization, the structural disorder achieved due to serpentine dehydroxylation on heating to temperatures in the range of 600 °C - 700 °C was noted as a factor in accelerating carbon mineralization behavior (McKelvy et al., 2004).

On heating serpentine beyond 650 °C, the recrystallization of amorphous serpentine to denser phases was observed. The onset of  $\text{Al}_{2.35}\text{Si}_{10.64}\text{O}_{4.82}$  (mullite),  $\text{SiO}_2$  (cristobalite),  $\text{Mg}_2\text{SiO}_4$  (forsterite), and  $\text{Fe}_{0.3}\text{Mg}_{0.7}(\text{SiO}_3)$  (enstatite) phases was observed in the range of 700 °C - 800 °C in the WAXS regime (Angel & Prewitt, 1986; Dove et al., 2000; Hazen, 1976; Smith, 1959). These observations are consistent with previous studies that reported a strong exotherm at 782 °C indicating the onset of new phase formation (McKelvy et al., 2004). The intensity of these phases increased on further heating suggesting the growth of these phases (**Figure 3.3**). These phases are indexed in serpentine heat-treated at 1150 °C. The respective densities of mullite, cristobalite, forsterite, and enstatite are 3.15, 2.3, 3.3, and 3.3 g/cm<sup>3</sup> compared to the density of lizardite of 2.6 g/cm<sup>3</sup> (Ahrens & Gaffney, 1971; Bafrooei et al., 2014; Downs & Palmer, 1994; Ismail et al., 1987; Viti & Hirose, 2010). To determine if less dense phases may have a more significant impact on mineralization compared to more dense phases, the corresponding morphological changes in lizardite on heat treatment were determined.

### **3.3.2 Morphological Changes in Lizardite on Thermal Treatment**

In the previous section, the structural basis for high conversions of heat-treated serpentine to magnesium carbonate was established with reasonable agreement with published data (McKelvy et al., 2004). However, there is a limited understanding of the corresponding morphological

changes in lizardite on heat treatment and how that may potentially impact carbon mineralization behavior. To develop the morphological perspective, the changes in the particle size, porosity, surface area, and changes in the pore-solid interface on heating were evaluated. To evaluate the changes in the particle size, porosity, and surface area, lizardite was heat-treated to 350 °C, 650 °C, 900 °C, and 1150 °C.

One of the hypotheses to explain the enhanced reactivity of lizardite heat-treated to 650 °C is the potential increase in the porosity which aids the diffusion of Mg or Si ions into the bulk solution, thereby enhancing the carbonation potential. To test this hypothesis, BET measurements were performed at 25 °C, 350 °C, 650 °C and 900 °C. The cumulative pore volume increased from 0.115 cm<sup>3</sup>/g to 0.888 cm<sup>3</sup>/g and 1.563 cm<sup>3</sup>/g on heating to 350 °C and 650 °C, respectively. The increase in cumulative pore volume corresponds to lizardite dehydroxylation. Heating to 900 °C reduced the cumulative pore volume to 0.047 cm<sup>3</sup>/g (**Table 2.1** and **Figure 3.4**). The reduction in porosity at 900 °C is consistent with the formation of denser phases (**Figure 3.3**). Similarly, an increase in the surface area was noted on the dehydroxylation of lizardite. The surface area increased from 36.3 m<sup>2</sup>/g to 580.4 m<sup>2</sup>/g and 1152 m<sup>2</sup>/g at 350 °C and 650 °C, respectively. Further heating to 900 °C reduced the surface area to 6.5 m<sup>2</sup>/g which corresponds to the growth of denser phases (**Table 2**). These data support the hypothesis that increase in porosity and surface area on heating to 650 °C along with the structural disorder noted in **Section 3.3.1** aids the high reactivity of lizardite with CO<sub>2</sub> at this temperature.

To probe the factors leading to the changes in the porosity particularly on heating from 650 °C to 900 °C, the particle sizes of the serpentine heat-treated at various temperatures were determined. The particle size of the unreacted lizardite was in the range of 0.5 μm – 50 μm. On heating to 350 °C and 650 °C, a small increase in the particle size from 10.8 μm at ambient

temperature to 12.4  $\mu\text{m}$  and 13.1  $\mu\text{m}$  was noted (**Table 2.2** and **Figure 3.5**). On further heating to 900  $^{\circ}\text{C}$ , the volume of particles larger than 50  $\mu\text{m}$  increased while the volume of particles smaller than 50  $\mu\text{m}$  decreased. This trend was observed on further heating to 1150  $^{\circ}\text{C}$ . The mean particle sizes of lizardite heat-treated at 900  $^{\circ}\text{C}$  and 1150  $^{\circ}\text{C}$  were 34.8  $\mu\text{m}$  and 142.1  $\mu\text{m}$ , respectively (**Table 2.2** and **Figure 3.5**). These increases in the particle sizes correspond to the growth of denser phases such as  $\text{Al}_{2.35}\text{Si}_{0.64}\text{O}_{4.82}$  (mullite),  $\text{SiO}_2$  (cristobalite),  $\text{Mg}_2\text{SiO}_4$  (forsterite), and  $\text{Fe}_{0.3}\text{Mg}_{0.7}(\text{SiO}_3)$  (enstatite) on heating (**Figure 3.3**). Further evidence of larger and well-defined particles in lizardite heat-treated to 900  $^{\circ}\text{C}$  and 1150  $^{\circ}\text{C}$  (**Figures 3.6 (b)** and **3.6 (c)**) were noted compared to untreated lizardite (**Figure 3.6 (a)**).

The changes in the pore-solid interface and the morphological transformations of lizardite from a lamellar to a pseudo-amorphous to a crystalline structure are supported by USAXS and SAXS measurements (**Figure 3.7**). At a high  $q$  of  $0.85 \text{ \AA}^{-1}$ , the peak corresponding to the interlayer basal reflection was noted. Shifts in the peak position were not noted on heating to 800  $^{\circ}\text{C}$  suggesting that the d-spacing of 7.39  $\text{\AA}$  did not change on heating. Significant changes in the intensity of this peak on heating were noted as shown in **Figure 3.1** and discussed in **Section 3.3.1**. A decrease in the nano-scale porosity corresponding to the reduction in the intensity of this basal peak was noted on heating above 550  $^{\circ}\text{C}$ . This peak completely disappears on heating to 825  $^{\circ}\text{C}$ .

It was interesting to note the growth of an additional feature in the  $q$  range of  $0.45 \text{ \AA}^{-1} - 0.70 \text{ \AA}^{-1}$  on heating from 50  $^{\circ}\text{C}$  to 725  $^{\circ}\text{C}$ . This feature decreased in intensity on heating above 800  $^{\circ}\text{C}$  before disappearing. The growth of this feature corresponded to the reduction in the intensity of  $d(0\ 0\ 1)$  peak. McKelvy and co-workers referred to this feature as the  $\alpha$  phase which reflects the diffuse interlamellar order in lizardite on heating (McKelvy et al., 2004). Our results are consistent with their observations that heat treating serpentine to temperatures up to 800  $^{\circ}\text{C}$  results

in the formation of pseudo-amorphous serpentine characterized by intralamellar disorder emerging from changes in the  $d(001)$  peak with the development of diffuse interlamellar order in  $q$  range of  $0.45 \text{ \AA}^{-1} - 0.70 \text{ \AA}^{-1}$ . This  $\alpha$  feature disappears on heating above  $800 \text{ }^\circ\text{C}$  which corresponds to the growth of dense crystalline phases (**Figure 3.3**).

In addition to providing insights into the changes in the lamellar structure on heating, the combined USAXS/SAXS data yielded detailed information of the changes in the pore-solid interface. One approach to quantify the changes in the pore-solid interface is the Porod slope. The Porod slope yields information about the “fractal dimension” of the scattering object. In this study, the Porod slope is calculated in the  $q$  region of  $0.02 - 0.4 \text{ \AA}^{-1}$  to probe the fractality of the local structure. The Porod slope is calculated using the following relationships where  $I(q)$  and  $n$  represent the scattering intensity and the slope, respectively.

$$I(q) = \frac{A}{q^n} + B \quad (\text{Equation 3.1})$$

$$\log_{10}[I(q) - B] = \log_{10} A - n \log_{10} q \quad (\text{Equation 3.2})$$

Porod slopes of 1 or 4 represent scattering from rigid rods or smooth surfaces, respectively. Porod slopes between 3 and 4 represent rough interfaces with a fractal dimension,  $D$  where  $n = 6 - D$  represents a surface fractal. A slope between 2 and 3 represents branched systems or networks also known as mass fractals. The Porod slopes of serpentine on heating from ambient temperature to  $425 \text{ }^\circ\text{C}$  are in the range of 3.1 and 3.2 indicating a rough interface (**Figure 3.8**). Further heating to  $675 \text{ }^\circ\text{C}$  and  $700 \text{ }^\circ\text{C}$  reduced the Porod slope to 3.0 and 2.8, respectively. The decreasing Porod slope is indicative of a branched network consistent with the formation of pseudo-amorphous structure at these temperatures. Further heating to  $1150 \text{ }^\circ\text{C}$  increased the Porod slope to 3.7

indicating the formation of increasingly smoother interfaces which is consistent with the growth of various crystalline phases (**Figure 3.3**). By combining *in-operando* USAXS/SAXS/WAXS measurements with complementary characterization tools, a detailed structural and morphological basis spanning from the angstrom – to – micrometer scale was established for the enhanced reactivity of serpentine heated to temperatures in the range of 600 °C to 700 °C.

### 3.4 Conclusions

In this study, the structural and morphological basis for the enhanced reactivity of serpentine heat-treated to temperatures in the range of 600 °C and 700 °C with CO<sub>2</sub> was evaluated. Heating serpentine to temperatures in the range of 600 °C and 700 °C resulted in the formation of a pseudo-amorphous serpentine structure which corresponded to a significant increase in the surface area and porosity on heating. These measurements provide a fundamental basis for reacting serpentine to temperatures in the range of 600 °C and 700 °C prior to accelerated conversion to carbonates. Further heating reduced the porosity and the reactive surface area of heat-treated serpentine which corresponded to the formation of high temperature crystalline phases such as Al<sub>2.35</sub>Si<sub>0.64</sub>O<sub>4.82</sub> (mullite), SiO<sub>2</sub> (cristobalite), Mg<sub>2</sub>SiO<sub>4</sub> (forsterite), and Fe<sub>0.3</sub>Mg<sub>0.7</sub>(SiO<sub>3</sub>) (enstatite). Dynamic changes in the pore-solid interface determined using USAXS/SAXS measurements showed an increasing roughness leading to the formation of a branched network on heating serpentine to 700 °C. Further heating yielded smoother interfaces consistent with the formation of high temperature crystalline phases.

**Table 3.1** Composition of lizardite

Components	Weight %	Components	Weight %
MgO	37.00	MnO	0.10
CaO	0.42	Na <sub>2</sub> O	0.04
Fe <sub>2</sub> O <sub>3</sub>	8.09	K <sub>2</sub> O	< 0.01
SiO <sub>2</sub>	38.90	TiO <sub>2</sub>	0.04
Cr <sub>2</sub> O <sub>3</sub>	0.40	P <sub>2</sub> O <sub>5</sub>	< 0.01
Al <sub>2</sub> O <sub>3</sub>	1.79	V <sub>2</sub> O <sub>5</sub>	0.02
		LOI%	13.20

**Table 3.2** Summary of the surface area, cumulative pore volume, and mean particle size of untreated serpentine at 25 °C and heat-treated at 350 °C, 650 °C, and 900 °C.

Sample Temperature (°C)	25	350	650	900	1150
Surface Area (m <sup>2</sup> /g)	36.3 ± 9.5	580.4 ± 14	1152 ± 37	6.6 ± 0.22	-
Cumulative Pore Volume (cc/g)	0.11 ± 0.01	0.89 ± 0.01	1.56 ± 0.01	0.05 ± 0.01	-
Average Mean of Particle Size (µm)	10.8 ± 0.5	12.4 ± 0.8	13.1 ± 1.4	34.8 ± 2.4	142.1 ± 1.6

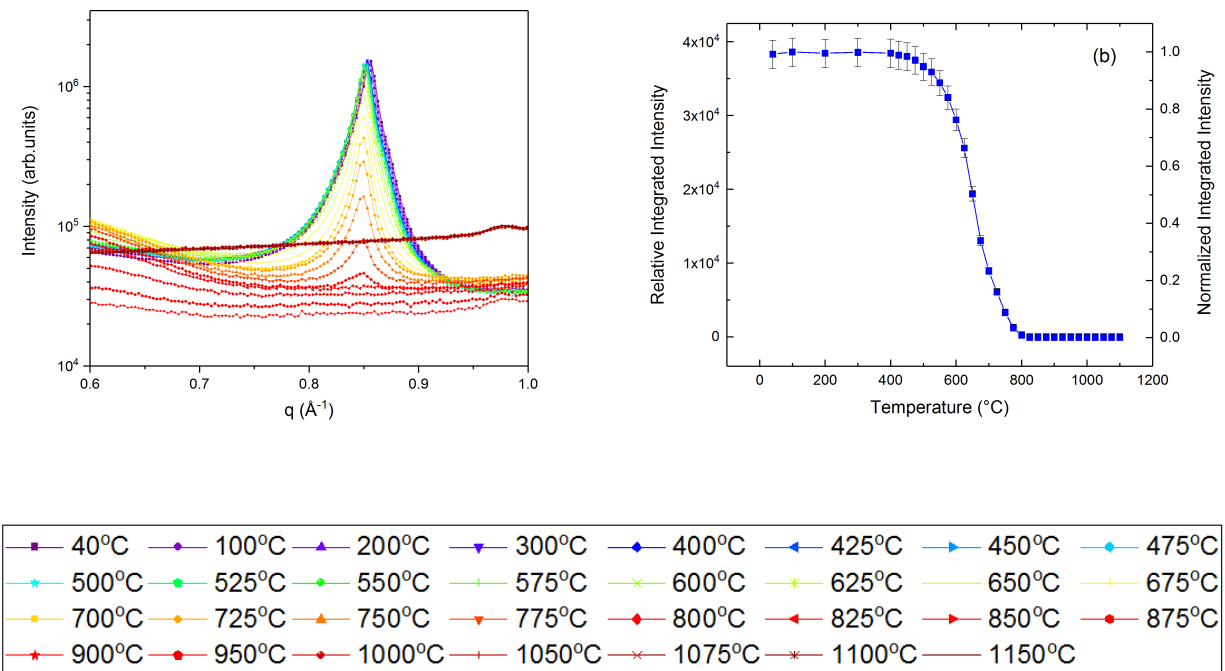


**Figure 3.1** Changes in (a) the characteristic lizardite peak ( $q = 0.85 \text{ \AA}^{-1}$ ,  $d = 7.39 \text{ \AA}$ , h k l: (0 0 1) (Mellini, 1982)) and (b) the integrated peak intensity in the temperature range of 40 °C to 1150 °C. The relative integrated intensity represented in (b) is the integrated intensity of the characteristic lizardite peak at a given temperature normalized to the integrated intensity at 40 °C. Vertical bars in (b) represent estimated 5% standard deviation uncertainties.

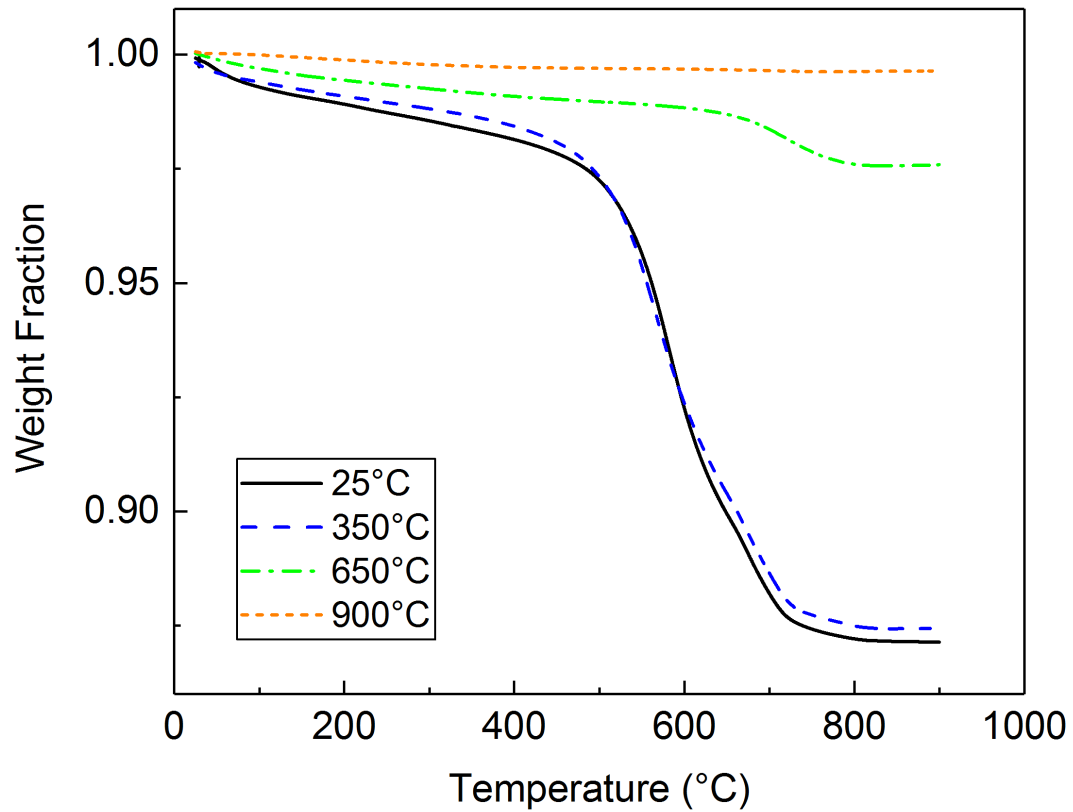


**Figure 3.2** Changes in the weight of lizardite heat-treated to 350°C, 650°C, and 900°C with respect to untreated lizardite at 25°C determined using thermogravimetric analysis.

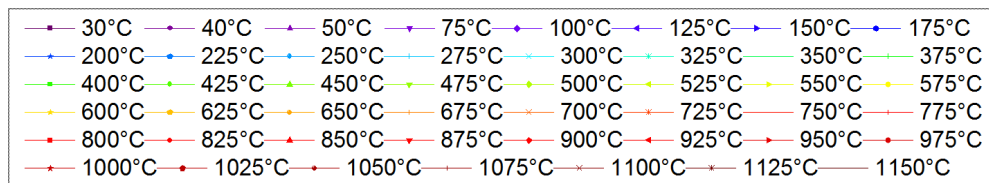
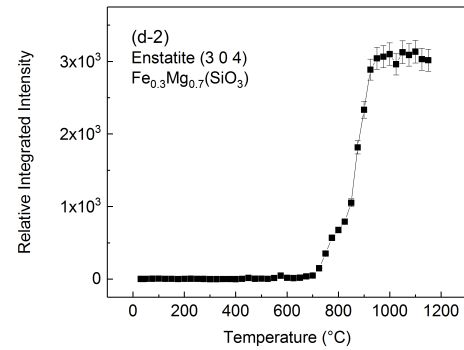
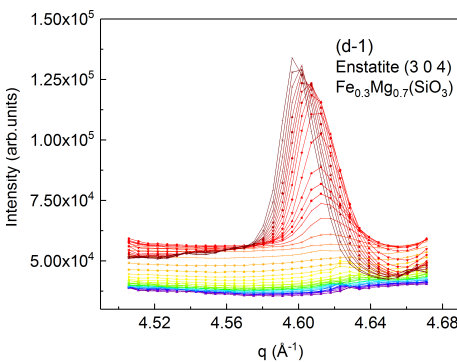
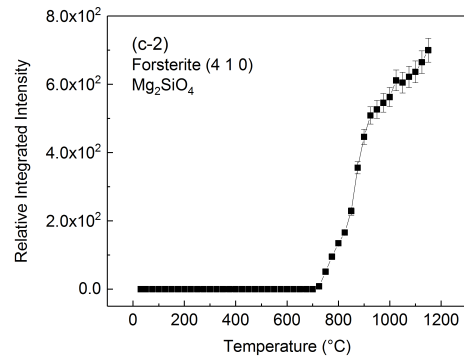
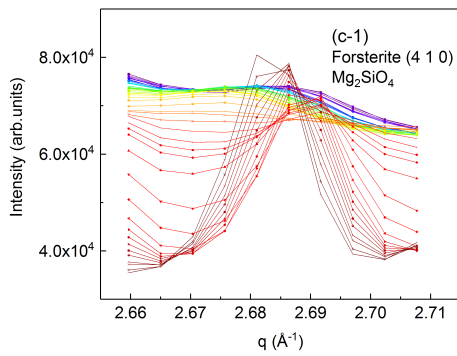
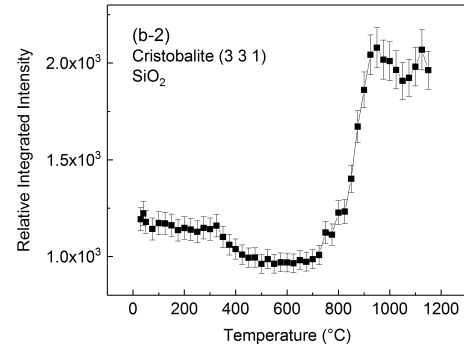
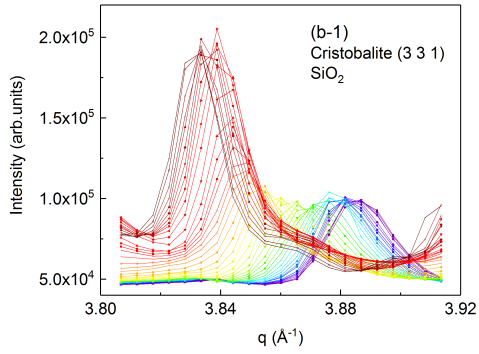
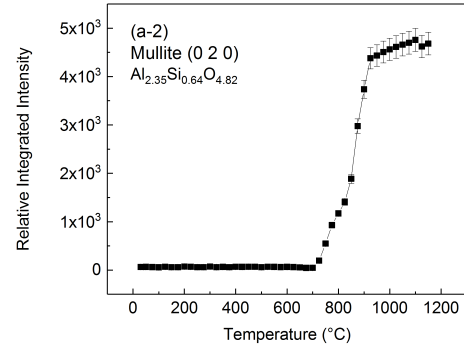
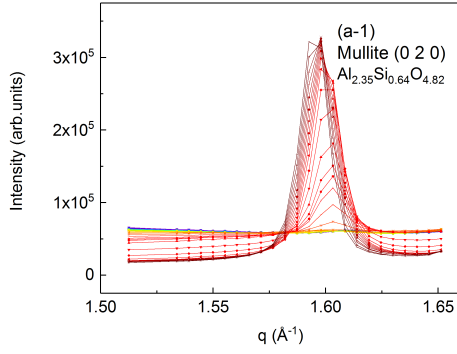


**Figure 3.3** Changes in the characteristic peaks of mullite ( $d = 3.84 \text{ \AA}$ ,  $q = 1.59 \text{ \AA}^{-1}$ , h k l: (0 2 0) (Angel & Prewitt, 1986)) (a-1), cristobalite ( $d = 1.64 \text{ \AA}$ ,  $q = 3.83 \text{ \AA}^{-1}$ , h k l: (3 3 1) (Dove et al., 2000)) (b-1), forsterite ( $d = 1.37 \text{ \AA}$ ,  $q = 4.60 \text{ \AA}^{-1}$ , h k l: (3 0 4) (Hazen, 1976)) (c-1), and enstatite ( $d = 1.37 \text{ \AA}$ ,  $q = 4.60 \text{ \AA}^{-1}$ , h k l: (3 0 4) (Smith, 1959)) (d-1) on heating from 30 °C to 1150 °C. The corresponding integrated intensities of mullite (a-2), cristobalite (b-2), forsterite (c-2), and enstatite (d-2) show the onset of these phases in the range of 725 °C and 750 °C. The relative integrated intensities represented in the right panel correspond to the integrated intensity of the characteristic peak at a given temperature normalized to the integrated intensity at 30 °C. Vertical bars in (a-2), (b-2), (c-2), and (d-2) represent estimated 5% standard deviation uncertainties.

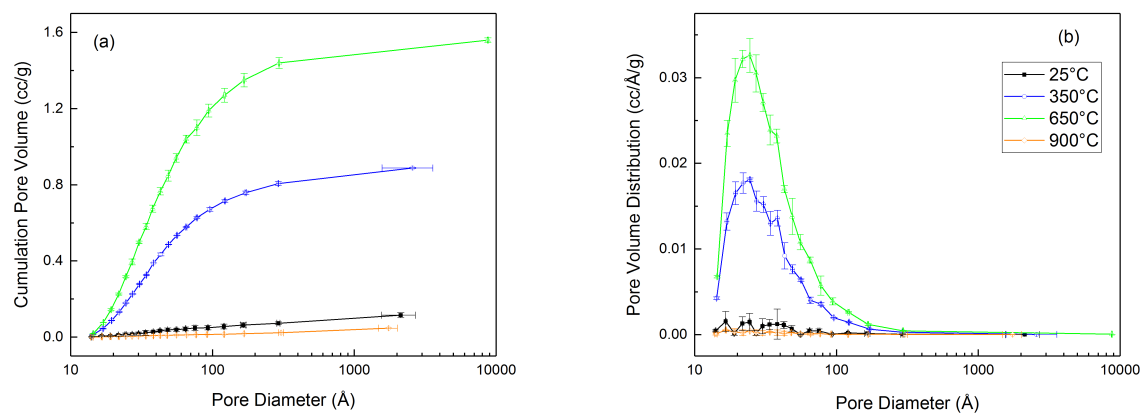


**Figure 3.4** Changes in the cumulative pore volume (a) and pore volume distributions (b) in lizardite heat treated at 350 °C, 650 °C, and 900 °C with respect to untreated lizardite at 25 °C.

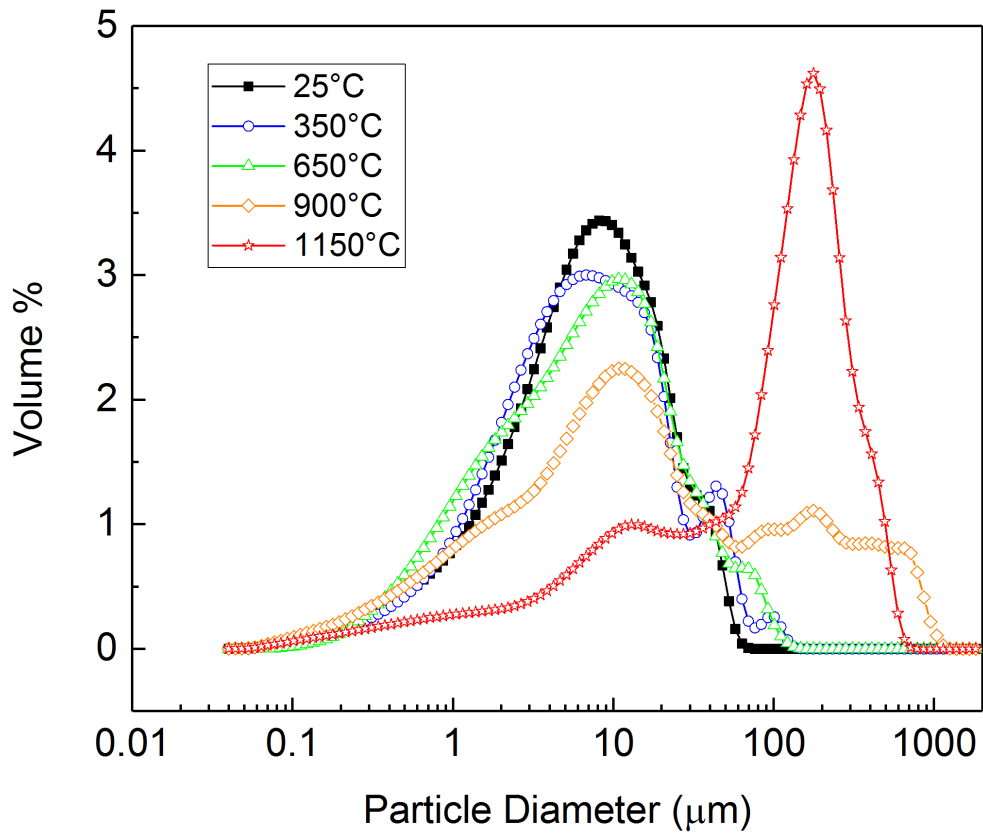


**Figure 3.5** Changes in the particle size distributions of lizardite heat treated at 350 °C, 650 °C, and 900 °C with respect to untreated lizardite at 25 °C.

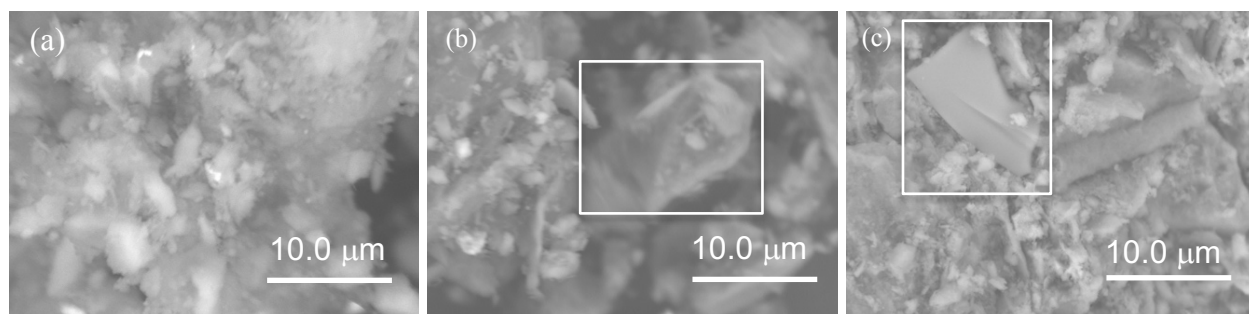


**Figure 3.6** Comparison of morphological changes of untreated lizardite at 25 °C (a) with lizardite heat-treated at 900 °C (b) and 1150 °C (c) using scanning electron microscopy images. The particles within the white square correspond to the crystalline phases formed at elevated temperatures.

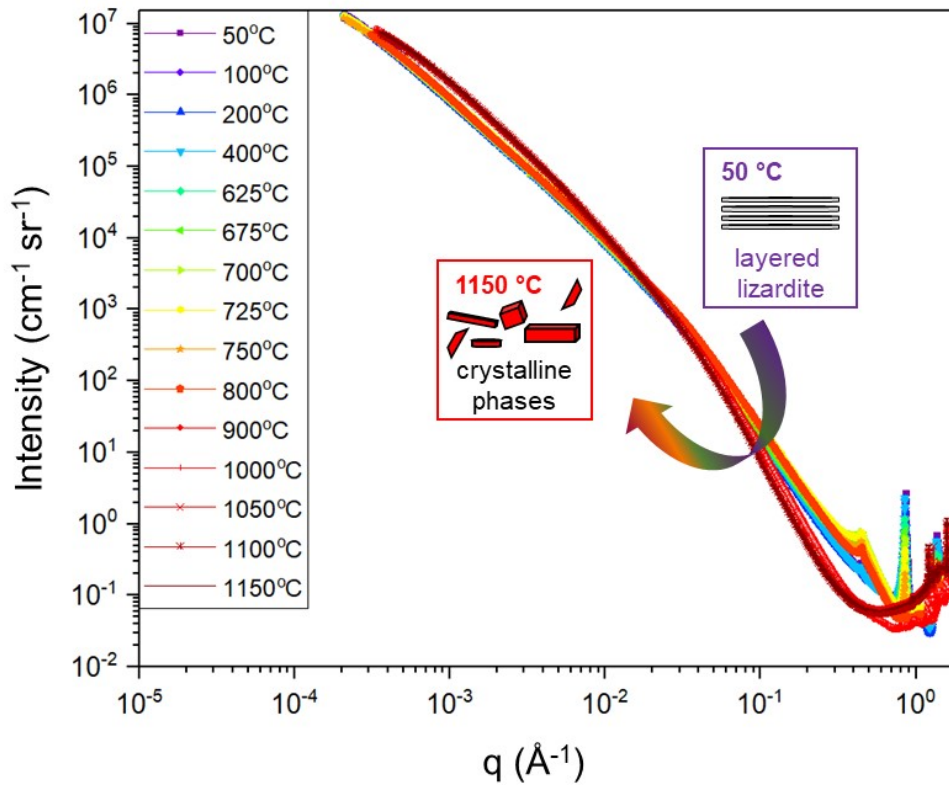


**Figure 3.7** Changes in the combined slit-smear USAXS/SAXS data on heating lizardite to a nominal temperature of 1150 °C. An increase in the scattering intensity is noted on heating to 700 °C at  $q$  larger than  $0.03 \text{ \AA}^{-1}$ . This transformation corresponds to the change in the lamellar morphology of lizardite at ambient temperature to a pseudo-amorphous structure. Further heating to 1150 °C results in the formation of crystalline phases (see Figure 3.3) and is accompanied by a reduction in the scattering intensity at  $q$  larger than  $0.03 \text{ \AA}^{-1}$ .

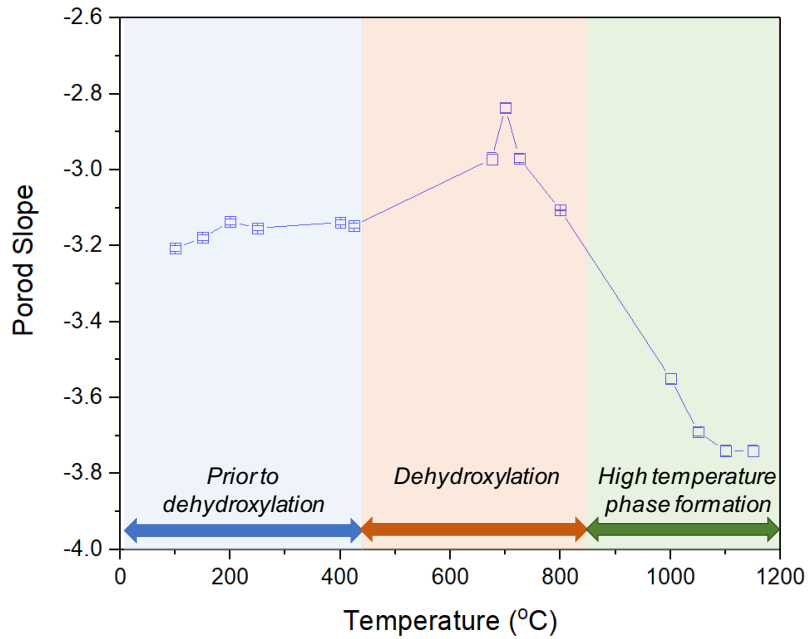


**Figure 3.8** Changes in Porod slopes for  $q$  in the range of  $0.02 \text{ \AA}^{-1}$  to  $0.4 \text{ \AA}^{-1}$ . The slopes are determined after desmearing the USAXS/SAXS data shown in Figure 7. The roughness of the pore-solid interfaces increases on serpentine dehydroxylation. Interfaces become smoother on the formation of high temperature phases such as  $\text{Al}_{2.35}\text{Si}_{0.64}\text{O}_{4.82}$  (mullite),  $\text{SiO}_2$  (cristobalite),  $\text{Mg}_2\text{SiO}_4$  (forsterite),  $\text{Fe}_{0.3}\text{Mg}_{0.7}(\text{SiO}_3)$  (enstatite).

## CHAPTER 4

# PHASE EVOLUTION AND TEXTURAL CHANGES DURING THE DIRECT CONVERSION AND STORAGE OF CO<sub>2</sub> TO PRODUCE CALCIUM CARBONATE FROM CALCIUM HYDROXIDE

*The contents of this chapter have been published as a scientific peer-reviewed journal at Liu, M., and Gadikota, G. “Phase Evolution and Textural Changes during the Direct Conversion and Storage of CO<sub>2</sub> to Produce Calcium Carbonate from Calcium Hydroxide.” *Geosciences* 8.12 (2018): 445. (Invited Article)*

### 4.1 Introduction

One of the emerging challenges in sustainable energy production is the development of integrated pathways for carbon dioxide capture, utilization and storage (CCUS). With CO<sub>2</sub> concentrations increasing from about 280 ppm before the industrial age to over 400 ppm now, the need for CCUS technologies is unprecedented (Fauth et al., 2000; Ith & Dukes, 1993; Lackner, 2002; Seifritz, 1990). The transition to a low carbon economy will require us to develop a portfolio of technologies for capturing, utilizing and storing CO<sub>2</sub> at the gigaton scale (Reichle et al., 1999). Carbon mineralization is one approach which involves the accelerated conversion and storage of CO<sub>2</sub> as water insoluble calcium and magnesium carbonate via thermodynamically downhill routes (Gadikota & Park, 2014; Gadikota et al., 2014; Gadikota et al., 2014; Gadikota & Park, 2015; Lackner, 2002; Liu & Gadikota, 2018). Various routes including gas-solid and gas-liquid-solid reaction routes have been explored to accelerate the conversion of CO<sub>2</sub> to calcium and magnesium carbonates (Gerdemann et al., 2007; McKelvy et al., 2004; Sanna et al., 2012). While gas-solid reaction routes are easier to implement, the kinetics of CO<sub>2</sub> conversion to calcium and magnesium

carbonates may be slower. However, with increasing interest in directly using dilute concentrations of CO<sub>2</sub> representative of flue gas concentrations or atmospheric CO<sub>2</sub> concentrations, the need to understand the phase transitions and the textural changes in sorbents such as calcium hydroxide as it is converted to calcium carbonate provides important insights into the composition of these materials for potential use.

One of the key motivations for investigating the phase transitions and textural changes of calcium hydroxide during carbon mineralization is the abundance of these materials in alkaline industrial residues including coal fly ash, steel slag, and red mud and less studied wastes such as carbide slag residues (Liu et al., 2009) which have been reported to have more than 90% calcium hydroxide in the dry state. Carbide slag is one of the by-products of the hydrolysis of calcium carbide (CaC<sub>2</sub>), a reaction generating ethylene, polyvinyl chloride (PVC) and other products in the industry (Li et al., 2012). Significant quantities of carbide slag are generated around the world. For example, in China, 70% of acetylene (C<sub>2</sub>H<sub>2</sub>), a raw material of polyvinyl chloride (PVC), is generated from calcium carbide. About one ton of PVC results in the production of 1.5–1.9 tons of carbide slag in an industrial plant (Cheng et al., 2009; Li et al., 2012). However, treating carbide slag in an economical manner has been a challenge. While landfilling these materials has been proposed, carbide slag is caustic and corrosive, which increases the risk of environmental contamination. Another approach to utilize carbide slag is to use it to produce cement (Cao et al., 2008; Cheng et al., 2009). Recently, a calcium looping process (CLP) was proposed to integrate carbide slag disposal and CO<sub>2</sub> capture (Blamey et al., 2010; Bobicki et al., 2012; Li et al., 2013). In this approach, carbide slag, recovered from energy-intensive industrial plants, could be used to capture CO<sub>2</sub>, which is generated by industrial plants, and then used as raw materials to produce cement (Liu et al., 2012; Manovic & Anthony, 2010; Valverde, 2013).

Previous studies discussing CO<sub>2</sub> capture with carbide slag or modified carbide slag reported that carbonate conversions up to 28% could be reached after 100 calcination/carbonation cycles in the optimal temperature range of 650–700 °C (Li et al., 2012). Modified sorbents produced from carbide slag using reagents such as aluminum nitrate hydrate and glycerol water solution and propionic acid has higher CO<sub>2</sub> capture capacity compared to untreated slag. While these studies focused on enhancing the conversion of carbide slag, there was a limited fundamental understanding of the phase transitions and textural behavior of the key constituents of carbide slag such as calcium hydroxide (Li et al., 2015; Sun et al., 2013). This fundamental understanding is essential for engineering efficient reaction routes for accelerated carbon mineralization with targeted conversions to minimize the associated energy consumption and costs.

In this paper, the evolution of calcium carbonate phases from calcium hydroxide and the corresponding changes in the roughness of the pore-solid interface are investigated using *in-operando* synchrotron ultra-small, small, and wide angle X-ray scattering (USAXS/SAXS/WAXS) measurements (Gadikota, 2014; Gadikota et al., 2014, 2015, 2017; Gadikota & Park, 2015, 2014; Ilavsky et al., 2018; Liu & Gadikota, 2018). The wide angle X-ray scattering measurements provide unambiguous insights into the structural changes, while ultra-small and small angle X-ray scattering measurements reveal the changes in the textures of the pore-solid interface during the carbon mineralization of calcium hydroxide to produce calcium carbonate. Calcium hydroxide is continuously reacted with CO<sub>2</sub> flowing at 1 atm while being heated from 30 °C to 500 °C in a capillary reaction cell as the multi-scale X-ray scattering measurements were taken. While recent efforts by Benedetti, Ilavsky and co-workers relate the reactivity of calcium oxide with CO<sub>2</sub> during carbonation and calcination cycles using

microstructural modeling of the USAXS (Benedetti et al., 2019), in this study, we systematically track the structural evolution of calcium carbonate as it is formed from calcium hydroxide.

## 4.2 Experimental Methods

### 4.2.1 Materials and Methods

Calcium hydroxide powder procured from Himedia Laboratories (West Chester, PA, USA) was placed in a quartz capillary with an internal diameter of 1.3 mm and thickness of 0.2 mm (Friedrich & Dimmock Inc., Millville, NJ, USA) and loaded into a capillary cell holder (Chupas et al., 2008). Glass wool was placed at both ends of the capillary to hold the powder in place. CO<sub>2</sub> was continuously supplied at a flow rate of 10 mL/min. Temperatures in the range of 29 °C to 502 °C were investigated and the ramp rate was set to 4.73 °C /min. The surface area and cumulative pore volume of Ca(OH)<sub>2</sub> used in this experiment is 8.65 (±0.82) m<sup>2</sup>/g and 0.0134 (±0.0017) mL/g, respectively. The pore size distribution of calcium hydroxide is shown in **Figure 4.1**.

### 4.2.2 USAXS/SAXS/WAXS Measurements

The multi-scale X-ray scattering measurements were performed at Sector 9-ID at the Advanced Photon Source (APS) in Argonne National Laboratory (ANL), Argonne, IL (Ilavsky et al., 2009). Temporal uncertainties in the collected data were reduced with rapid acquisition times which were set to 90 s, 30 s, and 30 s for USAXS, SAXS, and WAXS, respectively. The total X-ray flux, energy and corresponding wavelength were 10<sup>-13</sup> photon s<sup>-1</sup>, 21.0 keV, and 0.59 Å, respectively. SAXS and WAXS measurements were calibrated using silver behenate and the NIST standard reference material, SRM 640d (Si), respectively (Black et al., 2010). Data analyses were performed in the Irena and Nika software packages embedded in *IgorPro* (Wavemetrics, Lake Oswego, OR) (Ilavsky, 2012; Ilavsky & Jemian, 2009).

## 4.3 Results and Discussion

### 4.3.1 Phase transformations during the carbon mineralization of calcium hydroxide

The changes in the structure of calcium hydroxide were determined from the wide angle X-ray scattering data. The characteristic peak of calcium hydroxide which corresponds to the (1 0 0) reflection at  $q = 2.024 \text{ \AA}^{-1}$  undergoes significant changes with continuous  $\text{CO}_2$  flow as the temperature increases (**Figure 4.2**) (Petch, 1961). The shift in the characteristic peak to lower  $q$  or larger  $d$  values corresponds to thermal expansion, as reported in previous studies (Gadikota et al., 2017; Liu & Gadikota, 2018). Tracking the changes in the integrated intensity of calcium hydroxide peak yields important insights into the onset of carbon mineralization behavior. The relative integrated intensity of calcium hydroxide as it reacts with  $\text{CO}_2$  and with increasing temperature is shown in **Figure 4.2(b)**. As the reaction temperature is increased to  $400 \text{ }^\circ\text{C}$ , the peak intensity is reduced to 60% of the original value at ambient temperature (**Figure 4.2(b)**). A steeper reduction in the integrated peak intensity to 15% of the original value at ambient temperature is noted as the reaction temperature increases to  $500 \text{ }^\circ\text{C}$ . These observations were consistent with the changes in the characteristic (0 0 1) reflection of calcium hydroxide at  $q = 1.28 \text{ \AA}^{-1}$ . The relative integrated intensity of this peak decreases from 80 % at  $400 \text{ }^\circ\text{C}$  to 30 % at  $500 \text{ }^\circ\text{C}$ , which provides additional validation of major structural changes of calcium hydroxide to produce calcium carbonate. The disappearance of the characteristic peaks of calcium hydroxide as it is reacted with  $\text{CO}_2$  is consistent with previous studies (Li et al., 2012; Materic & Smedley, 2011; Nikulshina et al., 2007).

The disappearance of the calcium hydroxide peaks corresponds to the onset of calcium carbonate peaks. The onset of three different phases of calcium hydroxide: aragonite, vaterite and calcite is noted during the carbon mineralization process. The characteristic peaks of calcite (0 1

2) at  $q = 1.63 \text{ \AA}^{-1}$ , vaterite (1 1 0) at  $q = 3.02 \text{ \AA}^{-1}$ , and aragonite (2 1 0) at  $q = 2.53 \text{ \AA}^{-1}$  in WAXS regime, all start to emerge at 300 °C. These data suggest that all types of  $\text{CaCO}_3$  form at the same time, instead of transforming from one structure to another (Chessin et al., 1965; Negro & Ungaretti, 1971; Kamhi, 1963). The integrated peak intensities show that the growth of the calcium carbonate phases is significantly enhanced as the temperature increases above 400 °C (**Figure 4.3**). These observations are consistent with previous investigations (Materic & Smedley, 2011). It was also interesting to note that the formation of calcium carbonate phases did not level off on heating to 500 °C suggesting that less than 100% conversion of calcium hydroxide to calcium carbonate was achieved (**Figure 4.3**). A comparison of the wide angle X-ray scattering data at 30 °C and 497 °C suggests that the amount of calcium hydroxide present in the sample reacted at 497 °C may be too small to be detected compared to the abundance of the calcium carbonate present (**Figure 4.4**). It was also interesting to note the formation of denser calcium carbonate phases compared to the less dense calcium hydroxide material. The densities of calcite, vaterite, and aragonite are 2.71, 2.65, and 2.94  $\text{g/cm}^3$  respectively (Christy, 2017). In comparison, the density of calcium hydroxide is 2.21  $\text{g/cm}^3$ . The influence of forming more dense phases on the textural properties of the end product are discussed in the following section.

#### **4.3.2 Evolution of the pore-solid interface during the carbon mineralization of calcium hydroxide**

As discussed in the previous section, the changes in the density and shape of the product phases during carbon mineralization may potentially impact the morphology of the material as the reaction proceeds. Insights into the morphological changes of calcium hydroxide as it is converted to calcium carbonate are obtained from the combined Ultra-Small and Small Angle X-Ray Scattering (USAXS/SAXS) data. The combined USAXS/SAXS data of calcium hydroxide during

carbon mineralization is represented at temperatures in the range of 29-300 °C and 325-502 °C in **Figure 4.5 (a)** and **Figure 4.5 (b)**, respectively.

The intensity of the USAXS/SAXS data did not change significantly on heating from ambient temperature to 300 °C as shown in **Figure 4.5 (a)**. The small reduction in the intensity of the scattering data at  $q$  in the range of 0.1 to 2 Å<sup>-1</sup> suggests a coarsening in the morphology of the calcium hydroxide. Significant reduction in the scattering intensity, particularly in the range of 0.01 – 0.1 Å<sup>-1</sup> is noted. This reduction corresponds to the onset and growth of denser calcium carbonate phases and depletion of calcium hydroxide (**Figure 4.5 (b)**). These data suggest that the newly formed CaCO<sub>3</sub> phases may occupy the pores of calcium hydroxide resulting in a lower scattering intensity.

Determination of the Porod slopes in the  $q$ -range of 0.001-0.01 Å<sup>-1</sup> and 0.01-0.1 Å<sup>-1</sup> provided detailed insights into the pore-solid interface. Previous literature reports the fractal character of porous materials such as calcium hydroxide, (surface fractal dimension  $D_s = 2.0$  (Richards et al., 2000)) calcium carbonate, (surface fractal dimension,  $D_s = 1.7665$  (Liang et al., 2014)) cementitious materials (The fractal dimension found was universally 1.25 in pore boundary fractal terms (Diamond, 1999)), shales (surface fractal dimension based on the Porod slope is 3.4 (Liu & Gadikota, 2018d)) using scattering techniques. In this study, the fractality of the microstructure is probed in the  $q$  regions of 0.001-0.01 Å<sup>-1</sup> and 0.01-0.1 Å<sup>-1</sup> using the universal porod slope model. The porod slope is calculated based on the relationships shown below, where  $I(q)$  represents the scattering intensity and the  $n$  represents the porod slope.

$$I(q) = \frac{A}{q^n} + B \quad (\text{Equation 4.1})$$

$$\log_{10}[I(q) - B] = \log_{10} A - n \log_{10} q \quad (\text{Equation 4.2})$$

The growth of denser and crystalline calcium carbonate phases results in increasingly smoother pore-solid interfaces in the high  $q$  and low  $q$  regimes as shown in **Figure 4.5**. Porod slope in the low  $q$  regime is in the range of 2-3, which is indicative of a branched or mass fractal morphology at larger length scales. Porod slopes in the high  $q$  regime are in the range of 3-4, which is indicative of a surface fractal morphology or rough pore-solid interfaces. The changes in the porod slopes were much larger in the high  $q$  regime as opposed to in the low  $q$  regime suggesting that the morphologies at the larger length scales are branched while the local microstructures are characterized by surface fractal morphologies (**Figure 4.6**). These data also suggest that the changes in the local microstructure are much larger compared to the changes in the bulk morphology. The increase in the porod slope from 3.3 to 3.6 in the high  $q$  regime of the USAXS/SAXS data suggests that the relative smoothness of the pore-solid interface may be enhanced during the growth of the calcium carbonate phases. These observations are consistent with previously observed studies that report smoother pore-solid interfaces resulting from the growth of denser, crystalline phases.

#### **4.4 Conclusions**

In this study, we report the phase transitions and the textural changes as calcium hydroxide, one of the significant components of alkaline industrial residues, is converted to calcium carbonate using *in-operando* Ultra-Small, Small, and Wide Angle X-Ray Scattering (USAXS/SAXS/WAXS) measurements. The onset of calcium carbonate formation is noted at 300 °C and the progressive growth of these phases is noted as the temperature increases to 500 °C. The simultaneous onset of three different calcium carbonate phases identified as calcite, vaterite, and aragonite are reported. Textural changes as calcium hydroxide is converted to calcium carbonate

are noted. The pore-solid interface in the high  $q$  regime in the range of 0.01-0.1  $\text{\AA}^{-1}$  is representative of a surface fractal morphology. Reduced roughness of the pore-solid interface is noted due to the formation of denser and crystalline phases of calcium carbonate. These data suggest that connecting the phase transitions and the morphologies of alkaline-bearing materials as they are converted to their respective carbonates has important implications for process scale considerations such as the temperature conditions that yield optimal composition and morphology of the desired end-products.

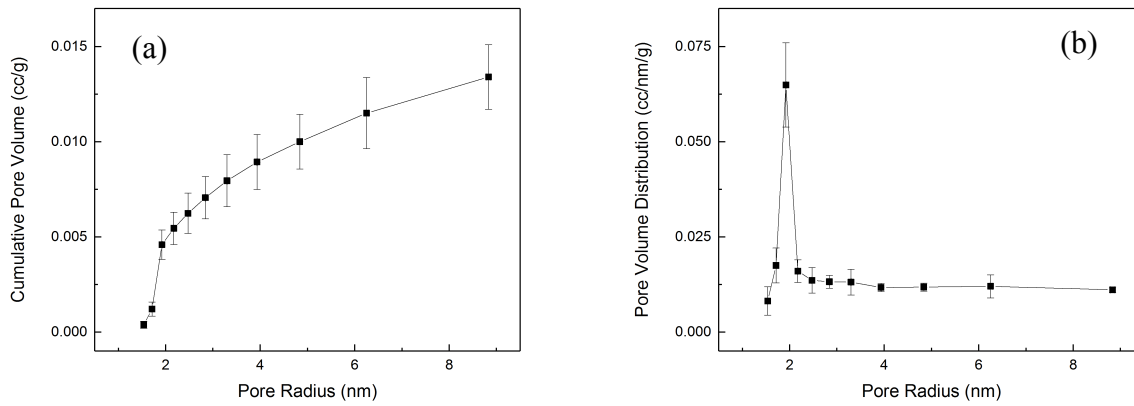


**Figure 4.1** The cumulative pore volume (a) and pore volume distribution (b) of unreacted calcium hydroxide using BET measurements.

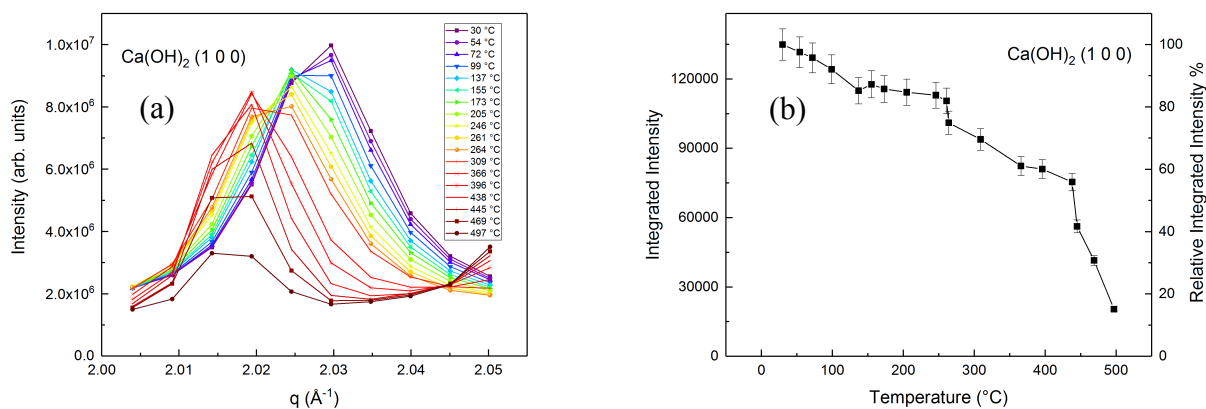


**Figure 4.2** Changes in the characteristic peak of calcium hydroxide ( $d = 3.105 \text{ \AA}$ ,  $q = 2.024 \text{ \AA}^{-1}$ ,  $h k l: (1 0 0)$ ) and the integrated peak intensity are represented in (a) and (b) respectively (Petch, 1961b). The relative integrated intensity of calcium hydroxide represented in (b) is the integrated intensity of the characteristic peak at a given temperature normalized to the integrated intensity at 30 °C. Vertical bars in (b) represent estimated 5% standard deviation uncertainties.

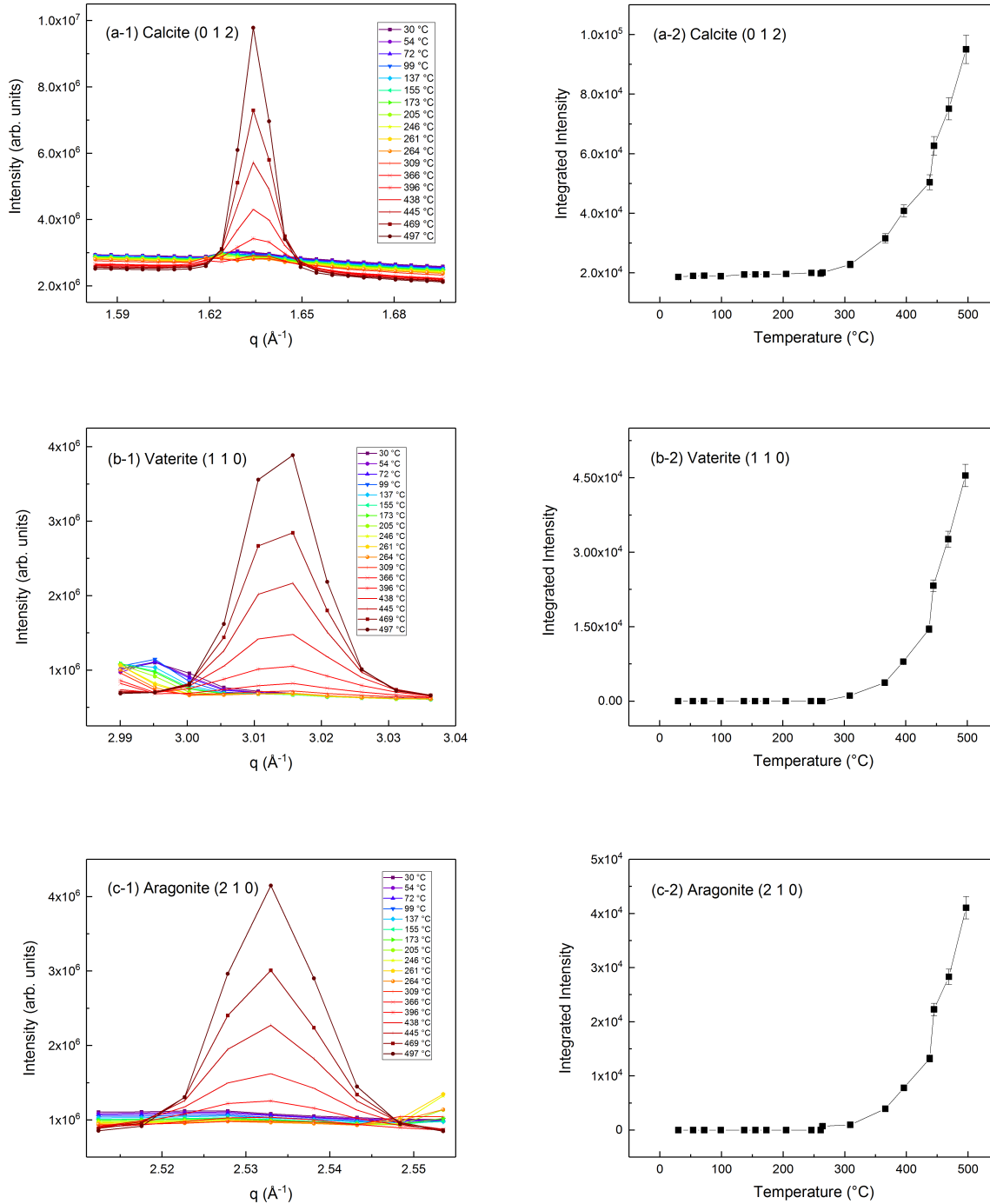


**Figure 4.3** Changes in the characteristic carbonates peaks: calcite ( $d = 3.85 \text{ \AA}$ ,  $q = 1.63 \text{ \AA}^{-1}$ , h k l: (0 1 2)) (Chessin et al., 1965) in (a-1), vaterite ( $d = 2,08 \text{ \AA}$ ,  $q = 3.02 \text{ \AA}^{-1}$ , h k l: (1 1 0)) (Kamhi, 1963) in (b-1), and aragonite ( $d = 2.48 \text{ \AA}$ ,  $q = 2.53 \text{ \AA}^{-1}$ , h k l: (2 1 0)) (Negro & Ungaretti, 1971)

in (c-1) as calcium hydroxide is reacted with CO<sub>2</sub> at reaction temperatures in the range of 30 °C to 500 °C. The integrated peak intensities of calcite, vaterite, and aragonite are shown in Figures (a-2), (b-2), and (c-2) respectively. Vertical bars represent estimated 5% standard deviation uncertainties in Figures (a-2), (b-2), and (c-2).

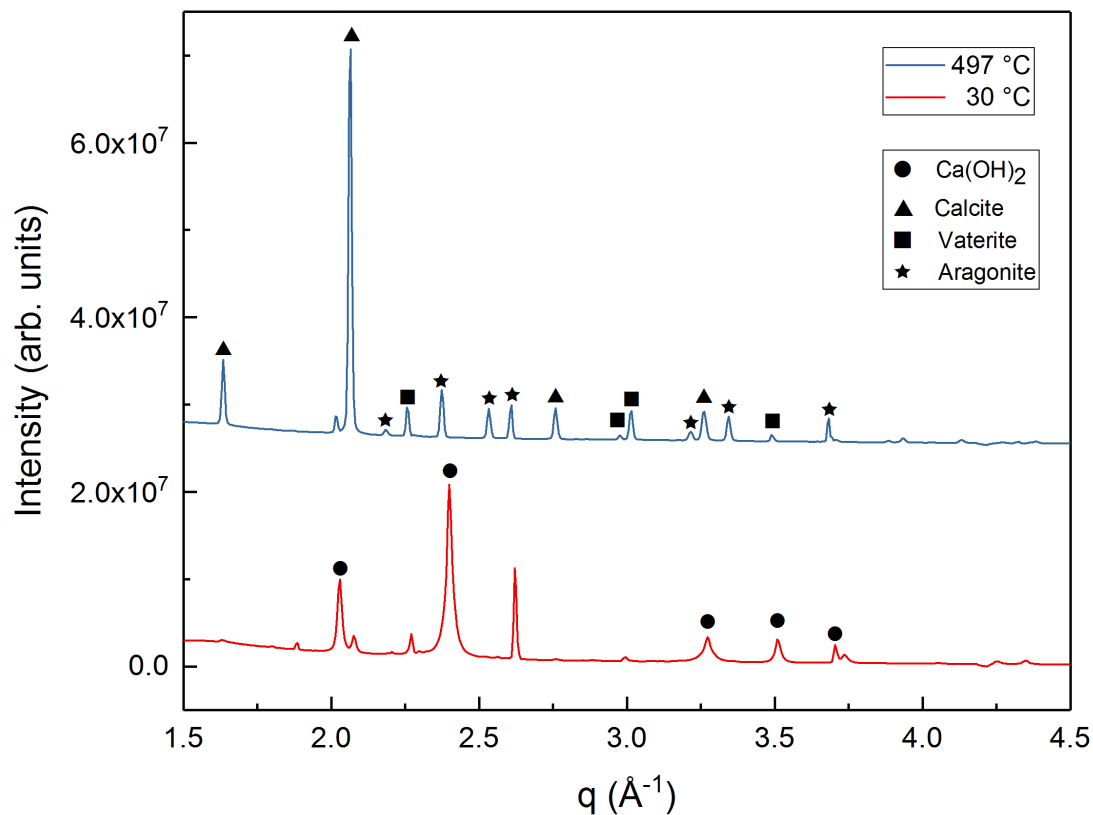


**Figure 4.4** Identification of the characteristic peaks in unreacted and reacted calcium hydroxide at 30 °C and 497 °C, respectively, using Wide Angle X-Ray Scattering (WAXS) measurements. Peak identification is based on the crystallographic data reported for calcium hydroxide (Petch, 1961b), calcite (Chessin et al., 1965; Maslen et al., 1993), vaterite (Christy, 2017; Kamhi, 1963), and aragonite (Negro & Ungaretti, 1971).

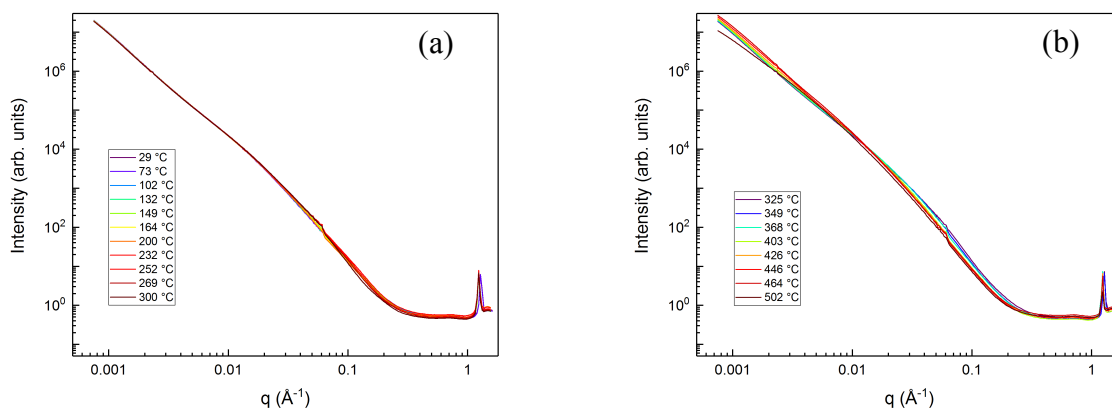


**Figure 4.5** Changes in the combined slit-smearred USAXS/SAXS data as calcium hydroxide is reacted with  $\text{CO}_2$  where (a) and (b) represent temperatures in the range of 29 °C to 300 °C and 325 °C to 502 °C, respectively.

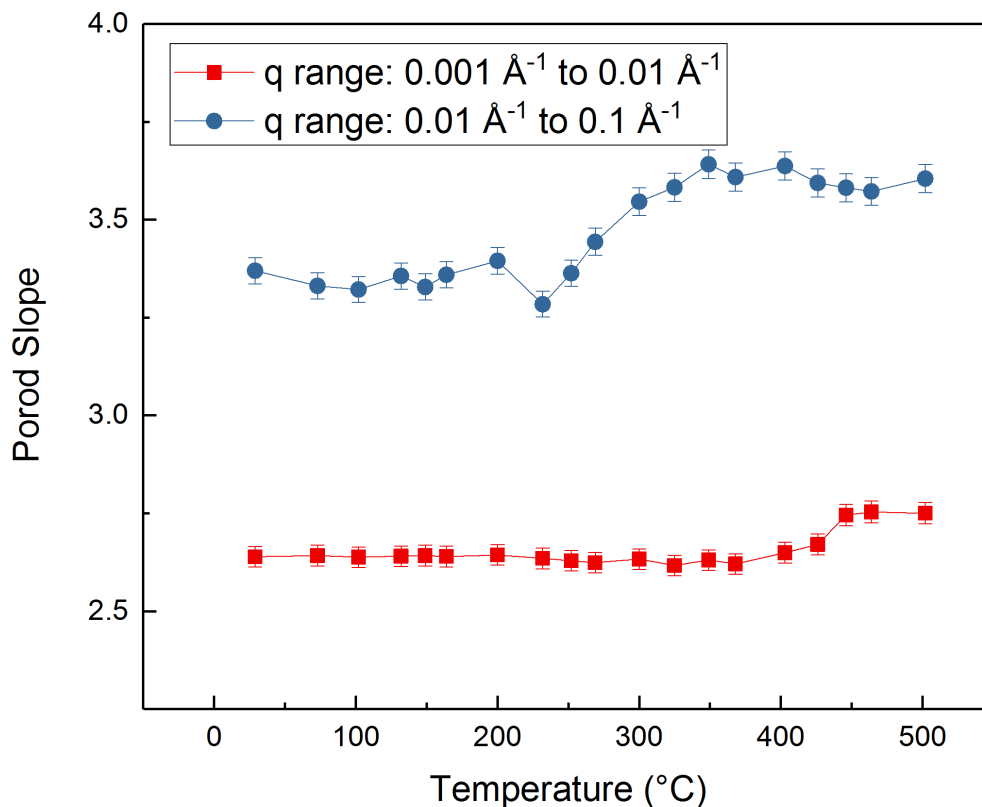


**Figure 4.6** Porod slopes as calcium hydroxide is reacted with calcium carbonate are represented. Low  $q$  and high  $q$  ranges represent  $0.001\text{-}0.01 \text{ \AA}^{-1}$  and  $0.01\text{-}0.1 \text{ \AA}^{-1}$ , respectively. The data was obtained after desmearing the USAXS/SAXS data shown in Figure 5. Porod slope of 1 and 4 indicated scattering from rigid rods and smooth surfaces, respectively. Porod slopes in the range of 2-3 and 3-4 are indicative of branched systems or networks also known as mass fractals and rough interfaces with a fractal dimension,  $D$  where  $n = 6 - D$  represents a surface fractal.

# CHAPTER 5

## INTEGRATED CO<sub>2</sub> CAPTURE, CONVERSION AND STORAGE TO PRODUCE CALCIUM CARBONATE USING AN AMINE LOOPING STRATEGY

*The contents of this chapter have been published as a scientific peer-reviewed journal at Liu, M., & Gadikota, G. “Integrated CO<sub>2</sub> Capture, Conversion and Storage to Produce Calcium Carbonate Using an Amine Looping Strategy.” *Energy & fuels* 33, 3 (2018): 1722-1733.*

### 5.1 Introduction

It has been shown that scalable reductions in CO<sub>2</sub> emissions at the gigaton scale can only be achieved by developing a portfolio of options. (Pacala & Socolow, 2004; Socolow & Pacala, 2006) In this context, several technologies have been developed to capture CO<sub>2</sub> from flue gas streams (Wilcox, 2012), and store CO<sub>2</sub> in geologic environments (Thomas & Benson, 2005). However, one approach that has been largely unexplored is the concept of integrating CO<sub>2</sub> capture and storage with the potential for utilization. Some of the key considerations with approaches that propose utilization is the potential permanence of the desired end product and the energy associated with the conversion process (Mac Dowell et al., 2017). The conversion of CO<sub>2</sub> to calcium and magnesium carbonates also known as carbon mineralization, is a thermodynamically downhill pathway that ensures the long-term and environmentally benign storage of CO<sub>2</sub>. With increasing interest in process intensification, we propose a novel integrated approach of looping CO<sub>2</sub>-bearing amine-bearing solvents such as monoethanolamine (MEA) with accelerated conversion of CO<sub>2</sub> to calcium and magnesium carbonate-bearing materials.

Extensive studies have been dedicated towards accelerated carbon mineralization via direct CO<sub>2</sub>-reaction fluid-mineral interactions (Chizmeshya et al., 2007; Gadikota et al., 2013; Gerdemann et al., 2007), and indirect approaches that involve decoupling the recovery of calcium and/or magnesium cations and the conversion of these cations to their respective carbonates (Park et al., 2008; Park & Fan, 2004; Zhao et al., 2013). These approaches were proposed to overcome kinetic challenges associated with CO<sub>2</sub> hydration, dissolution of the alkaline-bearing materials, and the precipitation of calcium and magnesium carbonates, depending on the temperature, pressure, and chemistry of the aqueous phase and the reacting solids (Gadikota et al., 2013; Giammar et al., 2005). While a few pathways explored the use of flue gas concentrations of CO<sub>2</sub> for carbon mineralization, the time-scales of these reactions are often to the order of several days (Harrison et al., 2012). Therefore, the use of temperatures above 100 °C and CO<sub>2</sub> partial pressures in the range of 1-150 atm were often used to accelerate carbon mineralization to the order of a few hours (Gadikota et al., 2013).

Further, solution compositions comprising strong acids (Maroto-Valer et al., 2009) or weak organic acids (Park et al., 2008; Park & Fan, 2004; Zhao et al., 2013) were proposed to aid the dissolution kinetics. Dual purpose additives such as NaHCO<sub>3</sub> which buffer the pH and serve as a carbon source were extensively investigated to achieve simultaneous dissolution and conversion to calcium and magnesium carbonates (Gadikota et al., 2013). The use of alkaline solutions such as NaOH and NH<sub>4</sub>OH were proposed to enhance the precipitation of calcium and magnesium carbonate. Efforts to enhance the hydration of CO<sub>2</sub> led to the use of natural and engineered bioenzymes such as carbonic anhydrase (Favre et al., 2009; Mirjafari et al., 2007). Challenges related to the formation of mass transfer limiting layers in calcium and magnesium bearing silicate rocks were surmounted using abrasives and via attrition grinding to increase the reactive surface

areas of these materials (Chizmeshya et al., 2007; Park & Fan, 2004). These efforts in exploring the parametric space for enhancing carbon mineralization along with chemical and physical activation approaches led to transformative insights for accelerating carbon mineralization which typically occurs to the order of several years at the field scale to the order of a few minutes and hours at the laboratory scale.

Another key consideration is the chemistry of the reacting solid. While the reactivities of calcium and magnesium oxides and hydroxides is high given the ease of dissolution of these materials to release calcium and magnesium ions into the solution phase, it is important to consider less reactive Ca and Mg-bearing silicate and alumino-silicate materials to achieve the scalable conversion of CO<sub>2</sub> to calcium and magnesium carbonates. Assessments of the reactivity of calcium and magnesium-bearing silicates and alumino-silicate bearing rocks and minerals showed that the materials with simpler crystal structures such as wollastonite (CaSiO<sub>3</sub>) and olivine (Mg<sub>2</sub>SiO<sub>4</sub>) yielded higher reactivities while complex alumino-silicates such as labradorite, anorthite, and basalt yielded lower reactivities (Gadikota, 2014). However, the abundance of basalt is much greater compared to that of wollastonite. These data suggested that the field scale conversion of CO<sub>2</sub> to calcium and magnesium carbonates may be achievable using less reactive but earth abundant materials such as basalt, while engineered and reproducible processes may be used to produce calcium and magnesium carbonates from highly reactive but less abundant materials such as wollastonite.

Assessing the potential for carbon mineralization as a potential CO<sub>2</sub> utilization and storage option is important. In this context, several gigatons of carbon can be stored in natural geologic materials while 200-300 Mt of CO<sub>2</sub> can be stored in alkaline industrial residues annually (Sanna et al., 2012). These alkaline industrial residues can include (but not limited to) fly ash, steel slag,

cement kiln dust, red mud, mining wastes and electronic-waste slags produced from coal-fired power plants, steel manufacturing plants, cement industries, aluminum production units, mining, and electronic waste processing industries, respectively. However, there is significant variability in the calcium and magnesium content of the alkaline industrial residues. Regardless, calcium oxides and calcium silicates are often the dominant constituents of these materials (Gadikota & Park, 2015). Therefore, in this study, we propose to explore a novel amine-looping strategy for the enhanced conversion of CO<sub>2</sub> to calcium carbonate using calcium oxide and silicate. With increasing deployment of CO<sub>2</sub> capture facilities with amine-bearing solvents such as the Petra Nova and Boundary Dam projects (Jenkins, 2015; Stéphenne, 2014), it is becoming increasingly important to integrate CO<sub>2</sub> conversion with capture.

In this study, we propose two modes for coupling the conversion of CO<sub>2</sub> to calcium and magnesium carbonates to the regeneration of amine-bearing solvents. In the first mode, CO<sub>2</sub> bearing flue gas streams are continuously fed to a slurry system composed of MEA as the amine-bearing solvent. In this mode, MEA aids the capture of CO<sub>2</sub> from the flue gas stream and the release of the bound CO<sub>2</sub> to the dissolved calcium to form calcium carbonate. In the second mode, CO<sub>2</sub>-loaded MEA is directly reacted with the alkaline industrial residues. The modes and the corresponding reactions occurring in the slurry phase are shown in **Figure 5.1**. The first mode is intended to explore the potential for capturing CO<sub>2</sub> from highly concentrated flue gas streams while utilizing pH-aided *in-situ* amine swing to produce calcium carbonate. In the second mode, the influence of CO<sub>2</sub>-loaded amines on the accelerated conversion to calcium carbonates is explored. A comparison of these two approaches will allow us to explore the potential two possibilities. The first approach allows us to explore the feasibility of using flue gas streams with accelerated carbon mineralization coupled to amine regeneration. The second approach explores

the potential integration of CO<sub>2</sub>-loaded amines with carbon mineralization for integration with an adsorption column for CO<sub>2</sub> capture. These proposed approaches are explored with calcium oxide and calcium silicate with varying concentrations of MEA in the aqueous phase and at temperatures in the range of 25-90 °C for reaction times of three hours.

Another consideration is the stability of calcium carbonate in varying pH conditions. The storage of calcium and magnesium carbonates in reclaimed mine sites has been suggested. However, the long-term stability is an important consideration along with the potential changes in the morphology and structure of these materials in the natural environment. In this study, we used synchrotron X-ray reflectivity measurements to evaluate the changes in the calcite surfaces when exposed to varying pH environments. While X-ray reflectivity and truncation rod measurements have been used to determine the arrangement of interfacial water at calcite surfaces (Fenter & Sturchio, 2012), and the surface speciation of calcite (Fenter et al., 2000), our studies provide direct evidence of the changes in the roughness of calcite interfaces at varying pH conditions. The experimental details are discussed in the following sections.

## **5.2 Experimental Methods**

The integrated carbon mineralization approach with amine looping was tested using calcium oxide and calcium silicate. Calcium oxide and calcium silicate were procured from Fisher Scientific and Alfa Aesar, respectively. The mean particle sizes of calcium oxide and calcium silicate are 95.3 μm and 12 μm, respectively. The surface area of calcium oxide and calcium silicate are 11.69 m<sup>2</sup>/g and 5.15 m<sup>2</sup>/g, respectively. The accumulative pore volume of calcium oxide and calcium silicate are 0.03765 cc/g and 0.03049 cc/g, respectively. The carbon mineralization

experiments were performed with MEA. MEA with a purity of 98% was purchased from Alfa Aesar.

### **5.2.1 Integrated carbon mineralization with in-situ amine looping**

The carbon mineralization experiments with *in-situ* CO<sub>2</sub> capture and release of MEA were performed in a reactor operated in batch and flow-through modes (Parr Reactor, Series 4590 Micro Stirred Reactor). A typical experiment involved mixing 3 g of the solid reactant with 17 g of the fluid, after which the reactor was sealed. The stirring rate was set to 300 rpm  $\pm$  5 rpm for all the experiments reported in this study which provided sufficient heat and mass transfer. In Mode 1, the aqueous phase was composed of MEA with compositions of 10, 30, and 50 wt%. The reactor was then connected to a CO<sub>2</sub> gas tank to continuously supply pure CO<sub>2</sub> at a pressure of 1 atm. The gas phase was composed of pure CO<sub>2</sub> in Mode 1. In Mode 2, MEA was loaded with CO<sub>2</sub> prior to the carbon mineralization experiments. The CO<sub>2</sub>-loaded MEA, water and unreacted solids were mixed in the reactor. CO<sub>2</sub> gas was not supplied to the reactor in this mode. Therefore, in Mode 2, carbon mineralization proceeds in a liquid-solid environment unlike in Mode 1 where a continuous supply of CO<sub>2</sub> is provided.

The experiments in Modes 1 and 2 were performed for a reaction time of 3 hours. The reactor system typically took about 15-20 minutes to reach the desired setpoint which marked the beginning of the experiment. After the reaction time of 3 hours, the reactor temperature was reset to room temperature and the CO<sub>2</sub> supply is turned off. The system typically takes about 20 minutes to cool down to room temperature, after which the contents are removed and separated using vacuum filtration. The collected solid product was dried in an oven at 105 °C for 12 hours prior to characterization.

### 5.2.2 Characterization of the reactants and products in the carbon mineralization process

The carbon content in the reacted solids was determined using Thermogravimetric Analyzer (TGA, TGA 550, TA Instruments) based on the change in the weight of the sample on heating. The heating rate was set to 5 °C/min and the flow rate of the N<sub>2</sub> gas was 25 mL/min. As discussed in Gadikota et al. (Gadikota et al., 2013), and summarized as follows, the extent of carbonation,  $Y_{CO_2, TGA}$  is a measure of the ratio of the amount of CO<sub>2</sub> present in the sample with respect to the CO<sub>2</sub> storage capacity, and is represented by the following equation:

$$Y_{CO_2, TGA} = R_{CO_2} \times \left( \frac{TGA}{100 - TGA} \right) \times 100\% \quad (\text{Equation 5.1})$$

In the equation above, the weight change (in percent) of the carbonate-bearing calcium oxide and calcium silicate precursors at the calcination temperature in the range of 650-800 °C is represented by TGA. The amount of CaO or CaSiO<sub>3</sub> needed for storing a unit mass of CO<sub>2</sub> is defined as  $R_{CO_2}$  (Gadikota et al., 2013).

Further, carbon mineralization is expected to have a significant influence on the morphology of the produced materials. To determine the morphologies of the materials before and after the carbon mineralization process, particle size analyses (LS 13 320, Beckman Coulter) and pore size analyses (BET Autosorb1, Anton Paar) were performed. These measurements were supported by scanning electron microscopy (SEM, Hitachi High Technologies America, Hitachi S3400-N) images. Attenuated Total Reflectance – Fourier Transform – Infrared Spectroscopy (ATR-FTIR, Thermo Fisher Nicolet iS10) measurements were performed to determine the chemical species formed.

### 5.2.3 X-ray reflectivity measurements

The X-ray reflectivity measurements were performed to determine the surface morphological changes in calcite when exposed to solutions in varying pH conditions. These measurements are intended to provide into the insights into the morphological stability of the calcite surfaces in the context of permanent carbon storage. To describe briefly, X-ray reflectivity (XRR) is the ratio of the reflected to incident X-ray flux and is based on the Fresnel reflectivity Law where reflected angle equal to incident angle on perfectly sharp and smooth surface. This approach can be used to describe the laterally averaged electron density profile,  $\rho(z)$  near a reflecting interface  $R = (4\pi r_e/Q)^2 \left| \int \rho(z)e^{iQz} dz \right|^2$ , where  $Q = (4\pi/\lambda)\sin(\theta)$ , and  $\theta$  is the angle of incidence to the surface plane, and  $\lambda$  is the wavelength of the X-ray (Feidenhans'l, 1989; Fenter et al., 2000). In this study, X-ray reflectivity measurements are used to determine the changes in the surface roughness of smooth calcite surfaces. While bulk measurements suggest that significant dissolution of calcite does not occur at pH conditions of 3 (Fenter, 2002), these XRR measurements are intended to probe possible morphological changes in calcite surfaces on dissolution.

The XRR measurements was performed at Sector 12-ID-D at Advanced Photon Source (APS) in Argonne National Laboratory (ANL), Argonne, IL. The X-ray energy used was 20 keV, which corresponds to a wavelength of 0.6199 Å. The beam size was set in the range of 100-110  $\mu\text{m}$ . The incident X-ray flux was measured by an ion chamber, and the reflected flux was measured using a NaI scintillation detector. The calcite sample used was Iceland spar donated by the Geology Museum at the University of Wisconsin. The calcite surface (1 0 4) was cleavage manually and the cleaved thin slide was mounted on the sample cell by a thin layer Kapton film. XRR

measurements of the calcite surface were performed when exposed to air, and fluidic environments in pH 3, 5, and 7 environments. The solution was continuously supplied using a flow-through system with the mounted sample connected to a 50 mL syringe. The air bubbles were carefully eliminated to prevent interference with the reflectivity measurements. The X-ray reflectivity measurements were performed at ambient temperature around 20 °C. Each measurement took around 45 – 60 minutes for one complete measurement.

#### **5.2.4 Wide Angle X-ray Scattering (WAXS) measurement**

To determine the structural and changes when reacting with CO<sub>2</sub> flowing through, the WAXS measurements were performed at Sector 9-ID at Advanced Photon Source (APS) in Argonne National Laboratory (ANL), Argonne, IL. The total X-ray flux used in this measurement was  $10^{13}$  photon s<sup>-1</sup>. The energy of the X-ray used in this experiment was 21.0 keV, which corresponded to a wavelength of 0.59 Å. The calibrations of measurements used silver behenate and the NIST standard reference material, SRM 640d (Si).

### **5.3 Results and Discussion**

#### **5.3.1 Effect of MEA concentration**

One of the primary objectives of this study is to investigate whether amine-bearing solvents can effectively capture and transfer CO<sub>2</sub> to dissolved cations to form water-insoluble calcium carbonate. To investigate this hypothesis, carbon mineralization experiments were performed in two modes as shown in **Figure 5.1**. In the first mode, high purity CO<sub>2</sub> gas was continuously supplied to a reactor system composed of a slurry of calcium oxide or calcium silicate mixed with MEA. MEA was chosen as the model solvent to investigate this hypothesis. In this mode, MEA is expected to actively capture CO<sub>2</sub> in the aqueous phase. Further, the alkalinity of the aqueous phase

is above pH 8 which aids the release of CO<sub>2</sub> as carbonate and bicarbonate species to precipitate calcium carbonate. In the second mode, MEA was pre-loaded with CO<sub>2</sub> before adding the alkaline calcium oxide and silicate substrates. CO<sub>2</sub> gas was not continuously supplied. Unlike in Mode 1, CO<sub>2</sub> supply is limited in Mode 2. However, the chemical reactions in the aqueous phase which include the uptake of CO<sub>2</sub>, release of bicarbonate and carbonate species, dissolution of calcium oxide and calcium silicate, and precipitation of calcium carbonate are expected to be similar in Modes 1 and 2.

To investigate the influence of variable concentrations of MEA, experiments were performed with deionized water without MEA, 10, 30, and 50 wt% of MEA at a reaction temperature of 50 °C for 3 hours and a stirring rate of 300 rpm. In the absence of MEA, the extents of carbonation of calcium oxide and calcium silicate are 24.3 % and 20.3 %, respectively (**Figure 5.2(a)**). These experiments were performed in Mode 1 where CO<sub>2</sub> at a pressure of 1 atm was continuously supplied to the reactor. The significant differences in the reactivity of calcium oxide and silicate are attributed to differences in these materials. Calcium oxide dissolves readily in water to produce calcium hydroxide while the recovering Ca<sup>2+</sup> cations from the calcium silicate matrix is challenged by the slow dissolution rates in the absence of induced acidic environments. Further, it was interesting to note a significant change in the particle size distribution of calcium oxide before and after the carbon mineralization process (**Figure 5.2(b-1)**). The mean particle size of calcium oxide reduced from 95.3 μm to 13.4 μm on reacting with CO<sub>2</sub> to form calcium carbonate. These data suggested that calcium oxide completely dissolves prior to the nucleation and growth of calcium carbonate. In comparison, the particle size distribution profiles of calcium silicate before and after carbon mineralization did not change significantly (**Figure 5.2(c-1)**). The mean particle size of calcium silicate changed from 12 μm to 6.5 μm on carbon mineralization. This

change is attributed to the reduction in the volume of particles in the range of 20  $\mu\text{m}$  to 100  $\mu\text{m}$ , and an increase in the volume of particles in the range of 2-10  $\mu\text{m}$ .

In Mode 1 which is characterized by a continuous supply of  $\text{CO}_2$ , the extents of carbonation achieved with CaO are 29.1, 89.2, and 92.9 % in a solution composed of 10, 30, and 50 wt % of MEA, respectively. These data provide direct evidence of near complete conversion of calcium oxide to calcium carbonate in high concentrations of MEA. In Mode 2 however, where amine-bearing solvents pre-loaded with  $\text{CO}_2$  were introduced into the reactor system, the extent of carbon mineralization of calcium oxide were 10.4, 36.7, and 80.0 % in a solution composed of 10, 30, and 50 wt% of MEA, respectively (**Figure 5.2(a)**). These data suggest that at higher MEA concentrations of 30 and 50 wt% enhance the availability of  $\text{CO}_2$ . It is also interesting to note that in Mode 1 with continuous flow of  $\text{CO}_2$ , the particle size of calcium carbonate synthesized in 50 wt% MEA was 9.7  $\mu\text{m}$  compared to 55.2  $\mu\text{m}$ . Further, the particle size distribution profiles indicate the formation of finer particles of calcium carbonate in Mode 1 as opposed to in Mode 2 (**Figures 5.2(b-1) and (b-2)**). The cumulative pore volume of calcium carbonate produced with 50 wt% MEA and via Mode 1 at 50  $^\circ\text{C}$  was 0.091 cc/g compared to that of unreacted calcium oxide at 0.038 cc/g, and the BET surface area changed from 11.69  $\text{m}^2/\text{g}$  to 14.04  $\text{m}^2/\text{g}$ , suggesting the formation of porous calcium carbonate starting from less porous precursors such as calcium oxide.

Unlike calcium oxide, the reactivity of calcium silicate was much lower in Modes 1 and 2 even at high concentrations of MEA. The extents of calcium carbonate formation starting with calcium silicate are 20.3, 9.6, 6.2, and 36.3 % in deionized water, 10, 30, and 50 wt% MEA, respectively in Mode 1 with a continuous supply of  $\text{CO}_2$ . The lower than expected extents of carbon mineralization of calcium silicate in the presence of 10 and 30 wt% MEA suggest that at these conditions, the pH may not be suitable to aid the simultaneous dissolution and carbon

mineralization behavior of calcium silicate. Further, the cumulative pore volumes of unreacted and reacted calcium silicate with an extent of carbon mineralization of 36 % were determined to be 0.001 and 0.005 cc/g, respectively. These data suggest a small increase in the cumulative pore volume of the carbonate-bearing calcium silicate compared to unreacted calcium silicate.

When these experiments are performed in Mode 2, i.e., with pre-loaded CO<sub>2</sub>-bearing MEA, the extents of carbonation were 14.0, 7.0, and 9.0 %. These low extents of carbon mineralization may be attributed to the limited availability of CO<sub>2</sub> along with lower than expected dissolution and carbon mineralization behaviors of calcium silicate. It was interesting to note the particle size distributions did not change significantly at low extents of carbon mineralization of calcium silicate (**Figures 5.2(c-1) and 5.2(c-2)**). The mean particle size decreased from 12 μm to 6.5 μm for an extent of carbon mineralization of 20.3 % when calcium silicate is reacted with water at 50 °C in Mode 1. A higher extent of carbon mineralization of calcium silicate to 36 % in the presence of 50 wt% MEA and at 50 °C resulted in a mean particle size of 10.7 μm (**Figure 5.2(c-1)**). The mean particle size of calcium silicate reacted in Mode 2 in 50 wt% MEA was 7.1 μm which corresponded to an extent of carbonation of 9.0 %. The cumulative pore volume of calcium carbonate produced with 50 wt% MEA and via Mode 1 at 50 °C was 0.041 cc/g compared to that of unreacted calcium oxide at 0.031 cc/g, and the BET surface area changed from 5.15 m<sup>2</sup>/g to 6.31 m<sup>2</sup>/g.

### **5.3.2 Effect of reaction temperature**

As discussed in the previous section, MEA concentrations as high as 50 wt% aid higher conversions of calcium-bearing materials such as calcium oxide and calcium silicate to calcium carbonate in the presence of a continuous supply of CO<sub>2</sub>, which is referred to as Mode 1. Further, the effect of MEA solvents pre-loaded with CO<sub>2</sub> (or Mode 2) yielded lower than expected

conversions owing to the limited availability of carbon-bearing species in the aqueous phase. When operated in Mode 1, the continuous supply of CO<sub>2</sub> facilitated the *in-situ* looping of MEA to capture and release CO<sub>2</sub> into the aqueous phase which aided the extent of carbon mineralization. Since Mode 1 facilitates higher conversions of CO<sub>2</sub> to calcium carbonate in the presence of 50 wt% MEA, the effect of temperature was probed to determine the optimal conditions that aid the conversion of CO<sub>2</sub> to calcium carbonate. The experiments were performed at 25, 50, 75, and 90 °C in the presence of 50 wt% MEA for a reaction time of 3 hours at constant stirring conditions of 300 rpm.

The extents of calcium oxide converted to calcium carbonate are 13.7, 92.9, 89.0, and 90.9 % at 25, 50, 75, and 90 °C, respectively in a solution bearing 50 wt% MEA with continuous CO<sub>2</sub> flow at 1 atm for 3 hours (**Figure 5.3(a)**). These data suggest that near complete conversion of calcium oxide to calcium carbonate can be achieved at temperatures as low as 50 °C in a solution bearing 50 wt% MEA with continuous CO<sub>2</sub> flow at 1 atm. In the absence of MEA, the extents of CaO converted to calcium carbonate are 22.1, 24.3, 19.0, and 36.4 % at 25, 50, 75, and 90 °C in water, respectively. The extents of carbonation are less than 50 % suggesting that in the absence of MEA, limited CO<sub>2</sub> supply results in lower conversions. It was interesting to note that at a lower conversion of 36.4 % at 90 °C, the mean particle size was 24.4 μm as opposed to 105.5 μm when 90.9 % conversion is achieved in the presence of 50 wt% MEA and at 90 °C, relative to unreacted calcium oxide that has a mean particle size of 95.3 μm.

The extents of calcium silicate converted to calcium carbonate are 19.2, 36.3, 7.2, and 15.2 % at 25, 50, 75, and 90 °C in a solution bearing 50 wt% MEA with continuous CO<sub>2</sub> flow at 1 atm for 3 hours. This interesting trend is attributed to the higher CO<sub>2</sub> absorption capacity of MEA at temperatures below 70 °C. At higher temperatures, the desorption of CO<sub>2</sub> may reduce the

availability of CO<sub>2</sub> for carbon mineralization. The highest reported extent of carbonation of calcium silicate via direct carbonation mineralization 100 % when reacted at a CO<sub>2</sub> partial pressure of 40 atm and a temperature of 100 °C in distilled water for one hour.(Gerdemann et al., 2007) However, in the absence of pressurized CO<sub>2</sub> and elevated temperature of 100 °C, an extent of carbonation of 36 % for calcium silicate at 50 °C in a solution bearing 50 wt% MEA with continuous CO<sub>2</sub> flow at 1 atm for 3 hours is reasonable.

Experiments with calcium silicate were also performed with deionized water to contrast with the effect of MEA. In the absence of MEA, the extents of calcium silicate conversion to calcium carbonate are 10.6, 20.3, 12.7, and 12.5 % at 25, 50, 75, and 90 °C, respectively. These data suggest that at 50 °C in the absence of chemical additives, the pH conditions may be conducive to aid the simultaneous dissolution and carbon mineralization behavior of calcium silicate. At 50 °C, the extent of carbon mineralized is 16 % greater in the presence of 50 wt% MEA as opposed to in deionized water. A comparison of the particle size distributions of the reacted and unreacted calcium silicate also yielded interesting insights. The particle size distributions of the reacted and unreacted calcium silicate did not vary significantly (**Figures 5.3 (c-1) and 5.3 (c-2)**) unlike those associated with calcium oxide (**Figures 5.3 (b-1) and 5.3 (b-2)**). The mean particle sizes of calcium silicate reacted in 50 wt% MEA and deionized water at 90 °C were 6.9 μm and 6.3 μm, respectively relative to that of unreacted calcium silicate which was 12 μm.

### **5.3.3 Characterization of the bulk phases and surface structure of calcium carbonate**

While the previous studies focused on the determination of the extents of carbon mineralization of calcium oxide and calcium silicate, the phases of carbonate-bearing species formed is an important consideration. Thermogravimetric analyses showed that calcium oxide was

converted to calcium carbonate and calcium hydroxide on reaction with CO<sub>2</sub> with the exception of the cases where high conversions to calcium carbonate are achieved in 50 wt% MEA at 50, 75 and 90 °C (**Figures 5.4 (a-1) and (a-2)**). The decomposition of calcium hydroxide and calcium carbonate occurs in the temperature ranges of 350 - 500 °C (Mikhail et al., 1966) and above 650 - 800 °C (Galan et al., 2013), respectively. The bulk thermogravimetric measurements showed that calcium carbonate was the only carbonate-bearing phase formed with calcium silicate as the precursor (**Figures 5.4 (b-1) and (b-2)**).

ATR-FTIR spectroscopic measurements provided further evidence of the products formed. There is clear evidence of -OH groups in calcium oxide reacted in water at 50 °C in Mode 1 and in unreacted calcium oxide at 3642 cm<sup>-1</sup> (Berzina-Cimdina & Borodajenko, 2012). Frequencies that correspond to the vibrational modes of carbonate ions in calcium carbonate at 712, 874, and 1435 cm<sup>-1</sup> (Al-Hosney & Grassian, 2005) in the carbonate-bearing calcium oxide materials are shown in **Figure 5.5 (a)**. Carbonate peak corresponding to 1435 cm<sup>-1</sup> is evident in the reacted calcium silicate materials (**Figure 5.5 (b)**).

The dominant phases of calcium carbonate which include orthorhombic aragonite with a spiky shape, hexagonal vaterite with plate-like morphology, and rhombohedral calcite are typically detected during the conversion of calcium oxide or calcium silicate to calcium carbonate (Gadikota et al., 2015). Scanning Electron Microscopy (SEM) images indicated the formation of calcite and vaterite when calcium oxide (**Figure 5.6 (a-1)**) was reacted with 50 wt% MEA at 50 °C characterized by a continuous flow of 100 % CO<sub>2</sub> at 1 atm (**Figure 5.6 (a-2)**). However, at similar experimental conditions with calcium silicate as the reactant (**Figure 5.6 (b-1)**), the formation of aragonite was evident (**Figure 5.6 (b-2)**). While previous studies extensively explored the phases of calcium carbonate formed starting with wollastonite as the precursor (Min et al., 2017; Zhao et

al., 2013). there has been a limited understanding of the stability of calcium carbonate under varying pH conditions. This is an important consideration since one of the permanent approaches for storing CO<sub>2</sub> is in its carbonate form in the natural environment, for example in reclaimed mine sites.

Considering that these carbonate interfaces may be exposed to varying levels of acidity (e.g., acid rain) and alkalinity in the natural environment, understanding the chemical and morphological stability of calcite in these environments is important. Further, if there is an interest in reusing the calcium carbonate material stored in the mines, it is important to understand how progressive exposure to acidic or alkaline environments may change the morphology of these materials. Solutions saturated with CO<sub>2</sub> typically result in a pH in the range of 3-4. Calcite dissolution rates at these pH conditions are to the order of 10<sup>-8</sup> mol/cm<sup>2</sup>/s (Pokrovsky et al., 2005) while the dissolution rates are lower as the pH increases to 7.

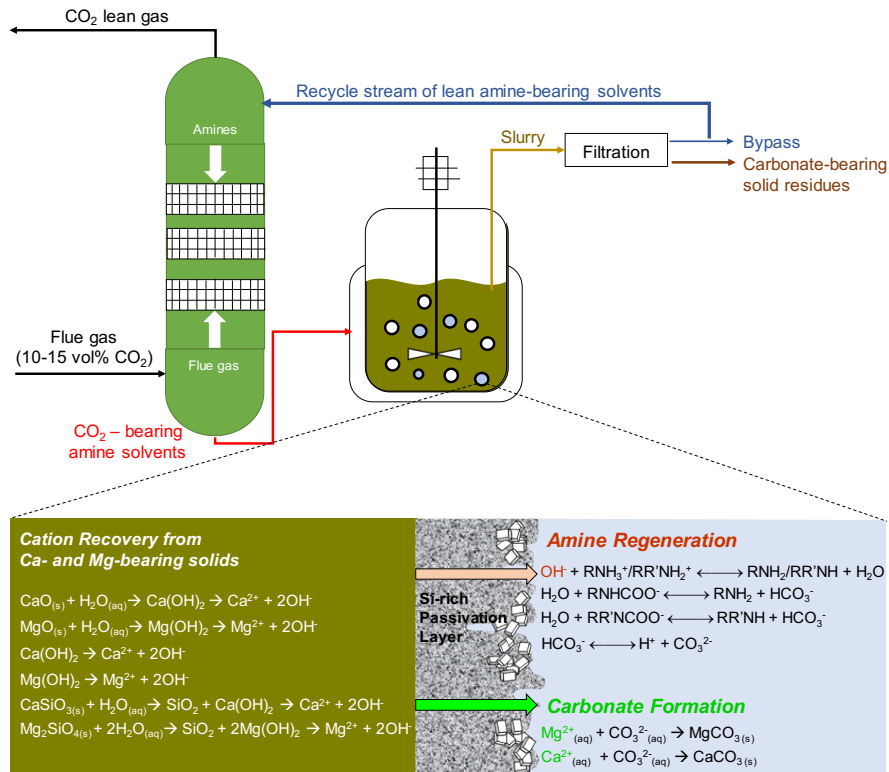
In this study, we probe the changes in the structural stability of calcium carbonate using X-ray reflectivity (XRR) measurements. Calcite surface cleaved along the (1 0 4) plane was exposed to aqueous fluids under various pH conditions, and high resolution X-ray reflectivity measurements were performed. These data are represented in **Figure 5.7**. The features observed in the data are in reasonable agreement with previous literature.(Chiarello et al., 1997; Chiarello & Sturchio, 1995; Fenter et al., 2000; Fenter & Sturchio, 2012; Geissbühler et al., 2004) The Q positions that correspond to the highest intensity which are 2.07, 4.14, and 6.21 Å<sup>-1</sup> represent the substrate Bragg reflections. The Q positions that correspond to the lowest intensity are the anti-Bragg positions. As the solution pH decreases from 7 to 5 and 3, a progressive reduction in the intensity is noted. Further, the lower intensity and larger error bars at pH 3 suggest that calcite

interfaces become increasingly rougher as dissolution progresses. Our studies provide direct evidence of a rapidly changing calcite interface at low pH conditions.

#### **5.4 Conclusions**

The feasibility of integrating CO<sub>2</sub> capture, conversion and storage for carbon mineralization is explored using the *in-situ* amine-looping approach. Two different modes of amine looping were explored. In the first mode, CO<sub>2</sub> was continuously circulated to facilitate the *in-situ* loading and release of CO<sub>2</sub> from MEA into the aqueous phase. In the second mode, MEA pre-loaded with CO<sub>2</sub> was introduced into the system without a continuous supply of CO<sub>2</sub>. While variations of the second mode were explored in previous studies, the concept of using a continuous flow of CO<sub>2</sub> for in-situ capture, conversion, and solvent regeneration without changing the process conditions shown in Mode 1 is novel. A comparison of both modes allowed us to probe the influence of limited CO<sub>2</sub> supply on the carbon mineralization behavior of calcium oxide and calcium silicate. Complete conversion of calcium oxide to calcium carbonate was achieved using both modes. Further, the extent of carbon mineralization achieved with calcium silicate was 36 % in Mode 1 as opposed to 20 % in Mode 2 at 50 °C for a reaction time of 3 hours. These data suggested that amine-bearing solvents undergo continuous looping between the CO<sub>2</sub> loaded and release states which facilitate the accelerated conversion of calcium-bearing oxides and silicates to calcium carbonate. The formation of calcium carbonate and calcium hydroxide phases was noted when less than complete conversions of calcium oxide were achieved. Calcium carbonate was the only phase formed on the complete conversion of calcium oxide and the carbon mineralization of calcium carbonate. This approach of simultaneous capture, conversion, and storage of CO<sub>2</sub> to CaCO<sub>3</sub> adds to the portfolio of options for integrated pathways reported by Lorenzo and coworkers.

(a) Mode 1



(b) Mode 2

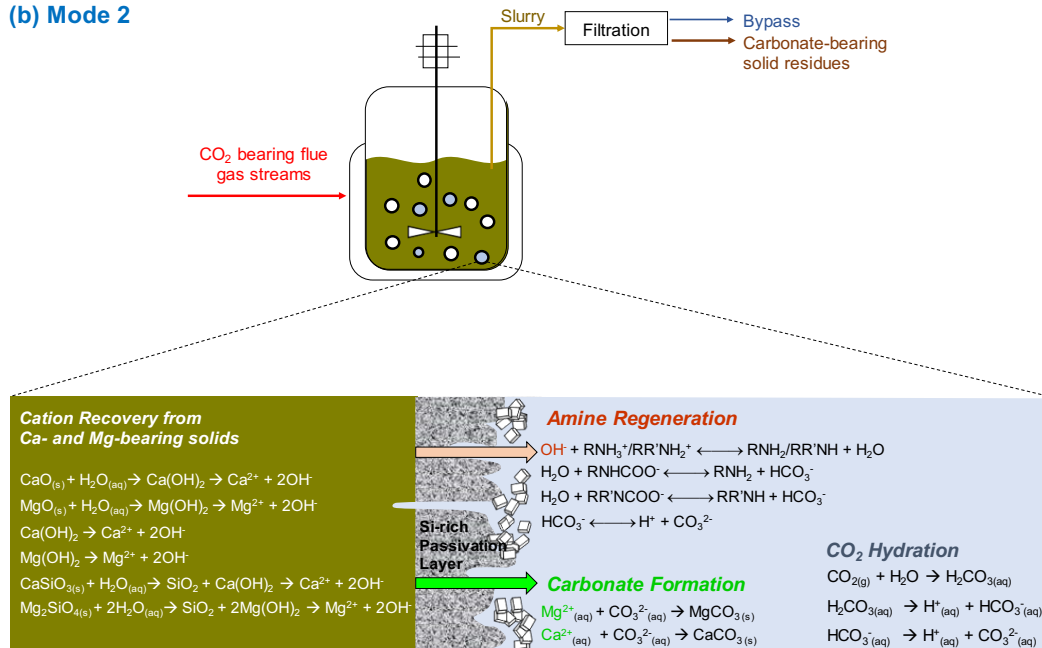


**Figure 5.1** Schematic representation of integrated carbon mineralization with *in-situ* amine looping with (a) a continuous supply of CO<sub>2</sub> as flue gas with *in-situ* capture and release of carbon-

bearing species, and (b) CO<sub>2</sub>-loaded amine-bearing solvents for *in-situ* release of carbon-bearing species for accelerated mineralization.

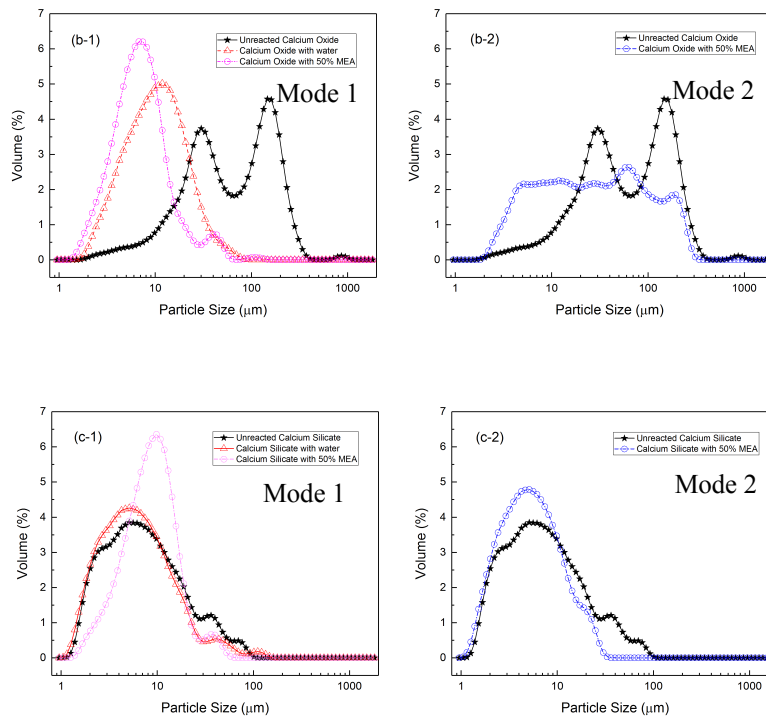
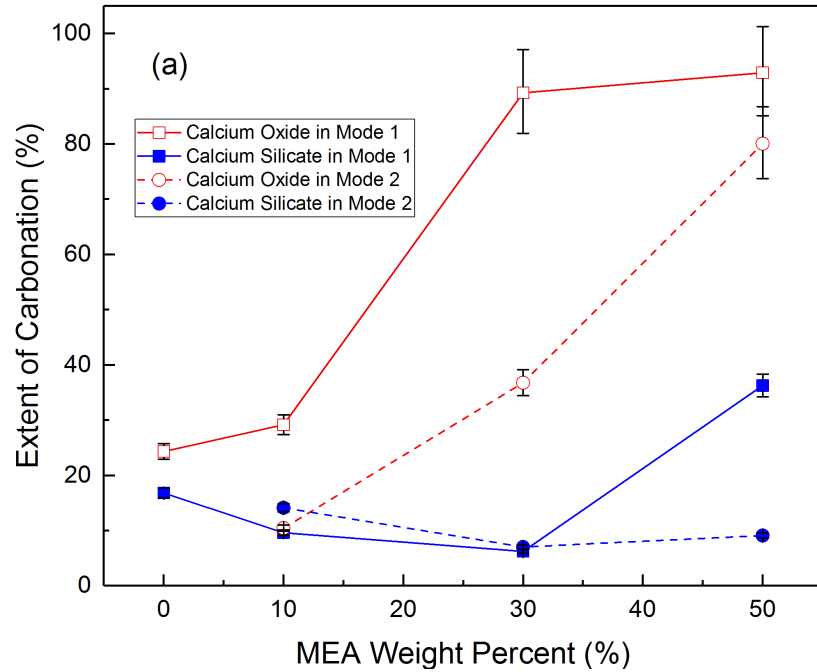


**Figure 5.2** (a) Extent of carbonation of CaO and CaSiO<sub>3</sub> reacted with water and 10 wt%, 30 wt%, and 50 wt% MEA at 50 °C for 3 hr at P<sub>CO<sub>2</sub></sub> = 1 atm and a stirring rate 300 rpm. Particle size

distribution of CaO (b-1) and CaSiO<sub>3</sub> (c-1) reacted with water and 50 wt% MEA at 50 °C in Mode 1 for 3 hr at P<sub>CO2</sub> = 1 atm and a stirring rate 300 rpm. Particle size distribution of CaO (b-2) and CaSiO<sub>3</sub> (c-2) reacted with 50 wt% CO<sub>2</sub> loaded-MEA at 50 °C in Mode 2 for 3 hr and a stirring rate 300 rpm.

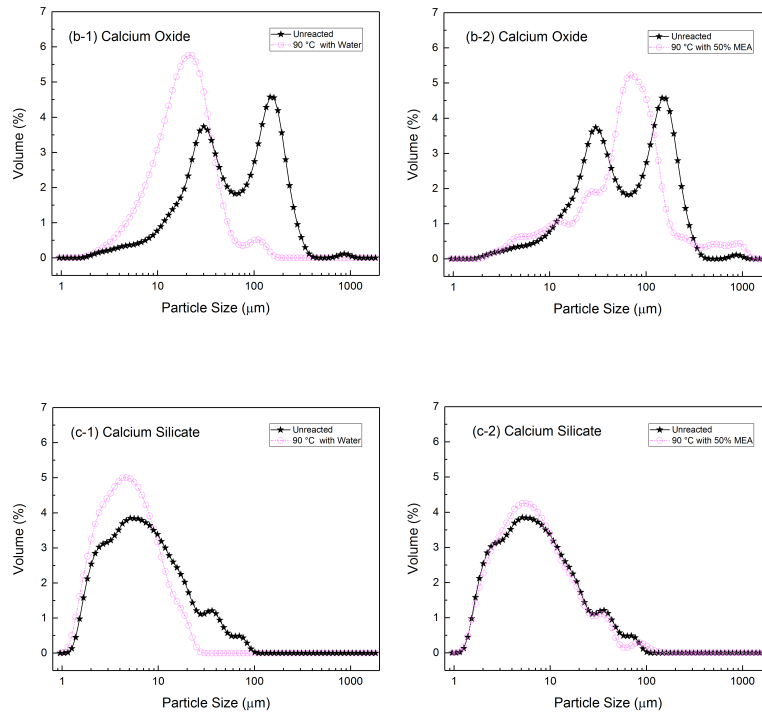
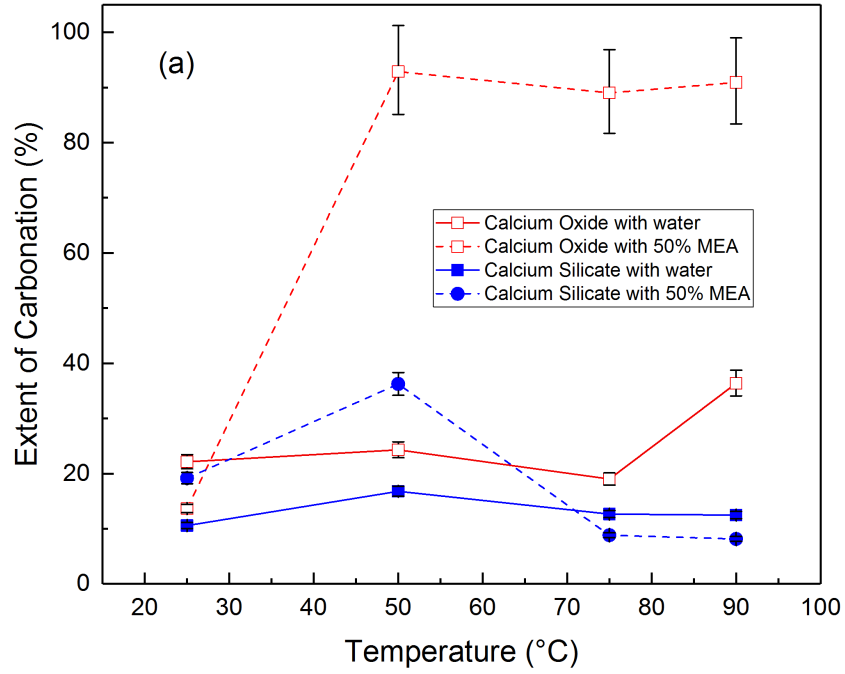


**Figure 5.3** (a) Extent of carbonation of CaO and CaSiO<sub>3</sub> with water and 50 wt% MEA at 25 °C, 50 °C, 75 °C, and 90 °C in Mode 1 for 3 hr at P<sub>CO2</sub> = 1 atm and a stirring rate 300 rpm. Particle

size distribution of CaO reacted with water (b-1) and 50 wt% MEA (b-2) at 90 °C in Mode 1 for 3 hr at  $P_{CO_2} = 1$  atm and a stirring rate 300 rpm. (c-1) Particle size distribution of CaSiO<sub>3</sub> reacted with water (c-1) and 50 wt% MEA (c-2) at 90 °C in Mode 1 for 3 hr at  $P_{CO_2} = 1$  atm and a stirring rate 300 rpm.

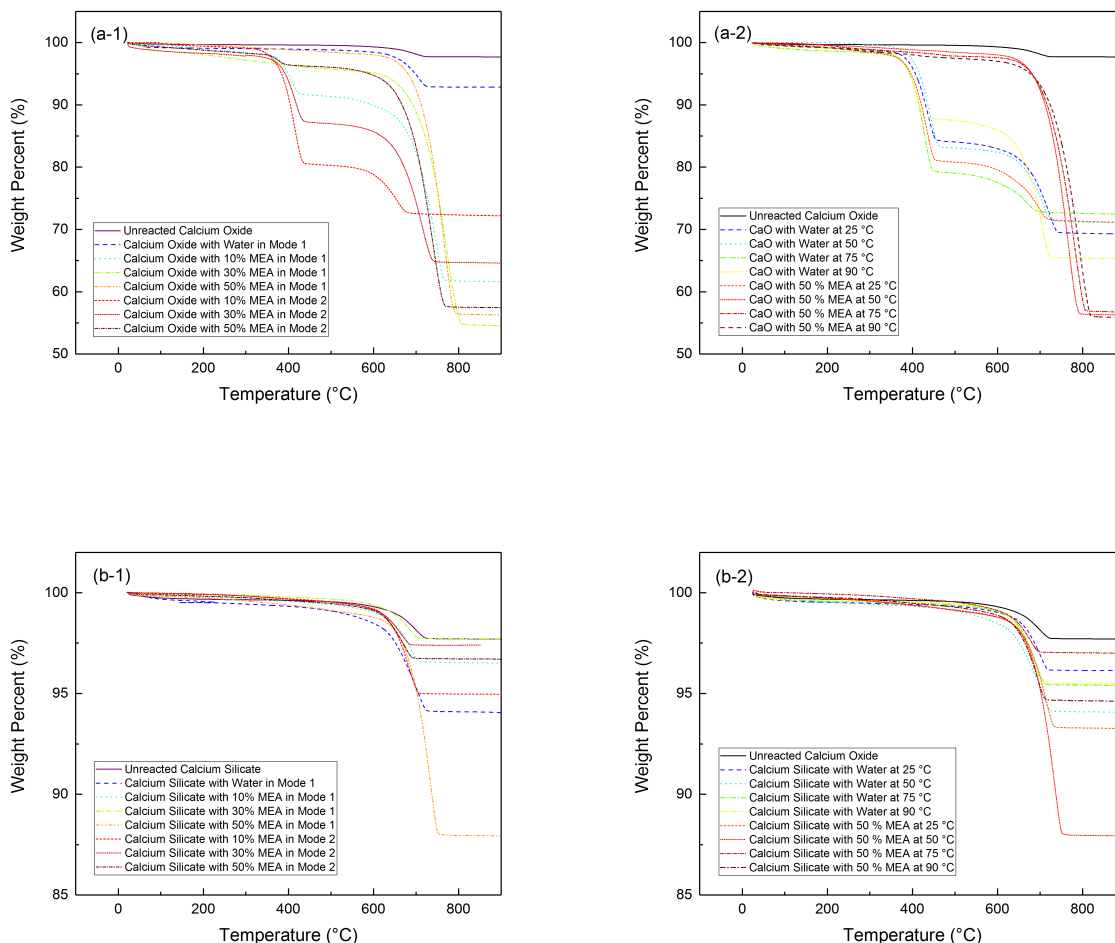


**Figure 5.4** Determination of the phases present in calcium oxide and calcium silicate using thermogravimetric analyses (TGA). Modes 1 and 2 represent continuous CO<sub>2</sub> flow ( $P_{\text{CO}_2} = 1 \text{ atm}$ ) through a slurry containing MEA and MEA pre-loaded with CO<sub>2</sub> without a continuous supply of CO<sub>2</sub> gas. The effect of water and 10 wt%, 30 wt%, and 50 wt% MEA at 50 °C when reacted for 3 hr and a stirring rate of 300 rpm with calcium oxide (a-1) and calcium silicate (b-1) are shown. The effect of temperature (25 °C, 50 °C, 75 °C, and 90 °C) in water and 50 wt% MEA when

reacted for 3 hr and a stirring rate of 300 rpm with calcium oxide (a-2) and calcium silicate (b-2) are shown.

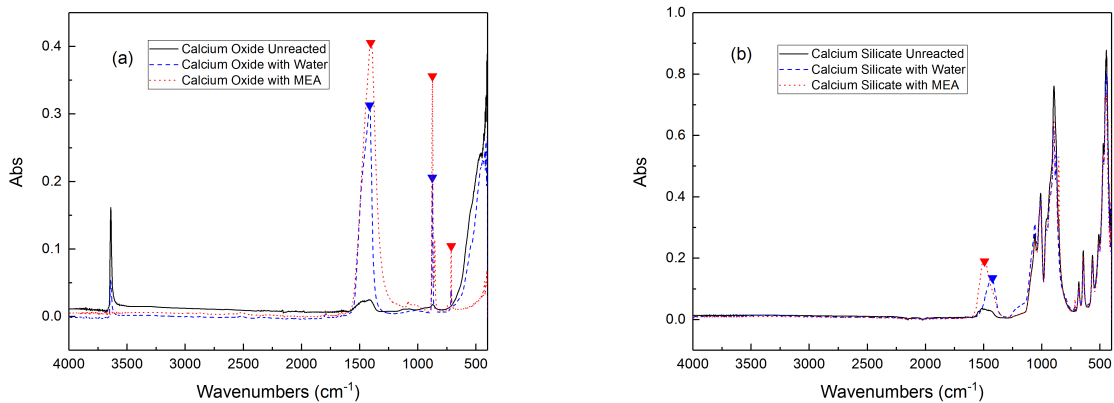


**Figure 5.5** Changes in the phases present in the reacted and unreacted calcium oxide (a) and calcium silicate (b) materials are represented by ATR-FTIR spectra. Spectra in black represents the unreacted calcium-bearing materials. Spectra in red and blue represents calcium oxide and calcium silicate reacted in water and MEA at 50 °C with continuous CO<sub>2</sub> flow ( $P_{\text{CO}_2} = 1 \text{ atm}$ ) for 3 hours and a stirring rate of 300 rpm.

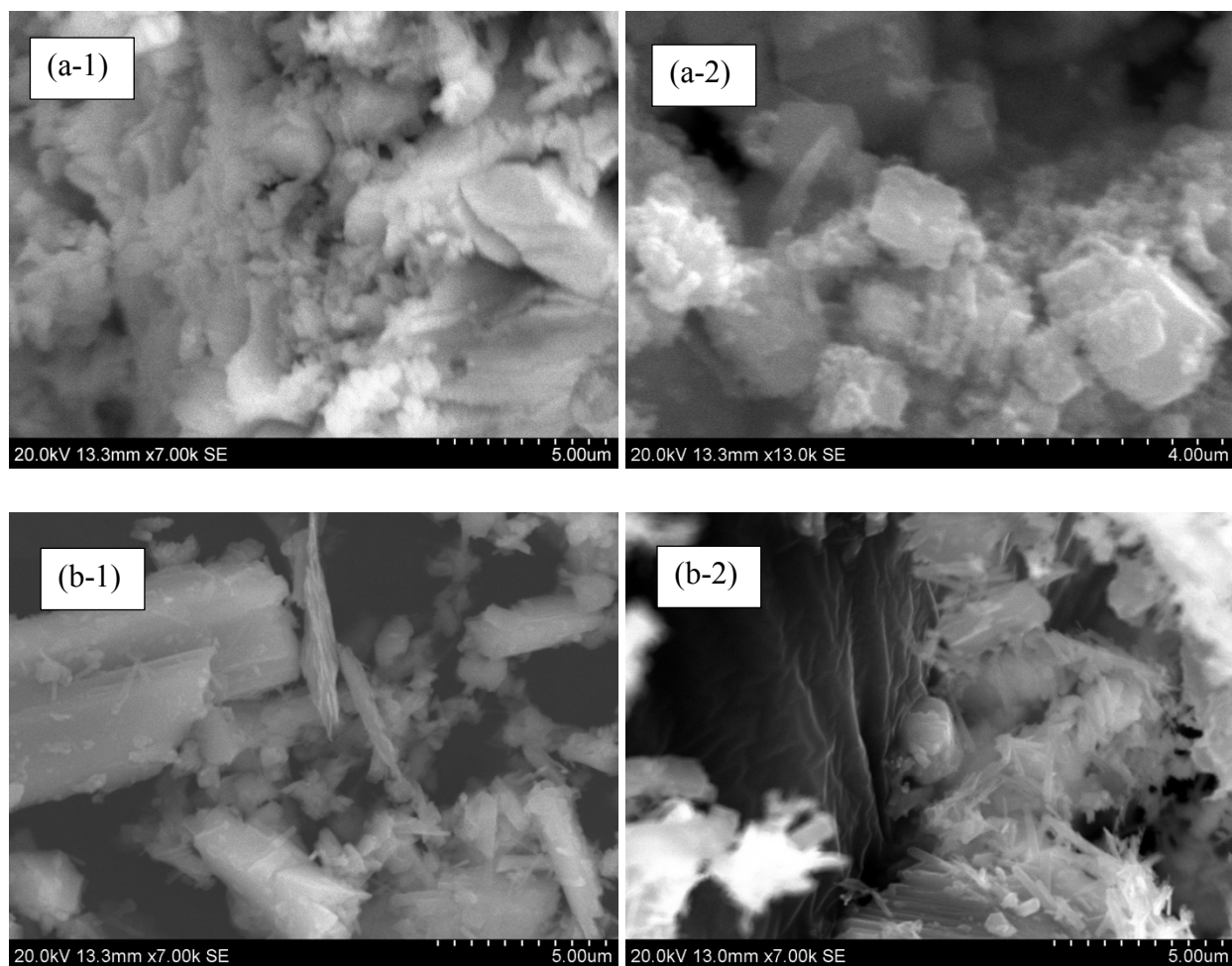


**Figure 5.6** Comparison of the morphological changes in unreacted calcium oxide (a-1) and calcium silicate (b-1) with calcium oxide (a-2) and calcium silicate (b-2) reacted with 50 wt% MEA at 50 °C when reacted for 3 hours and a stirring rate of 300 rpm.

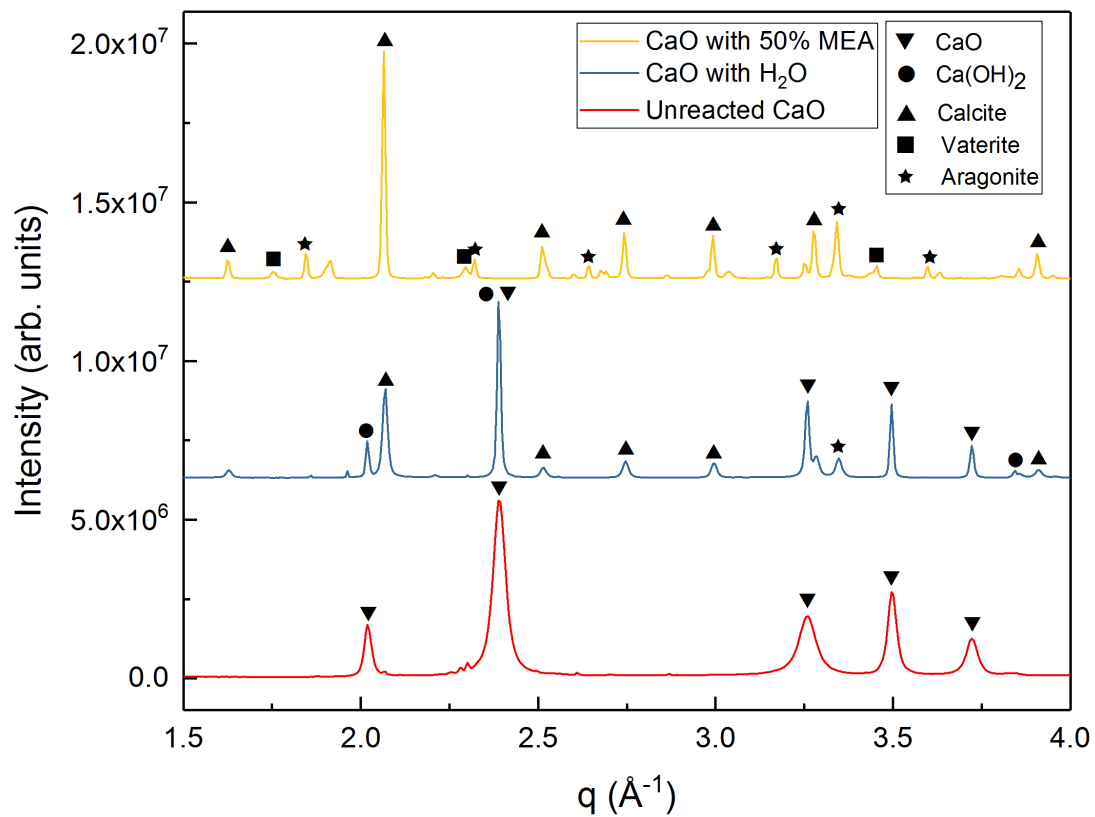


**Figure 5.7** Identification of unreacted CaO, CaO reacted with H<sub>2</sub>O and 50 wt % MEA at 50 °C in Mode 1. Peak identification is based on the crystallographic data reported for CaO, Ca(OH)<sub>2</sub>, calcite, vaterite, and aragonite.

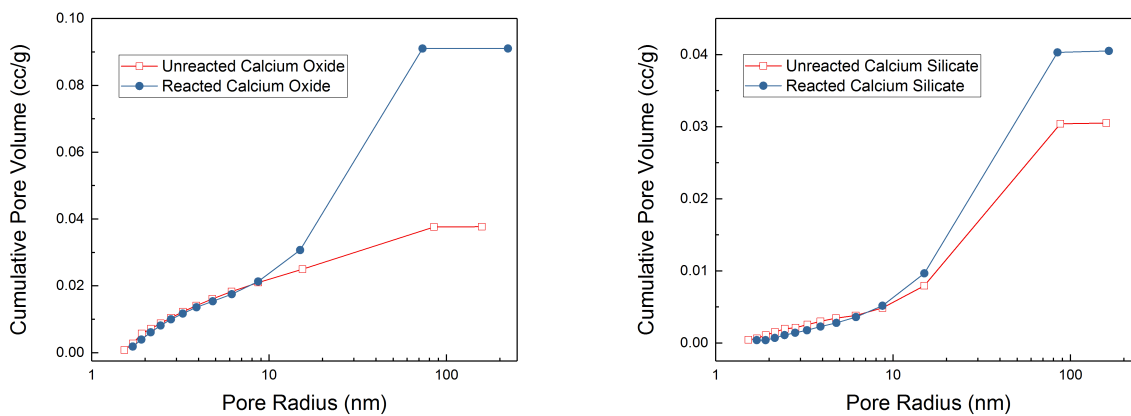


**Figure 5.8** Cumulative pore volume of unreacted CaO and CaSiO<sub>3</sub> and reacted with 50 wt% MEA at 50 °C when reacted for 3 hours and a stirring rate of 300 rpm.

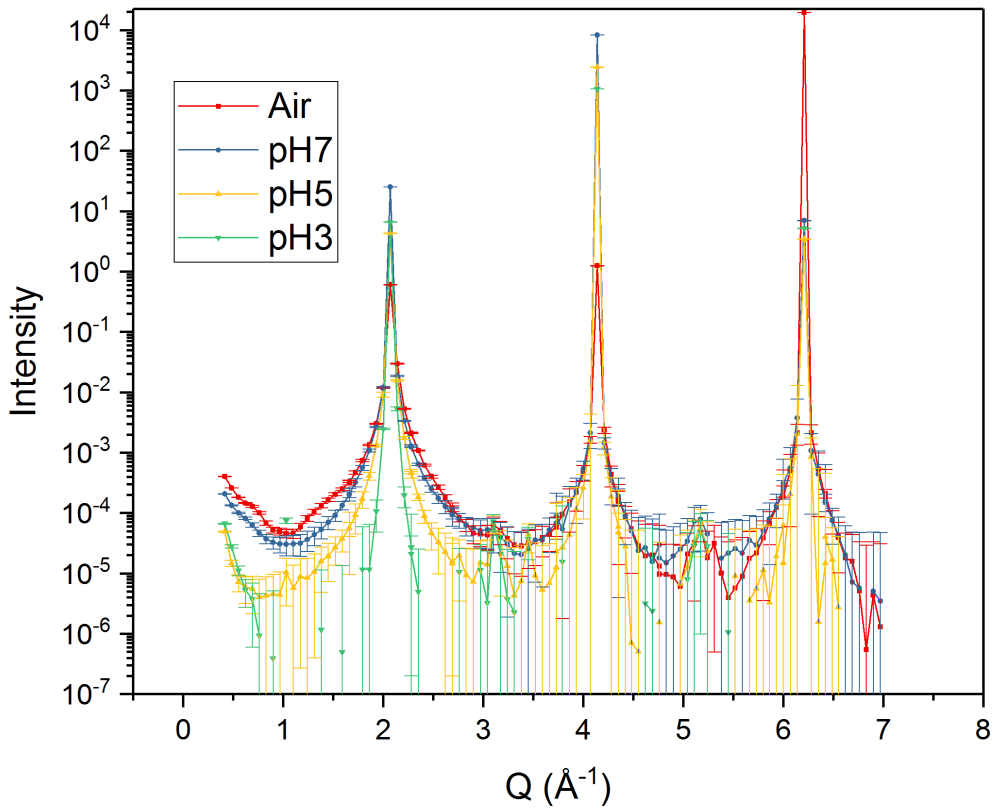


**Figure 5.9** X-ray reflectivity data representing changes in the calcite surface when exposed to air, solutions with a pH of 7, 5, and 3. Larger error bars in the data at pH 3 condition correspond to the increasing surface roughness of the calcite surface.

## CHAPTER 6

# NOVEL AQUEOUS AMINE LOOPING APPROACH FOR THE DIRECT CAPTURE, CONVERSION AND STORAGE OF CO<sub>2</sub> TO PRODUCE MAGNESIUM CARBONATE

*The contents of this chapter have been published as an article at Liu, M., Asgar, H., Seifert, S., & Gadikota, G. “Novel Aqueous Amine Looping Approach for the Direct Capture, Conversion and Storage of CO<sub>2</sub> to Produce Magnesium Carbonate.” *Sustainable Energy & Fuels* 4, 3 (2020): 1265-1275.*

### 6.1 Introduction

Rising anthropogenic carbon emissions to the atmosphere to the order of 35,000 million metric tons of CO<sub>2</sub> and the heterogeneity in gaseous waste streams call for the development of adaptive and transformative technologies for integrated CO<sub>2</sub> capture, utilization and storage. (National Academies of Sciences Engineering and Medicine, 2019) Carbon mineralization which involves converting CO<sub>2</sub> to water insoluble and stable Ca- and Mg-carbonates is a thermodynamically downhill pathway for the integrated capture, utilization and storage of CO<sub>2</sub>. Ca- and Mg-bearing alkaline feedstocks include earth abundant silicate-rich minerals such as olivine ((Mg, Fe)<sub>2</sub>SiO<sub>4</sub>), wollastonite (CaSiO<sub>3</sub>), and serpentine ((Mg, Fe)<sub>3</sub>Si<sub>2</sub>O<sub>5</sub>(OH)<sub>4</sub>), and alkaline industrial residues such as coal fly ash, steel slag, cement kiln dust, and red mud. (Bobicki et al., 2012; Huntzinger et al., 2009; Salman et al., 2014; Yadav et al., 2010)

Broadly, two main approaches have been developed for the accelerated conversion of CO<sub>2</sub> to Ca- and Mg-carbonates. In the first approach, high purity silica and carbonates are produced through the sequential use of acids and bases. Acids are used for extracting Ca and Mg ions into

the aqueous phase with concurrent production of silica. Bases are then used to increase pH and enhance the generation of carbonate ions for producing Ca- and Mg-carbonates (Eloneva et al., 2011; Fagerlund & Zevenhoven, 2011; Gadikota & Park, 2015; Park et al., 2003; Park & Fan, 2004; Sanna et al., 2014). This approach facilitates the production of high purity silica and Ca- and Mg-carbonates. Another approach involves using elevated temperatures greater than 90°C and high CO<sub>2</sub> pressures greater than 50 atm to accelerate carbon mineralization (Gadikota & Park, 2014; Gadikota & Park, 2015; Gerdemann et al., 2007). Several rate limiting steps such as CO<sub>2</sub> hydration, mineral dissolution and carbonate precipitation are overcome at these experimental conditions. For example, elevated CO<sub>2</sub> pressures enable enhanced CO<sub>2</sub> solvation in the aqueous phase (Duan et al., 2006; Duan & Sun, 2003). Elevated temperatures accelerate dissolution of Ca- and Mg-bearing silicate minerals (Awad et al., 2000; Chen & Brantley, 2000; Hänchen et al., 2007; Y. Liu et al., 2006; Wogelius & Walther, 1992). The solubility of Ca- and Mg-carbonates decreases with increasing temperature which aids the precipitation of Ca- and Mg-carbonates (Ellis, 2010; Werner et al., 2014; White, 2016). Various researches have been conducted using methods mentioned above with relatively promising results. Lackner et al reported 60% extent of carbonation with Mg(OH)<sub>2</sub> at 40 bar and 510 °C in gas-solid phase in 6 hours (Lackner et al., 1997). Chizmeshya et al reported 73% extent of carbonation with olivine, which contained 47.3% MgO at 141 bar and 185 °C in aqueous phase with 1.0 M NaCl and 0.64 M NaHCO<sub>3</sub> in 3 hours. Maroto-Valer et al reported 60% extent of carbonation with serpentine, which contained 38.7% MgO at 128 bar and 155 °C in aqueous phase with 1.0 M NaCl and 0.64 M NaHCO<sub>3</sub> in 1 hour. Lackner et al reported 30% extent of carbonation with olivine, which contained about 40% MgO at 340 bar and 300 °C in gas-solid phase.(Lackner et al., 1997) However, due to the slow kinetics of the mineralization reaction, these approaches required high-temperature and high-pressure

reaction environments to facilitate the carbonation reaction, which turns out to be high energy consumption. Therefore, one of the scientific challenges lies here is how we could accelerate the carbon mineralization with low-energy consumption.

Besides, various chemical pathways were proposed to accelerate the rate limiting steps. To overcome the challenge of low solubility of CO<sub>2</sub> in water, additives such as carbonic anhydrase have been proposed (Power et al., 2016; Sahoo et al., 2013; Vinoba et al., 2011). The use of organic ligands such as oxalate, citrate or acetate were proposed to enhance mineral dissolution (Xue et al., 2005; Zhao et al., 2013). Seeding surfaces of calcite and magnesite were found to aid the accelerated precipitation of the same phases (Bénézech et al., 2011; Reddy & Gaillard, 1981). However, these accelerated pathways were developed independently, without considering their intended influence on coupling multiple reactions for accelerated carbon mineralization. Therefore, the scientific challenge lies in accelerating "step change" advancements in carbon mineralization. This is achieved by synergistically coupling multiple reaction pathways to direct the synthesis of Ca- and Mg-carbonates at temperatures below 100 °C using dilute flue gas streams of CO<sub>2</sub>.

In this study, we evaluate the hypothesis that utilizing aqueous amine-bearing solvents such as monoethanolamine (MEA) enhances CO<sub>2</sub> hydration via the enhanced formation of bicarbonate and carbonate species in the aqueous phase at relatively low temperature and low pressure. Carbonate and bicarbonate ions then react with dissolved Ca and Mg in the aqueous phase to produce Ca- and Mg-carbonates. **Figure 6.1** is a schematic representation of the proposed mechanism. The integrated gas-liquid-solid reaction pathways shown in **Figure 6.1** represent the coupling of multiple reactions including enhanced CO<sub>2</sub> capture and hydration using MEA solvents, mineral dissolution and carbonate precipitation. Alternatively, CO<sub>2</sub>-loaded amine-bearing

solutions can be directly reacted with oxides, hydroxides or silicates of Ca and Mg in a slurry reaction environment to produce Ca- and Mg-carbonates. Both pathways involve the looping of the amine-bearing solvents from the CO<sub>2</sub>-loaded to CO<sub>2</sub>-release states by converting CO<sub>2</sub> to Ca- and Mg-carbonates. This novel aqueous alkaline amine looping process was successfully demonstrated for the accelerated mineralization of calcium oxide and calcium chloride to produce calcium carbonate (Arti et al., 2017; Ji et al., 2018; Liu & Gadikota, 2018). Carbonate-induced solidification of calcium silicate using MEA was extensively studied (Li et al., 2016; Riman & Li, 2011).

However, the carbon mineralization of Mg-bearing oxides, hydroxides or silicates using aqueous alkaline amine looping approach has not been established. Given the abundance of Mg-bearing minerals around the world, evaluating the reactivity of Mg-bearing minerals to produce Mg-bearing carbonates using the aqueous alkaline amine looping approach needs to be explored (Falkowski et al., 2000; Shand, 2006). The successful demonstration of the proposed process will allow us to unlock the potential of vast resources of Mg-bearing minerals for the accelerated capture, conversion and storage of CO<sub>2</sub> in a single step. The aim of this study is to explore the feasibility of using Mg-bearing materials using simple precursors such as magnesium oxide for the accelerated capture, conversion and storage of CO<sub>2</sub> to produce magnesium carbonates. To achieve this aim, several research questions need to be addressed: (i) What is the influence of reaction temperature and MEA composition on the extent of carbon mineralization of magnesium oxide? (ii) What is the chemical composition of the carbonate-bearing materials? (3) How do the structural and morphological features of MgO dynamically evolve in these fluidic environments?

To address these research questions, laboratory-scale experiments were designed to probe the sensitivity of carbon mineralization behavior on the reaction conditions such as temperature

and the composition of the MEA. This gas-liquid-solid reaction environment was designed for a constant pressure of 1 atm. The influence of aqueous phase compositions of 10-50 wt% MEA at temperatures in the range of 25 °C - 90 °C on the carbon mineralization behavior of MgO was probed. A slurry composition of 15 wt% solid was held constant for all the experiments. Continuous stirring at the rate of  $300 \text{ rpm} \pm 5 \text{ rpm}$  was maintained to reduce mass transfer limitations. A second of experiments were designed to probe dynamic time-resolved structural and microstructural evolution of magnesium oxide as it is reacted to produce magnesium carbonate using Ultra Small/Small/Wide Angle X-Ray Scattering (USAXS/SAXS/WAXS) measurements (Benedetti et al., 2019; Gadikota et al., 2017; Ilavsky et al., 2013; Ilavsky et al., 2009, 2018; Liu & Gadikota, 2018). Further, Grazing Incidence - Small Angle X-Ray Scattering (GI-SAXS) measurements were performed to determine the size of the nucleating magnesium carbonate particles on silica interfaces. This comprehensive research approach was used to evaluate the effectiveness of the coupled reaction pathways in directing the synthesis of magnesium carbonates in multiphase reaction environments and the underlying structural and morphological basis for the observed reactivity.

## **6.2 Experimental Materials and Methods**

Magnesium oxide used in this integrated carbon mineralization approach with aqueous alkaline amine looping approach was procured from Sigma-Aldrich. The mean particle size, surface area, and cumulative pore volume of magnesium oxide are  $8.54 \mu\text{m}$ ,  $3.59 \text{ m}^2/\text{g}$ , and  $0.0078 \text{ cm}^3/\text{g}$ , respectively. Monoethanolamine (MEA) with a purity of 98% used in these studies was procured from Alfa Aesar.

### **6.2.1 Aqueous alkaline amine looping process for accelerated carbon mineralization**

The experiments to evaluate the influence of temperature and MEA concentrations on the accelerated conversion of magnesium oxide to magnesium carbonate using the aqueous alkaline amine looping process were performed in a batch environment (Parr Reactor, Series 4590 Micro Stirred Reactor). The slurry environment comprised 17 g of liquid and 3 g of solid sample. Aqueous phase compositions comprising deionized water, 10, 30, and 50 wt % MEA were used. A constant pressure of 1 atm of CO<sub>2</sub> was maintained throughout the length of the experiments. A constant stirring rate of 300 rpm  $\pm$  5 rpm was applied. Each experiment was performed over a length of 3 hours. Extents of carbon mineralization at reaction temperatures of 25 °C, 50 °C, 75 °C and 90 °C were evaluated. About 5-10 minutes were needed to reach the desired reaction temperature, which marked the beginning of the experiment. All experiments were performed over 3 hours. At the end of 3 hours, vacuum filtration was used to separate the liquid contents from the solids. The recovered solid was dried in a vacuum oven for 24 hours at 90 °C to remove any residual water in the solid sample.

### **6.2.2 Characterization of chemical and morphological properties**

The carbon mineralization efficiency using the aqueous alkaline amine looping process was evaluated based on the extent of magnesium mineralized to produce magnesium carbonate. The carbonate content used in these calculations was determined using Thermogravimetric Analyses (TGA, TGA 550, TA Instruments). TGA data provides quantitative information into the changes in the weight of the samples on heating at specific temperatures. The heating rate was set to 5 °C/min from 25 °C to 800 °C and the flow rate of the N<sub>2</sub> gas was 25 mL/min. The carbonate content in nesquehonite was determined from the weight change in the temperature range of 350 °C – 450 °C (Swanson et al., 2014). The stoichiometric mass of MgO needed for storing a unit mass

of CO<sub>2</sub> was defined as  $R_{CO_2}$  (Gadikota et al., 2014; Gerdemann et al., 2007). As reported in previous studies, the extent of carbon mineralization,  $Y_{CO_2,TGA}$ , a measure of the ratio of the amount of CO<sub>2</sub> present in the sample with respect to the CO<sub>2</sub> storage capacity was determined by the following relationship:  $Y_{CO_2,TGA} = R_{CO_2} \times \left(\frac{TGA}{100-TGA}\right) \times 100\%$  where TGA represents the weight change that corresponds to the carbonate content in the reacted materials. To identify the species in the aqueous and solid phases, Attenuated Total Reflection – Fourier Transform Infrared spectroscopy analyses were performed (ATR-FTIR, Thermo Fisher Nicolet iS 10). The spectra were collected in the range of 650 ~ 4000 cm<sup>-1</sup>. The morphological features of the products were determined using Scanning Electron Microscopy (SEM, Hitachi High Technologies America, Hitachi S3400-N).

Time-resolved structural and microstructural features as MgO is reacted in the aqueous amine looping process were determined using *in-operando* Ultra Small/Small/Wide Angle X-Ray Scattering (USAXS/SAXS/WAXS) measurements at Sector 9-ID at the Advanced Photon Source (APS) in Argonne National Laboratory (ANL) (Gadikota et al., 2017; Ilavsky et al., 2009, 2018; Liu & Gadikota, 2018). The arrangement comprised of a cell with a continuous flow of CO<sub>2</sub> at the rate of 10 mL/min. In this *in-situ* measurement, 1 mL 30 wt% CO<sub>2</sub>-loaded MEA and 0.15 g MgO were added to an NMR tube with an internal diameter of 4 mm. CO<sub>2</sub> was continuously supplied to the aqueous phase to ensure high concentrations of inorganic carbon in the aqueous phase. The acquisition times for USAXS, SAXS, and WAXS were 90 s, 20 s, and 30 s respectively. Silver behenate was used to calibrate SAXS and LaB6 was used to calibrate WAXS measurements (Black et al., 2010). The total X-ray flux, energy and corresponding wavelength were 10<sup>-13</sup> photon s<sup>-1</sup>, 21.0 keV, and 0.59 Å, respectively. Irena (Ilavsky & Jemian, 2009) and Nika (Ilavsky, 2012) software packages embedded in *IgorPro* (Wavemetrics, Lake Oswego, OR) were used for data

analyses (Ilavsky, 2012; Ilavsky & Jemian, 2009). To capture the hierarchical morphological features during the carbonation of MgO, the combined USAXS/SAXS data were modeled using the “Modeling II” tool in Irena package (Ilavsky & Jemian, 2009).

In-situ Grazing Incidence – Small Angle X-Ray Scattering (GI-SAXS) measurements were performed to determine the sizes of the nucleating particles. These measurements were conducted at the beamline 12 ID-B at the Advanced Photon Source (Argonne National Laboratory, USA). A custom designed cell was used for these measurements. The internal dimensions of this cell are 10 mm × 10 mm × 15 mm. 30 wt% CO<sub>2</sub>-loaded MEA solution with a volume of 0.1988 mL was injected into 5 mL of 0.1 M Mg(NO<sub>3</sub>)<sub>2</sub> solution, which marked the beginning of the *in-situ* measurement. The X-ray beam was directed to the substrate with an incidence angle of  $\alpha_i = 0.11^\circ$  through the two Kapton windows. This incident angle is lower than the critical angle for total reflection ( $\alpha_c\text{-quartz} = 0.14^\circ$  at 14 KeV incident X-ray energy). The scattered intensity from the nucleated magnesium carbonate particles was collected using a 2-dimensional Pilatus 2 M detector (Dectris Ltd., Baden, Switzerland). The incidence X-Ray energy, a sample-to-detector distance (ds-d), and q-range for these measurements were 14 keV, 2060 mm, and 0.005 Å<sup>-1</sup> to 0.6 Å<sup>-1</sup>, respectively. After background subtraction and 2D data reduction, the reduced data was fitted by Guinier-Porod fit (Hammouda, 2010) as shown in **Figure 6.7 (c)**. The equations that describe the relationships of the generalized Guinier Law are listed below (Hammouda, 2010).

$$I(Q) = \frac{G}{Q_s} \exp\left(\frac{-Q^2 R_g^2}{3-s}\right) \text{ for } Q \leq Q_1 \quad (\text{Equation 6.1})$$

$$I(Q) = \frac{D}{Q^d} \text{ } Q \geq Q_1 \quad (\text{Equation 6.2})$$

$$Q_1 = \frac{1}{R_g} \left(\frac{3d}{2}\right)^{1/2} \quad (\text{Equation 6.3})$$

$$D = G \exp\left(\frac{-Q^2 R_g^2}{3}\right) Q_1^d = G \exp\left(\frac{-d}{2}\right) \left(\frac{3d}{2}\right)^{\frac{d}{2}} \frac{1}{R_g^d} \quad (\text{Equation 6.4})$$

$G$  and  $D$  are the Guinier and Porod scale factors.  $Q$  is the scattering variable,  $I(Q)$  is the scattered intensity,  $R_g$  is the radius of gyration,  $d$  is the Porod exponent.  $Q_1$  is set up to ensure the continuity of the slopes (derivatives). A dimensionality parameter  $(3 - s)$  is defined to provide more flexibility for modeling different shapes of objects. For example, objects with spherical, rod-like, and lamellae or platelet dimensions,  $s = 0, 1$ ; or  $2$ , respectively (Hammouda, 2010). The  $R_g$  is calculated based on the equations represented above.

## 6.3 Results and Discussion

### 6.3.1 Effect of temperature and MEA concentration

To evaluate the influence of temperature and MEA concentration on the extent of carbon mineralization of MgO, multiphase reaction environments are constructed. The pressure of CO<sub>2</sub> in the gas phase is held at 1 atm over the course of the experiment. The slurry was composed of 15 wt% solid. MEA compositions were evaluated as 10, 20, 30 and 50 wt% at temperatures of 25 °C, 50 °C, 75 °C, and 90 °C. Reaction times were set to 3 hours and the stirring rates at 300 rpm  $\pm$  5 rpm. The extents of carbon mineralization of MgO as a function of MEA concentration and temperature are noted in **Figure 6.2**. A non-linear relationship of the influence of temperature and MEA on the carbon mineralization of MgO was noted. The highest conversion of MgO to magnesium carbonate achieved with 30 wt% MEA at 50 °C is 70%. Beyond that point, the extent of carbon mineralization decreased as the temperature increased. This is a result of the competition of the CO<sub>2</sub>-MEA reaction kinetics and thermodynamics. On the one hand, as the temperature increases, the CO<sub>2</sub>-MEA reaction kinetics increases, which, in another word, indicates the time to

reach equilibrium decreases (Kim et al., 2013). However, the equilibrium constant of the CO<sub>2</sub>-MEA reaction decreases as the reaction temperature increases (Gupta et al., 2013).

The carbonation dropping at higher temperature is a result of equilibrium limitation.(Kim & Svendsen, 2007) At similar experimental conditions, 100% conversion of CaO to calcium carbonate was reported.(Liu & Gadikota, 2018) As MEA concentrations are increased starting from DI water to 10 wt% and 20 wt% MEA, high conversions of MgO to magnesium carbonate are achieved at 75 °C. At 30 wt% MEA, higher extents of carbon mineralization were achieved at 50 °C. At 50 wt% MEA, gel formation was noted with MgO which made it challenging to separate the solid and liquid constituents. Our hypothesis is that the enhanced hydrogen bonding resulting from the interactions between the dissolved fluidic constituents result in gel formation. This observation is consistent with the formation of magnesium carbonate-based porous gels (Frykstrand et al., 2014). Our hypothesis for the limited reactivity of MgO at high concentrations of MEA, i.e., 50 wt% emerges from the mass transfer limitations caused by gel formation.

To identify the constituents in the solid phase and aqueous phase, ATR-FTIR analyses were performed. A wide range of phases were identified. Absorption bands at 1471 cm<sup>-1</sup> and 1515 cm<sup>-1</sup> indicates  $\nu_3$  asymmetric CO<sub>3</sub><sup>2-</sup> stretching mode, which matches with features of nesquehonite (MgCO<sub>3</sub>·3H<sub>2</sub>O), and lansfordite (MgCO<sub>3</sub>·5H<sub>2</sub>O) (Hopkinson et al., 2012; Morgan et al., 2015; Yin et al., 2014). The bands at 1097 cm<sup>-1</sup> and 852 cm<sup>-1</sup> reflect the  $\nu_1$  symmetric C–O, and the  $\nu_2$  C–O non-planar bending vibrations, respectively (Hopkinson et al., 2012; Morgan et al., 2015; Yin et al., 2014). These observations are consistent with previous studies that show the formation of hydrated magnesium carbonates at the experimental conditions of interest (**Figures 6.3(a)**) (Hopkinson et al., 2012; Morgan et al., 2015; Yin et al., 2014). Analyses of the liquid recovered post-reaction at 30 wt% MEA and 50°C showed that MEAH<sup>+</sup>, MEACOO<sup>-</sup>, and CO<sub>3</sub><sup>2-</sup> ions are the

dominant species present in the aqueous phase (**Figures 6.3(b)** and S2). At lower MEA concentrations of 10 wt% and 20 wt%, the relative intensities of these liquid species, in particular carbonate species is lower compared to that at 30 wt% MEA. The aqueous species are identified using FT-IR analyses in this study with MgO as the reactant are consistent with the observations reported by Ji and co-workers with CaO as the reactant. (Ji et al., 2018) The various MEA species detected in the FT-IR analysis indicates that the MEA was serving as a “catalysis” to aid the mineralization process and did fall into a looping process, capturing and releasing CO<sub>2</sub> continuously. Otherwise, single dominated specie would appear.

### **6.3.2 Morphological characterization of magnesium carbonates**

The morphological features before and after reacting CO<sub>2</sub> with MgO were determined using scanning electron microscopy images. The sizes of the unreacted MgO grains is to the order of a few micrometers (**Figure 6.4(a)**). Needle-shaped nesquehonite (MgCO<sub>3</sub>·3H<sub>2</sub>O) is dominant after MgO is reacted with 30 wt% MEA at 50 °C in pCO<sub>2</sub> = 1 atm (**Figure 6.4(b)**). Further, *in-operando* Ultra Small and Small Angle X-Ray Scattering (USAXS/SAXS) measurements were performed to determine the dynamic evolution in the structural and morphological features as MgO is reacted with CO<sub>2</sub>-loaded MEA (**Figure 6.5 (a)**). The experimental conditions at which these measurements were performed are 25 °C, 1 atm, and CO<sub>2</sub>-loaded MEA concentrations of 30 wt%. These time-resolved measurements show the emergence of carbonate phases in the high  $q$  regimes that corresponds to the SAXS regime. The peaks at  $q \sim 1.02 \text{ \AA}^{-1}$  and  $q \sim 0.51 \text{ \AA}^{-1}$  correspond to the (0 0 2) and (0 0 1) reflections of lansfordite (MgCO<sub>3</sub>·5H<sub>2</sub>O) (Giester et al., 2000; Ming & Franklin, 2010). These data suggest that lansfordite growth is a precursor to the formation of nesquehonite (Ming & Franklin, 2010). In hydrothermal environments where the effects of temperature and MEA compositions on the accelerated carbon mineralization of MgO to magnesium carbonate are

evaluated as shown in **Figure 6.2**, it is hypothesized that lansfordite undergoes pseudomorphic transformations to produce nesquehonite (Ming & Franklin, 2010).

The influence of structural evolution on the microstructural changes can be inferred from the X-ray scattering curves from the smaller  $q$  regimes. Power law slopes determined in the  $q$  range of  $0.08 \text{ \AA}^{-1}$  to  $10^{-3} \text{ \AA}^{-1}$  show the influence of reactivity on the microstructural evolution. The integrated intensity of the characteristic lansfordite peak at  $q \sim 0.51 \text{ \AA}^{-1}$  (**Figure 6.5(b)**) and the corresponding changes in the pore-solid interfaces (**Figure 6.6(a)**) can be interpreted together to evaluate the influence of magnesium carbonate growth on the morphology of the solid interfaces. At reaction times of 100 minutes, the onset of the lansfordite peak is noted and continues growing. The fractal dimensions of the scattering objects can be determined from the power law slopes. Power law slopes calculated in the range of  $10^{-3} \text{ \AA}^{-1} - 8 \times 10^{-2} \text{ \AA}^{-1}$  for the USAXS/SAXS data in **Figure 6.5 (a)** shows the changes in the fractality of the pore-solid interfaces resulting from carbon mineralization. As summarized in previous publication, the Power law slope was calculated using the following equations (Liu & Gadikota, 2018).

$$(i) I(Q) = \frac{A}{Q^n} + B \text{ and } (ii) \log_{10}[I(Q) - B] = \log_{10}A - n \log_{10}Q. \quad (\text{Equation 6.5})$$

In these equations,  $I(Q)$  is the scattering intensity and  $n$  is the slope (Liu & Gadikota, 2018). A power law slope between 2 and 3 represents scattering from branched networks or mass fractals, while a value between 3 and 4 represents scattering from rough interfaces with a fractal dimension,  $D$ , where  $n = 6 - D$  represents a surface fractal.  $D$  equals to 1, 2, and 3, representing scattering from rods, disks, and spheres, respectively (Schaefer & Keefer, 1986). Power law slopes of 1 and 4 represent scattering from smooth surfaces and rigid rods. Power law slopes between 2 and 3 during the reactivity of MgO show the mass fractal nature of the surfaces (**Figure 6.6 (a)**). It was

interesting to note the progressive growth of the lansfordite peak in **Figure 6.5 (b)** with the decreasing power law slope (**Figure 6.6 (a)**). Also, from the SEM image of the unreacted MgO sample in **Figure 6.4 (a)**, clear sphere-shape particles and branched networks could be observed. The porosity was contributed by the random branched-polymer-like structure (Schaefer & Keefer, 1986). From the SEM image of the reacted MgO (with with 30 wt% MEA at 50 °C with  $P_{CO_2} = 1$  atm for 3 hours) in **Figure 6.4 (b)**, the branched networks could still be observed. However, the particles shape changed from sphere to rod shape with layer structures inside the particles, which corresponded to the decrease of power law slope.

Since the characteristic peak for (001) plane of lansfordite ( $MgCO_3 \cdot 5H_2O$ ) emerged after 89 min of reaction time, the data were modeled in two stages (Hopkinson et al., 2012; Morgan et al., 2015; Yin et al., 2014). In the first stage, the USAXS/SAXS curves were modeled using two unified fit levels in two different  $q$  regions, where  $q = (4\pi/\lambda)\sin(\theta/2)$  and  $\lambda$  is the wavelength of incident X-ray and  $\theta$  is the scattering angle (Stuhrmann, 1989). The two  $q$ -regions  $0.001 - 0.02 \text{ \AA}^{-1}$  and  $0.02 - 0.8 \text{ \AA}^{-1}$ , were modeled based on the approach proposed by Beaucage (Beaucage, 1995, 1996). The fit in each level can be described by a Guinier regime and a power-law regime. Typically, the model assumes a spherical and centrosymmetric shape of particles (Beaucage, 1996). However, it can be applied to a broad range of scatterer shapes, including spheres, rods, lamellae, cylinders etc. based on its formulation in terms of radius of gyration ( $R_g$ ) and free power-law slope. In the second stage of fitting, for all the data curves after 89 min, the scattering profiles were fitted using three levels of fits. Like the approach in first stage, two regions of unified fit were modeled in  $q$  ranges of  $0.001 - 0.02 \text{ \AA}^{-1}$  and  $0.02 - 0.3 \text{ \AA}^{-1}$ , respectively. Additionally, a Lorentzian diffraction peak was fitted in the  $q$  range of  $0.3 - 0.8 \text{ \AA}^{-1}$ . The normalized integrated intensity of (001) peak of lansfordite is presented in **Figure 6.5 (b)** (Hopkinson et al., 2012;

Morgan et al., 2015; Yin et al., 2014). Additionally, the modeling results from the unified fit in  $q$  range of  $0.02 - 0.8 \text{ \AA}^{-1}$ , were of interest and are discussed further. The power-law slope and radius of gyration ( $R_g$ ) obtained from the unified fit are presented in **Figure 6.6(a)**. The  $R_g$  values are representative of pore dimensions and will be discussed to understand the evolution of pore morphology during the carbonation of MgO to MgCO<sub>3</sub>. Initially, a  $R_g$  values of  $\sim 5 \text{ nm}$  was noted for the precursor, MgO. This value was compared to the pore size distribution data for MgO obtained from N<sub>2</sub> adsorption measurements (**Figure 6.6(b-1)**). Further, an increase in  $R_g$  values was noted until 61 minutes of reaction time, which could be attributed to the dissolution of MgO. As discussed earlier, the (001) peak for lansfordite first emerged after 89 minutes of reaction time, the  $R_g$  values started to decrease and achieved a value of  $\sim 3.4 \text{ nm}$  as the carbonation of MgO began. The changes in the  $R_g$  values corresponding to the phase change (MgO to MgCO<sub>3</sub>) during reaction are mapped in (**Figure 6.6(b-2)**). These values of  $R_g$  remained persistent till the end of reaction (385 minutes). For comparison, the pore dimensions of MgCO<sub>3</sub> powder obtained after reaction of MgO with 30 wt.% MEA in a batch reactor for 3 hours was compared with the  $R_g$  value at 183 minutes. The comparison is mapped on **Figure 6.6(a)** in **Figure 6.6(b-3)**. It can be concluded that the values of  $R_g$  and pore-radius are comparable.

While USAXS/SAXS measurements provide insights into the influence of bulk morphological changes and structural evolution during the carbon mineralization of magnesium oxide, it is challenging to determine the sizes of the magnesium carbonate particles using this approach. The research question in this context is as follows: How can we determine the sizes of the carbonate particles once the Mg cations are mobilized in the aqueous phase? To address this research question, we utilize *in-operando* Grazing Incidence – Small Angle X-Ray Scattering (GI-SAXS) measurements to determine the sizes of the particles. **Figure 6.7(a)** is a schematic of the

GI-SAXS cell. 0.1988 mL of 30 wt% CO<sub>2</sub>-loaded MEA solution was injected into 5 mL 0.1 M Mg(NO<sub>3</sub>)<sub>2</sub> solution. The reaction vessel used in these experiments was made from silica. To mimic the formation of magnesium carbonate particles on these silica surfaces, we used solid quartz substrate (100). These quartz surfaces were rinsed with acetone to remove any organic contaminants (Fernandez-Martinez et al., 2013). **Figure 6.7 (b)** is an example of raw 2D GISAXS scattering pattern from quartz (100) substrates with MgO. The original image is shown, without background subtraction and further processing. After background subtraction and 2D data reduction, the reduced data was fitted by Guinier-Porod fit (Hammouda, 2010) as shown in **Figure 6.7 (c)**.

The formation of magnesium carbonate particles was noted after about 60 minutes. The scattering curves were obtained by reducing the data contained in the 2-D images (Fernandez-Martinez et al., 2013). The sizes of the particles are obtained by fitting the Guinier-Porod fit based on Eq2-Eq5 (Hammouda, 2010). Also, the factor  $s$  was set as 1 based on the formation of rod-like shape particles observed in the SEM images in **Figure 6.4 (b)**. The size distribution in **Figure 6.7 (d)** was extrapolated from the **Figure 6.7 (c)** based on the maximum entropy method using Irena and Nika packages. From these data, we infer that the sizes of the precipitates are to the order of 15-16 nm (**Figure 6.7 (d)**). At these experimental conditions, the formation of hydrated magnesium carbonates is expected (Fernandez-Martinez et al., 2013). In comparison, the sizes of the calcium carbonate is approximately 2 nm (Fernandez-Martinez et al., 2013; Radha et al., 2012). These USAXS/SAXS and GI-SAXS measurements allows us to bridge our understanding of the nucleation behavior of magnesium carbonate, with the evolution in the structural and morphological features as magnesium oxide is mineralized to produce magnesium carbonate using the aqueous alkaline amine looping process.

## 6.4 Conclusions

In this paper, we investigate the effectiveness of utilizing aqueous alkaline amine looping process for the directed synthesis of magnesium carbonate starting from magnesium oxide as the precursor. Experiments were performed in a multiphase reaction environment comprising CO<sub>2</sub> at a pressure of 1 atm with temperature varying between 25 °C to 90 °C, and aqueous concentrations of MEA varying from 0 to 50 wt%. The maximum extent of carbon mineralization achieved with magnesium oxide was 70 % in 30 wt% MEA solution at 50 °C for a reaction time of 3 hours. The formation of hydrated phases of magnesium carbonate such as nesquehonite (MgCO<sub>3</sub>·3H<sub>2</sub>O) was noted. Small angle X-ray scattering measurements showed the formation of lansfordite at system conditions as likely precursors prior to the formation of nesquehonite. The high carbonate conversions achieved with the use of magnesium oxide using the aqueous alkaline amine looping demonstrate the effectiveness of using the proposed approach for the direct capture, conversion and storage of CO<sub>2</sub>. The aqueous alkaline amine looping system enable the acceleration of CO<sub>2</sub> mineralization at relatively low temperature and low pressure using less reactive materials. This approach also integrates the CO<sub>2</sub> capture, conversion, and storage into one single step. With less energy cost and simpler pathway, this method allows the production of the energy and resources that we need while reducing environmental impacts.

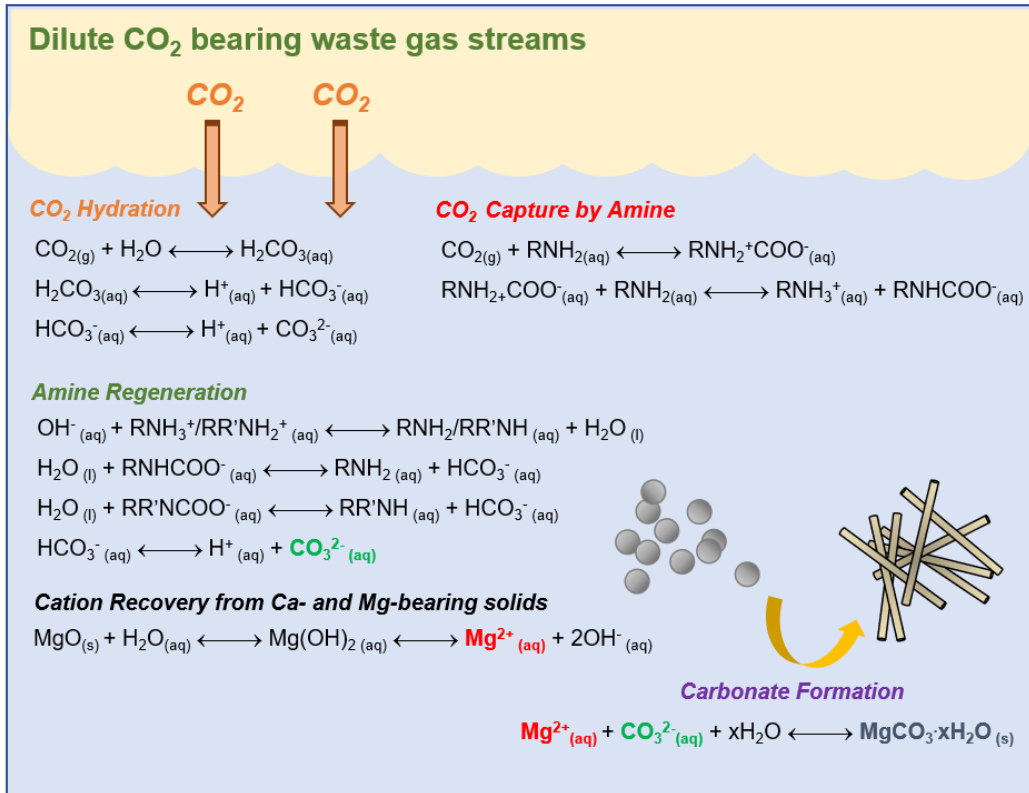


**Figure 6.1** Schematic representation of the alkaline aqueous amine looping process for the carbon mineralization of magnesium oxide to produce magnesium carbonate.

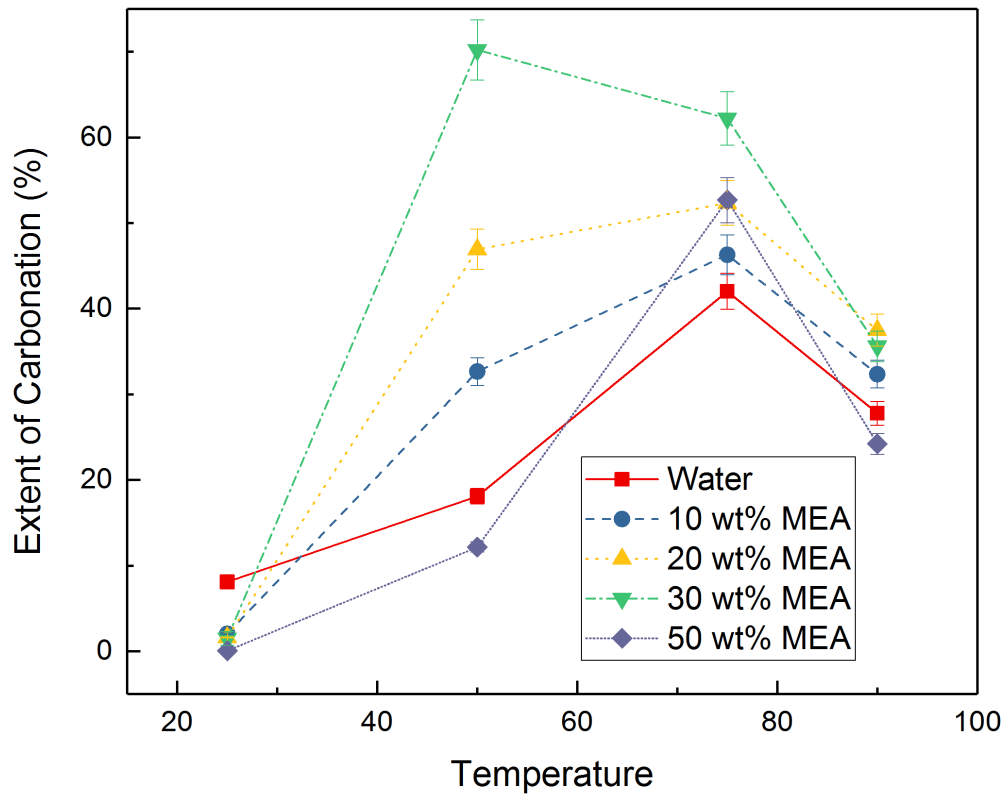


**Figure 6.2** Extent of carbon mineralization of MgO reacted with water, 10 wt%, 20 wt%, 30 wt%, and 50 wt% at 25 °C, 50 °C, 75 °C, and 90 °C at  $P_{CO_2} = 1$  atm for 3 hrs and stirring rate of 300 rpm  $\pm$  5 rpm. Estimated error is based on 5% uncertainty. Experiments were performed in duplicate.

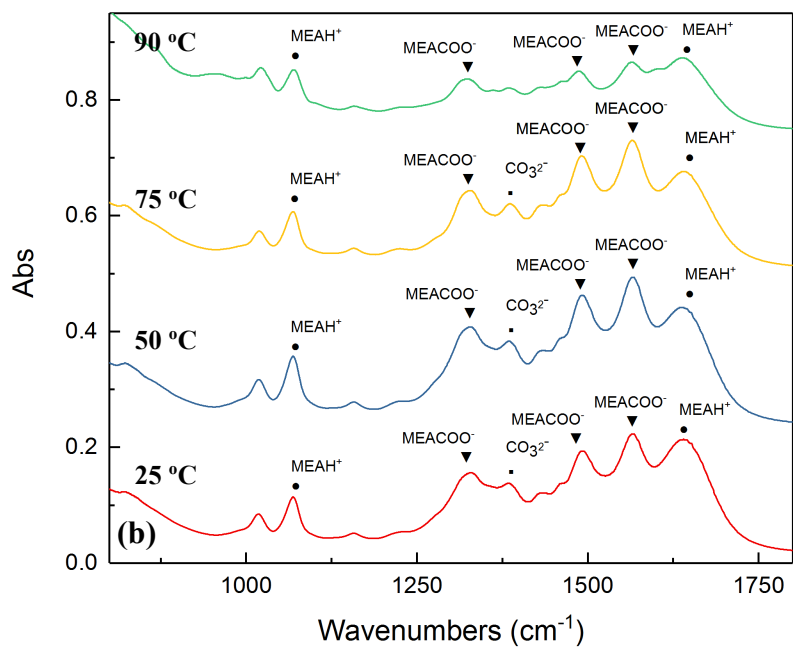
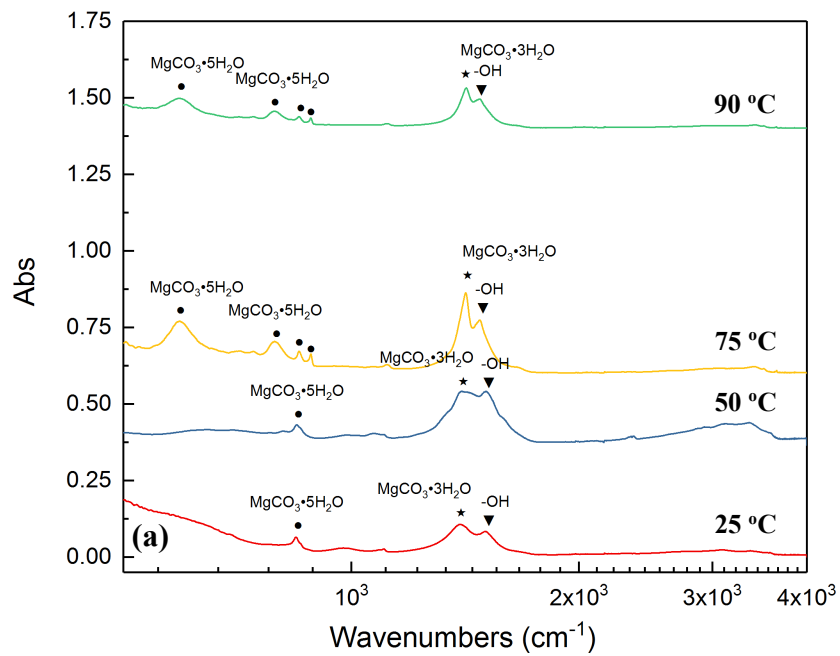


**Figure 6.3** Identification of the functional groups present in the (a) reacted solid and (b) fluid obtained from reacting MgO with 30 wt% MEA at 50 °C with  $P_{CO_2} = 1$  atm for 3 hours and stirring rate of  $300 \text{ rpm} \pm 5 \text{ rpm}$ , using ATR-FTIR measurements.

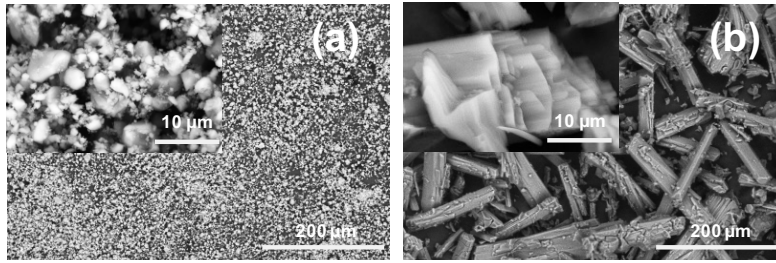


**Figure 6.4** Comparison of the morphological changes in (a) unreacted magnesium oxide and (b) MgO reacted with 30 wt% MEA at 50 °C with  $P_{CO_2} = 1$  atm for 3 hours and stirring rate of  $300 \text{ rpm} \pm 5 \text{ rpm}$ . The needle-shaped particles in (b) correspond to nesquehonite particles.

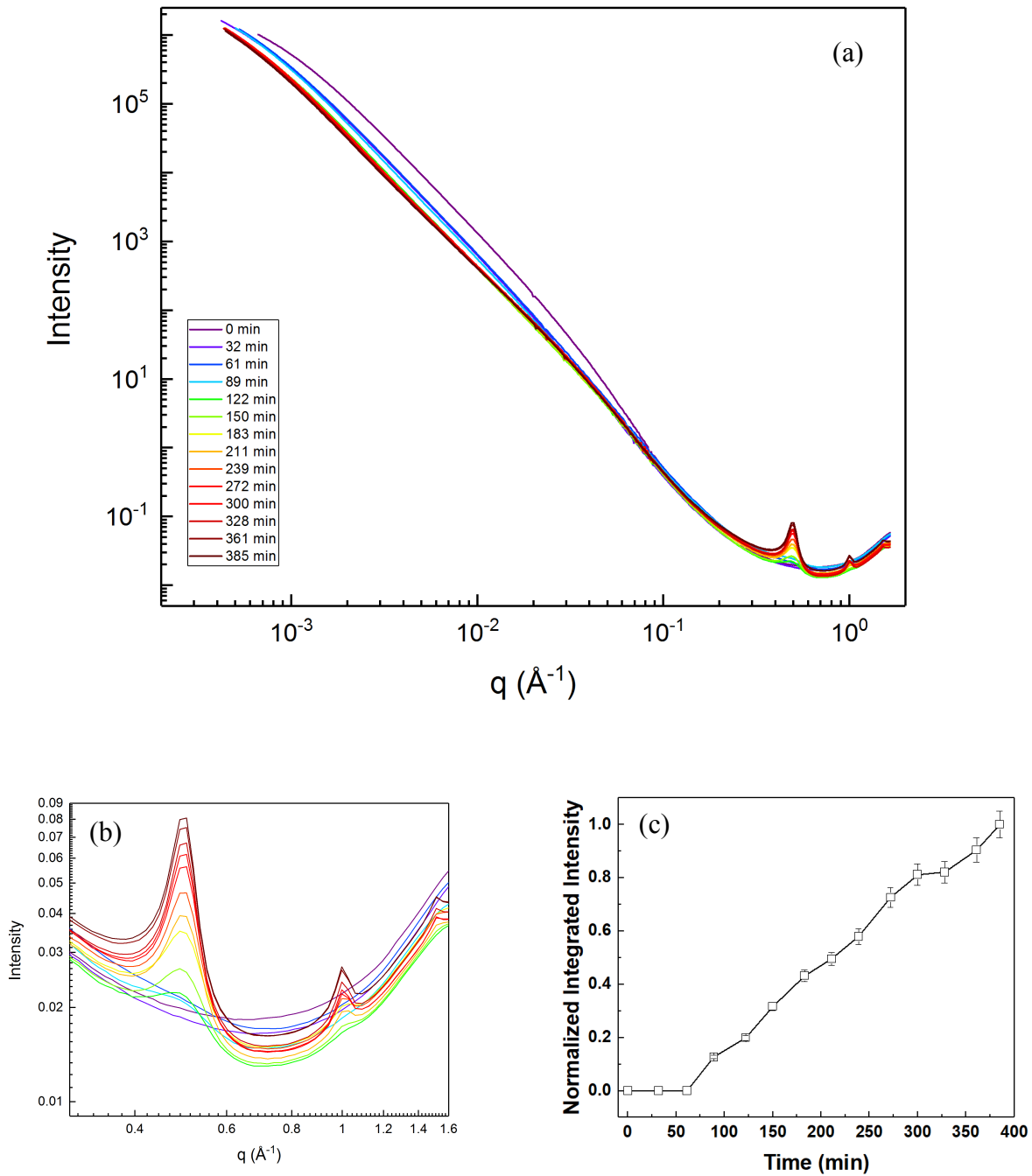


**Figure 6.5** Changes in the combined slit-smearred USAXS/SAXS data as MgO is reacted with CO<sub>2</sub>-loaded MEA to produce magnesium carbonate as shown in (a). The characteristic peak of

lansfordite at  $q = 0.5 \text{ \AA}^{-1}$  is shown in (b) and the integrated intensity of the characteristic peak of lansfordite at  $q = 0.5 \text{ \AA}^{-1}$  is shown in (c).

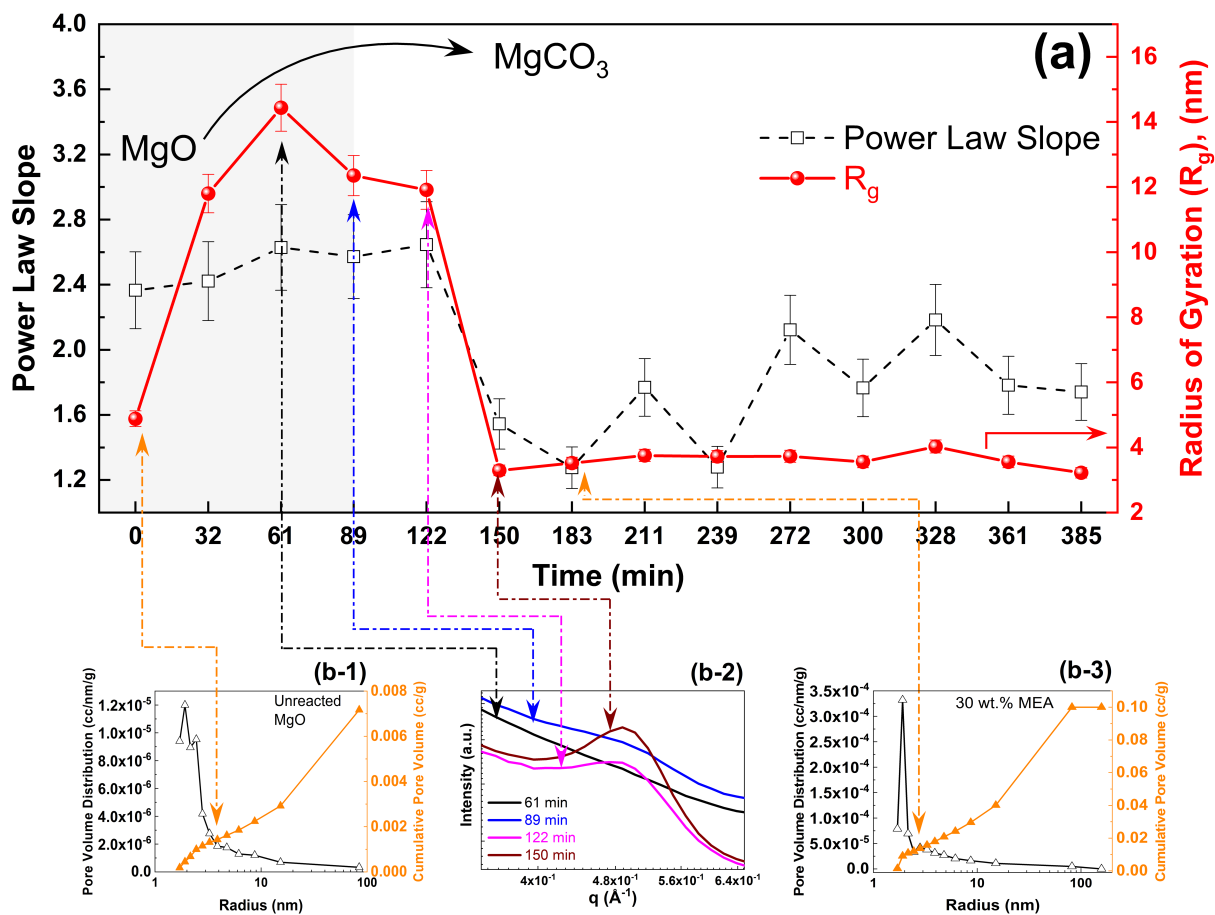


**Figure 6.6** (a) Power law slope and radius of gyration ( $R_g$ ) values obtained from the fitting of experimental USAXS/SAXS curves in the  $q$ -range of 0.02 - 0.8  $\text{\AA}^{-1}$ . (b-1) and (b-3) pore size distribution and cumulative pore volume for unreacted MgO and MgO reacted with 30 wt% MEA for 3 hours, respectively. The curves were obtained by using the BJH method on N<sub>2</sub> desorption isotherm. (b-2) early stage emergence of (001) lansfordite (Giester et al., 2000; Ming & Franklin, 2010) peak during carbonation of MgO to MgCO<sub>3</sub>.

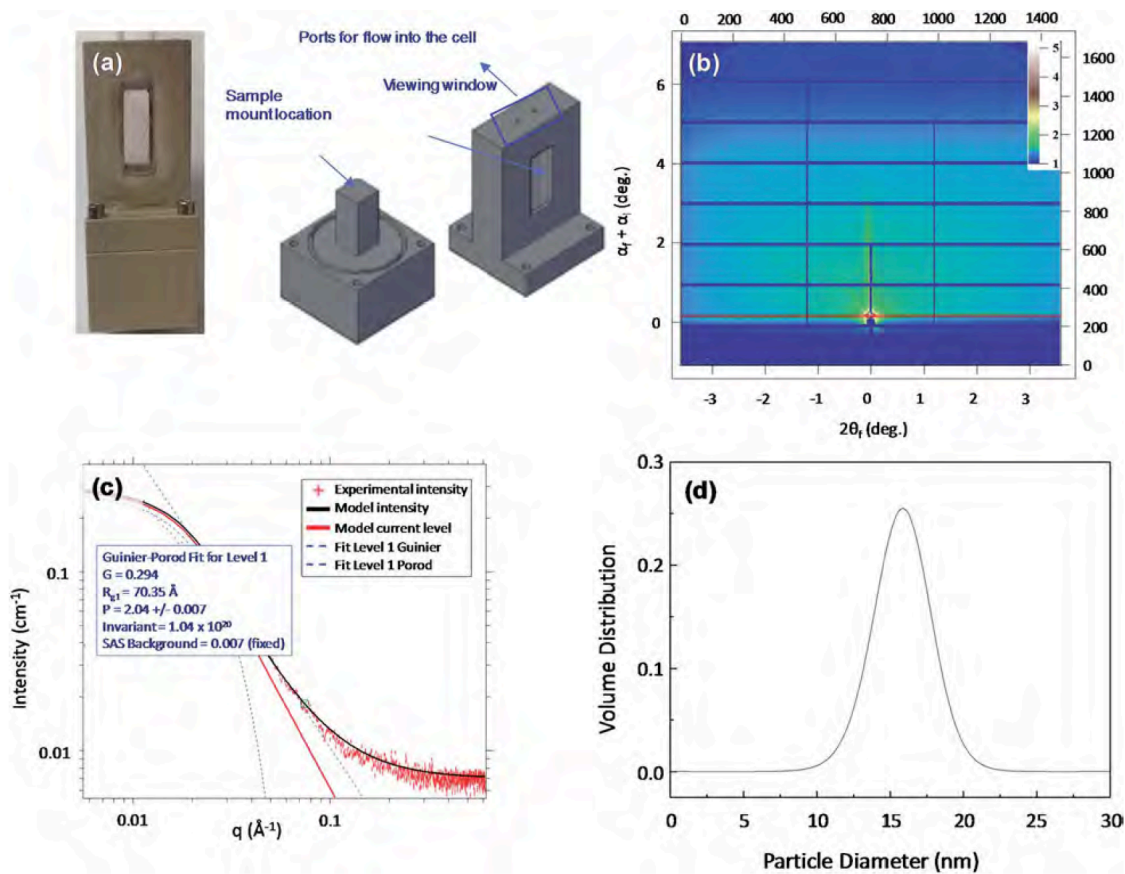


**Figure 6.7** The *in-situ* cell for Grazing Incidence – Small Angle X-Ray Scattering (GI-SAXS) measurements is shown in (a). A representative scattering image (b) and the scattering curve (c) that correspond to the nucleation of magnesium carbonate particles on quartz (0 0 1) surface are shown. The size distribution obtained from fitting the scattering curve using the Guinier-Porod slope is shown in (d). The experiments were performed at 25 °C. 0.1988 mL 30 wt% CO<sub>2</sub>-loaded MEA solution was injected into 5 mL 0.1 M Mg(NO<sub>3</sub>)<sub>2</sub> solution, which marked the beginning of the *in-situ* measurement.

# CHAPTER 7

## SINGLE-STEP, LOW TEMPERATURE AND INTEGRATED CO<sub>2</sub> CAPTURE AND CONVERSION USING SODIUM GLYCINATE TO PRODUCE CALCIUM CARBONATE

*The contents of this chapter have been published as an article Liu, M., & Greeshma G. “Directing Capture, Conversion, and Storage of CO<sub>2</sub> Using Sodium Glycinate to Produce Calcium Carbonate.” Fuel 275 (2020): 11178-11187.*

### 7.1 Introduction

Rising concentrations of CO<sub>2</sub> in the atmosphere and our unabated reliance on carbonaceous energy sources has called for advancing engineered pathways with quantifiable controls on the extent of CO<sub>2</sub> captured, converted and stored. As noted in the recent reports by the Intergovernmental Panel on Climate Change (IPCC), there is urgency in developing pathways to remove carbon from the atmosphere in addition to curbing CO<sub>2</sub> emissions into the atmosphere (Intergovernmental Panel on Climate Change, 2014; Ith & Dukes, 1993). One of the versatile pathways that can be engineered to remove CO<sub>2</sub> from air and capture CO<sub>2</sub> from flue gas streams is carbon mineralization, in which CO<sub>2</sub> is converted to inorganic carbonates (Gadikota et al., 2014; Gadikota & Park, 2014; Gadikota et al., 2015; Gupta et al., 2007; Pan et al., 2018; Park et al., 2008; Park & Fan, 2004; Smit et al., 2014; Swanson et al., 2014; Zhao et al., 2013). Despite the thermodynamically downhill and environmentally benign characteristics of these pathways, conventional carbon mineralization pathways have been kinetically challenged (Arti et al., 2017; Gadikota, 2016, 2017, 2018, 2020; Lackner et al., 2014; Mirjafari et al., 2007; Murnandari et al., 2017; Sivanesan et al., 2017; Vinoba et al., 2013). The slow kinetics may arise from the low

solubility of CO<sub>2</sub> in water, dissolution of Ca- and Mg-bearing silicates to release Ca and Mg, or the precipitation of inorganic carbonates (Liu et al., 2020; Liu & Gadikota, 2018; Wang et al., 2019). Projections indicating that 10<sup>4</sup>-10<sup>6</sup> gigatons of carbon can be stored via carbon mineralization motivated several research efforts to accelerate carbon mineralization behavior (Sanna et al., 2012; Zhao et al., 2019).

One of the earliest approaches investigated involved direct gas-solid reactions in which CO<sub>2</sub> was reacted with magnesium silicate minerals, such as olivine, serpentine, talc, and industrial waste, at temperatures as high as 300°C and pressures as high as 50 atm (Chizmeshya et al., 2007; Gadikota et al., 2014; Lackner et al., 1997; Maroto-Valer et al., 2005; O'Connor et al., 2004; Zhao et al., 2020). However, complete conversion to carbonates was challenging to achieve due to mass transfer limitations (Gadikota & Park, 2014, 2015; Gerdemann et al., 2007; Puxty et al., 2010). Alternatively, gas-liquid-solid configurations were explored in which CO<sub>2</sub>-water-Ca- or Mg-silicate minerals were reacted at temperatures in the range of 100-200 °C and CO<sub>2</sub> partial pressures in the range of 67-200 atm (Gadikota, 2014, 2016; Gadikota & Park, 2015). For example, 85% conversion of Mg<sub>2</sub>SiO<sub>4</sub> (olivine) to MgCO<sub>3</sub> (magnesite) was noted at 185 °C, reaction time of 3 hours, pCO<sub>2</sub> of 139 atm, and a fluid composition of 1.0 M NaCl + 0.64 M NaHCO<sub>3</sub> (Gadikota et al., 2014). Complete conversion of CaSiO<sub>3</sub> (wollastonite) to calcium carbonate was achieved at 100 °C, pCO<sub>2</sub> of 40 atm when reacted in distilled water for one hour (Gerdemann et al., 2004; Gerdemann et al., 2007). Elevated temperatures favor dissolution and carbonate precipitation. High CO<sub>2</sub> partial pressures and the bicarbonate solution provide an abundant supply of carbonate ions for the carbon mineralization reactions (Gadikota et al., 2014; Gadikota & Park, 2014, 2015; Gerdemann et al., 2007). Alternatively, the two step carbon mineralization pathways in which low pH solutions are used to dissolve the minerals and high pH solutions are used to precipitate the

solid carbonates were extensively investigated (Eloneva et al., 2011; Fagerlund & Zevenhoven, 2011; Gadikota & Park, 2015; Park et al., 2008; Park & Fan, 2004; Sanna et al., 2014; Zhao et al., 2013). Further, the use of organic chelating agents such as acetate, gluconate, EDTA, oxalate, ascorbate, and glutamate were studied to enhance the dissolution behavior of Ca- and Mg-bearing minerals (Bonfils et al., 2012; Chiarello et al., 1997; Olsen & Rimstidt, 2008; Park et al., 2008; Vinoba et al., 2011; Zhao et al., 2013). To overcome the limited solubility of CO<sub>2</sub>, the use of biocatalysts such as carbonic anhydrase were studied (Lorenzo et al., 2018; Vinoba et al., 2011). Despite the advancements made in accelerating mineral dissolution or CO<sub>2</sub> hydration, the need for multiple unit operations to accelerate each of these steps motivated the design of multiphase reaction chemistries to accelerate carbon mineralization integrated with CO<sub>2</sub> capture.

During integrated capture and mineralization of CO<sub>2</sub>, CO<sub>2</sub> is captured using a solvent in an absorber. The CO<sub>2</sub>-loaded solvent then reacts with solutions or solids bearing Ca<sup>2+</sup> ions to produce calcium carbonate solids, while chemically regenerating the solvent. The effectiveness of this two-step capture-mineralization approach was demonstrated by Ji and co-workers using monoethanolamine (MEA) as the solvent and fly ash (Ji et al., 2018; Yu et al., 2019). Yu and co-workers investigated the influence of diamine solvents such as N,N-Dimethylethylenediamine, N,N-Diethylethylenediamine, 3-(Diethylamino)propylamine, 1-(2-hydroxyethyl)-4-aminopiperidine) and CO<sub>2</sub> mineralization by CaO-rich fly ash (Yu et al., 2019). Calcium chloride solution was investigated for CO<sub>2</sub> capture and mineralization using various solvents including monoethanolamine (MEA), diethanolamine (DEA), N-methyldiethanolamine (MDEA), and 2-amino-2-methyl-1-propanol (AMP) (Arti et al., 2017; Hong et al., 2020). In the two-step approach, the CO<sub>2</sub> was flow through the aqueous environment, and the liquid was mixed with minerals later; while in the single-step, the CO<sub>2</sub>, liquid face, and solid minerals were mixed together. In this case,

there would be continuous CO<sub>2</sub> source available in the head space, leading to higher conversion. However, the single step integration of capture and mineralization in which the solvent dynamically captures CO<sub>2</sub> and the released carbonate or bicarbonate ions react with the dissolved Ca<sup>2+</sup> or Mg<sup>2+</sup> ions to precipitate Ca- and Mg-carbonates with in-situ solvent regeneration has been less explored. This process, also known as the Aqueous Amine Looping Approach was successfully demonstrated for the single-step capture, conversion and storage of CO<sub>2</sub> to produce Ca- and Mg-bearing carbonates starting from calcium oxide (CaO), calcium silicate (CaSiO<sub>3</sub>), and magnesium oxide (MgO) precursors using monoethanolamine (MEA) (Liu et al., 2020; Liu & Gadikota, 2018).

Prior work on the aqueous alkaline amine looping approach showed that complete conversion of CaO to calcium carbonate and 70% conversion of MgO to hydrated magnesium carbonate was achieved at 50 °C with 30 wt% MEA and 15 wt% solid on reacting for 3 hours (Liu et al., 2020; Liu & Gadikota, 2018). However, solvents with lower vapor pressures compared to MEA to reduce solvent loss, higher resistance to oxidative degradation and lower toxicity need to be explored. Given this criteria, amino acid salts such as sodium or potassium glycinate were identified as appropriate solvents for CO<sub>2</sub> capture. Further, sodium or potassium glycinate were effective in capturing CO<sub>2</sub> from very dilute sources including directly from air (Brethomé et al., 2018; Custelcean et al., 2019; Garrabrant et al., 2019; Williams et al., 2019). These factors motivated the investigation of sodium glycinate in the single-step capture and conversion of CO<sub>2</sub> to calcium carbonate using calcium oxide and calcium silicate as the alkaline precursors. **Figure 7.1** is a schematic representation of the reactions that correspond to CO<sub>2</sub> capture and regeneration using Na-glycinate. In the context of using Na-glycinate, we are interested in addressing the following research questions: **(i)** What is the influence of reaction temperature, concentration of

sodium glycinate, and reaction time on the conversion of CaO and CaSiO<sub>3</sub> to calcium carbonate? **(ii)** What are the speciation mechanisms that correspond to CO<sub>2</sub> capture and regeneration of solvent on reacting with the alkalinity in the aqueous phase? **(iii)** What are the structural and morphological features of calcium carbonate precipitated in the presence of Na-glycinate? To address these questions, we investigate the influence of temperature in the range of 25-90 °C, Na-glycinate concentrations in the range of 0-1 M and reaction times up to 5 hours on the carbon mineralization behavior of CaO and CaSiO<sub>3</sub>. The compositions of the carbonate-bearing products, the structures and morphologies of the reacted materials are determined in these experiments. These investigations are designed to probe the effectiveness of Na-glycinate as an agent for CO<sub>2</sub> capture and transfer in the aqueous phase for the accelerated carbon mineralization of CaO and CaSiO<sub>3</sub> at temperatures below 100 °C and CO<sub>2</sub> partial pressure of 1 atm.

## **7.2 Experimental Materials and Methods**

The alkaline precursors used in this study calcium oxide (CaO) and calcium silicate (CaSiO<sub>3</sub>) were procured from Sigma-Aldrich. Glycine was purchased from Alfa Aesar with 99 % purity. Sodium hydroxide was procured from Fisher Scientific. Na-glycinate solutions with varying concentrations was prepared by combining pre-determined concentrations of NaOH with glycine and stirring at 500 rpm for 60 minutes. The reaction associated with producing Na-glycinate is as follows:  $\text{CH}_2\text{COOHNH}_2 + \text{NaOH} \leftrightarrow \text{CH}_2\text{COOHNH}^- + \text{Na}^+ + \text{H}_2\text{O}$ . As noted in this reaction, the stoichiometric ratio of NaOH and glycine is 1:1 (Hu et al., 2018).

### **7.2.1 Aqueous alkaline amino acid looping process for accelerated carbon mineralization**

The experiments were performed in the Parr Reactor (Series 4590 Micro Stirred Reactor). The solid to liquid ratio is maintained at 3:17 by weight for all the experiments. Experiments were performed in water and Na-glycinate concentrations of 0.5 M and 1.0 M. The reactor was purged with pure CO<sub>2</sub> for 1 min to remove air from the headspace. CO<sub>2</sub> partial pressure was maintained at 1 atm for all the experiments. A stirring rate of 300 rpm  $\pm$  5 rpm was held constant for all the experiments. The experiments were performed for 1 hour, 3 hours, and 5 hours. Reaction temperatures of 25 °C, 50 °C, 75 °C and 90 °C were studied. At the end of the experiment, the liquid and solid contents were separated using vacuum filtration. Residual water in the solid samples was removed by drying in a vacuum oven for 12 hours at 90 °C.

### **7.2.2 Quantification of Carbonate Formation and the Corresponding Morphological Features**

The effectiveness of Na-glycinate in enabling the mineralization of CO<sub>2</sub> was determined using the extent of carbon mineralized. The carbonate content was determined using Thermogravimetric Analyses (SDT, TA Instruments, SDT 650). The heating rate was set to 5 °C/min, with starting and ending temperatures of 25 °C and 800 °C, respectively. The flow rate of the N<sub>2</sub> gas in the TGA balance was set to 10 mL/min. The carbonate content in the recovered samples was determined based on the change in the weight of the samples. Calcium carbonate decomposition to produce CaO and CO<sub>2</sub> occurs in the temperature range of 600-800 °C (Li et al., 2017). The following relationship was used to determine the extent of carbon mineralized, where TGA represents the weight change that corresponds to the carbonate content in the reacted materials and  $R_{CO_2}$  represents to the amount of the mineral needed to store a unit mass of CO<sub>2</sub> (Gadikota et al., 2014; O'Connor et al., 2004).

$$Y_{CO_2, TGA} = R_{CO_2} \times \left( \frac{TGA}{100 - TGA} \right) \times 100\% \quad \text{Equation 7.1}$$

The changes in the functional groups were identified based on the infrared absorption spectra determined using Attenuated Total Reflection – Fourier Transform Infrared spectroscopy analyses (ATR-FTIR, Thermo Fisher Nicolet iS50) in the range of 300 ~ 4000  $\text{cm}^{-1}$ . The morphological features of the products were determined using Scanning Electron Microscopy (SEM, LEO 1550 FESEM). The crystalline features were determined using Wide Angle X-Ray Scattering (WAXS) measurements were performed at Sector 9-ID at the Advanced Photon Source (APS) in Argonne National Laboratory (ANL) (Gadikota et al., 2017; Ilavsky et al., 2009, 2018; Liu & Gadikota, 2018). The total X-ray flux, energy and corresponding wavelength were  $10^{13}$  photon  $\text{s}^{-1}$ , 21.0 keV, and 0.59 Å, respectively. The WAXS measurements were calibrated using LaB6 (Black et al., 2010), and the acquisition time for each measurement was set to 30 seconds. Data reduction and analyses were performed using the Nika (Ilavsky, 2012a) software packages embedded in *IgorPro* (Wavemetrics, Lake Oswego, OR). (Ilavsky, 2012; Ilavsky & Jemian, 2009) X-Ray Diffraction (XRD) analyses was performed using the Bruker D8 Advance ECO powder diffractometer. The acquisition times for each data point is 0.1 s, and the increment of the time step is 0.0195°.

## 7.3 Results and Discussions

### 7.3.1 CO<sub>2</sub> reaction with sodium glycinate

To determine the dynamic changes in the functional groups as CO<sub>2</sub> is captured using Na-glycinate, in-situ ATR FT-IR analyses were performed. 1 mL 1 M Na-glycinate is loaded into the cell and CO<sub>2</sub> at a pressure of 1 atm is supplied to this cell. CO<sub>2</sub> reacts with glycinate to generate the corresponding carbamic acid, followed by deprotonation by a second equivalent of glycine to

produce carbamate and zwitterionic glycine (**Reactions 7.1**) (Brethomé et al., 2018; Custelcean et al., 2019; Guo et al., 2013; Hu et al., 2018; Zhang et al., 2013). Hydrolysis of the carbamate results in glycinate and bicarbonate ions (**Reaction 7.2**).

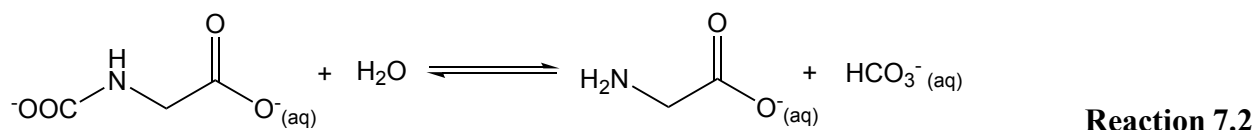
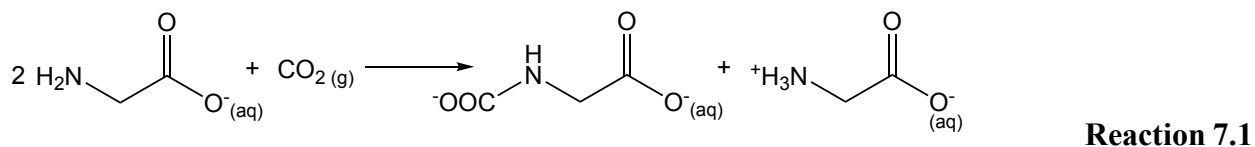


**Table 7.1** summarizes the band assignments of species. As  $\text{CO}_2$  is captured by Na-glycinate, the peak that corresponds to the asymmetric stretching vibration of C-O at  $1395 \text{ cm}^{-1}$  in  $\text{CO}_3^{2-}$  ions increases rapidly from the start of the experiment to the first 90 minutes, and the peak increase slows from 90 min to 180 min (Davis & Oliver, 1972). This tendency is similar to the stretching modes in -CN and bending mode of -NH at  $1120 \text{ cm}^{-1}$ ,  $1413 \text{ cm}^{-1}$  and  $1545 \text{ cm}^{-1}$  corresponding to the formation of  $\text{NH}_2\text{COO}^-$  species (Milella & Mazzotti, 2019). The area under the peaks of these representative peaks is integrated and normalized to determine the temporal evolution of the species. Further the evolution in the bicarbonate peaks that correspond to the  $\delta(-\text{C}-\text{OH})$  vibrations of the -C-OH group and  $\nu(-\text{C}-\text{O})$  vibrations of the -C-O group are consistent with Reaction 2 in which the hydrolysis of the carbamate ions results in the formation of glycinate and bicarbonate ions (**Reaction 7.2**). The availability of bicarbonate ions during the capture of  $\text{CO}_2$  using Na-glycinate motivate the combination of this pathway with carbon mineralization of CaO and  $\text{CaSiO}_3$ .

### 7.3.2 Effect of temperature

In these carbon mineralization experiments, we explore the hypothesis that there is a non-monotonic temperature dependence on the carbon mineralization behavior of CaO and CaSiO<sub>3</sub> in the single step capture and carbonate mineralization approach. CO<sub>2</sub> capture by aqueous solvents is generally favored below 40 °C, while regeneration is favored at higher temperatures (Brethomé et al., 2018; Garrabrant et al., 2019; Hu et al., 2018). However, higher temperatures favor the dissolution of CaO and CaSiO<sub>3</sub> and the precipitation of calcium carbonates (Gadikota, 2016; Gerdemann et al., 2004; Gerdemann et al., 2007). To investigate the influence of temperature on the overall kinetics of CO<sub>2</sub> capture and mineralization, experiments were performed at 25 °C, 50 °C, 75 °C, and 90 °C in 1.0 M Na-glycinate for a reaction time of 3 hours with 15 wt% solid and a stirring rate of 300 rpm.

The extents of carbon mineralization of CaO at 25 °C, 50 °C, 75 °C, and 90 °C are 77.0 %, 95.1%, 94.2%, and 97%, respectively. The extents of carbon mineralization of CaSiO<sub>3</sub> at 25 °C, 50 °C, 75 °C, and 90 °C are 6.6 %, 16.6%, 31.0 %, and 27.9 %, respectively. These data show that near complete conversion of CaO to CaCO<sub>3</sub> can be achieved at temperatures in the range of 50-90 °C. However, the conversion of CaSiO<sub>3</sub> to CaCO<sub>3</sub> does not exceed 31.0 % in this temperature range. These data are consistent with prior published work using MEA as the solvent (Liu & Gadikota, 2018). The highest reported conversion of CaSiO<sub>3</sub> to CaCO<sub>3</sub> was 36% with 50 wt% MEA. Lower extents of carbon mineralization with CaSiO<sub>3</sub> compared to CaO are attributed to slower dissolution rates and the formation of mass transfer limiting silica passivation layers (Daval et al., 2010, 2013).

The effect of competing reactions is more clearly delineated in the case of CaSiO<sub>3</sub> where complete conversion to CaSiO<sub>3</sub> is not achieved. One of the key considerations is the change in the

reaction rate of CO<sub>2</sub> captured using glycinate as a function of temperature. Guo and co-workers showed that the rate constant of the glycine anion NH<sub>2</sub>CH<sub>2</sub>CO<sub>2</sub><sup>-</sup> reacting with CO<sub>2</sub> is represented by the following expression:

$$k(M^{-1}s^{-1}) = 1.24 \times 10^{12} \exp [-5459/T(K)] \quad \text{Reaction 7.4}$$

The rate constants for the reaction between CO<sub>2</sub> and NH<sub>2</sub>CH<sub>2</sub>CO<sub>2</sub><sup>-</sup> at 25 °C, 50 °C, 75 °C, and 90 °C are  $1.37 \times 10^4 M^{-1}s^{-1}$ ,  $5.67 \times 10^4 M^{-1}s^{-1}$ ,  $1.91 \times 10^5 M^{-1}s^{-1}$ , and  $3.65 \times 10^5 M^{-1}s^{-1}$ , respectively (Guo et al., 2013). However, the highest extents of carbon mineralization of CaSiO<sub>3</sub> are noted at 75 °C as opposed to 90 °C. The higher dissolution rates of CaSiO<sub>3</sub> and the decreasing solubility of CaCO<sub>3</sub> with increasing temperature favor carbonate formation at 75 °C as opposed to lower temperatures of 25 °C (Palandri & Kharaka, 2004; Weyl, 1959). FTIR analysis of the aqueous phase showed that the intensity of -N-H peak corresponding to NH<sub>2</sub>COO<sup>-</sup> species at 1545 cm<sup>-1</sup> in unreacted 1 M Na-glycinate progressively decreases with increase in temperature in the case of CaO (**Figure 7.4 (a)**) and CaSiO<sub>3</sub> (**Figure 7.5 (a)**). The reduced concentration of COO<sup>-</sup> peak corresponding to the bicarbonate species in the fluids recovered post-reaction is consistent with the uptake of CO<sub>2</sub> from the aqueous phase to produce calcium carbonates.

### 7.3.3 Effect of amino acid salt concentration

To evaluate if carbon mineralization is limited by the concentration of the CO<sub>2</sub> capture solvent, we investigate concentrations of 0, 0.5 M, 1.0 M, and 3.0 M Na-glycinate at 75 °C for 3 hours with 15 wt% solid and a stirring rate of 300 rpm. The extents of carbon mineralization with CaO at 0, 0.5 M, 1.0 M, and 3.0 M Na-glycinate are 42.6%, 68.4%, 94.2%, and 92.1%, respectively. The extents of carbon mineralization with CaSiO<sub>3</sub> at 0, 0.5 M, 1.0 M, and 3.0 M Na-

glycinate are 16.7 %, 14.1 %, 31.0 %, and 23.6 %, respectively. In the case of  $\text{CaSiO}_3$  and  $\text{CaO}$ , the highest extents of carbon mineralization are achieved at 75 °C. FT-IR analyses of the liquid effluents showed that the  $\text{-COO}^-$  peak at a wavelength of  $1595 \text{ cm}^{-1}$  is prominent in the effluent associated with the 3 M Na-glycinate case compared to concentrations at 0.5 M and 1.0 M (**Figure 7.5**). These data suggest that carbon mineralization at elevated concentrations of Na-glycinate is not limited by the availability of carbonate or bicarbonate ions. However, in the case of  $\text{CaSiO}_3$ ,  $\text{-COO}^-$  peak is not prominent, suggested that the carbonate-bearing species are consumed. It is also interesting to note that the  $\text{-OH}$  peak in the FT-IR data (**Figures 7.4 and 7.5**) increases with the concentration of Na-glycinate. This is because the pH of the sodium glycinate used is high.

#### 7.3.4 Effect of Reaction Time

To understand if the carbon mineralization reactions with Na-glycinate occur rapidly in the first hour of the reaction or gradually increases with time, carbon mineralization experiments were performed with Na-glycinate. The experiments were performed at 1, 3, and 5 hour time periods with 1 M Na-glycinate at 75 °C with a stirring rate of 300 rpm. The extents of carbon mineralization with  $\text{CaO}$  are 82.5, 94.2, and 95.9% at 1, 3, and 5 hours, respectively. The extents of carbon mineralization with  $\text{CaSiO}_3$  are 12.8, 31.0, and 34.6 % at 1, 3, and 5 hours, respectively. Significant carbon mineralization occurs in the first hour of the reaction in the case of  $\text{CaO}$ . A small increase in the extent of carbon mineralization of  $\text{CaO}$  between 3 hours and 5 hours is noted. In contrast, the kinetics of carbon mineralization of  $\text{CaSiO}_3$  were considerably slower in the first hour of the reaction, with sufficiently high extents achieved at 31.0%. A small increase in the extent of carbon mineralization of  $\text{CaSiO}_3$  between 3 hours and 5 hours is noted (**Figure 7.3 (c)**). A progressive decrease in the intensity of the  $\text{-COO}^-$  group in the aqueous phase is consistent with the higher extent of carbon mineralization (**Figures 7.4 (c) and 7.5 (c)**).

### 7.3.5 Structural and morphological characterization of recovered materials

During the carbon mineralization of CaO and CaSiO<sub>3</sub>, various forms of calcium carbonate such as calcite (rhombohedral), aragonite (spiky/orthorhombic), and vaterite (plate-like/hexagonal) can be formed. Prior studies showed that the process parameters such as the solvent for CO<sub>2</sub> capture and the temperature influence the crystalline habit of calcium carbonate (Arti et al., 2017; Murnandari et al., 2017). To investigate the influence of temperature, amino acid salt concentration, and reaction time, the products were analyzed using Wide Angle X-Ray Scattering (WAXS) measurements. The carbonate-bearing products were identified and characterized in the presence of 1 M sodium glycinate at different temperatures of 25, 50, 75, and 90 °C for 3 h in **Figure 7.6 (a)**, with different concentration of 0, 0.5, 1, and 3 M sodium glycinate at 75 °C for 3 h in **Figure 7.6 (b)**, with 1 M sodium glycinate at 75 °C for different reaction time of 1, 3, and 5 hr in **Figure 7.6 (c)**.

CO<sub>2</sub> absorption and mineralization at 25 °C in 1 M Na-glycinate results in the formation of Ca(OH)<sub>2</sub> and CaCO<sub>3</sub>. With increasing temperature, Ca(OH)<sub>2</sub> phase disappears and calcite remains as the dominant phase (**Figure 7.6 (a)**) (Chessin et al., 1965; Negro & Ungaretti, 1971; Müller, 2010; Petch, 1961; Primak et al., 1948; Wang & Becker, 2009). The presence of calcium hydroxide at 25 °C is consistent with the lower extent of carbon mineralization of 77.0 % compared to 95.1 %, 94.2 % and 97.0 % at 50, 75, and 90 °C, respectively. Similarly, calcium hydroxide is present in the samples when reacted in water or 0.5 M Na-glycinate, which correspond to extents of carbon mineralization of 42.6 % and 68.4 % respectively (**Figure 7.6 (b)**). However, in the case of 3 M Na-glycinate, vaterite and calcite are co-present. These data suggest that higher concentrations of carbamate ions (**Figure 7.4 (b)**) in case of 3 M Na-glycinate influence the formation of calcium carbonate polymorphs. Further, increase in the reaction time enhances the formation of calcite

(**Figure 7.6 (c)**). The morphological features are images using SEM. **Figures 7.6 (a), (b) and (c)** represent unreacted CaO, CaO reacted in water and CaO reacted in 1 M Na-glycinate at 75 °C for 3 hours. The formation of rhombohedral calcite is noted when CaO is reacted in water and in 1 M Na-glycinate (**Figures 7.6 (b) and (c)**).

Unlike CaO, lower extents of carbon mineralization are noted in CaSiO<sub>3</sub>. This is also evident from the presence of calcium silicate present in all the reacted samples. The co-presence of calcite, vaterite, and aragonite is noted in all the reacted samples (**Figure 7.7**) (Chessin et al., 1965; Negro & Ungaretti, 1971; Müller, 2010; Petch, 1961; Primak et al., 1948; Wang & Becker, 2009). Interestingly, the extent of carbon mineralization of CaSiO<sub>3</sub> in water and 1.0 M Na-glycinate are 16.7 % and 31.0 %, respectively. For this reason, the presence of rhombohedral calcite, spiky aragonite and plate-like vaterite is more sparse in **Figure 7.6 (e)** representing the water case compared to **Figure 7.6 (f)** representing the 1.0 M Na-glycinate case.

#### 7.4 Conclusion

In this paper, we investigate the single-step capture and mineralization of CaO and CaSiO<sub>3</sub> to calcium carbonate using Na-glycinate, an amino acid salt. The influence of reaction temperature in the range of 25 °C – 90 °C, reaction time in the range of 1 – 3 hours, and Na-glycinate concentrations in the range of 0.5 – 3 M on the carbon mineralization behavior of CaO and CaSiO<sub>3</sub> were probed. While lower temperatures aid the thermodynamics of CO<sub>2</sub> capture, higher temperatures favor the kinetics of mineral dissolution and carbonate precipitation. In this single step CO<sub>2</sub> capture and mineralization pathway, highest conversion of CaO and CaSiO<sub>3</sub> were achieved at 1.0 M Na-glycinate at 75 °C and with a reaction time of 3 hours in a system comprising 15 wt% solid and at a stirring rate of 300 rpm. Extents of carbon mineralization with CaO and CaSiO<sub>3</sub> are 94.2 % and 31.0 %, respectively. These data suggest that Na-glycinate undergoes

multiple CO<sub>2</sub> capture and regeneration cycles into the aqueous phase facilitating greater availability of aqueous carbon species for carbonate precipitation. The dominant crystalline phase in materials with CaO as the precursor is calcite. Aragonite, calcite and vaterite are present in the materials with CaSiO<sub>3</sub> as the precursor. Our results demonstrate that Na-glycinate is an environmentally benign alternative to aqueous amines for the single step CO<sub>2</sub> capture and mineralization with inherent chemical regeneration of the solvent.

**Table 7.1** Main infrared band assignments of the species present in the CO<sub>2</sub>–Na-glycinate–H<sub>2</sub>O system. The symbols  $\nu$ ,  $\nu_a$  and  $\delta$  indicate the stretching mode, the asymmetric stretching mode, and the bending mode of the relevant molecules, respectively (Davis & Oliver, 1972; Frasco, 1964; Hisatsune, 1984; Milella & Mazzotti, 2019; Pretsch et al., 2009).

Species	Band Position (cm <sup>-1</sup> )	Assignment	Reference
NH <sub>2</sub> COO <sup>-</sup>	1120	$\nu(-\text{CN})$	(Hisatsune, 1984; Milella & Mazzotti, 2019; Pretsch et al., 2009)
	1413	$\nu(-\text{CN})$	(Frasco, 1964; Milella & Mazzotti, 2019)
	1545	$\delta(-\text{N-H})$	(Milella & Mazzotti, 2019; Pretsch et al., 2009)
HCO <sub>3</sub> <sup>-</sup>	1105	$\nu_a(-\text{C-OH})$	(Milella & Mazzotti, 2019)
	1300	$\delta(-\text{C-OH})$	(Milella & Mazzotti, 2019)
	1365	$\nu(-\text{C-O})$	(Milella & Mazzotti, 2019)
CO <sub>3</sub> <sup>2-</sup>	1395	$\nu_a(-\text{CO})$	(Davis & Oliver, 1972)

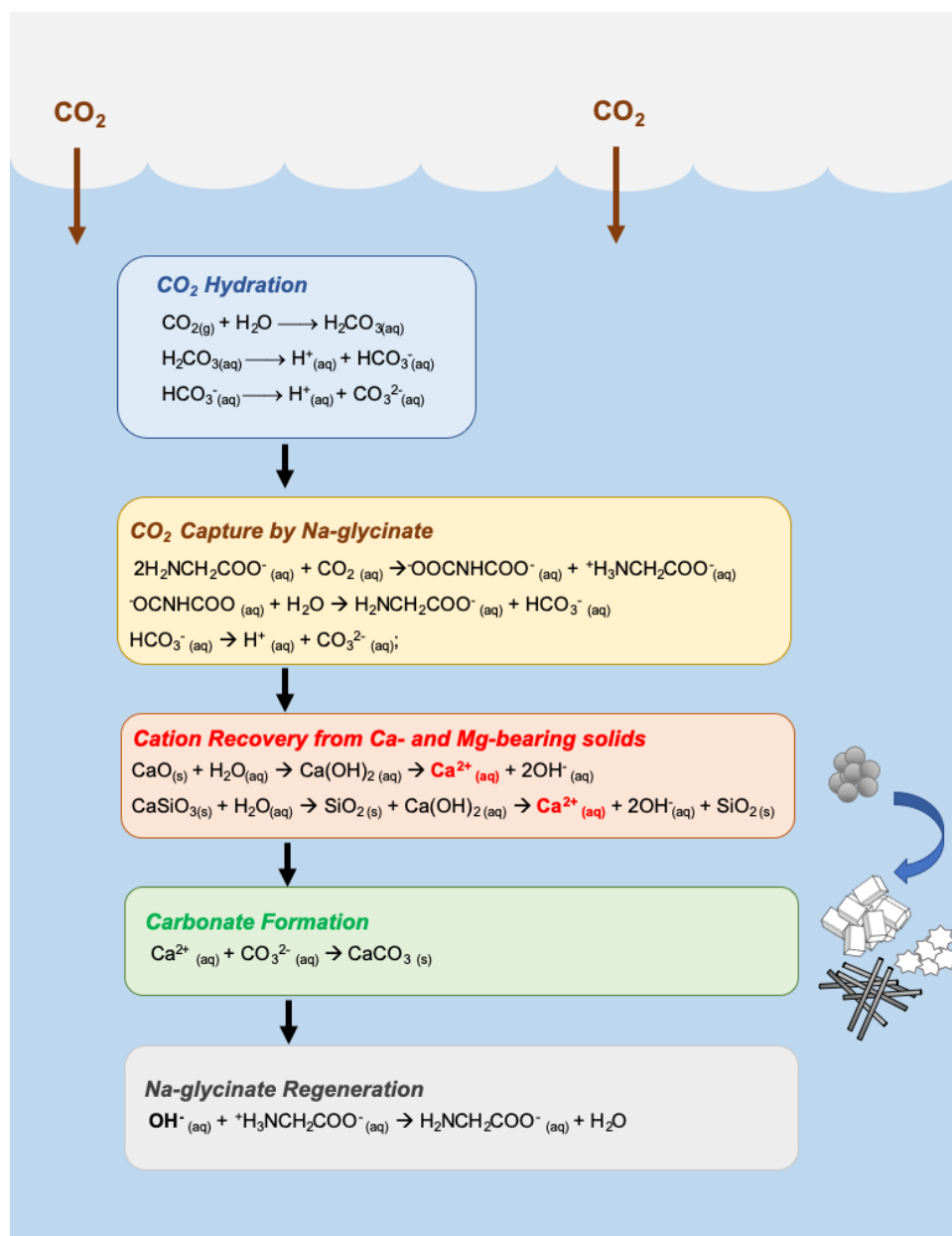


**Figure 7.1** Schematic representation of the alkaline aqueous amino acid salt looping process for the single step, low temperature and integrated CO<sub>2</sub> capture and conversion using sodium glycinate to produce calcium carbonate. Reactions representing CO<sub>2</sub> hydration, CO<sub>2</sub> capture using amino acid salts, amino acid salt regeneration, cation recovery from Ca- and Mg-bearing solids, and carbonate formation are shown here.

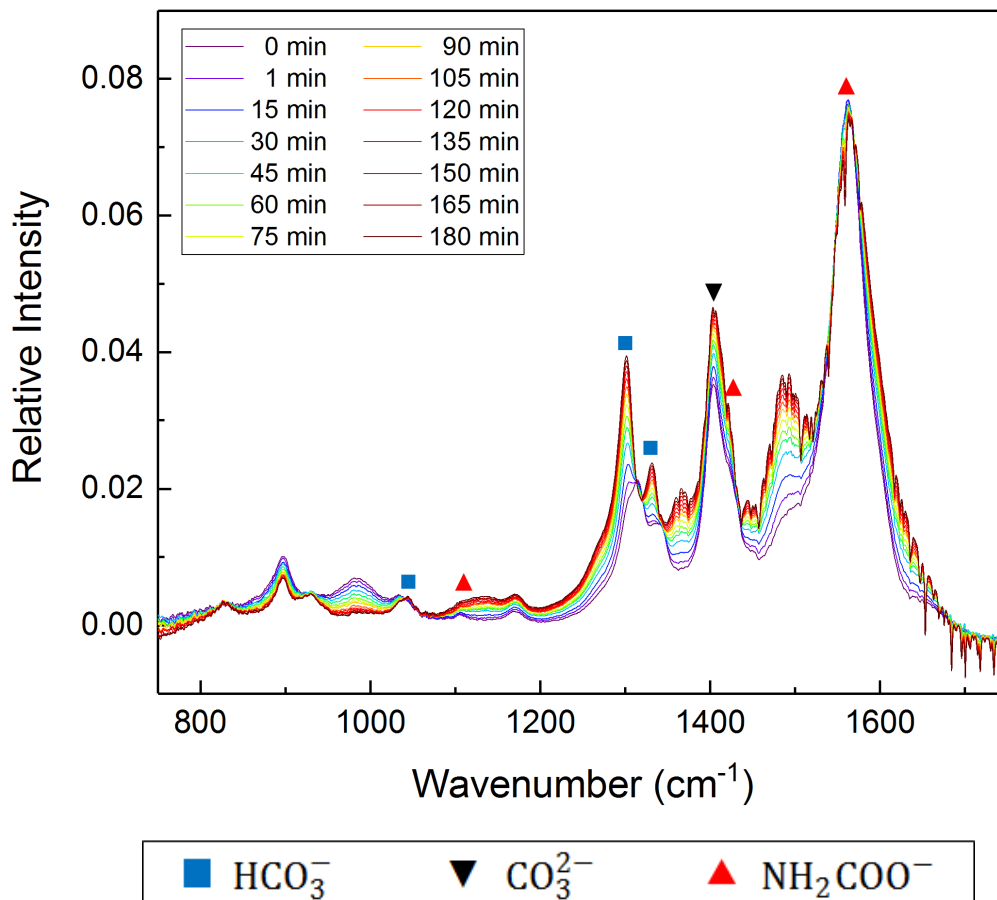


**Figure 7.2** Changes of aqueous species during CO<sub>2</sub> capture using Na-glycinate determined using ATR-FTIR analyses. HCO<sub>3</sub><sup>-</sup> at 1005 cm<sup>-1</sup>, 1300 cm<sup>-1</sup>, and 1365 cm<sup>-1</sup> (Milella & Mazzotti, 2019). CO<sub>3</sub><sup>2-</sup> at 1395 cm<sup>-1</sup> (Davis & Oliver, 1972). NH<sub>2</sub>COO<sup>-</sup> at 1120 cm<sup>-1</sup>, 1413 cm<sup>-1</sup>, and 1545 cm<sup>-1</sup> (Hisatsune, 1984; Milella & Mazzotti, 2019; Pretsch et al., 2009).

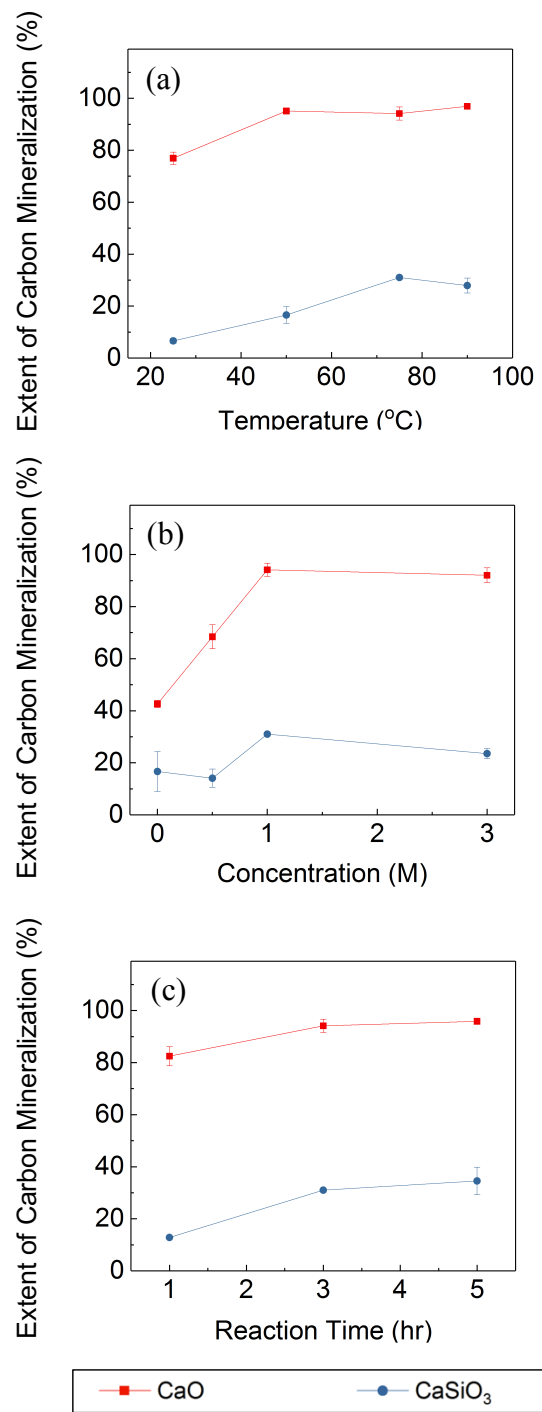


**Figure 7.3** Extent of carbon mineralization of CaO (red) and CaSiO<sub>3</sub> (blue) with 1 M sodium glycinate at temperatures of 25, 50, 75, and 90 °C for 3 hours in (a), with different concentration of 0, 0.5, 1, and 3 M sodium glycinate at 75 °C for 3 hours in (b), with 1 M sodium glycinate at 75

°C for different reaction times of 1, 3, and 5 hours in (c). All the experiments are performed at  $P_{\text{CO}_2} = 1 \text{ atm}$  and a stirring rate of 300 rpm.

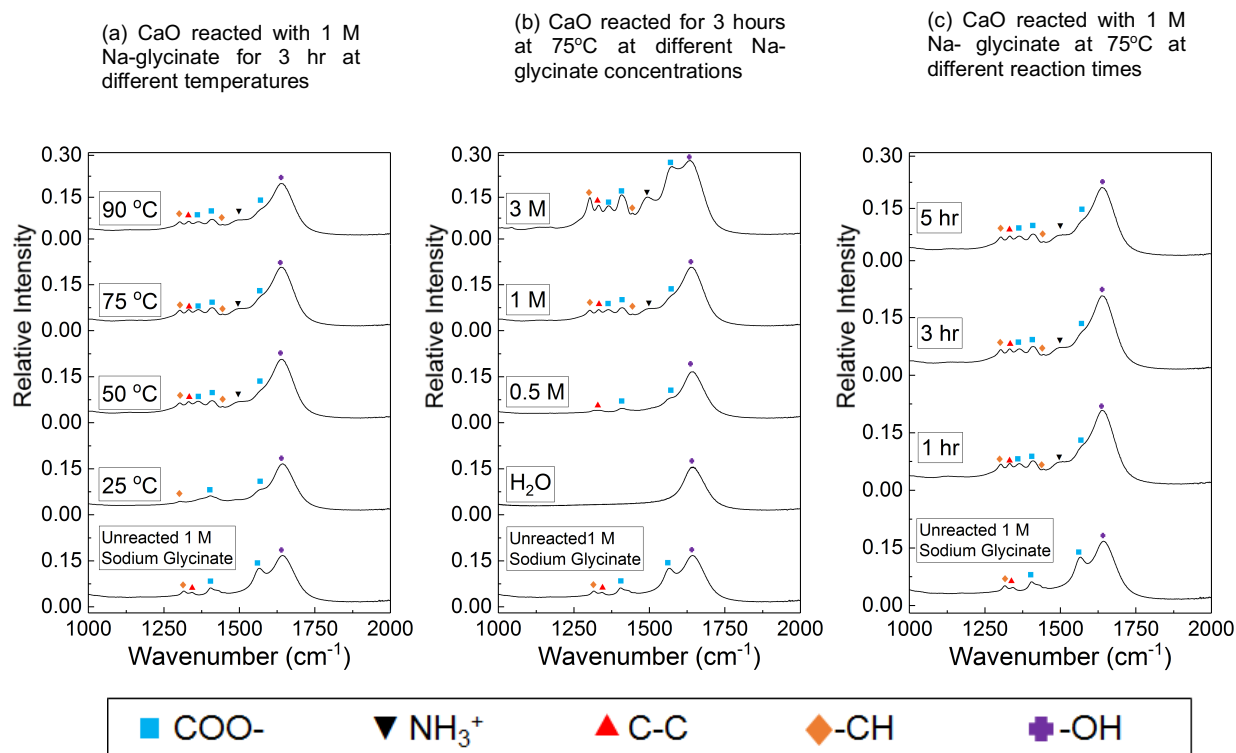


**Figure 7.4** Changes in the species present in the aqueous phase recovered after the carbon mineralization of CaO using ATR-FTIR analyses. Figures (a), (b) and (c) represent experiments performed to investigate the influence of temperature, amino acid salt concentration, and reaction time, respectively (Ahmed et al., 2013; Doki et al., 2004; Ramachandran et al., 2007).

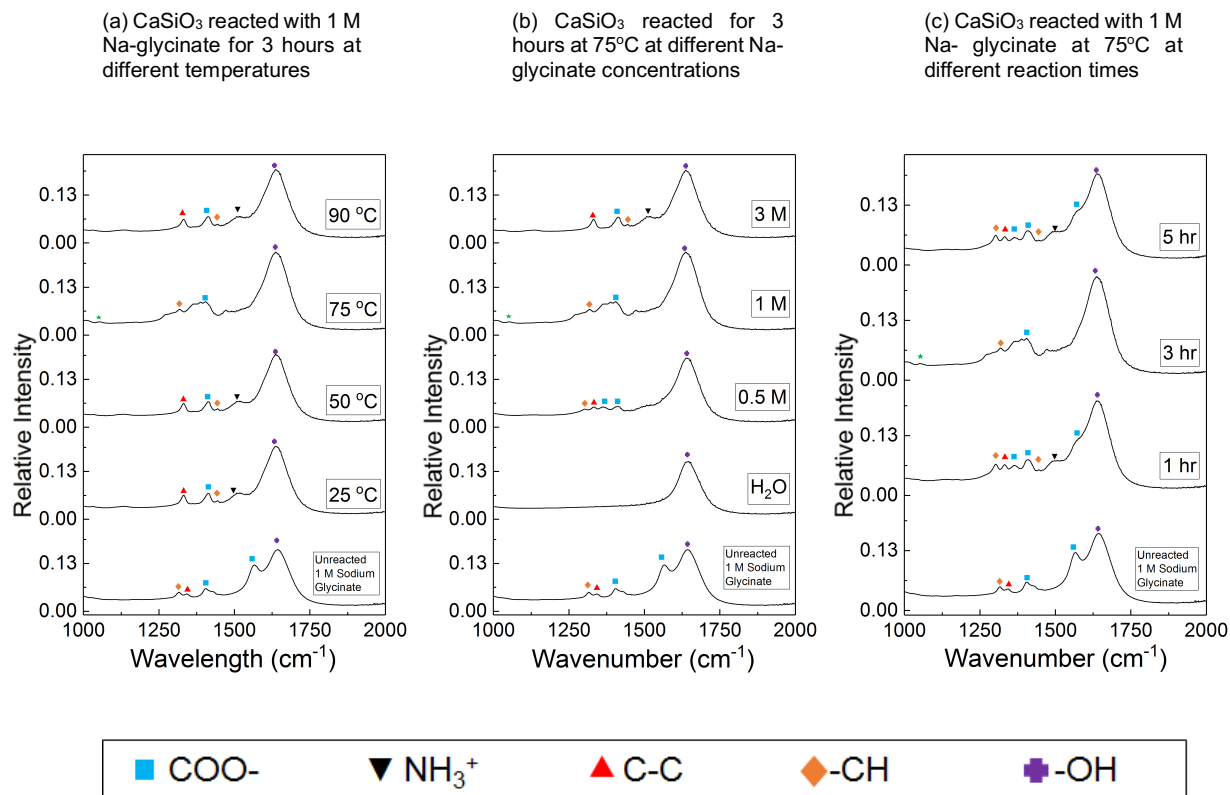


**Figure 7.5** Changes in the species present in the aqueous phase recovered after the carbon mineralization of CaSiO<sub>3</sub> using ATR-FTIR analyses. Figures (a), (b) and (c) represent experiments performed to investigate the influence of temperature, amino acid salt concentration, and reaction time, respectively (Ahmed et al., 2013; Doki et al., 2004; Ramachandran et al., 2007).

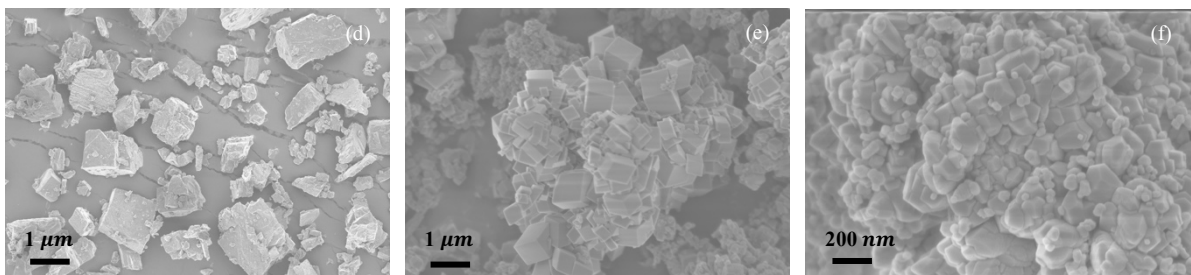
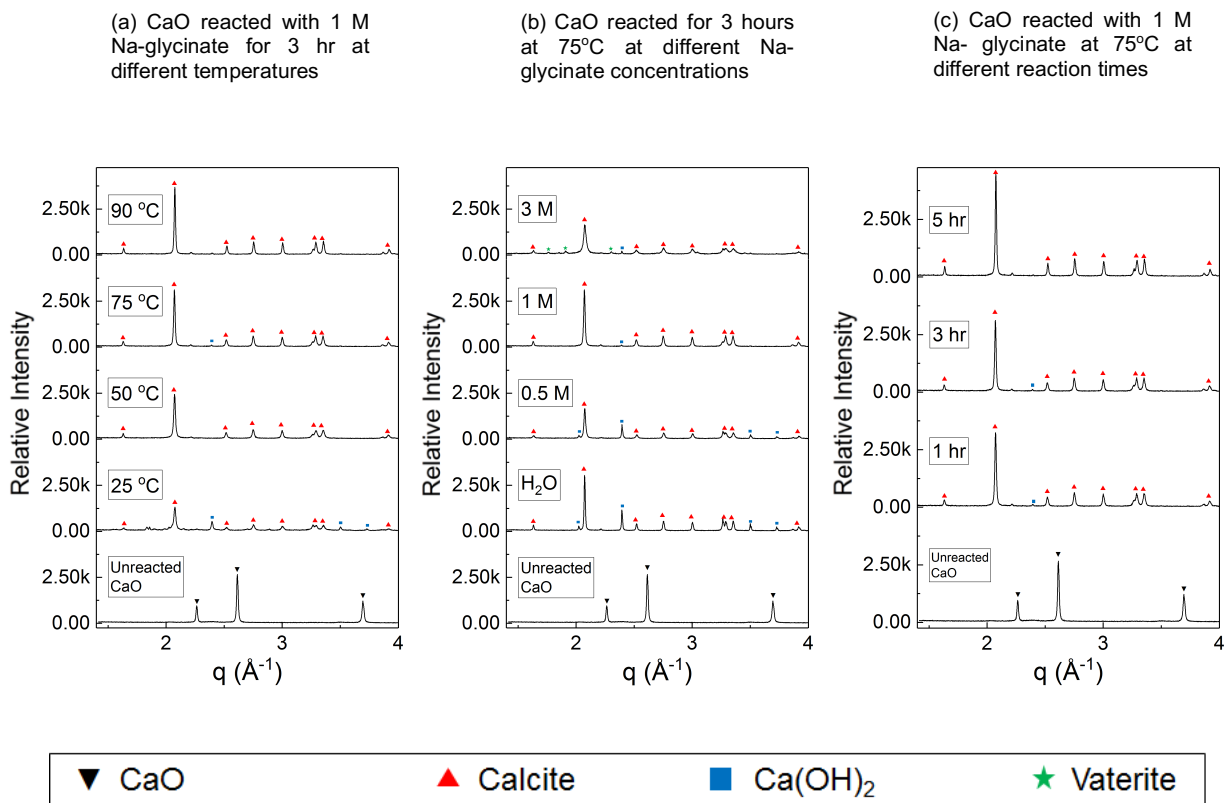


**Figure 7.6** Changes in the phases present in calcium oxide on carbon mineralization in the presence of 1 M sodium glycinate at 25, 50, 75, and 90 °C reacted for 3 hours in (a), with different concentration of 0, 0.5, 1, and 3 M sodium glycinate at 75 °C for 3 hours in (b), with 1 M sodium glycinate at 75 °C for different reaction time of 1, 3, and 5 hours in (c). All the experiments are performed at  $P_{CO_2} = 1$  atm and a stirring rate of 300 rpm. Peaks are identified based on the crystallographic data reported for calcium oxide, calcite, vaterite, and aragonite. Crystallographic

phases are identified based on the data presented in references (Chessin et al., 1965; Negro & Ungaretti, 1971; Müller, 2010; Petch, 1961a; Primak et al., 1948; Wang & Becker, 2009). The morphological changes of the CaO samples on carbonation are probed by SEM with (d) representing the unreacted CaO, (e) representing the reaction with H<sub>2</sub>O at 75 °C for 3 hours, and (f) representing CaO after the reaction with 1 M sodium glycinate at 75 °C for 3 hr (Chessin et al., 1965; Negro & Ungaretti, 1971; Maslen et al., 1993; Müller, 2010; Wang & Becker, 2009).

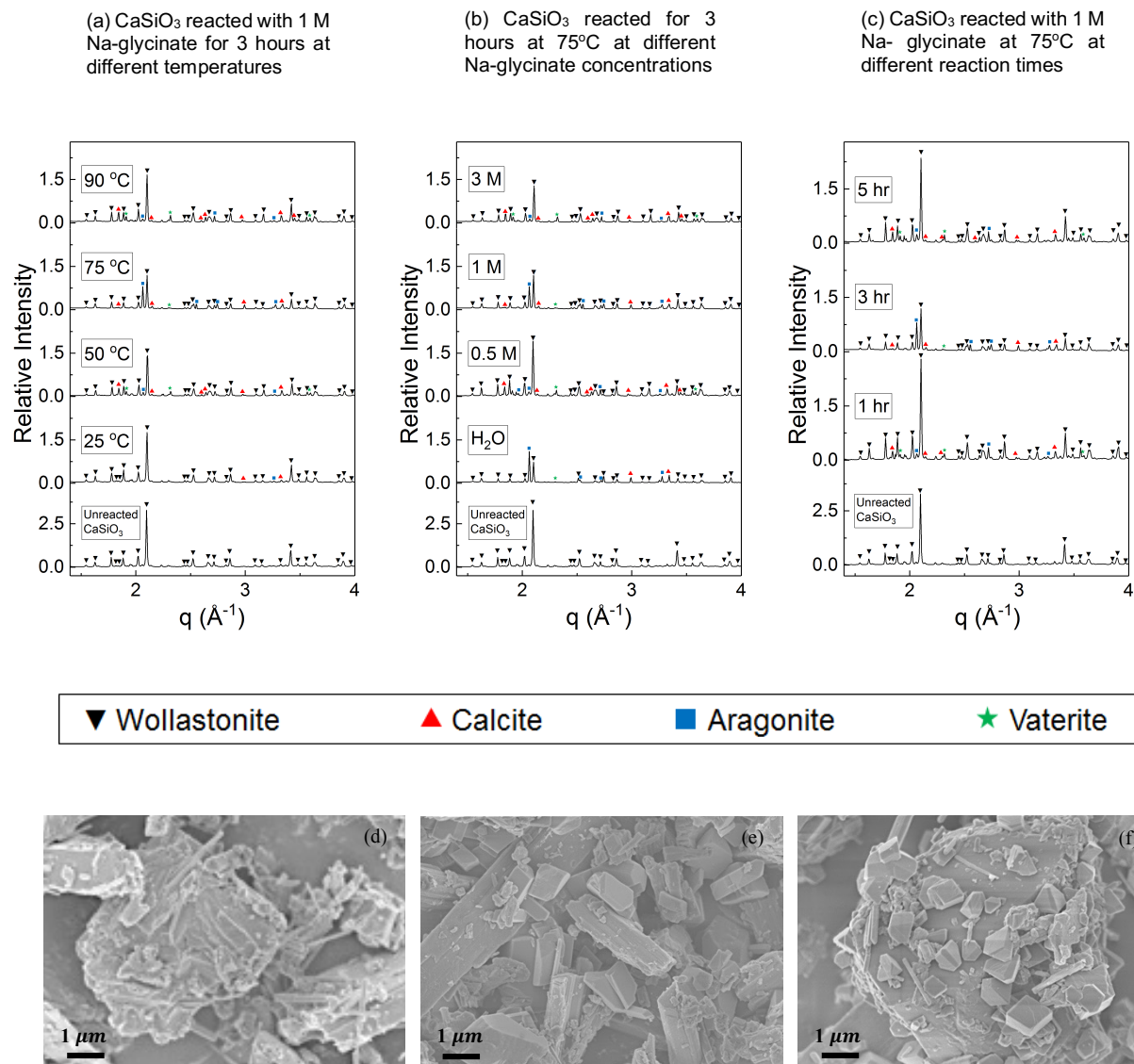


**Figure 7.7** Changes in the phases present in calcium silicate on carbon mineralization in the presence of 1 M sodium glycinate at 25, 50, 75, and 90 °C reacted for 3 hours in (a), with different concentration of 0, 0.5, 1, and 3 M sodium glycinate at 75 °C for 3 hours in (b), with 1 M sodium glycinate at 75 °C for different reaction time of 1, 3, and 5 hours in (c). All the experiments are performed at  $P_{\text{CO}_2} = 1$  atm and a stirring rate of 300 rpm. Peaks are identified based on the crystallographic data reported for calcium silicate (or wollastonite), calcite, vaterite, and aragonite.

Crystallographic phases are identified based on the data presented in referenc (Chessin et al., 1965; Negro & Ungaretti, 1971; Müller, 2010; Petch, 1961a; Primak et al., 1948; Wang & Becker, 2009). The morphological changes of the CaSiO<sub>3</sub> samples on carbonation are probed by SEM with (d) representing the unreacted CaSiO<sub>3</sub>, (e) representing the reaction with H<sub>2</sub>O at 75 °C for 3 hours, and (f) representing CaSiO<sub>3</sub> after the reaction with 1 M sodium glycinate at 75 °C for 3 hr (Chessin et al., 1965; Negro & Ungaretti, 1971; Maslen et al., 1993; Müller, 2010; Wang & Becker, 2009).

## CHAPTER 8

# INTEGRATED CO<sub>2</sub> CAPTURE AND REMOVAL VIA CARBON MINERALIZATION WITH INHERENT REGENERATION OF AQUEOUS SOLVENTS

*The contents of this chapter have been accepted for publication as an article: Liu, M., Hohenshil, A., & Gadikota G. “Integrated CO<sub>2</sub> Capture and Removal via Carbon Mineralization with Inherent Regeneration of Aqueous Solvents.” *Energy and Fuels* (2021).*

### 8.1 Introduction

Meeting our energy and resource needs while reducing detrimental environmental impacts is one of our grand societal challenges. In this context, novel engineered pathways are needed to remove CO<sub>2</sub> emission from our energy and resource conversion pathways. Conventional carbon capture and storage (CCS) technologies have been proposed for capturing the emitted CO<sub>2</sub>, followed by storing CO<sub>2</sub> in geologic environments. However, in some locations, the limited availability of suitable geologic reservoirs for CO<sub>2</sub> storage can be a challenge for capturing and storing CO<sub>2</sub> emitted from various energy and resource generating processes. As an alternative, engineered CO<sub>2</sub> capture and removal to produce solid carbon-bearing products can be integrated with CO<sub>2</sub> emitting processes. The ability to develop predictive controls and quantify the rates and scales of CO<sub>2</sub> that can be successfully removed by turning our CO<sub>2</sub> emissions into solid products are unique to engineered processes for CO<sub>2</sub> removal such as carbon mineralization. Carbon mineralization involves producing solid inorganic carbonates from CO<sub>2</sub>. In the interest of ensuring that these solid products can store CO<sub>2</sub> over very long periods of time, solid carbonates need to be environmentally benign, stable, and water insoluble (Gadikota & Park, 2015; Morrow &

Thompson, 2020). Accelerating the kinetics of carbon mineralization is essential for the scalable implementation of this engineered carbon removal strategy (Chiang & Pan, 2017; Gadikota & Park, 2014; Hopkins, 2008; Morrow & Thompson, 2020).

Carbon mineralization typically involves dissolving CO<sub>2</sub> in water, mobilizing cations for CO<sub>2</sub> capture by dissolving calcium and magnesium-bearing solids, and precipitating solid carbonates. These steps can be decoupled and performed in separate processes or coupled to reduce the number of unit operations and for process intensification. Prior studies focused on enhancing CO<sub>2</sub> dissolution in water by using bio-inspired catalysts such as carbonic anhydrase (Favre et al., 2009; Mirjafari et al., 2007; Power et al., 2016; Vinoba et al., 2011). Accelerated dissolution of calcium and magnesium bearing materials and minerals, including naturally occurring minerals as well as alkaline solid residuals, by using calcium or magnesium targeting chelating agents (e.g., EDTA) and weak mineral acids (e.g., citric acid or acetic acid), strong acids (e.g., nitric acid or sulfuric acid), and reagents such as ammonium bisulphate have been reported (Bonfils et al., 2012; Bui et al., 2018; Drever & Stillings, 1997; Jun et al., 2016; Li et al., 2013). Silica targeting chelating agents such as catechol have been proposed to accelerate the dissolution of silicates (Drever & Stillings, 1997; Gadikota, 2020; Jun et al., 2016; Kim, 2009; Zhao et al., 2013). The precipitation of solid carbonates is aided by the use of similar carbonate seeding surfaces and in alkaline environments (Han & Wee, 2016; Jun et al., 2010; Li et al., 2014).

Decoupling the dissolution of CO<sub>2</sub> from the gas phase into the aqueous phase, mineral dissolution, and carbonate precipitation are useful in elucidating underlying mechanisms and developing specific strategies to accelerate each step. Alternatively, single-step conversion pathways where CO<sub>2</sub>, minerals, and fluids such as water with varying levels of salinities, or in the presence of pH buffers such as sodium bicarbonate have been investigated for accelerated carbon

mineralization (Gadikota et al., 2014; Gadikota & Park, 2015, 2014; Maroto-Valer et al., 2005; Park et al., 2003). However, the use of regenerable solvents to aid carbon mineralization and in fewer units operations remains less explored. Regenerable solvents, which have the potential to be used over multiple cycles, can reduce the operating costs associated with carbon mineralization processes. Fewer number of unit operations have the potential to reduce the capital expenditures associated with carbon mineralization processes. One approach to achieve process intensification is by molecularly coupling CO<sub>2</sub> capture and carbonate formation.

Naturally occurring Ca- and Mg-bearing minerals, and alkaline industrial wastes are ideal precursors for CO<sub>2</sub> capture and carbonate mineralization due to the abundance in the nature environment and production in industrial manufactory. Major CO<sub>2</sub> emission industries, such as mining, iron and steel, power generation, cement industries, also have CO<sub>2</sub> waste stream. This co-location advantage provides the great opportunities to use the solid waste stream to capture the CO<sub>2</sub> waste gas stream.<sup>1</sup> Fly ash from power generation industry contains as high as 55% of CaO and 10% MgO; steel slag from iron and steel industry contains as high as 58% of CaO and 11% MgO; oil shale waste contains as high as 51% of CaO and 15% MgO; kiln dust from cement industry contains as high as 35% of CaO and 2% MgO; asbestos contains as high as 35% of CaO and 40% MgO.

Prior research efforts demonstrated the feasibility of coupling CO<sub>2</sub> capture and carbonate mineralization pathways with the inherent regeneration of the CO<sub>2</sub> capture solvent using different precursors. Two-step approaches involving CO<sub>2</sub> capture using aqueous solvents followed by carbonate precipitation and solvent regeneration, and single step approaches where CO<sub>2</sub>-solvent-Ca or Mg-bearing materials are co-reacted with the inherent regeneration of the solvent were investigated.(Liu et al., 2020; Liu & Gadikota, 2018, 2020) Near complete carbon mineralization

of calcium oxide to calcium carbonate, and about 35% conversion of calcium silicate to calcium carbonate was achieved in single- and two-step approaches at 50°C in 50 wt% monoethanolamine (MEA) and a reaction time of 3 hours.(Liu & Gadikota, 2018) Various other studies evaluated the efficacy of the two-step CO<sub>2</sub> capture and carbonate mineralization approach using MEA, diethanolamine, piperazine (PZ), N-methyldiethanolamine and 2-amino-2-methyl-1-propanol, and diamine solvents such as N,N-Dimethylethylenediamine, N,N-Diethylethylenediamine, 3-(Diethylamino)propylamine, 1-(2-hydroxyethyl)-4-aminopiperidine) (Ji et al., 2018; Yu et al., 2018, 2019). Calcium carbonate formation and the regeneration of 2-amino-2-methylpropanol (AMP) solutions was achieved without additional thermal energy by reacting CaO with CO<sub>2</sub>-loaded 2-amino-2-methylpropanol (AMP) solution (Kang et al., 2018).

As an alternative to amines such as monoethanolamine which is corrosive and can degrade to produce nitrosamines, amino acid salts such as sodium glycinate was investigated as a regenerable solvent for integrated CO<sub>2</sub> capture and carbonate formation. Sodium glycinate has similar CO<sub>2</sub> capture capacities as monoethanolamine but is less corrosive and more environmentally benign (Liu & Gadikota, 2020). About 94% conversion of calcium oxide to calcium carbonate, and about 31% conversion of calcium silicate to calcium carbonate was achieved in a single-step approaches at 75°C in 1.0 M sodium glycinate and a reaction time of 3 hours (Liu & Gadikota, 2020). Despite these advancements, single step CO<sub>2</sub> capture and carbon mineralization pathways remain less studied. In single step CO<sub>2</sub> capture and carbon mineralization pathways, there is no shortage of CO<sub>2</sub> supply and availability for carbon mineralization. However, the hypothesis that single step CO<sub>2</sub> capture and carbon mineralization can be realized using wide-ranging CO<sub>2</sub> capture solvents such as primary amines, amino acid solvents, hindered amines, and cyclical amine has not been reported in previous studies, and is therefore the focus of this

investigation. The specific research questions addressed in this study are: (i) What is the influence of the chemical structure of the solvent, solvent concentration on the inorganic carbon content available to react with calcium or magnesium minerals to produce the respective inorganic carbonates? (ii) What are the extents of carbon mineralization achieved using calcium oxide, magnesium oxide, and calcium silicate using various solvents? (iii) What are the carbonate phases formed and what are the key features of the solvent as it is regenerated during carbonate formation?

To address these research questions, we evaluated the thermodynamics of speciation associated with single-step CO<sub>2</sub> capture and carbonate formation, starting from CaO, CaSiO<sub>3</sub>, and MgO as the precursors. The influence of various regenerable solvents including monoethanolamine (MEA, primary amine), sodium glycinate (amino acid solvent), 2-amino-2-methylpropanol (AMP, hindered amine), and 1,8-diazabicyclo [5.4.0] undec-7-ene (DBU, cyclical amine) at various concentrations of 0 eq mol/L, 0.5 eq mol/L, 1.0 eq mol/L, and 2.5 eq mol/L on CO<sub>2</sub> capture and carbonate formation are investigated. We will investigate the effects of varying CO<sub>2</sub> capture mechanisms on carbon mineralization. Experiments are performed at 75 °C, pCO<sub>2</sub> of 1 atm, 15 wt% solid for a reaction time of 3 hours under constant stirring. These experimental conditions were chosen based on prior studies demonstrating the effectiveness of these conditions on achieving high levels of carbonate formation (Liu et al., 2020; Liu & Gadikota, 2018, 2020). CO<sub>2</sub> capture using aqueous solvents is aided at lower temperatures, while calcium carbonate or magnesium carbonate formation is favored at higher temperatures. Our prior results showed that temperatures of 50°C or 75 °C is optimal for achieving high conversions of captured CO<sub>2</sub> to calcium or magnesium carbonates. The experimental conditions are noted in **Table 8.1**. CO<sub>2</sub> capture in primary amines, such as MEA, proceeds via the formation of carbamate species through the cooperative binding of two adjacent primary amines (Hahn et al., 2016; Krounbi et al., 2020;

Yu & Chuang, 2016). Steric hindrance of the molecule (ex. AMP) could increase the conversion of carbamates to bicarbonate and release amine (Ji et al., 2018). Thus, sterically hindered amines form bicarbonate instead of carbamate through absorption (Ji et al., 2018). As for secondary amines, such as DEA, the CO<sub>2</sub> uptake forms carbamic acid without cooperative binding (Hahn et al., 2016; Krounbi et al., 2020; Yu & Chuang, 2016). In tertiary amines, such as DBU, bicarbonate species are produced on CO<sub>2</sub> capture (**Table 8.2**) (Hahn et al., 2015; Krounbi et al., 2020; Lee et al., 2017). The influence of CO<sub>2</sub> capture capacities on carbon mineralization behaviors are discussed in this study. The thermodynamic and kinetic basis for the differences in observed carbonate formation with various CO<sub>2</sub> capture solvents are elucidated in this study. As we advance towards a low carbon future, energetically and atomistically efficient engineered carbon removal strategies such as integrated CO<sub>2</sub> capture and carbonate formation pathways are needed, as shown in **Figure 8.1**.

## **8.2 Experimental Materials and Methods**

Calcium oxide, calcium silicate, and magnesium oxide used in this study are procured from Sigma-Aldrich. The solvents used in this study such as monoethanolamine (MEA), glycine which is the precursor for producing sodium glycinate, sodium hydroxide, 2-amino-2-methylpropanol (AMP), and 1,8-diazabicyclo [5.4.0] undec-7-ene (DBU) are purchased from Fisher Scientific. Sodium glycinate (NaGly) is synthesized using sodium hydroxide mixed with glycine. The physical and chemical properties of these solvents are noted in **Table 8.1**.

### **8.2.1 Experimental Approach for Integrated CO<sub>2</sub> Capture and Carbonate Formation**

The experiments were performed in a slurry multiphase reaction environment comprising CO<sub>2</sub> - aqueous solvent - alkaline solid (e.g., CaO, MgO, and CaSiO<sub>3</sub>) in a continuously stirred environment (Series 4590 Micro Stirred Reactor, Parr Reactor Company, PA). The experiments

are performed at 75 °C, pCO<sub>2</sub> of 1 atm, 15 wt% solid for a reaction time of 3 hours under constant stirring, as noted in **Table 8.3**. Prior to the beginning the experiments, the reactor was purged with pure CO<sub>2</sub> gas for one minute to ensure that CO<sub>2</sub> is the only gas phase component in the head space of the reactor. Once the slurry comprising the aqueous solvent and the alkaline solid is introduced into the reactor, the reaction temperature is set to 75 °C. This reactor takes about 15 minutes to reach the reaction temperature. The reaction time is set to 3 hours once the reaction temperature is reached. After the reaction is completed, the slurry is removed, and the contents are separated into liquid and solid constituents by vacuum filtration. The recovered solid materials are dried in a vacuum oven for 12 hours at 90 °C before they are characterized.

### 8.2.2 Characterization of chemical and morphological properties

The inorganic carbonate content in the reacted samples is determined using Thermogravimetric Analyses (TGA, TA Instruments, SDT 650). During the TGA measurements, the temperature is ramped at the rate of 10 °C/min from 25 °C to 1000 °C. The N<sub>2</sub> gas flow rate of 50 mL/min is used during the analyses of the samples. The dissociation of magnesium carbonate and calcium carbonate occurs at temperatures in the range of 350-450 °C and 650-800 °C, respectively (Liu et al., 2020; Liu & Gadikota, 2018, 2020). This weight change in the sample is used to determine the extent of carbon mineralization. The extent of carbon mineralization

$Y_{CO_2, TGA}$  is determined using the following relationship:  $Y_{CO_2, TGA} = R_{CO_2} \times \left( \frac{TGA}{100 - TGA} \right) \times 100\%$

In this relationship, TGA represents the weight change that corresponds to the carbonate content in the reacted materials and  $R_{CO_2}$  is the amount of the mineral needed to store a unit mass of CO<sub>2</sub> (Gadikota et al., 2013; Liu et al., 2020; Liu & Gadikota, 2018, 2020).

The structural features in the carbonate-bearing materials are determined using X-ray diffraction (XRD, Bruker D8 Advance ECO powder diffractometer). The voltage of the X-ray generator is 40 V and the current is 25 mA. The acquisition time for each data point is 0.1 s, and the increment of the time step is 0.0195°. Jade software is used to analyze the XRD data and the ICDD database is used to identify different phases and materials. Key functional groups in the solid and aqueous phases that provide mechanistic insights are determined using Attenuated Total Reflection – Fourier Transform Infrared spectroscopy (ATR-FTIR, Thermo Fisher Nicolet iS50). The morphological features of the unreacted and reacted materials are determined using Scanning Electron Microscopy (SEM, LEO 1550 FESEM).

### **8.3 Results and Discussion**

To contrast the effectiveness of various solvents such as MEA, NaGly, AMP, and DBU on the carbon mineralization of CaO, CaSiO<sub>3</sub>, and MgO, thermodynamic analyses are performed to investigate the effect of pH, solvent concentrations, and temperature on the concentrations of dissolved inorganic carbon needed to produce solid carbonates. Experimental investigations are aimed at determining the effectiveness of solvents in aiding carbon mineralization at a consistent set of experimental conditions. CO<sub>2</sub> capture mechanisms are inferred from FT-IR analyses of the solid and the liquid samples. The carbonate phases formed are determined using X-Ray Diffraction measurements.

#### **8.3.1 Effect of the solvent concentration on carbon mineralization**

While the thermodynamic studies provide insights into the effects of solvent concentration and temperature on pH and inorganic, organic, and total carbon, and provide insights into feasibility bounds, detailed experimental studies shed light into unanticipated phenomena arising from fluid-particle interactions in integrated CO<sub>2</sub> capture and carbon mineralization pathways. In

this study, we investigate the influence of 0 mol/L, 0.5 eq mol/L, 1.0 eq mol/L, and 2.5 eq mol/L of MEA, NaGly, AMP, and DBU on the carbon mineralization behavior of CaO, CaSiO<sub>3</sub>, and MgO at 75°C in 15 wt% solid for a reaction time of 3 hours (**Figure 8.3**). These experimental conditions are based on prior work demonstrating that high extents of carbon mineralization are achieved at 75°C, pCO<sub>2</sub> of 1 atm in 15 wt% solid for a reaction time of 3 hours. These experiments are performed in a CO<sub>2</sub> - aqueous solvent – alkaline solid environment where CO<sub>2</sub> is captured and converted into calcium or magnesium carbonates with the inherent regeneration of the solvent. The extents of carbon mineralization achieved are noted in **Table 8.3**.

Variations in the reactivities of CaO, CaSiO<sub>3</sub>, and MgO in various solvents such as MEA, sodium glycinate, AMP, and DMP are noted. Near complete conversion of CaO was noted in MEA at concentrations of 1 M or higher. The reactivity of MEA was followed by sodium glycinate, AMP, and DBU. Of the three alkaline materials studied, calcium oxide dissolves readily to release calcium into the solution phase. The limiting factor in this case is the availability of CO<sub>2</sub>. The fast kinetics of CO<sub>2</sub> capture with MEA favor carbon mineralization, particularly with highly reactive alkaline materials. Further, CO<sub>2</sub> capture via the formation of carbamate species in the case of MEA is effective in integrated CO<sub>2</sub> capture and carbonate formation systems with reactive alkaline materials such as CaO.

Comparing with CaO, lower reactivity of CaSiO<sub>3</sub> to produce the respective solid carbonates at the same experimental conditions is noted. Lower dissolution rates of calcium silicate and the presence of passivating silica interfaces are known to be factors limiting carbon mineralization behavior. The extent of carbon mineralization of CaSiO<sub>3</sub> increases with the concentration of MEA and sodium glycinate, with conversions of about 31% and 36% achieved at 1.0 eq mol/L and 2.5 eq mol/L, respectively. In contrast, the extent of carbon mineralization of CaSiO<sub>3</sub> with AMP is

43.4% and 21.7% at 1 eq mol/L and 2.5 eq mol/L of AMP, respectively. A similar trend is noted with DBU in which extents of carbon mineralization of 26.7% and 10.3% are noted at 1 eq mol/L and 2.5 eq mol/L, respectively. The fluids obtained after reactions occurred in 2.5 eq mol/L of AMP and DBU were more viscous and nearly gel-like. The higher viscosity and gel-like states of the fluidic environment impose transport limitations on carbon mineralization behavior. This gel-like formation is prominent in carbon mineralization pathways involving calcium silicate.

It was interesting to note that the highest conversion of  $\text{CaSiO}_3$  is achieved with AMP at a concentration of 1 eq mol/L. Because MEA and AMP are both primary amines, the  $\text{CO}_2$  capture mechanisms occur through the formation of carbamates. However, AMP is a more sterically hindered amine than MEA as shown in **Table 8.1**. This sterically hindered AMP structure facilitates easier dissociation of carbamate to enhance the availability of carbonate species. Thus, at lower concentrations, AMP exhibits higher reactivity for carbon mineralization compared to MEA.

Comparing with  $\text{CaSiO}_3$ , the reactivity of MgO for carbon mineralization was higher but lower than CaO. Sodium glycinate resulted in higher extents of carbon mineralization followed by MEA, DBU, and AMP. The highest extent of carbon mineralization achieved with MgO is 87.5% with 1 M sodium glycinate at 75°C. Higher reactivity of MgO with sodium glycinate is noted at 75°C compared to when MEA is used. This significant difference in reactivity is attributed to the higher concentrations of dissolved inorganic and organic carbon constituents with sodium glycinate compared to with MEA at 75°C, as shown in **Figure 8.2 (a-1)** and **Figure 8.2 (b-1)**. The reactivity of sodium glycinate is followed by MEA, DBU, and AMP. It was interesting to note that MgO conversions to magnesium carbonate are lower at 2.5 eq mol/L compared to at 1 eq mol/L with sodium glycinate, DBU, and AMP. At these high concentrations of sodium glycinate, DBU,

and AMP at 2.5 eq mol/L, the solution has a higher viscosity and is gel-like. However, this gel-like behavior is not observed with MEA at 2.5 eq mol/L and an increase in carbon mineralization extents with MEA concentrations is noted, unlike with the other solvents.

To determine if the solvents are regenerated after carbonate formation, the species present in the aqueous phase are determined before and after the reaction using ATR-FTIR analyses. In the case of MEA, a decrease in the concentration of  $\text{MEA}^{\text{H}^+}$  corresponds to the regeneration of the MEA solvent after carbon mineralization. Thus, the changes in the peak at  $1642\text{ cm}^{-1}$  which corresponds to the  $\text{MEA}^{\text{H}^+}$  species are tracked to determine MEA regeneration (**Figure 8.4**) (Ji et al., 2018). After integrated  $\text{CO}_2$  capture and carbonate formation, the  $\text{MEA}^{\text{H}^+}$  peak at  $1642\text{ cm}^{-1}$  is significantly diminished. The regeneration of sodium glycinate is indicated by the decrease in the intensity of the  $\text{NH}_2\text{COO}^-$  peak at  $1545\text{ cm}^{-1}$  (**Figure 8.5**) (Milella & Mazzotti, 2019; Pretsch et al., 2009). The increase in the peak intensity of  $\text{NH}_2\text{COO}^-$  for the CaO case at 2.5 eq mol/L is due to the excess concentration of the solvent as nearly complete carbon mineralization is achieved in this case (**Figure 8.4 (a)**). The changes of the intensity of the peaks in the  $\text{CaSiO}_3$  case with 0.5, 1.0, and 2.5 eq mol/L concentration are not obvious in **Figure 8.5 (b)**. This is due to the lower reactivity of  $\text{CaSiO}_3$ . The high peak intensity of  $\text{NH}_2\text{COO}^-$  for MgO at 2.5 eq mol/L in sodium glycinate (**Figure 8.7 (c)**) and for  $\text{CaSiO}_3$  at 2.5 eq mol/L in AMP (**Figure 8.6 (b)**) is due to the formation of gels that limit carbon mineralization behavior. Different from the spectra of the  $\text{CaSiO}_3$  and MgO in the AMP cases (**Figure 8.6 (b)** and **Figure 8.6 (c)**, respectively), the spectra of the CaO in the AMP in **Figure 8.6 (a)** change significantly in different concentration due to the increasing carbonation. The decrease in the intensity of the bicarbonate peaks in the fluids obtained after carbon mineralization in DBU suggests that bicarbonate species are consumed during the reaction (**Figure 8.7**).

### 8.3.2 Compositions of the Carbonate-Bearing Products

To determine the compositions of the products obtained after integrated CO<sub>2</sub> capture and carbon mineralization, ATR FT-IR, and X-Ray Diffraction (XRD) analyses were performed. The hypothesis that metastable carbonate phases such as vaterite (CaCO<sub>3</sub>), aragonite (CaCO<sub>3</sub>), nesquehonite (MgCO<sub>3</sub>·3H<sub>2</sub>O), lansfordite (MgCO<sub>3</sub>·5H<sub>2</sub>O), and hydromagnesite (Mg<sub>5</sub>(CO<sub>3</sub>)<sub>4</sub>(OH)<sub>2</sub>·4H<sub>2</sub>O) may be co-present with stable phases such as calcite (CaCO<sub>3</sub>) and magnesite (MgCO<sub>3</sub>) are evaluated by characterizing the products. This hypothesis is based on prior evidence that temperature, reaction time, solvent concentration could influence the composition of the products. (Arti et al., 2017; Lackner et al., 2014; Sivanesan et al., 2017) The carbonate-bearing products obtained after reacting in concentrations of 0.5 eq mol/L, 1.0 eq mol/L, and 2.5 eq mol/L MEA, NaGly, AMP, and DBU are characterized to determine the compositions. The formation of carbonates is evident from the evolution of the C-O bond in the reacted CaO and CaSiO<sub>3</sub> materials (**Figures 8.8 and Figure 8.9**) (Al-Hosney & Grassian, 2005; Böke et al., 2004; Plav et al., 1999). The presence of Si-O-Si and Si-O phases in the recovered materials shows that siliceous phases are co-present with the carbonates (**Figure 8.9**) (Basavaraj et al., 2019; Thompson et al., 2012). The presence of lansfordite (MgCO<sub>3</sub>·5H<sub>2</sub>O) and nesquehonite (MgCO<sub>3</sub>·3H<sub>2</sub>O) phases are evident in the reacted MgO materials (**Figure 8.10**).

Metastable phases such as aragonite (spiky/orthorhombic) and vaterite (plate-like/hexagonal) and stable phases such as calcite (rhombohedral) are present in the products obtained after the carbon mineralization of CaO and CaSiO<sub>3</sub> (**Figures 8.11 and Figure 8.12**) (Chessin et al., 1965; Negro & Ungaretti, 1971; Maslen et al., 1993; Müller, 2010; Wang & Becker, 2009). In the case of CaO reacted in the presence of MEA, calcite is the dominant phase at lower concentrations. At higher MEA concentrations, vaterite emerges as the dominant phase (**Figure**

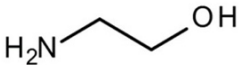
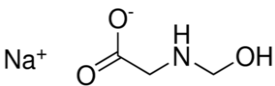
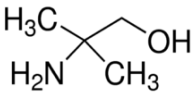
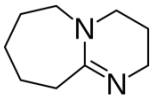
**8.11).** Unlike CaO, CaSiO<sub>3</sub> has a much lower extent of carbon mineralization. Wollastonite is the dominant phase in every case due to low carbonate conversion (**Figure 8.12**) Calcite and vaterite are the dominant phases, while aragonite is the minor phase. The carbon mineralization of MgO in various solvents results in the formation of various metastable phases such as nesquehonite (MgCO<sub>3</sub>·3H<sub>2</sub>O), lansfordite (MgCO<sub>3</sub>·5H<sub>2</sub>O), and hydromagnesite (Mg<sub>5</sub>(CO<sub>3</sub>)<sub>4</sub>(OH)<sub>2</sub>·4H<sub>2</sub>O) (**Figure 8.13**) (Ballirano et al., 2013; Davies & Bubela, 1973; Hopkinson et al., 2008, 2012; Ming & Franklin, 2010; Morgan et al., 2015; Wang et al., 2020).

#### **8.4 Conclusion**

In this study, we investigate the single-step integrated CO<sub>2</sub> capture and carbon mineralization of CaO, CaSiO<sub>3</sub>, and MgO with the inherent regeneration of solvents such as MEA, sodium glycinate, AMP, and DBU at concentrations of 0 eq mol/L, 0.5 eq mol/L, 1.0 eq mol/L, and 2.5 eq mol/L at 75 °C and with a reaction time of 3 hr with a 15 wt% solid ratio and at a 300 rpm stirring rate. The highest extents of carbon mineralization of CaO, CaSiO<sub>3</sub>, and MgO are 98.9% at 30 wt% MEA, 43.40% at 2 M AMP, and 87.50% at 1 M sodium glycinate. The factors that could potentially limit carbon mineralization are the formation of highly viscous, gel-like fluidic environment that limit mass transfer, low dissolution rates and presence of silica passivation layers as in the case of calcium silicate. These data show that these regenerable solvents undergo multiple CO<sub>2</sub> capture and release cycles into the aqueous phase, thus providing a steady source of bicarbonate or carbonate species needed to achieve high extents of carbon mineralization. The formation of stable and metastable calcium carbonate phases is evident when CaO and CaSiO<sub>3</sub> are the reactants. Metastable magnesium carbonate phases are present in the reacted MgO materials. In addition to the effectiveness of the CO<sub>2</sub> capture solvent in aiding carbon mineralization behavior, the environmental benign attributes of the solvent need to be considered. In this context,

sodium glycinate, an environmentally benign and less corrosive amino acid solvent was found to be effective in aiding carbon mineralization.

**Table 8.1** Physical and chemical properties of the solvents used for integrated CO<sub>2</sub> capture and carbon mineralization.

Chemical	Abbr.	Structure	Molar Weight g/mol	Density g/cm <sup>3</sup>	Boiling Point °C	Melting Point °C	pKa	Reference
Monoethanolamine	MEA		61.08	1.012	170	10.3	9.5	(Ji et al., 2018)
Sodium Glycinate	NaGly		97.05	-	-	-	-	(Caplow, 1968; Guo et al., 2013; Vaidya et al., 2010)
2-amino-2-methylpropanol	AMP		89.14	0.934	165	30.5	-	(Barzagli et al., 2013; Caplow, 1968; Mandal et al., 2003; Zhang et al., 2008)
1,8-diazabicyclo[5.4.0] undec-7-ene	DBU		152.24	1.02	80	-70	13.5	(Heldebrant et al., 2005; Kaupmees et al., 2014)

**Table 8.2** Summary of the reactions representing CO<sub>2</sub> hydration, CO<sub>2</sub> capture and speciation associated with various solvents including monoethanolamine (MEA), sodium glycinate (NaGly), 2-amino-2-methylpropanol (AMP), and 1,8-diazabicyclo [5.4.0] undec-7-ene (DBU).

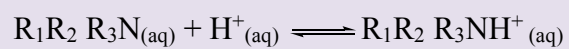
Phenomena	Reactions	Equilibrium constant	Reaction #
Water dissociation	$\text{H}_2\text{O}_{(l)} \rightleftharpoons \text{H}^+_{(aq)} + \text{OH}^-_{(aq)}$	${}^a\text{K}_w = 10^{-13.997}$	1
CO <sub>2</sub> hydration	$\text{CO}_{2(g)} + \text{H}_2\text{O}_{(l)} \rightleftharpoons \text{H}_2\text{CO}_3^*_{(aq)}$	$\text{K}_h = 10^{-1.46}$	2
	$\text{H}_2\text{CO}_3^*_{(aq)} \rightleftharpoons \text{HCO}_3^-_{(aq)} + \text{H}^+_{(aq)}$	${}^a\text{K}_{a1} = 10^{-6.33}$	3
	$\text{HCO}_3^-_{(aq)} \rightleftharpoons \text{CO}_3^{2-}_{(aq)} + \text{H}^+_{(aq)}$	${}^a\text{K}_{a2} = 10^{-10.33}$	4
CO <sub>2</sub> capture and speciation in MEA	$\text{MEA}\text{H}^+_{(aq)} \rightleftharpoons \text{MEA} + \text{H}^+_{(aq)}$	$\text{K}_5 = 10^{-9.44}$	5
	$\text{MEA} + \text{HCO}_3^-_{(aq)} \rightleftharpoons \text{MEACOO}^-_{(aq)} + \text{H}_2\text{O}_{(l)}$	$\text{K}_6 = 10^{1.76}$	6
CO <sub>2</sub> capture and speciation in NaGly	$\text{H}_3\text{N}^+\text{CH}_2\text{COOH}_{(aq)} \rightleftharpoons \text{H}_3\text{N}^+\text{CH}_2\text{COO}^-_{(aq)} + \text{H}^+_{(aq)}$	${}^a\text{K}_{b1} = 10^{-2.34}$	7
	$\text{H}_3\text{N}^+\text{CH}_2\text{COO}^-_{(aq)} \rightleftharpoons \text{H}_2\text{NCH}_2\text{COO}^-_{(aq)} + \text{H}^+_{(aq)}$	${}^a\text{K}_{b2} = 10^{-9.60}$	8
	$\text{H}_2\text{NCH}_2\text{COO}^-_{(aq)} + \text{CO}_{2(aq)} \rightleftharpoons \text{H}_2\text{NCH}_2\text{COO}^-_{(aq)} + \text{H}^+_{(aq)}$	${}^a\text{K}_{\text{Gly}1} = 10^{-4.63}$	9
	$\text{H}_2\text{NCH}_2\text{COO}^-_{(aq)} + \text{CO}_{2(aq)} \rightleftharpoons \text{H}_2\text{NCH}_2\text{COO}^-_{(aq)} + \text{H}^+_{(aq)}$		
	$\text{H}_2\text{NCH}_2\text{COO}^-_{(aq)} + \text{H}^+_{(aq)} \rightleftharpoons \text{H}_3\text{N}^+\text{CH}_2\text{COO}^-_{(aq)}$		
	$\text{H}_2\text{NCH}_2\text{COO}^-_{(aq)} + \text{H}_2\text{O}_{(l)} \rightleftharpoons \text{H}_2\text{NCH}_2\text{COO}^-_{(aq)} + \text{H}^+_{(aq)}$	/	10

	$H_2NCH_2COO^-_{(aq)} + HCO_3^-_{(aq)}$		
CO <sub>2</sub> capture and speciation in AMP	$AMPH^+_{(aq)} \rightleftharpoons AMP + H^+_{(aq)}$	$K_5 = 10^{-9.88}$	11
	$AMP + HCO_3^-_{(aq)} \rightleftharpoons$	$K_6 = 10^{-1.319}$	12
	$AMPCOO^-_{(aq)} + H_2O_{(l)}$		
CO <sub>2</sub> capture and speciation in DBU	$DBUH^+_{(aq)} \rightleftharpoons DBU + H^+_{(aq)}$	$K_5 = 10^{-13.5}$	13
	$DBU + CO_2 + H_2O_{(l)} \rightleftharpoons$	/	14
	$DBUH^+_{(aq)} + HCO_3^-_{(aq)}$		
Cation recovery from Ca- and Mg-bearing solids	$CaO_{(s)} + H_2O_{(l)} \rightleftharpoons Ca(OH)_2_{(aq)} \rightleftharpoons$		
	$Ca^{2+}_{(aq)} + 2 OH^-_{(aq)}$		
	$CaSiO_3_{(s)} + H_2O_{(l)} \rightleftharpoons$		
	$Ca(OH)_2_{(aq)} + SiO_2_{(s)} \rightleftharpoons$		15
	$Ca^{2+}_{(aq)} + 2 OH^-_{(aq)} + SiO_2_{(s)}$		
Carbonate formation	$MgO_{(s)} + H_2O_{(l)} \rightleftharpoons Mg(OH)_2_{(aq)} \rightleftharpoons$		
	$Mg^{2+}_{(aq)} + 2 OH^-_{(aq)}$		
	$Ca^{2+}_{(aq)} + CO_3^{2-}_{(aq)} \rightleftharpoons CaCO_3_{(s)}$		16
Bicarbonate formation in amines that proceed via carbamate formation	$Mg^{2+}_{(aq)} + CO_3^{2-}_{(aq)} \rightleftharpoons MgCO_3_{(s)}$		
	$R_1R_2NH_{(aq)} + CO_2_{(aq)} \rightleftharpoons R_1R_2NH^+COO^-_{(aq)}$		
	$R_1R_2NH^+COO^-_{(aq)} + R_1R_2NH_{(aq)} \rightleftharpoons$		
	$R_1R_2NCOO^-_{(aq)} + R_1R_2NH_2^+_{(aq)}$		17
	$R_1R_2NCOO^-_{(aq)} + H_2O_{(l)} \rightleftharpoons$		
	$R_1R_2NH_{(aq)} + HCO_3^-_{(aq)}$		

Bicarbonate

formation in tertiary

amines



18

**Table 8.3** Summary of extents of carbonation of CaO, CaSiO<sub>3</sub>, and MgO at 75°C, CO<sub>2</sub> partial pressure of 1 atm, reaction time of 3 hours, 15 wt% solid, and a stirring rate of 300 rpm. The carbonate content used to obtain the extent of carbon mineralization is based on Thermogravimetric Analysis (TGA).

Minerals	Solvents	Concentration	Extent of Carbonation (%)	Std. Dev. (%)
CaO	H <sub>2</sub> O	/	42.6	1.3
	MEA	1 M	58.7	2.3
		2 M	98.6	0.4
		5 M	98.9	0.7
	NaGly	0.5 M	68.4	4.6
		1 M	94.2	2.5
		2.5 M	92.1	2.8
	AMP	1 M	73.0	1.5
		2 M	85.4	4.5
		5 M	93.1	2.1
	DBU	0.5 M	60.5	15.0
		1 M	69.2	9.1
2.5 M		83.4	2.6	
CaSiO <sub>3</sub>	H <sub>2</sub> O	/	16.7	7.7
	MEA	1 M	18.4	0.7
		2 M	31.7	8.3
		5 M	36.0	1.8

	NaGly	0.5 M	14.1	3.5
		1 M	31.0	0.8
		2.5 M	35.9	0.8
	AMP	1 M	23.4	1.1
		2 M	43.4	2.5
		5 M	21.7	4.1
	DBU	0.5 M	17.0	0.7
		1 M	26.7	1.1
		2.5 M	10.3	0.1
MgO	H <sub>2</sub> O	/	34.7	10.3
	MEA	1 M	60.9	2.1
		2 M	61.9	1.1
		5 M	66.6	2.0
	NaGly	0.5 M	66.5	2.4
		1 M	87.5	2.4
		2.5 M	73.7	1.1
	AMP	1 M	53.2	6.9
		2 M	46.6	1.2
		5 M	32.7	0.6
	DBU	0.5 M	55.7	3.90
		1 M	53.9	2.16
2.5 M		39.5	13.75	

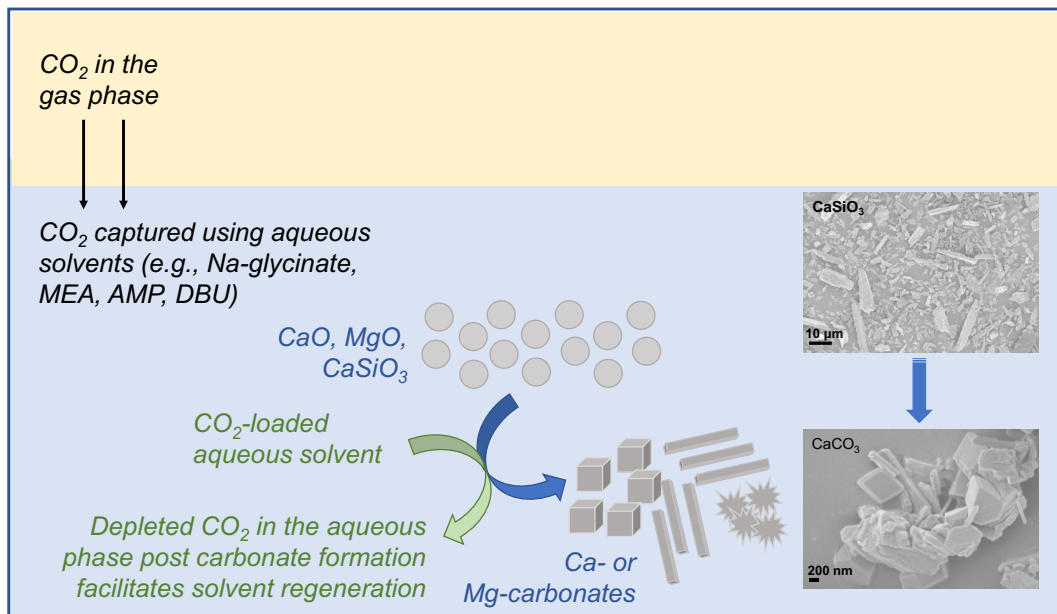


**Figure 8.1** Schematic representation of using regenerable solvents to capture and remove CO<sub>2</sub> via carbon mineralization.

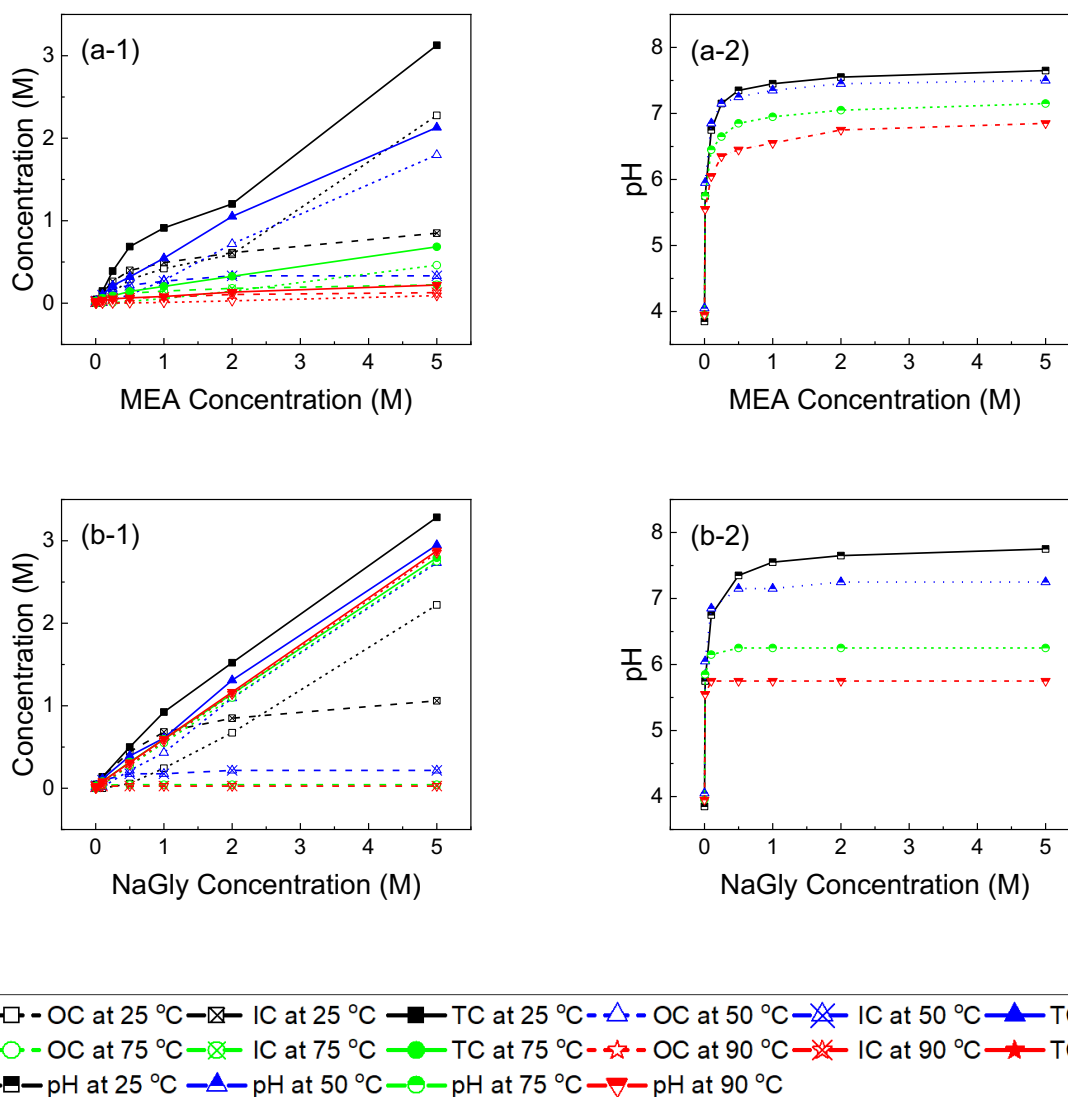


**Figure 8.2** Total carbon (TC), Organic carbon (OC), and Inorganic Carbon (OC) concentrations in the aqueous phase as a function of the concentration of MEA (a-1) and sodium glycinate (b-1) are shown. pH as a function of MEA concentration (a-2) and sodium glycinate concentration (b-2) are also shown.

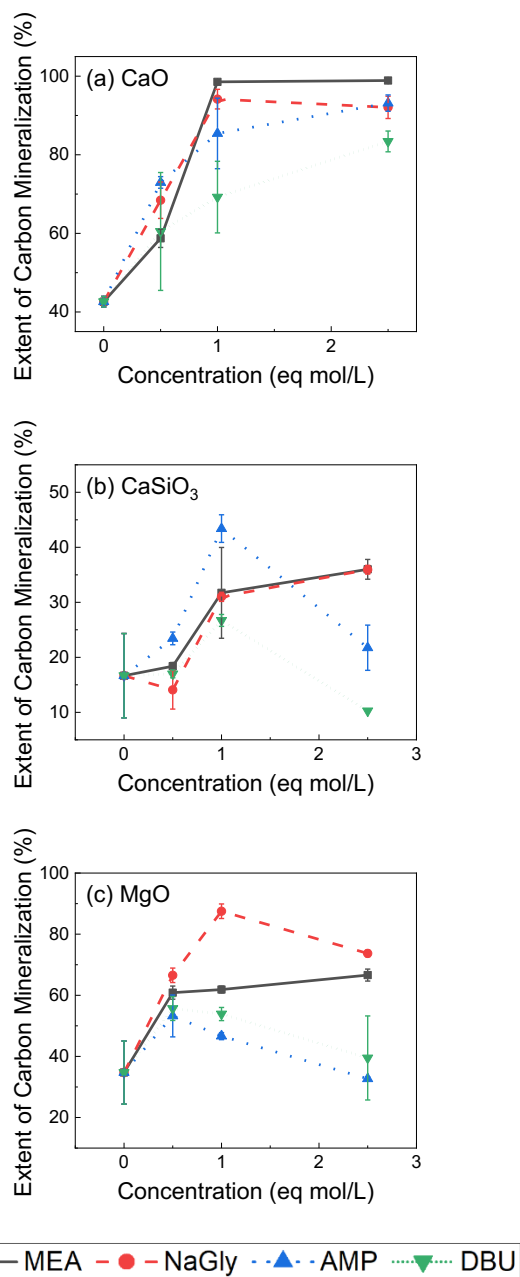


**Figure 8.3** Extent of carbon mineralization of CaO (a), CaSiO<sub>3</sub> (b), and MgO (c) reacted in the presence of 0 eq mol/L, 0.5 eq mol/L, 1.0 eq mol/L, and 2.5 eq mol/L monoethanolamine (MEA, black square), sodium glycinate (NaGly, red circle), 2-amino-2-methylpropanol (AMP, blue upward facing triangle), and 1,8-diazabicyclo [5.4.0] undec-7-ene (DBU, green downfacing triangle). All the experiments are performed at 75 °C, pCO<sub>2</sub> = 1 atm, reaction time of 3 hours and a stirring rate of 300 rpm.

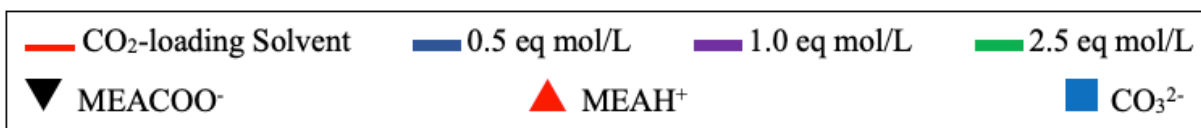
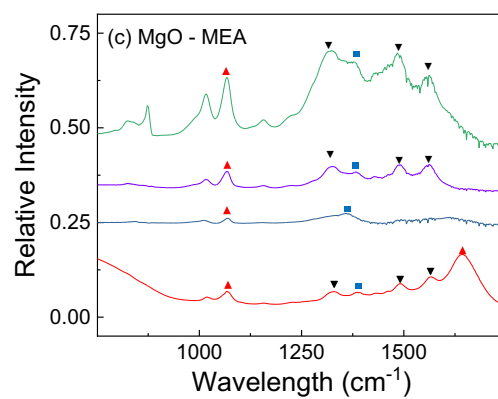
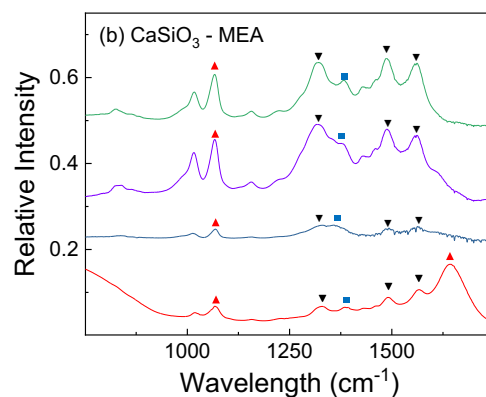
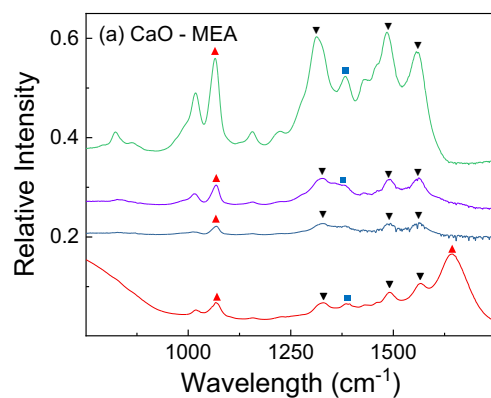


**Figure 8.4** Identification of the species in the aqueous phase obtained after the carbon mineralization of (a) CaO, (b) CaSiO<sub>3</sub>, and (c) MgO reacted in monoethanolamine (MEA) using ATR-FTIR analyses. Species are identified based on spectra reported in reference.

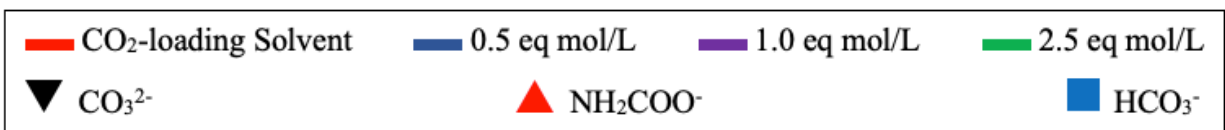
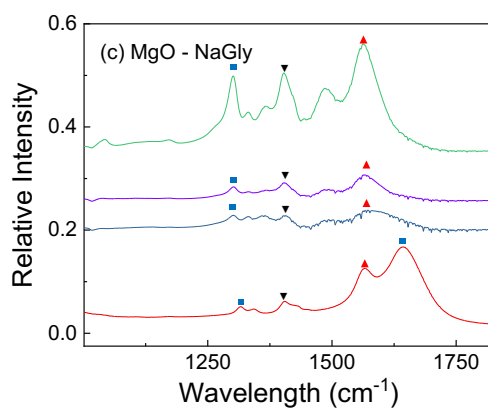
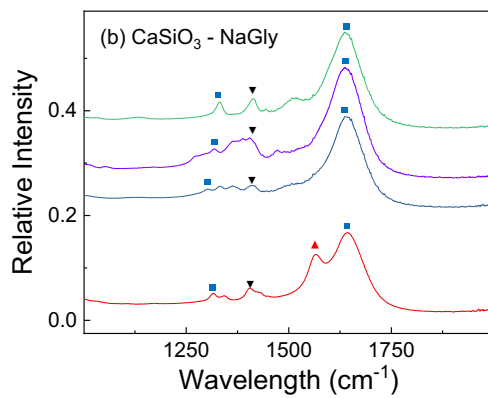
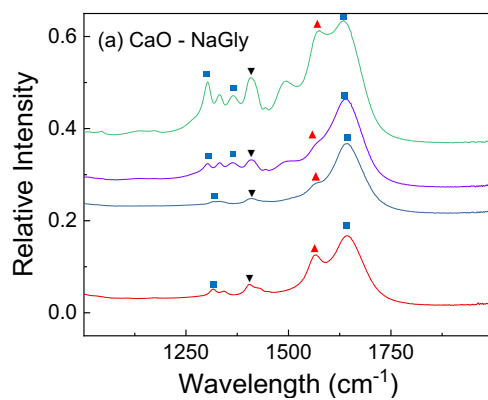


**Figure 8.5** Identification of the species in the aqueous phase obtained after the carbon mineralization of (a) CaO, (b) CaSiO<sub>3</sub>, and (c) MgO reacted in sodium glycinate (NaGly) using ATR-FTIR analyses. Species are identified based on spectra reported in references (Ahmed et al., 2013; Doki et al., 2004; Ramachandran et al., 2007).

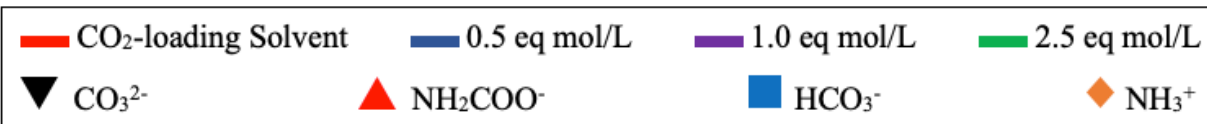
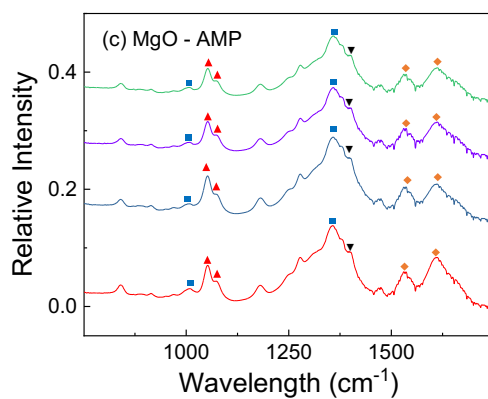
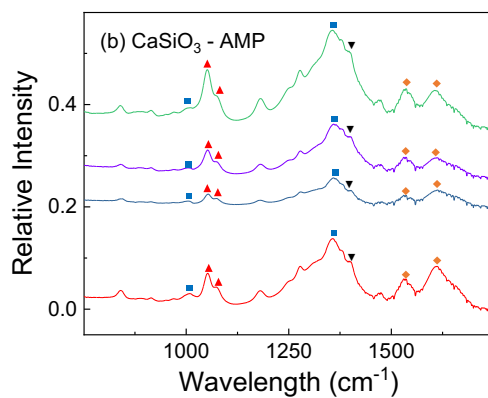
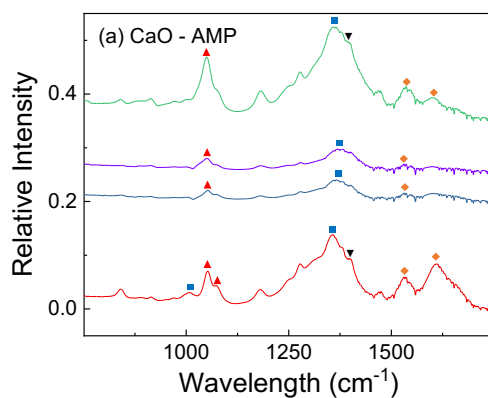


**Figure 8.6** Identification of the species in the aqueous phase obtained after the carbon mineralization of (a) CaO, (b) CaSiO<sub>3</sub>, and (c) MgO reacted in 2-amino-2-methylpropanol (AMP) using ATR-FTIR analyses. Species are identified based on spectra reported in references (Ahmed et al., 2013; Doki et al., 2004; Ramachandran et al., 2007).

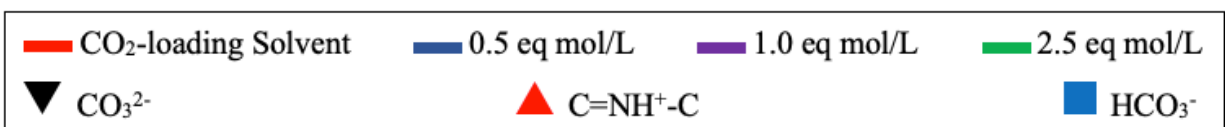
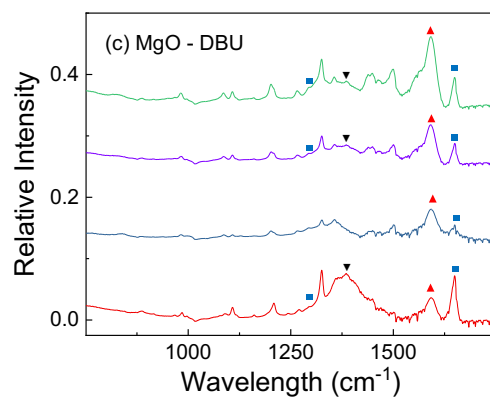
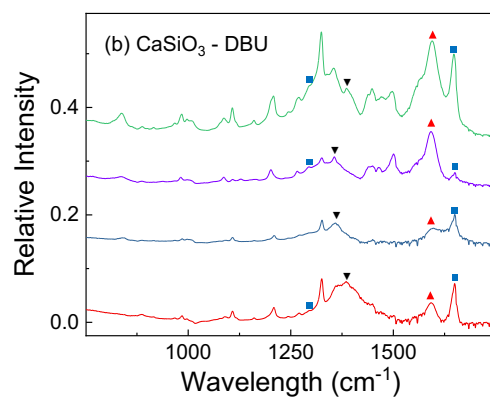
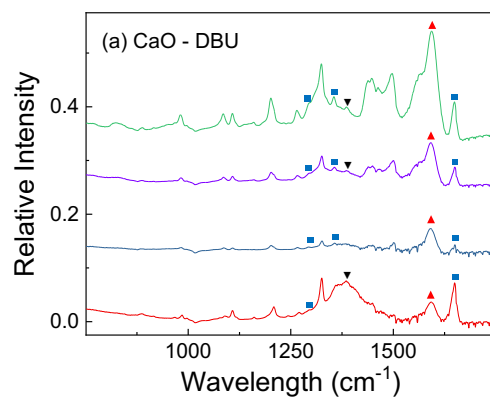


**Figure 8.7** Identification of the species in the aqueous phase obtained after the carbon mineralization of (a) CaO, (b) CaSiO<sub>3</sub>, and (c) MgO reacted in 1,8-diazabicyclo [5.4.0] undec-7-ene (DBU) using ATR-FTIR analyses. Species are identified based on spectra reported in references (Ahmed et al., 2013; Doki et al., 2004; Ramachandran et al., 2007).

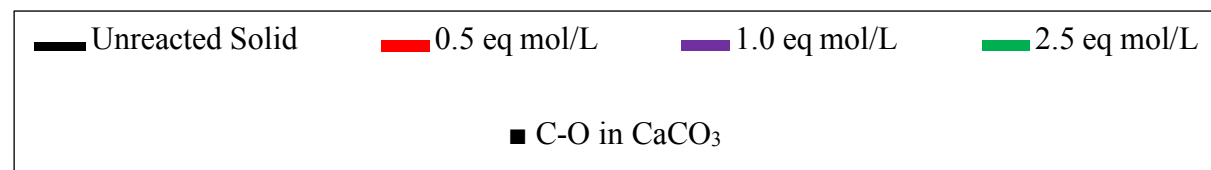
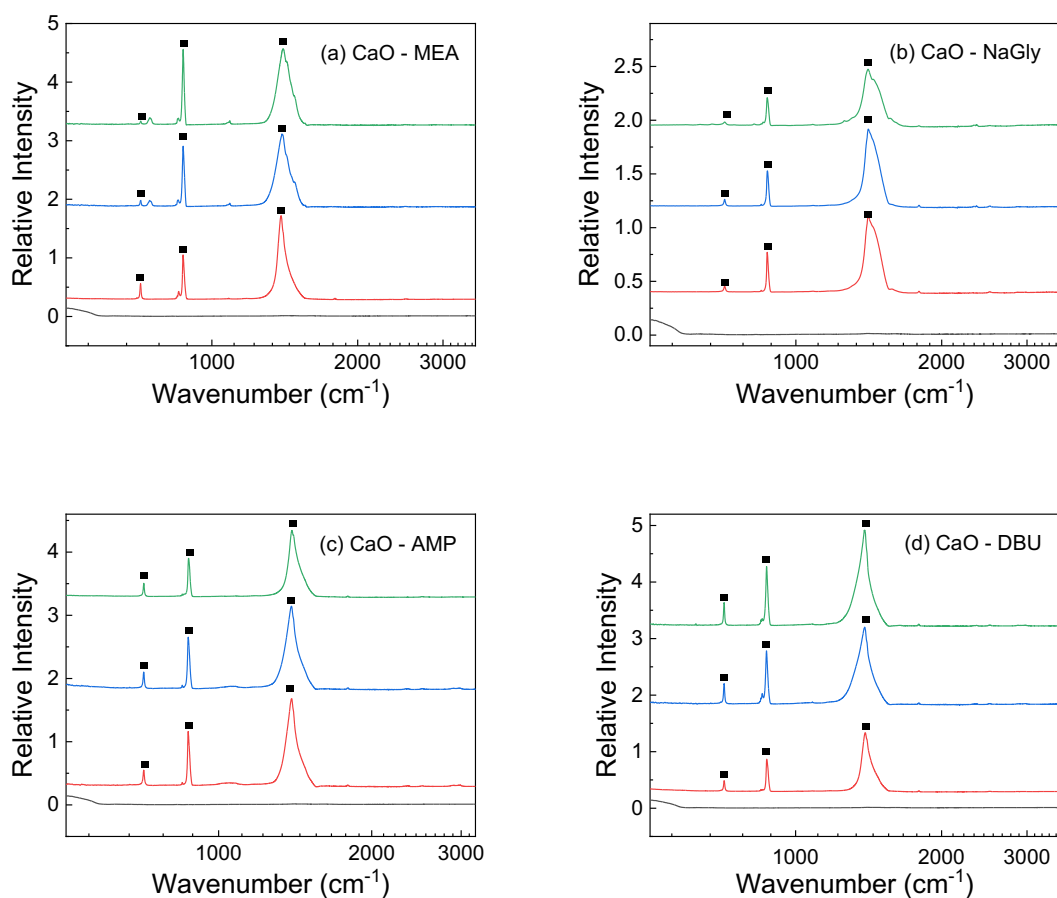


**Figure 8.8** Identification of the species in the solid product obtained after the carbon mineralization of CaO in (a) monoethanolamine (MEA), (b) sodium glycinate (NaGly), (c) 2-amino-2-methylpropanol (AMP), and (d) 1,8-diazabicyclo [5.4.0] undec-7-ene (DBU) using ATR-FTIR analyses. Species are identified based on spectra reported in references (Al-Hosney & Grassian, 2005; Böke et al., 2004; Plav et al., 1999).

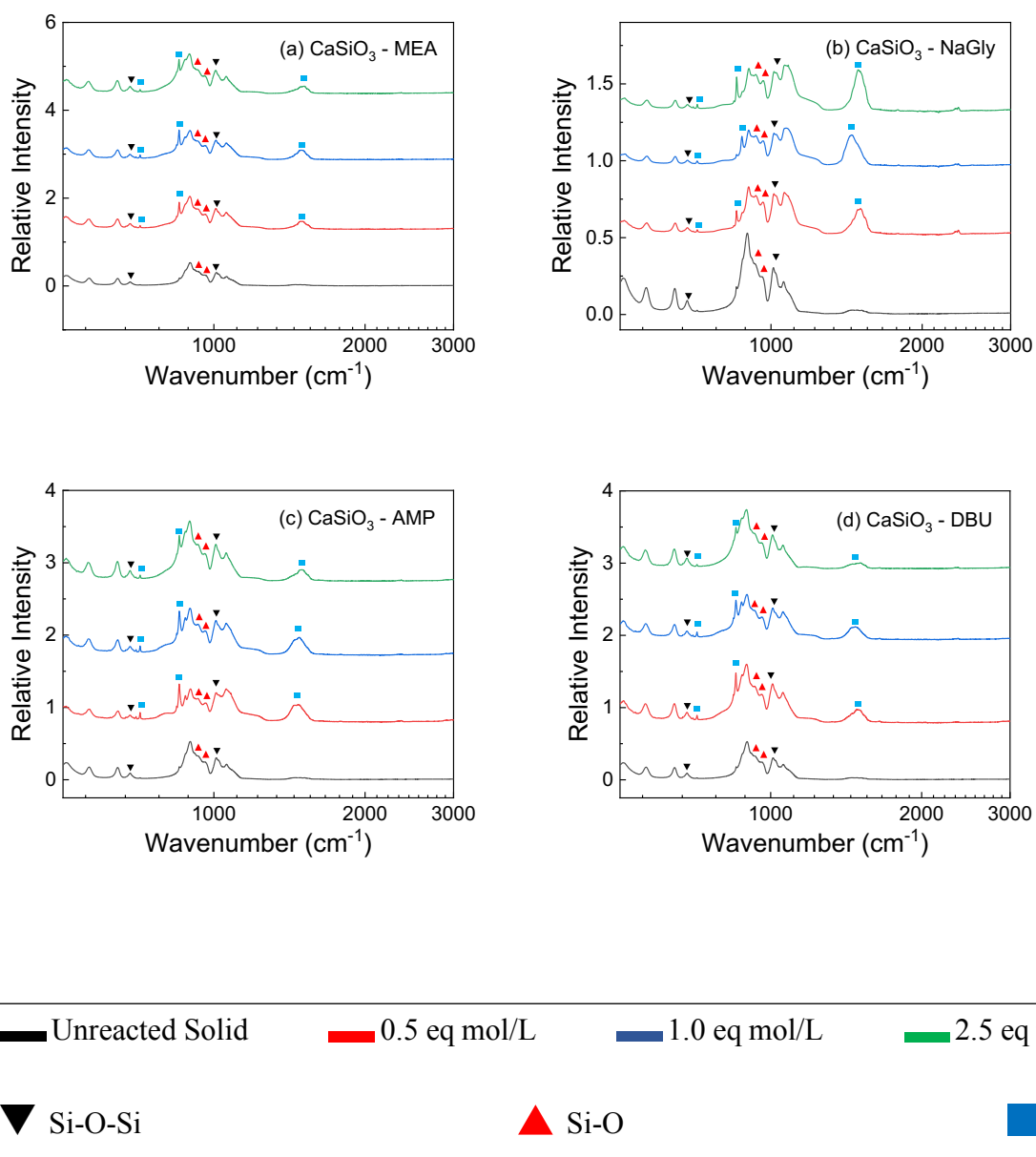


**Figure 8.9** Identification of the species in the solid product obtained after the carbon mineralization of  $\text{CaSiO}_3$  in (a) monoethanolamine (MEA), (b) sodium glycinate (NaGly), (c) 2-amino-2-methylpropanol (AMP), and (d) 1,8-diazabicyclo [5.4.0] undec-7-ene (DBU) using ATR-FTIR analyses. Species are identified based on spectra reported in references (Al-Hosney & Grassian, 2005; Basavaraj et al., 2019; Böke et al., 2004; Plav et al., 1999; Thompson et al., 2012).

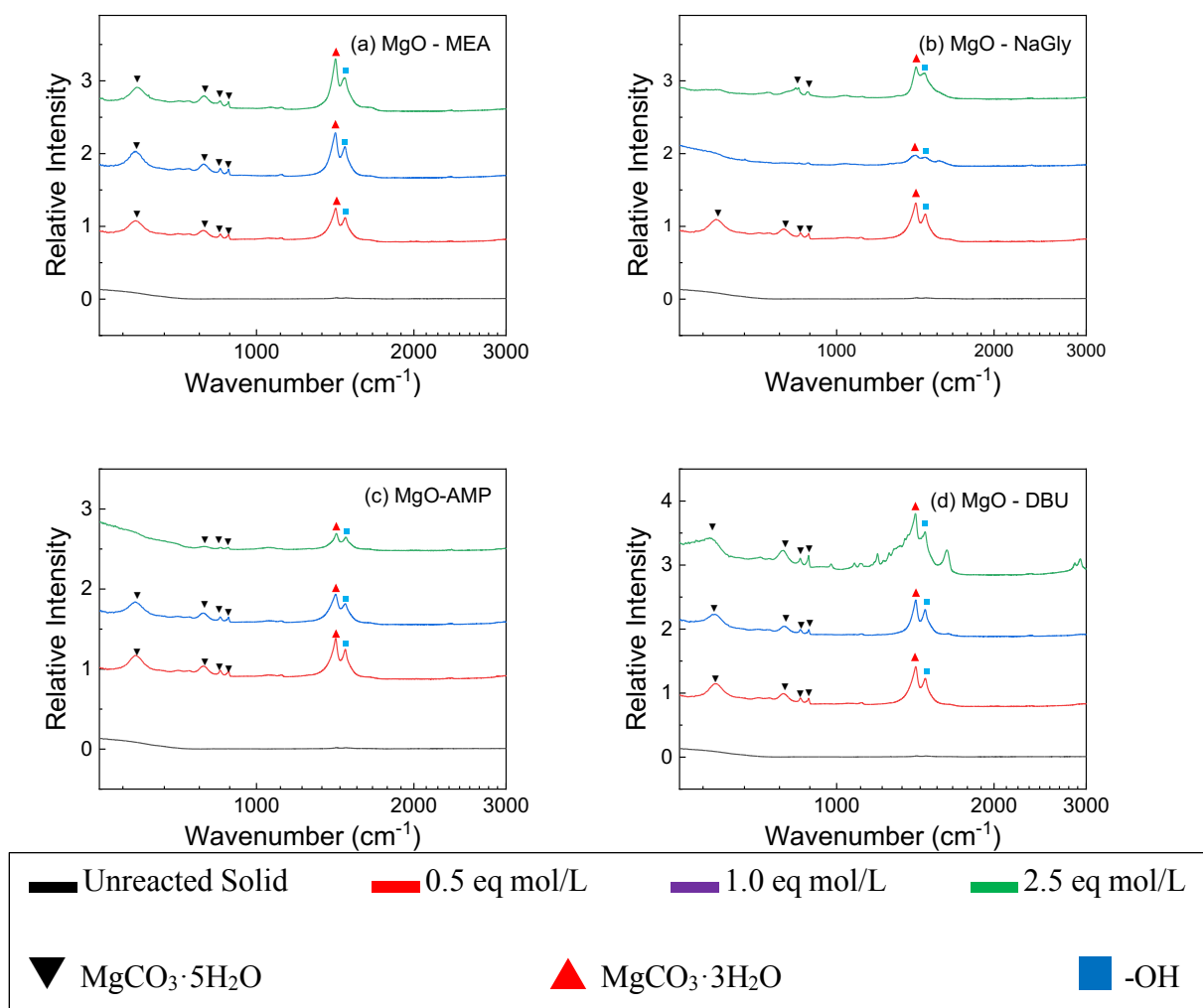


**Figure 8.10** Identification of the species in the solid product obtained after the carbon mineralization of MgO in (a) monoethanolamine (MEA), (b) sodium glycinate (NaGly), (c) 2-amino-2-methylpropanol (AMP), and (d) 1,8-diazabicyclo [5.4.0] undec-7-ene (DBU) using ATR-FTIR analyses. Species are identified based on spectra reported in references (Hopkinson et al., 2012; Morgan et al., 2015).

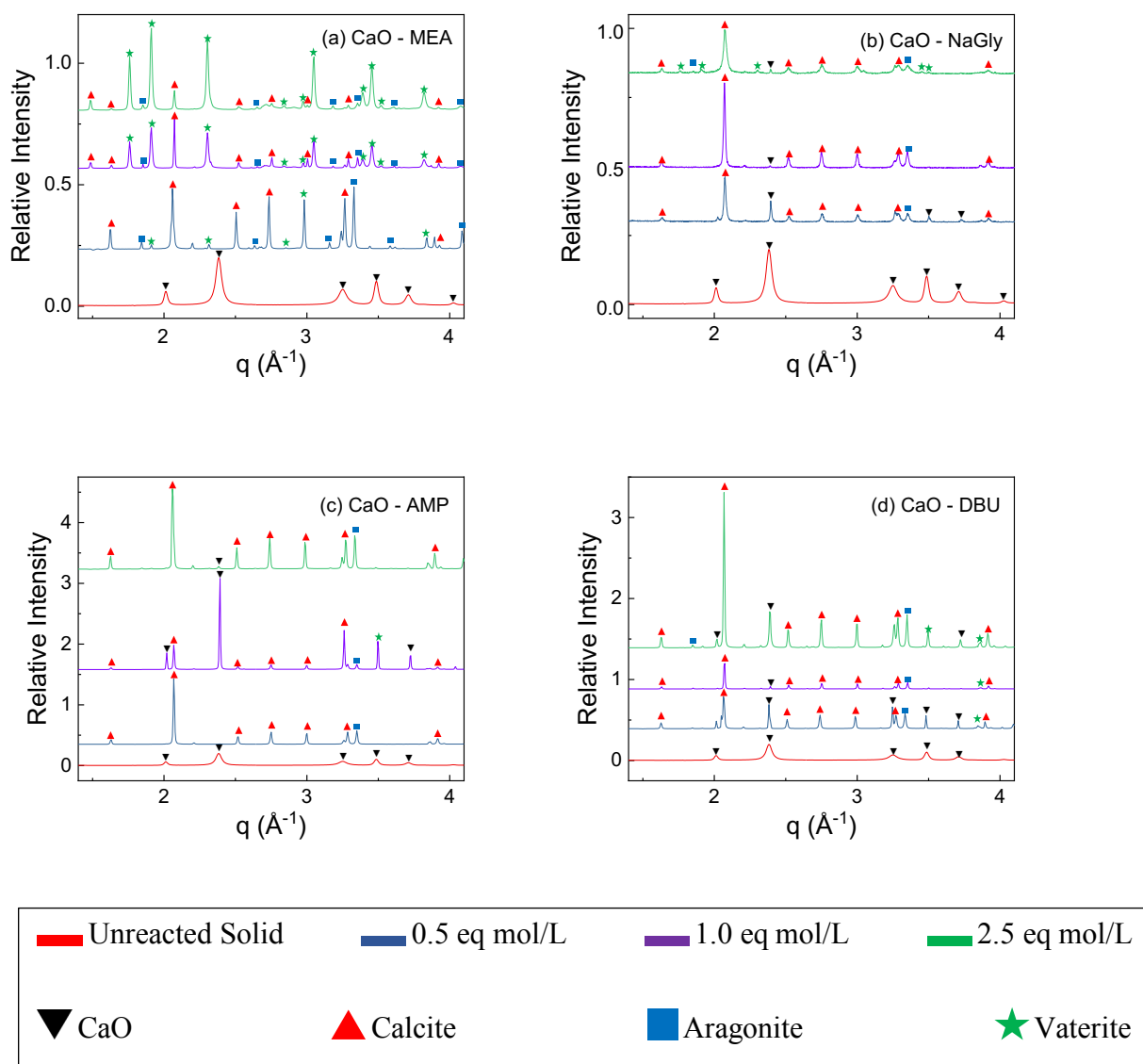


**Figure 8.11** Identification of the crystalline species in the solid product obtained after the carbon mineralization of CaO in (a) monoethanolamine (MEA), (b) sodium glycinate (NaGly), (c) 2-amino-2-methylpropanol (AMP), and (d) 1,8-diazabicyclo [5.4.0] undec-7-ene (DBU) using XRD analyses. Crystallographic phases are identified based on the data presented in references (Chessin et al., 1965; Negro & Ungaretti, 1971; Maslen et al., 1993; Müller, 2010; Petch, 1961; Primak et al., 1948; Wang & Becker, 2009).

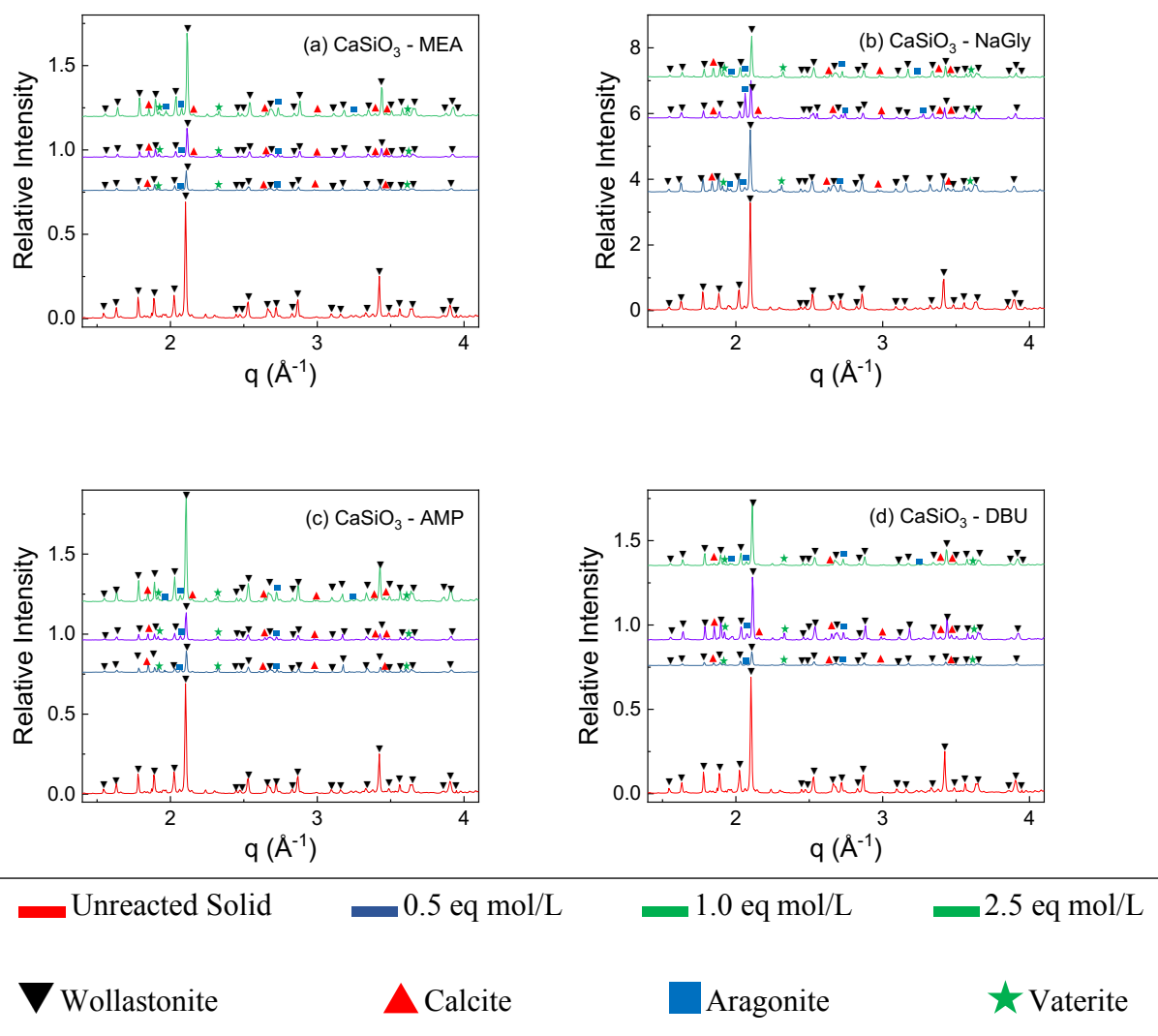


**Figure 8.12** Identification of the crystalline species in the solid product obtained after the carbon mineralization of  $\text{CaSiO}_3$  in (a) monoethanolamine (MEA), (b) sodium glycinate (NaGly), (c) 2-amino-2-methylpropanol (AMP), and (d) 1,8-diazabicyclo [5.4.0] undec-7-ene (DBU) using XRD analyses. Crystallographic phases are identified based on the data presented in references (Chessin et al., 1965; Negro & Ungaretti, 1971; Maslen et al., 1993; Müller, 2010; Petch, 1961a; Primak et al., 1948; Wang & Becker, 2009)].

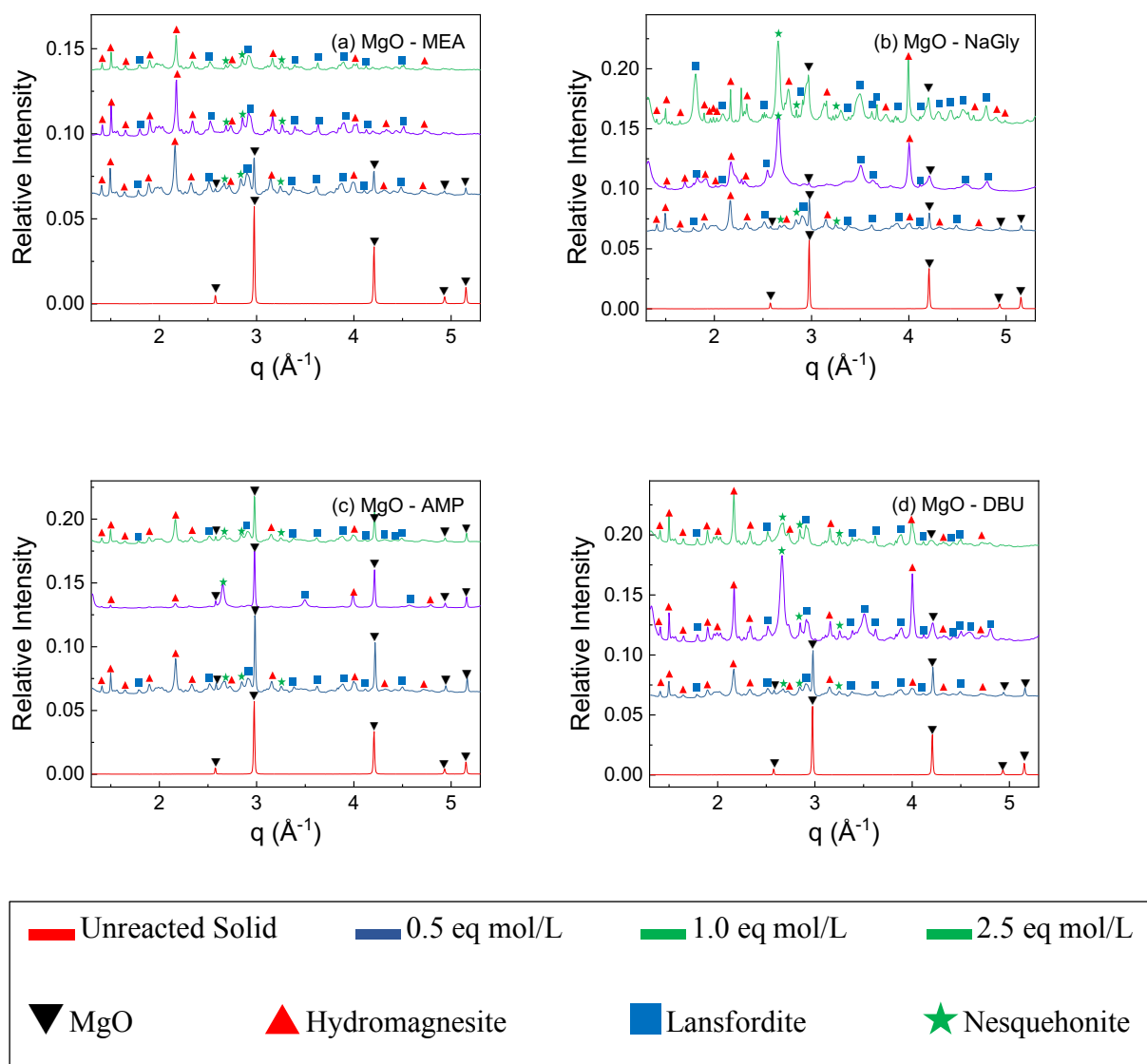


**Figure 8.13** Identification of the crystalline species in the solid product obtained after the carbon mineralization of MgO in (a) monoethanolamine (MEA), (b) sodium glycinate (NaGly), (c) 2-amino-2-methylpropanol (AMP), and (d) 1,8-diazabicyclo [5.4.0] undec-7-ene (DBU) using XRD analyses. Crystallographic phases are identified based on the data presented in references (Ballirano et al., 2013; Davies & Bubela, 1973; Ming & Franklin, 2010; Wang et al., 2020).

## CHAPTER 9

### CONCLUSION AND FUTURE WORK

#### 9.1 Conclusion

The studies reported in this thesis demonstrate that integrated reactive CO<sub>2</sub> capture and carbon mineralization pathways can be designed to harness CO<sub>2</sub> in flue gas streams with fewer unit operations, enhance the solubility of CO<sub>2</sub> to increase the supply of carbonate and bicarbonate ions available for mineralization, and facilitate the chemical regeneration of the solvents as carbonates are formed. This approach provides an alternative to the thermal regeneration of solvents which occurs as 80-150°C as opposed to chemical solvent regeneration at 50-75°C. Further, *in-operando* X-ray scattering (e.g., Ultra Small, Small and Wide Angle X-Ray Scattering, USAXS, SAXS, WAXS; X-Ray Reflectivity, XRR; Grazing Incidence – Small Angle X-Ray Scattering, GI-SAXS) and spectroscopic (Attenuated Total Reflectance – Fourier Transform Infrared Spectroscopy, ATR FT-IR) measurements provide mechanistic insights into carbon mineralization.

The feasibility of operating these reaction pathways in different modes: single step CO<sub>2</sub>-solvent-alkaline solids and two step modes with CO<sub>2</sub>-solvent and CO<sub>2</sub>-loaded solvent-alkaline solid interactions is demonstrated experimentally using CaO and CaSiO<sub>3</sub> as alkaline solids and monoethanolamine as the solvent for CO<sub>2</sub> capture. Near complete conversions of CaO and about 35% conversion of CaSiO<sub>3</sub> at 50°C with 30 wt% MEA, a reaction time of 3 hours, and in well-mixed environments in single step gas-liquid-solid and two step gas-liquid and liquid-solid configurations demonstrate the effectiveness of reactive CO<sub>2</sub> capture and carbon mineralization

approaches. The effectiveness of mineralizing MgO using reactive CO<sub>2</sub> capture and carbon mineralization with regenerable solvents is demonstrated.

As an alternative to MEA which can be corrosive at high concentrations, environmentally benign amino acid salts such as sodium glycinate with similar CO<sub>2</sub> capture capacities as MEA were shown to be effective in aiding the mineralization of CaO and CaSiO<sub>3</sub>. Evaluation of the effectiveness of various CO<sub>2</sub> capture solvents such as MEA, Na-glycinate, AMP, and DBU demonstrated that high extents of carbon mineralization were achieved with MEA and Na-glycinate at higher concentrations. However, the formation of gel-like phases with AMP and DBU at higher concentrations impacted carbon mineralization conversion. Further, the mechanisms of CO<sub>2</sub> capture in primary, tertiary, and cyclical amines, and amino acid salts differ. For example, amino acid salts such as sodium glycinate and tertiary and cyclical amines such as AMP and DBU proceed via the formation of bicarbonate and carbonate species. MEA, in contrast, proceeds via the formation of carbamate species.

The potential for increasing the reactive resources available for carbon mineralization are explored by heat treating serpentine, a hydrated magnesium silicate mineral. Reactive, high reactive magnesium silicates by heat treating serpentine have faster kinetics of carbon mineralization. The structural and the microstructural features of serpentine as it is heated are elucidated using USAXS/SAXS/WAXS measurements in conjunction with pore size distributions.

These results are transformative for several reasons. First, integrating carbon mineralization with CO<sub>2</sub> capture enables accelerated carbon mineralization and facilitates the chemical regeneration of the solvents at 50-75°C, which is lower than the thermal regeneration of solvents. Second, these reactions can be designed to operate in a single step gas-liquid-solid configuration

and in a two-step gas-solid and liquid-solid configuration. Thus, carbon mineralization can be easily integrated with existing CO<sub>2</sub> capture plants using aqueous solvents. Third, high pressures of CO<sub>2</sub> are not needed to accelerate carbon mineralization. These transformative aspects pave the way for low cost integrated CO<sub>2</sub> capture and carbon mineralization pathways that can be operated using heat generated from low-grade geothermal sources. Participation in the NSF I-Corps project further allowed us to identify the key knowledge gaps for commercial realization including the need for energy efficient, low temperature integrated processes for CO<sub>2</sub> capture and carbon mineralization to treat alkaline industrial residues, which paved the way for the scientific and technological advancements reported in this thesis.

## **9.2 Future Work**

The results reported in this thesis demonstrate that integrated reactive CO<sub>2</sub> capture and carbon mineralization pathways can be designed to achieve high conversion of Ca- and Mg-oxides, and Ca-silicate. These materials are abundant in alkaline industrial residues such as steel slag. Thus, integrated CO<sub>2</sub> capture and carbon mineralization pathways can be deployed for the scalable realization of low temperature continuous processing of alkaline industrial residues to produce inorganic carbonates. The formation of highly viscous, gel-like fluids on capturing CO<sub>2</sub> at high concentrations of solvents such as AMP and DBU needs to be further resolved for scalable implementation using these solvents. The transformations of Ca- and Mg-silicates as they react to produce inorganic carbonates using this integrated CO<sub>2</sub> capture and carbon mineralization approach need to be further explored. Another less explored but highly transformative approach to accelerate carbon mineralization can be through the use of multi-solvent systems to recover specific constituents of a mineral. Novel reactor configurations to probe the kinetics of CO<sub>2</sub> capture and carbon mineralization with inherent solvent regeneration are needed. The potential to

decarbonize various industrial sectors including iron and steel making and cement using this approach need to be investigated. These forward-looking research directions set the stage for the scalable realization of integrated CO<sub>2</sub> capture and carbon mineralization pathways with inherent solvent regeneration.

## REFERENCES

- Ahmed, M. H., Byrne, J. A., McLaughlin, J. A. D., Elhissi, A., & Ahmed, W. (2013). Comparison between FTIR and XPS characterization of amino acid glycine adsorption onto diamond-like carbon (DLC) and silicon doped DLC. *Applied Surface Science*, 273, 507-514.
- Ahrens, T. J., & Gaffney, E. S. (1971). Dynamic compression of enstatite. *Journal of Geophysical Research*, 76(23), 5504–5513.
- Al-Hosney, H. A., & Grassian, V. H. (2005). Water, sulfur dioxide and nitric acid adsorption on calcium carbonate: A transmission and ATR-FTIR study. *Physical Chemistry Chemical Physics*, 7(6), 1266–1276.
- Andrew V. G., Chizmeshya, M. J., McKelvy, K. S., Ray W. C., & Hamdallah B. (2007). *A Novel Approach to Mineral Carbonation: Enhancing Carbonation While Avoiding Mineral Pretreatment Process Cost*.
- Angel, R. J., & Prewitt, C. T. (1986). Crystal structure of mullite: a re-examination of the average structure. In *American Mineralogist*, 71(11–12), 1476–1482.
- Arti, M., Youn, M. H., Park, K. T., Kim, H. J., Kim, Y. E., & Jeong, S. K. (2017). Single process for CO<sub>2</sub> capture and mineralization in various alkanolamines using calcium chloride. *Energy and Fuels*, 31(1), 763-769.
- Awad, A., Koster Van Groos, A. F., & Guggenheim, S. (2000). Forsteritic olivine: Effect of crystallographic direction on dissolution kinetics. *Geochimica et Cosmochimica Acta*, 64(10), 1765-1722.
- Azdarpour, A., Asadullah, M., Mohammadian, E., Hamidi, H., Junin, R., & Karaei, M. A. (2015). A review on carbon dioxide mineral carbonation through pH-swing process. In *Chemical Engineering Journal*, 279, 615–630.
- Ballirano, P., De Vito, C., Mignardi, S., & Ferrini, V. (2013). Phase transitions in the MgCO<sub>2</sub>H<sub>2</sub>O system and the thermal decomposition of dypingite, Mg<sub>5</sub>(CO<sub>3</sub>)<sub>4</sub>(OH)<sub>2</sub>5H<sub>2</sub>O: Implications for geosequestration of carbon dioxide. *Chemical Geology*, 340, 59-67.
- Barnes, V. E., Shock, D. A. ., & Cunningham, W. A. (1950). Utilization of Texas Serpentine. In *University of Texas, Bureau of Economic Geology* (Issue 4720).
- Barzagli, F., Mani, F., & Peruzzini, M. (2013). Efficient CO<sub>2</sub> absorption and low temperature desorption with non-aqueous solvents based on 2-amino-2-methyl-1-propanol (AMP). *International Journal of Greenhouse Gas Control*, 16, 217-223.
- Barzegar, B. H., Ebadzadeh, T., & Majidian, H. (2014). Microwave synthesis and sintering of forsterite nanopowder produced by high energy ball milling. *Ceramics International*, 40(2), 2869–2876.
- Basavaraj, R. B., Darshan, G. P., Daruka, P. B., Sharma, S. C., & Nagabhushana, H. (2019). Rapid visualization of latent fingerprints using novel CaSiO<sub>3</sub>:Sm<sup>3+</sup> nanophosphors fabricated via ultrasound route. *Journal of Rare Earths*, 37(1), 32-44.
- Béarat, H., McKelvy, M. J., Chizmeshya, A. V. G., Gormley, D., Nunez, R., Carpenter, R. W., Squires, K., & Wolf, G. H. (2006). Carbon Sequestration via Aqueous Olivine Mineral

- Carbonation: Role of Passivating Layer Formation. *Environmental Science & Technology*, 40(15), 4802–4808.
- Beaucage, G. (1995). Approximations Leading to a Unified Exponential/Power-Law Approach to Small-Angle Scattering. *Journal of Applied Crystallography*, 28(6), 717–728.
- Beaucage, G. (1996). Small-angle scattering from polymeric mass fractals of arbitrary mass-fractal dimension. *Journal of Applied Crystallography*, 29(2), 134–146.
- Benedetti, A., Ilavsky, J., Segre, C., & Strumendo, M. (2019). Analysis of textural properties of CaO-based CO<sub>2</sub> sorbents by ex situ USAXS. *Chemical Engineering Journal*, 355, 760–776.
- Bénézech, P., Saldi, G. D., Dandurand, J. L., & Schott, J. (2011). Experimental determination of the solubility product of magnesite at 50 to 200°C. *Chemical Geology*, 37(1), 32–44.
- Berzina-Cimdina, L., & Borodajenko, N. (2012). Research of Calcium Phosphates Using Fourier Transform Infrared Spectroscopy. In *Infrared Spectroscopy - Materials Science, Engineering and Technology*, 7, 251–263.
- Black, D. R., Windover, D., Henins, A., Gil, D., Filliben, J., & Cline, J. P. (2010). Certification of nist standard reference material 640d. *Powder Diffraction*, 25(2), 187–190.
- Blamey, J., Anthony, E. J., Wang, J., & Fennell, P. S. (2010). The calcium looping cycle for large-scale CO<sub>2</sub> capture. *Progress in Energy and Combustion Science*, 36(2), 260–279.
- Bobicki, E. R., Liu, Q., Xu, Z., & Zeng, H. (2012). Carbon capture and storage using alkaline industrial wastes. In *Progress in Energy and Combustion Science*, 38(2), 302–320.
- Böke, H., Akkurt, S., Özdemir, S., Göktürk, E. H., & Caner Saltik, E. N. (2004). Quantification of CaCO<sub>3</sub>-CaSO<sub>3</sub>·0.5H<sub>2</sub>O-CaSO<sub>4</sub>·2H<sub>2</sub>O mixtures by FTIR analysis and its ANN model. *Materials Letters*, 58(5), 723–726.
- Bonfils, B., Julcour-Lebigue, C., Guyot, F., Bodéan, F., Chiquet, P., & Bourgeois, F. (2012). Comprehensive analysis of direct aqueous mineral carbonation using dissolution enhancing organic additives. *International Journal of Greenhouse Gas Control*, 9, 334–346.
- Bonse, U., & Hart, M. (1965). Tailless x-ray single-crystal reflection curves obtained by multiple reflection. *Applied Physics Letters*, 7(9), 238–240.
- Brethomé, F. M., Williams, N. J., Seipp, C. A., Kidder, M. K., & Custelcean, R. (2018). Direct air capture of CO<sub>2</sub> via aqueous-phase absorption and crystalline-phase release using concentrated solar power. *Nature Energy*, 3(7), 553–559.
- Bui, M., Adjiman, C. S., Bardow, A., Anthony, E. J., Boston, A., Brown, S., Fennell, P. S., Fuss, S., Galindo, A., Hackett, L. A., Hallett, J. P., Herzog, H. J., Jackson, G., Kemper, J., Krevor, S., Maitland, G. C., Matuszewski, M., Metcalfe, I. S., Petit, C., ... Mac Dowell, N. (2018). Carbon capture and storage (CCS): The way forward. In *Energy and Environmental Science*, 11(5), 1062–1176.
- Cao, J., Liu, F., Lin, Q., & Zhang, Y. (2008). Hydrothermal synthesis of xonotlite from carbide slag. *Progress in Natural Science*, 18(9), 1147–1154.
- Caplow, M. (1968). Kinetics of Carbamate Formation and Breakdown. *Journal of the American Chemical Society*, 90(24), 6795–6803.
- Chen, Y., & Brantley, S. L. (2000). Dissolution of forsteritic olivine at 65 °C and 2 < pH < 5. *Chemical Geology*, 165(3–4), 267–281.

- Cheng, J., Zhou, J., Liu, J., Cao, X., & Cen, K. (2009). Physicochemical characterizations and desulfurization properties in coal combustion of three calcium and sodium industrial wastes. *Energy and Fuels*, 23(5), 2506–2516.
- Chessin, H., Hamilton, W. C., & Post, B. (1965). Position and thermal parameters of oxygen atoms in calcite. *Acta Crystallographica*, 18(4), 689–693.
- Chiang, P. C., & Pan, S. Y. (2017). Carbon dioxide mineralization and utilization. In *Carbon Dioxide Mineralization and Utilization*.
- Chiarello, R. P., & Sturchio, N. C. (1995). The calcite (10 $\bar{1}$ 4) cleavage surface in water: Early results of a crystal truncation rod study. *Geochimica et Cosmochimica Acta*, 59(21), 4557–4561.
- Chiarello, R. P., Sturchio, N. C., Grace, J. D., Geissbuhler, P., Sorensen, L. B., Cheng, L., & Xu, S. (1997). Otavite-calcite solid-solution formation at the calcite-water interface studied in situ by synchrotron X-ray scattering. *Geochimica et Cosmochimica Acta*, 61(7), 1467–1474.
- Christy, A. G. (2017). A review of the structures of vaterite: the impossible, the possible, and the likely. *Crystal Growth & Design*, 17(6), 3567–3578.
- Chupas, P. J., Chapman, K. W., Kurtz, C., Hanson, J. C., Lee, P. L., & Grey, C. P. (2008). A versatile sample-environment cell for non-ambient X-ray scattering experiments. *Journal of Applied Crystallography*, 41(4), 822-824.
- Costelcean, R., Williams, N. J., Garrabrant, K. A., Agullo, P., Brethomé, F. M., Martin, H. J., & Kidder, M. K. (2019). Direct Air Capture of CO<sub>2</sub> with Aqueous Amino Acids and Solid Bis-iminoguanidines (BIGs). *Industrial and Engineering Chemistry Research*, 58(51), 23338-23346.
- Dal Negro, A., & Ungaretti, L. (1971). Refinement of the Crystal Structure of Aragonite. *The American Mineralogist*, 56, 768–772.
- Daval, D., Sissmann, O., Corvisier, J., Garcia, B., Martinez, I., Guyot, F., & Hellmann, R. (2010). The effect of silica coatings on the weathering rates of wollastonite (CaSiO<sub>3</sub>) and forsterite (Mg<sub>2</sub>SiO<sub>4</sub>): An apparent paradox. In *Water-Rock Interaction*, 713-717.
- Daval, D., Hellmann, R., Saldi, G. D., Wirth, R., & Knauss, K. G. (2013). Linking nm-scale measurements of the anisotropy of silicate surface reactivity to macroscopic dissolution rate laws: New insights based on diopside. *Geochimica et Cosmochimica Acta*, 107, 121-134.
- Davies, P. J., & Bubela, B. (1973). The transformation of nesquehonite into hydromagnesite. *Chemical Geology*, 4, 289-300.
- Davis, A. R., & Oliver, B. G. (1972). A vibrational-spectroscopic study of the species present in the CO<sub>2</sub>-H<sub>2</sub>O system. *Journal of Solution Chemistry*, 1(4), 329-339.
- Di Lorenzo, F., Ruiz-Agudo, C., Ibañez-Velasco, A., Gil-San Millán, R., Navarro, J., Ruiz-Agudo, E., & Rodriguez-Navarro, C. (2018). The Carbonation of Wollastonite: A Model Reaction to Test Natural and Biomimetic Catalysts for Enhanced CO<sub>2</sub> Sequestration. *Minerals*, 8(5), 209.
- Diamond, S. (1999). Aspects of concrete porosity revisited. *Cement and Concrete Research*, 29(8), 1181-1188.
- Doki, N., Seki, H., Takano, K., Asatani, H., Yokota, M., & Kubota, N. (2004). Process control of seeded batch cooling crystallization of the metastable  $\alpha$ -form glycine using an in-situ ATR-

- FTIR spectrometer and an in-situ FBRM particle counter. *Crystal Growth and Design*, 4(5), 949-953.
- Dove, M. T., Craig, M. S., Keen, D. A., Marshall, W. G., Redfern, S. A. T., Trachenko, K., & Tucker, M. G. (2000). Crystal structure of the high-pressure monoclinic phase-II of cristobalite, SiO<sub>2</sub>. *Mineralogical Magazine*, 64(3), 569–576.
- Downs, R. T., & Palmer, D. C. (1994). The pressure behavior of alpha cristobalite. *American Mineralogist*, 79, 9–14.
- Drever, J. I., & Stillings, L. L. (1997). The role of organic acids in mineral weathering. *Colloids and Surfaces A: Physicochemical and Engineering Aspects*, 120(1-3), 167-181.
- Duan, Z., & Sun, R. (2003). An improved model calculating CO<sub>2</sub> solubility in pure water and aqueous NaCl solutions from 273 to 533 K and from 0 to 2000 bar. *Chemical Geology*, 193, 257-271.
- Duan, Z., Sun, R., Zhu, C., & Chou, I. M. (2006). An improved model for the calculation of CO<sub>2</sub> solubility in aqueous solutions containing Na<sup>+</sup>, K<sup>+</sup>, Ca<sup>2+</sup>, Mg<sup>2+</sup>, Cl<sup>-</sup>, and SO<sub>4</sub><sup>2-</sup>. *Marine Chemistry*, 98, 131-139.
- Ellis, A. J. (2010). The solubility of calcite in carbon dioxide solutions. *American Journal of Science*, 257, 354-365.
- Eloneva, S., Mannisto, P., Said, A., Fogelholm, C. J., & Zevenhoven, R. (2011). Ammonium salt-based steelmaking slag carbonation: Precipitation of CaCO<sub>3</sub> and ammonia losses assessment. *Greenhouse Gases: Science and Technology*, 1(4), 305-311.
- Fagerlund, J., & Zevenhoven, R. (2011). An experimental study of Mg(OH)<sub>2</sub> carbonation. *International Journal of Greenhouse Gas Control*, 5(6), 1406–1412.
- Falkowski, P., Scholes, R. J., Boyle, E., Canadell, J., Canfield, D., Elser, J., Gruber, N., Hibbard, K., Hogberg, P., Linder, S., Mackenzie, F. T., Moore, B., Pedersen, T., Rosental, Y., Seitzinger, S., Smetacek, V., & Steffen, W. (2000). The global carbon cycle: A test of our knowledge of earth as a system. In *Science*, 290(5490), 291–296.
- Farhang, F., Oliver, T. K., Rayson, M., Brent, G., Stockenhuber, M., & Kennedy, E. (2016). Experimental study on the precipitation of magnesite from thermally activated serpentine for CO<sub>2</sub> sequestration. *Chemical Engineering Journal*, 303, 439–449.
- Fauth, D. J., Goldberg, P. M., Knoer, J. P., Soong, Y., O'Connor, W. K., Dahlin, D. C., Nilsen, D. N., Walters, R. P., Lackner, K. S., Ziocck, H. J., McKelvy, M. J., & Chen, Z. Y. (2000). Carbon dioxide storage as mineral carbonates. *ACS Division of Fuel Chemistry, Preprints*, 45(4), 708–711.
- Favre, N., Christ, M. L., & Pierre, A. C. (2009). Biocatalytic capture of CO<sub>2</sub> with carbonic anhydrase and its transformation to solid carbonate. *Journal of Molecular Catalysis B: Enzymatic*, 60(3–4), 163–170.
- Feidenhans'l, R. (1989). Surface structure determination by X-ray diffraction. *Surface Science Reports*, 10(3), 105–188.
- Fenter, P. A. (2002). X-ray reflectivity as a probe of mineral-fluid interfaces: A user guide. *Reviews in Mineralogy and Geochemistry*, 49(1), 149–221.
- Fenter, P., Geissbühler, P., Dimasi, E., Srajer, G., Sorensen, L. B., & Sturchio, N. C. (2000).

- Surface speciation of calcite observed in situ by high-resolution X-ray reflectivity. *Geochimica et Cosmochimica Acta*, 64(7), 1221–1228.
- Fenter, P., & Sturchio, N. C. (2012). Calcite (104)-water interface structure, revisited. *Geochimica et Cosmochimica Acta*, 97, 58–69.
- Fernandez-Martinez, A., Hu, Y., Lee, B., Jun, Y. S., & Waychunas, G. A. (2013). In situ determination of interfacial energies between heterogeneously nucleated CaCO<sub>3</sub> and quartz substrates: Thermodynamics of CO<sub>2</sub> mineral trapping. *Environmental Science and Technology*, 47(1), 102–109.
- Ferrage, E., Lanson, B., Malikova, N., Plançon, A., Sakharov, B. A., & Drits, V. A. (2005). New insights on the distribution of interlayer water in bi-hydrated smectite from X-ray diffraction profile modeling of 00l reflections. *Chemistry of Materials*, 17, 3499–3512.
- Ferrage, E., Kirk, C. A., Cressey, G., & Cuadros, J. (2007). Dehydration of Ca-montmorillonite at the crystal scale. Part I: Structure evolution. *American Mineralogist*, 92(7), 994–1006.
- Frasco, D. L. (1964). Infrared spectra of ammonium carbamate and deuterioammonium carbamate. *The Journal of Chemical Physics*, 47(1), 2134–2140.
- Frykstrand, S., Forsgren, J., Mihranyan, A., & Strømme, M. (2014). On the pore forming mechanism of Upsalite, a micro- and mesoporous magnesium carbonate. *Microporous and Mesoporous Materials*, 190, 99–104.
- Gadikota, G. (2017). Connecting the morphological and crystal structural changes during the conversion of lithium hydroxide monohydrate to lithium carbonate using multi-scale X-ray scattering measurements. *Minerals*, 7(9).
- Gadikota, G., & Allen, A. J. (2018). Microstructural and structural characterization of materials for CO<sub>2</sub> storage using multi-scale X-ray scattering methods. In L. Li & W. Wong-Ng (Eds.), *Materials and Processes for CO<sub>2</sub> Capture, Conversion, and Sequestration*. Wiley Books.
- Gadikota, G., Matter, J., Kelemen, P., & Park, A.-H. A. (2014). Chemical and morphological changes during olivine carbonation for CO<sub>2</sub> storage in the presence of NaCl and NaHCO<sub>3</sub>. *Physical Chemistry Chemical Physics*, 16(10), 4679–4693.
- Gadikota, G., & Park, A. H. A. (2015). Chapter 8 – Accelerated Carbonation of Ca- and Mg-Bearing Minerals and Industrial Wastes Using CO<sub>2</sub>. In *Carbon Dioxide Utilisation*, 115–137.
- Gadikota, G., Swanson, E. J., Zhao, H., & Park, A. H. A. (2014). Experimental design and data analysis for accurate estimation of reaction kinetics and conversion for carbon mineralization. *Industrial and Engineering Chemistry Research*, 53(16), 6664–6676.
- Gadikota, G., Zhang, F., & Allen, A. J. (2017). Towards understanding the microstructural and structural changes in natural hierarchical materials for energy recovery: In-operando multi-scale X-ray scattering characterization of Na- and Ca-montmorillonite on heating to 1150 °C. *Fuel*, 196, 195–209.
- Gadikota, G. (2014). *Geo-chemo-physical studies of carbon mineralization for natural and engineered carbon storage*. Columbia University.
- Gadikota, G. (2016). Commentary: Ex Situ Aqueous Mineral Carbonation. *Frontiers in Energy Research*, 4, 21.
- Gadikota, G. (2018). Multiscale X-Ray Scattering for Probing Chemo-Morphological Coupling in

- Pore-to-Field and Process Scale Energy and Environmental Applications. In *Small Angle Scattering and Diffraction*, 29.
- Gadikota, G. (2020). Multiphase carbon mineralization for the reactive separation of CO<sub>2</sub> and directed synthesis of H<sub>2</sub>. In *Nature Reviews Chemistry*, 4(2), 78-89.
- Gadikota, G, Fricker, K., Jang, S. H., & Park, A. H. A. (2015). Carbonation of Silicate Minerals and Industrial Wastes and Their Potential Use as Sustainable Construction Materials. In *Advances in CO<sub>2</sub> Capture, Sequestration, and Conversion*, 1194, 12–295. American Chemical Society.
- Gadikota, G, Natali, C., Boschi, C., & Park, A. H. A. (2014). Morphological changes during enhanced carbonation of asbestos containing material and its comparison to magnesium silicate minerals. *Journal of Hazardous Materials*, 264, 46-52.
- Gadikota, G, Zhang, F., & Allen, A. (2017). In Situ Angstrom-to-Micrometer Characterization of the Structural and Microstructural Changes in Kaolinite on Heating Using Ultrasmall-Angle, Small-Angle, and Wide-Angle X-ray Scattering (USAXS/SAXS/WAXS). *Industrial and Engineering Chemistry Research*, 56(41), 11797-11801.
- Galan, I., Glasser, F. P., & Andrade, C. (2013). Calcium carbonate decomposition. *Journal of Thermal Analysis and Calorimetry*, 111(2), 1197–1202.
- Garrabrant, K. A., Williams, N. J., Holguin, E., Brethomé, F. M., Tsouris, C., & Custelcean, R. (2019). Energy-efficient CO<sub>2</sub> capture from flue gas by absorption with amino acids and crystallization with a bis-iminoguanidine. *Industrial and Engineering Chemistry Research*, 58(24), 11510-11515.
- Geissbühler, P., Fenter, P., DiMasi, E., Srajer, G., Sorensen, L. B., & Sturchio, N. C. (2004). Three-dimensional structure of the calcite–water interface by surface X-ray scattering. *Surface Science*, 573(2), 191–203.
- Gerdemann, S., Dahlin, D., & O’Connor, W. (2004). Ex-situ and in-situ mineral carbonation as a means to sequester carbon dioxide. *Osti.Gov*.
- Gerdemann, S. J., O’Connor, W. K., Dahlin, D. C., Penner, L. R., & Rush, H. (2007). Ex situ aqueous mineral carbonation. *Environmental Science & Technology*, 41(7), 2587–2593.
- Giammar, D. E., Bruant, R. G., & Peters, C. (2005). Forsterite dissolution and magnesite precipitation at conditions relevant for deep saline aquifer storage and sequestration of carbon dioxide. *Chemical Geology*, 217(3–4), 257–276.
- Giester, G., Lengauer, C. L., & Rieck, B. (2000). The crystal structure of nesquehonite, MgCO<sub>3</sub>·3H<sub>2</sub>O, from Lavrion, Greece. *Mineralogy and Petrology*, 70, 153-163.
- Guo, D., Thee, H., Tan, C. Y., Chen, J., Fei, W., Kentish, S., Stevens, G. W., & Da Silva, G. (2013). Amino acids as carbon capture solvents: Chemical kinetics and mechanism of the glycine + CO<sub>2</sub> reaction. *Energy and Fuels*, 27(7), 3898-3904.
- Gupta, H., Thomas, T. J., Park, A. H. A., Iyer, M. V., Gupta, P., Agnihotri, R., Jadhav, R. A., Walker, H. W., Weavers, L. K., Butalia, T., & Fan, L. S. (2007). Pilot-scale demonstration of the oscar process for high-temperature multipollutant control of coal combustion flue gas, using carbonated fly ash and mesoporous calcium carbonate. *Industrial and Engineering Chemistry Research*, 46(14), 5051-5060.

- Gupta, M., Da Silva, E. F., Hartono, A., & Svendsen, H. F. (2013). Theoretical study of differential enthalpy of absorption of CO<sub>2</sub> with MEA and MDEA as a function of temperature. *Journal of Physical Chemistry B*, 117(32), 9457-9468.
- Hahn, M. W., Jelic, J., Berger, E., Reuter, K., Jentys, A., & Lercher, J. A. (2016). Role of Amine Functionality for CO<sub>2</sub> Chemisorption on Silica. *Journal of Physical Chemistry B*, 120(8), 1988-1995.
- Hahn, M. W., Steib, M., Jentys, A., & Lercher, J. A. (2015). Mechanism and kinetics of CO<sub>2</sub> adsorption on surface bonded amines. *Journal of Physical Chemistry C*, 8, 4126-4135.
- Hammouda, B. (2010). A new Guinier-Porod model. *Journal of Applied Crystallography*.
- Han, S. J., & Wee, J. H. (2016). Carbon Dioxide Fixation via the Synthesis of Sodium Ethyl Carbonate in NaOH-Dissolved Ethanol. *Industrial and Engineering Chemistry Research*, 55(46), 12111-12118.
- Hänchen, M., Krevor, S., Mazzotti, M., & Lackner, K. S. (2007). Validation of a population balance model for olivine dissolution. *Chemical Engineering Science*, 6412-6422.
- Harrison, A. L., Power, I. M., & Dipple, G. M. (2012). Accelerated carbonation of brucite in mine tailings for carbon sequestration. *Environmental Science & Technology*, 47(1), 126-134.
- Hazen, R. M. (1976). Effects of temperature and pressure on the crystal structure of forsterite. *American Mineralogist*, 61(1), 1280-1293.
- Heldebrant, D. J., Jessop, P. G., Thomas, C. A., Eckert, C. A., & Liotta, C. L. (2005). The reaction of 1,8-diazabicyclo[5.4.0]undec-7-ene (DBU) with carbon dioxide. *Journal of Organic Chemistry*, 70(13), 5335-5338.
- Highfield, J., Lim, H., Fagerlund, J., & Zevenhoven, R. (2012). Activation of serpentine for CO<sub>2</sub> mineralization by flux extraction of soluble magnesium salts using ammonium sulfate. *RSC Advances*, 2(16), 6535.
- Hisatsune, C. (1984). Low-temperature infrared study of ammonium carbamate formation. *Canadian Journal of Chemistry*, 62, 945-948.
- Hong, S., Sim, G., Moon, S., & Park, Y. (2020). Low Temperature Regeneration of Amines Integrated with Production of Structure-Controlled Calcium Carbonates for Combined CO<sub>2</sub> Capture and Utilization. *Energy & Fuels*, 34(3), 3532-3539.
- Hopkins, D. W. (2008). Carbon mineralization. In *Soil Sampling and Methods of Analysis*, 589-598.
- Hopkinson, L., Kristova, P., Rutt, K., & Cressey, G. (2012). Phase transitions in the system MgO-CO<sub>2</sub>-H<sub>2</sub>O during CO<sub>2</sub> degassing of Mg-bearing solutions. *Geochimica et Cosmochimica Acta*, 67, 1-13.
- Hopkinson, L., Rutt, K., & Cressey, G. (2008). The transformation of nesquehonite to hydromagnesite in the system CaO-MgO-H<sub>2</sub>O-CO<sub>2</sub>: An experimental spectroscopic study. *Journal of Geology*, 116(4), 387-400.
- Hu, G., Smith, K. H., Wu, Y., Mumford, K. A., Kentish, S. E., & Stevens, G. W. (2018). Carbon dioxide capture by solvent absorption using amino acids: A review. In *Chinese Journal of Chemical Engineering*, 26(11), 2229-2237.
- Huijgen, W. J. J., & Comans, R. N. J. (2003). *Carbon dioxide sequestration by mineral*

- carbonation. *Literature Review*. Energy research Centre of the Netherlands ECN.
- Huntzinger, D. N., Gierke, J. S., Kawatra, S. K., Eisele, T. C., & Sutter, L. L. (2009). Carbon dioxide sequestration in cement kiln dust through mineral carbonation. *Environmental Science and Technology*, 43(6), 1986-1992.
- Ilavsky, J., Zhang, F., Allen, A. J., Levine, L. E., Jemian, P. R., & Long, G. G. (2013). Ultra-small-angle X-ray scattering instrument at the advanced photon source: History, recent development, and current status. *Metallurgical and Materials Transactions A: Physical Metallurgy and Materials Science*, 44(1), 68-76.
- Ilavsky, J. (2012). Nika: Software for Two- Dimensional Data Reduction. *Journal of Applied Crystallography*, 45(2), 324–326.
- Ilavsky, J., & Jemian, P. R. (2009). Irena: Tool suite for modeling and analysis of small-angle scattering. *Journal of Applied Crystallography*, 42(2), 347–353.
- Ilavsky, J., Jemian, P. R., Allen, A. J., Zhang, F., Levine, L. E., & Long, G. G. (2009). Ultra-small-angle X-ray scattering at the Advanced Photon Source. *Journal of Applied Crystallography*, 42(3), 469–479.
- Ilavsky, J., Zhang, F., Andrews, R. N., Kuzmenko, I., Jemian, P. R., Levine, L. E., & Allen, A. J. (2018). Development of combined microstructure and structure characterization facility for in situ and operando studies at the advanced photon source. *Journal of Applied Crystallography*, 3, 867-882.
- Intergovernmental Panel on Climate Change. (2014). Climate Change 2014 Mitigation of Climate Change. In *Climate Change 2014 Mitigation of Climate Change*.
- Intergovernmental Panel on Climate Change (IPCC). (2005). IPCC Special Report on Carbon Dioxide Capture and Storage. In *Working Group III of the Intergovernmental Panel on Climate Change*.
- Ismail, M. G. M. U., Nakai, Z., & Sōmiya, S. (1987). Microstructure and Mechanical Properties of Mullite Prepared by the Sol-Gel Method. *Journal of the American Ceramic Society*, 70(1).
- Ith, N. G. S., & Dukes, J. S. (1993). *The Intergovernmental Panel on Climate Change*.
- Jenkins, J. (2015). *A Case Study of the Petra Nova Carbon Capture Project*. The Paulson Institute.
- Ji, L., Yu, H., Li, K., Yu, B., Grigore, M., Yang, Q., Wang, X., Chen, Z., Zeng, M., & Zhao, S. (2018). Integrated absorption-mineralisation for low-energy CO<sub>2</sub> capture and sequestration. *Applied Energy*, 225, 356–366.
- Ji, L., Yu, H., Yu, B., Jiang, K., Grigore, M., Wang, X., Zhao, S., & Li, K. (2018). Integrated absorption–mineralisation for energy-efficient CO<sub>2</sub> sequestration: Reaction mechanism and feasibility of using fly ash as a feedstock. *Chemical Engineering Journal*, 352,151-162.
- Jun, Y. S., Kim, D., & Neil, C. W. (2016). Heterogeneous Nucleation and Growth of Nanoparticles at Environmental Interfaces. *Accounts of Chemical Research*, 49(9), 1681-1690.
- Jun, Y. S., Lee, B., & Waychunas, G. A. (2010). In situ observations of nanoparticle early development kinetics at mineral-water interfaces. *Environmental Science and Technology*, 44(21), 8182-8189.
- Kamhi, S. R. (1963). On the structure of vaterite, CaCO<sub>3</sub>. *Acta Crystallographica*, 16(8), 770–772.

- Kang, J. M., Murnandari, A., Youn, M. H., Lee, W., Park, K. T., Kim, Y. E., Kim, H. J., Kang, S. P., Lee, J. H., & Jeong, S. K. (2018). Energy-efficient chemical regeneration of AMP using calcium hydroxide for operating carbon dioxide capture process. *Chemical Engineering Journal*, 335, 338-344.
- Kaupmees, K., Trummal, A., & Leito, I. (2014). Basicities of strong bases in water: A computational study. *Croatica Chemica Acta*, 87(4), 385-395.
- Kim, H. R. (2009). Synthesis of Iron-Based Chemical Looping Sorbents Integrated with pH Swing Carbon Mineral Sequestration. *Journal of Nanoscience and Nanotechnology*, 9(12), 7422-7427.
- Kim, I., & Svendsen, H. F. (2007). Heat of absorption of carbon dioxide (CO<sub>2</sub>) in monoethanolamine (MEA) and 2-(aminoethyl)ethanolamine (AEEA) solutions. *Industrial and Engineering Chemistry Research*, 46(17), 5803-5809.
- Kim, Y. E., Lim, J. A., Jeong, S. K., Yoon, Y. Il, Bae, S. T., & Nam, S. C. (2013). Comparison of carbon dioxide absorption in aqueous MEA, DEA, TEA, and AMP solutions. *Bulletin of the Korean Chemical Society*, 34, 783-787.
- Krounbi, L., Enders, A., Anderton, C. R., Engelhard, M. H., Hestrin, R., Torres-Rojas, D., Dynes, J. J., & Lehmann, J. (2020). Sequential Ammonia and Carbon Dioxide Adsorption on Pyrolyzed Biomass to Recover Waste Stream Nutrients. *ACS Sustainable Chemistry & Engineering*, 18, 7121-7131.
- Lackner, K. S. (2002). Carbonate chemistry for sequestering fossil carbon. *Annual Review of Energy and the Environment*, 27(1), 193-232.
- Lackner, K. S., Butt, D. P., & Wendt, C. H. (1997). Progress on binding CO<sub>2</sub> in mineral substrates. *Energy Conversion and Management*, 38, S259-256.
- Lackner, K. S., Grimes, P., & Ziock, H. J. (2014). Capturing carbon dioxide from air. In *Carbon Capture and Storage: CO<sub>2</sub> Management Technologies*, 363-376.
- Lee, J. J., Chen, C. H., Shimon, D., Hayes, S. E., Sievers, C., & Jones, C. W. (2017). Effect of Humidity on the CO<sub>2</sub> Adsorption of Tertiary Amine Grafted SBA-15. *Journal of Physical Chemistry C*, 42, 23480-23487.
- Li, B., Duan, Y., Luebke, D., & Morreale, B. (2013). Advances in CO<sub>2</sub> capture technology: A patent review. *Applied Energy*, 102, 1439-1447.
- Li, J., & Hitch, M. (2017). Structural and chemical changes in mine waste mechanically-activated in various milling environments. *Powder Technology*, 308, 13-19.
- Li, Q, Gupta, S., Tang, L., Quinn, S., Atakan, V., & Riman, R. E. (2016). A Novel Strategy for Carbon Capture and Sequestration by rHLPD Processing. *Frontiers in Energy Research*, 3, 53.
- Li, Q, Fernandez-Martinez, A., Lee, B., Waychunas, G. A., & Jun, Y. S. (2014). Interfacial energies for heterogeneous nucleation of calcium carbonate on mica and quartz. *Environmental Science and Technology*, 10, 5745-5753.
- Li, X. G., Lv, Y., Ma, B. G., Wang, W. Q., & Jian, S. W. (2017). Decomposition kinetic characteristics of calcium carbonate containing organic acids by TGA. *Arabian Journal of Chemistry*, 10, S2534-2538.

- Li, Y., Su, M., Xie, X., Wu, S., & Liu, C. (2015). CO<sub>2</sub> capture performance of synthetic sorbent prepared from carbide slag and aluminum nitrate hydrate by combustion synthesis. *Applied Energy*, 145, 60–68.
- Li, Y., Sun, R., Liu, C., Liu, H., & Lu, C. (2012). CO<sub>2</sub> capture by carbide slag from chlor-alkali plant in calcination/carbonation cycles. *International Journal of Greenhouse Gas Control*, 9, 117–123.
- Liang, J. Z., Duan, D. R., Tang, C. Y., & Tsui, C. P. (2014). Correlation between impact strength and fractal dimensions of fracture surface for PLLA/nano-CaCO<sub>3</sub> composites. *Polymer Testing*, 39, 109–115.
- Liu, M., Asgar, H., Seifert, S., & Gadikota, G. (2020). Novel aqueous amine looping approach for the direct capture, conversion and storage of CO<sub>2</sub> to produce magnesium carbonate. *Sustainable Energy & Fuels*, 4(3), 1256–1275.
- Liu, M., & Gadikota, G. (2018). Chemo-morphological coupling during serpentine heat treatment for carbon mineralization, *Fuel*, 227, 379–385.
- Liu, M., & Gadikota, G. (2018). Integrated CO<sub>2</sub> capture, conversion and storage to produce calcium carbonate using an amine looping strategy. *Energy & Fuels*, 3(33), 1722–1733.
- Liu, M., & Gadikota, G. (2018). Phase evolution and textural changes during the direct conversion and storage of CO<sub>2</sub> to produce calcium carbonate from calcium hydroxide. *Geosciences*, 8(12), 445.
- Liu, M., & Gadikota, G. (2018). Probing the Influence of Thermally Induced Structural Changes on the Microstructural Evolution in Shale using Multiscale X-ray Scattering Measurements, *Energy & Fuels*, 32(8), 8193–8201.
- Liu, M., & Gadikota, G. (2020). Single-step, low temperature and integrated CO<sub>2</sub> capture and conversion using sodium glycinate to produce calcium carbonate. *Fuel*, 275, 1178–1187.
- Liu, W, Yang, J., & Xiao, B. (2009). Review on treatment and utilization of bauxite residues in China. In *International Journal of Mineral Processing*, 93(3–4), 220–231.
- Liu, W, An, H., Qin, C., Yin, J., Wang, G., Feng, B., & Xu, M. (2012). Performance Enhancement of Calcium Oxide Sorbents for Cyclic CO<sub>2</sub> Capture—A Review. *Energy & Fuels*, 26(5), 2751–2767.
- Liu, Y., Olsen, A. A., & Rimstidt, J. D. (2006). Mechanism for the dissolution of olivine series minerals in acidic solutions. *American Mineralogist*, 91(2–3), 455–458.
- Mac Dowell, N., Fennell, P. S., Shah, N., & Maitland, G. C. (2017). The role of CO<sub>2</sub> capture and utilization in mitigating climate change. *Nature Climate Change*, 7(4), 243–249.
- Mandal, B. P., Biswas, A. K., & Bandyopadhyay, S. S. (2003). Absorption of carbon dioxide into aqueous blends of 2-amino-2-methyl-1-propanol and diethanolamine. *Chemical Engineering Science*, 58(18), 4137–4144.
- Manovic, V., & Anthony, E. J. (2010). Lime-based sorbents for high-temperature CO<sub>2</sub> capture—a review of sorbent modification methods. In *International Journal of Environmental Research and Public Health*, 7(8), 3129–3140.
- Marini, L. (2007). *Geological Sequestration of Carbon Dioxide: Thermodynamics, Kinetics, and Reaction Path Modeling*. Elsevier.

- Maroto-Valer, M. M., Fauth, D. J., Kuchta, M. E., Zhang, Y., & Andrésen, J. M. (2005). Activation of magnesium rich minerals as carbonation feedstock materials for CO<sub>2</sub> sequestration. *Fuel Processing Technology*, 86(14–15), 1627–1645.
- Maroto-Valer, M. M., Zhang, Y., Kuchta, M. E., Andresen, J. M., & Fauth, D. J. (2009). *Process for sequestering carbon dioxide and sulfur dioxide*. US Patent No. 7,604,787.
- Maslen, E. N., Streltsov, V. A., & Streltsova, N. R. (1993). X-ray study of the electron density in calcite, CaCO<sub>3</sub>. *Acta Crystallographica Section B*, 49(4), 636–641.
- Materic, V., & Smedley, S. I. (2011). High Temperature Carbonation of Ca(OH)<sub>2</sub>. *Industrial & Engineering Chemistry Research*, 50(10), 5927–5932.
- McKelvy, M. J., Chizmeshya, A. V. G., Diefenbacher, J., Béarat, H., & Wolf, G. (2004). Exploration of the role of heat activation in enhancing serpentine carbon sequestration reactions. *Environmental Science and Technology*, 38(24), 6897–6903.
- Mellini, M. (1982). The crystal structure of lizardite 1T: hydrogen bonds and polytypism. *American Mineralogist*, 67(5–6), 587–598.
- Mikhail, R. S., Brunauer, S., & Copeland, L. E. (1966). Kinetics of the thermal decomposition of calcium hydroxide. *Journal of Colloid and Interface Science*, 21(4), 394–404.
- Milella, F., & Mazzotti, M. (2019). Estimating speciation of aqueous ammonia solutions of ammonium bicarbonate: Application of least squares methods to infrared spectra. *Reaction Chemistry and Engineering*, 7, 1284–1320.
- Min, Y., Li, Q., Voltolini, M., Kneafsey, T., & Jun, Y. S. (2017). Wollastonite carbonation in water-bearing supercritical CO<sub>2</sub>: Effects of particle size. *Environmental Science & Technology*, 51(21), 13044–13053.
- Ming, D. W., & Franklin, W. T. (2010). Synthesis and Characterization of Lansfordite and Nesquehonite1. *Soil Science Society of America Journal*, 49(5), 1303–1308.
- Mirjafari, P., Asghari, K., & Mahinpey, N. (2007). Investigating the application of enzyme carbonic anhydrase for CO<sub>2</sub> sequestration purposes. *Industrial & Engineering Chemistry Research*, 46(3), 921–926.
- Mission Innovation, Accelerating Breakthrough Innovation in Carbon Capture, Utilization, and Storage, Report of the Carbon Capture, Utilization and Storage. (2018).
- Morgan, B., Wilson, S. A., Madsen, I. C., Gozukara, Y. M., & Habsuda, J. (2015). Increased thermal stability of nesquehonite (MgCO<sub>3</sub>·3H<sub>2</sub>O) in the presence of humidity and CO<sub>2</sub>: Implications for low-temperature CO<sub>2</sub> storage. *International Journal of Greenhouse Gas Control*, 39, 366–376.
- Morrow, D.R. & Thompson, M. S. (2020). Reduce, Remove, Recycle: Clarifying the Overlap between Carbon Removal and CCUS. *Institute for Carbon Removal Law and Policy, American University, Washington, DC, Working Paper No. 2*.
- Müller, P. (2010). Crystal structure refinement. In *Crystal Structure Refinement: A Crystallographer's Guide to SHELXL*.
- Murnandari, A., Kang, J., Youn, M. H., Park, K. T., Kim, H. J., Kang, S. P., & Jeong, S. K. (2017). Effect of process parameters on the CaCO<sub>3</sub> production in the single process for carbon capture and mineralization. *Korean Journal of Chemical Engineering*, 34(3), 935–941.

- National Academies of Sciences Engineering and Medicine. (2019). Gaseous Carbon Waste Streams Utilization: Status and Research Needs. In *The National Academies Press*.
- Nikulshina, V., Gálvez, M. E., & Steinfeld, A. (2007). Kinetic analysis of the carbonation reactions for the capture of CO<sub>2</sub> from air via the Ca(OH)<sub>2</sub>-CaCO<sub>3</sub>-CaO solar thermochemical cycle. In *Chemical Engineering Journal*, 129(1-3), 75–83.
- O'Connor, W. K., Dahlin, D. C., Rush, G. E., Gerdemann, S. J., & Nilsen, D. N. (2004). *Aqueous Mineral Carbonation, Final Report DOE/ARC-TR-04-002*.
- Oelkers, E.H., & Schott, J. (1995). The dependence of silicate dissolution rates on their structure and composition. In Y. K. Kharaka & O. V. Chudaev (Eds.), *Water Rock Interaction*, 153–156.
- Oelkers, E. H. (1996). Summary and review of the physical and chemical properties of rocks and fluids. *Reviews in Mineralogy*, 34, 131–191.
- Oelkers, E. H., Gislason, S. R., & Matter, J. (2008). Mineral carbonation of CO<sub>2</sub>. *Elements*, 4(5), 333–337.
- Olsen, A. A., & Rimstidt, J. D. (2008). Oxalate-promoted forsterite dissolution at low pH. *Geochimica et Cosmochimica Acta*, 72(7), 1758–1766.
- Pacala, S., & Socolow, R. (2004). Stabilization wedges: solving the climate problem for the next 50 years with current technologies. *Science*, 305(5686), 968–972.
- Palandri, J. L., & Kharaka, Y. K. (2004). A compilation of rate parameters of water-mineral interaction kinetics for application to geochemical modeling. In *USGS Open File Report*.
- Pan, S. Y., Ling, T. C., Park, A. H. A., & Chiang, P. C. (2018). An overview: Reaction mechanisms and modelling of CO<sub>2</sub> utilization via mineralization. In *Aerosol and Air Quality Research*, 18(4), 829-848.
- Park, A. H. A., Jadhav, R., & Fan, L. S. (2003). CO<sub>2</sub> Mineral Sequestration Chemically Enhanced Aqueous Carbonation of Serpentine.pdf. *Canadian Journal of Chemical Engineering*, 81(3–4), 885–890.
- Park, A. H. A., & Fan, L.-S. (2004). CO<sub>2</sub> mineral sequestration: physically activated dissolution of serpentine and pH swing process. *Chemical Engineering Science*, 59(22–23), 5241–5247.
- Park, A. H. A., Jadhav, R., & Fan, L.-S. (2008). CO<sub>2</sub> Mineral Sequestration: Chemically Enhanced Aqueous Carbonation of Serpentine. *The Canadian Journal of Chemical Engineering*, 81, 885-890.
- Petch, H. E. (1961). The hydrogen positions in portlandite, Ca(OH)<sub>2</sub>, as indicated by the electron distribution. *Acta Crystallographica*, 14(9), 950–957.
- Plav, B., Kobe, S., & Orel, B. (1999). Identification of crystallization forms of CaCO<sub>3</sub> with FTIR spectroscopy. *Kovine Zlitine Tehnol*, 33,6.
- Pokrovsky, O. S., Golubev, S. V., & Schott, J. (2005). Dissolution kinetics of calcite, dolomite and magnesite at 25 C and 0 to 50 atm P<sub>CO2</sub>. *Chemical Geology*, 217(3–4), 239–255.
- Power, I. M., Harrison, A. L., Dipple, G. M., Wilson, S. A., Kelemen, P. B., Hitch, M., & Southam, G. (2013). Carbon Mineralization: From Natural Analogues to Engineered Systems. *Reviews in Mineralogy and Geochemistry*, 77(1), 305–360.

- Power, I. M., Harrison, A. L., & Dipple, G. M. (2016). Accelerating Mineral Carbonation Using Carbonic Anhydrase. *Environmental Science and Technology*, 50(5), 2610-2618.
- Pretsch, E., Bühlmann, P., & Badertscher, M. (2009). Structure determination of organic compounds: Tables of spectral data. In *Structure Determination of Organic Compounds: Tables of Spectral Data*.
- Primak, W., Kaufman, H., & Ward, R. (1948). X-Ray Diffraction Studies of Systems Involved in the Preparation of Alkaline Earth Sulfide and Selenide Phosphors. *Journal of the American Chemical Society*, 70(6), 2043-2046.
- Puxty, G., Rowland, R., & Attalla, M. (2010). Comparison of the rate of CO<sub>2</sub> absorption into aqueous ammonia and monoethanolamine. *Chemical Engineering Science*, 65(2), 915-922.
- Radha, A. V., Fernandez-Martinez, A., Hu, Y., Jun, Y.-S., Waychunas, G. A., & Navrotsky, A. (2012). Energetic and structural studies of amorphous Ca<sub>1-x</sub>Mg<sub>x</sub>CO<sub>3</sub>·nH<sub>2</sub>O (0 ≤ x ≤ 1). *Geochimica et Cosmochimica Acta*, 90, 83-95.
- Ramachandran, E., Baskaran, K., & Natarajan, S. (2007). XRD, thermal, FTIR and SEM studies on gel grown γ-glycine crystals. *Crystal Research and Technology*, 42, 73-77.
- Reddy, M. M., & Gaillard, W. D. (1981). Kinetics of calcium carbonate (calcite)-seeded crystallization: Influence of solid/solution ratio on the reaction rate constant. *Journal of Colloid and Interface Science*, 80(1), 171-178.
- Reichle, D., Houghton, J., & Benson, S. (1999). Working paper on carbon sequestration science and technology. *Draft, February*.
- Richards, R., Li, W., Decker, S., Davidson, C., Koper, O., Zaikovski, V., Volodin, A., Rieker, T., & Klabunde, K. J. (2000). Consolidation of metal oxide nanocrystals. Reactive pellets with controllable pore structure that represent a new family of porous, inorganic materials. *Journal of the American Chemical Society*, 122(20), 4921-4925.
- Riman, R. E., & Li, Q. (2011). *Sequestration of a gas emitted by an industrial plant*. US Patents 13/008.464.
- Ryu, K. W., Jo, H., Choi, S. H., Chae, S. C., & Jang, Y. N. (2016). Changes in mineral assemblages during serpentine carbonation. *Applied Clay Science*, 134, 62-67.
- Sahoo, P. C., Jang, Y. N., & Lee, S. W. (2013). Enhanced biomimetic CO<sub>2</sub> sequestration and CaCO<sub>3</sub> crystallization using complex encapsulated metal organic framework. *Journal of Crystal Growth*, 373, 96-101.
- Salman, M., Cizer, Ö., Pontikes, Y., Santos, R. M., Snellings, R., Vandewalle, L., Blanpain, B., & Van Balen, K. (2014). Effect of accelerated carbonation on AOD stainless steel slag for its valorisation as a CO<sub>2</sub>-sequestering construction material. *Chemical Engineering Journal*, 246, 39-52.
- Sanna, A., Hall, M. R., & Maroto-Valer, M. (2012). Post-processing pathways in carbon capture and storage by mineral carbonation (CCSM) towards the introduction of carbon neutral materials. *Energy & Environmental Science*, 5(7), 7781-7796.
- Sanna, A., Uibu, M., Caramanna, G., Kuusik, R., & Maroto-Valer, M. M. (2014). A review of mineral carbonation technologies to sequester CO<sub>2</sub>. In *Chemical Society Reviews*, 43(23) 8049-8080.

- Schaefer, D. W., & Keefer, K. D. (1986). Structure of random porous materials: Silica aerogel. *Physical Review Letters*, 56(20), 2199.
- Seifritz, W. (1990). CO<sub>2</sub> disposal by means of silicates. *Nature*, 345(6275), 486–486.
- Shand, M. A. (2006). The Chemistry and Technology of Magnesia. In *The Chemistry and Technology of Magnesia*.
- Sivanesan, D., Youn, M. H., Murnandari, A., Kang, J. M., Park, K. T., Kim, H. J., & Jeong, S. K. (2017). Enhanced CO<sub>2</sub> absorption and desorption in a tertiary amine medium with a carbonic anhydrase mimic. *Journal of Industrial and Engineering Chemistry*, 52, 287-294.
- Smit, B., Park, A. H. A., & Gadikota, G. (2014). The grand challenges in carbon capture, utilization, and storage. *Frontiers in Energy Research*, 2, 55.
- Smith, J. V. (1959). The crystal structure of proto-enstatite, MgSiO<sub>3</sub>. *Acta Crystallographica*, 12(7), 515–519.
- Socolow, R. H., & Pacala, S. W. (2006). A plan to keep carbon in check. *Scientific American*, 295(3), 50–57.
- Stéphenne, K. (2014). Start-up of world's first commercial post-combustion coal fired CCS project: contribution of Shell Cansolv to SaskPower Boundary Dam ICCS Project. *Energy Procedia*, 63, 6106–6110.
- Stuhrmann, H. B. (1989). Small-angle scattering of X-rays. *Progress In Crystal Growth And Characterization*.
- Sun, R., Li, Y., Zhao, J., Liu, C., & Lu, C. (2013). CO<sub>2</sub> capture using carbide slag modified by propionic acid in calcium looping process for hydrogen production. *International Journal of Hydrogen Energy*, 38(31), 13655–13663.
- Swanson, E. J., Fricker, K. J., Sun, M., & Park, A. H. A. (2014). Directed precipitation of hydrated and anhydrous magnesium carbonates for carbon storage. *Physical Chemistry Chemical Physics*, 42, 23440-23450.
- Thomas, D. C., & Benson, S. M. (2005). *Carbon Dioxide Capture for Storage in Deep Geologic Formations-Results from the CO<sub>2</sub> Capture Project: Vol 1-Capture and Separation of Carbon Dioxide from Combustion, Vol 2-Geologic Storage of Carbon Dioxide with Monitoring and Verification*. Elsevier.
- Thompson, S. P., Day, S. J., Parker, J. E., Evans, A., & Tang, C. C. (2012). Fine-grained amorphous calcium silicate CaSiO<sub>3</sub> from vacuum dried sol-gel production, characterisation and thermal behaviour. *Journal of Non-Crystalline Solids*, 5, 885-892.
- Trittschack, R., & Grob ty, B. (2012). Dehydroxylation kinetics of lizardite. *European Journal of Mineralogy*, 24(1), 47–57.
- Vaidya, P. D., Konduru, P., Vaidyanathan, M., & Kenig, E. Y. (2010). Kinetics of carbon dioxide removal by aqueous alkaline amino acid salts. *Industrial and Engineering Chemistry*, 49(21), 11067-11072.
- Valverde, J. M. (2013). Ca-based synthetic materials with enhanced CO<sub>2</sub> capture efficiency. *Journal of Materials Chemistry A*, 1(3), 447–468.
- Vinoba, M., Bhagiyalakshmi, M., Grace, A. N., Chu, D. H., Nam, S. C., Yoon, Y., Yoon, S. H., & Jeong, S. K. (2013). CO<sub>2</sub> absorption and sequestration as various polymorphs of CaCO<sub>3</sub> using

- sterically hindered amine. *Langmuir*, 29(50), 15655-15663.
- Vinoba, M., Kim, D. H., Lim, K. S., Jeong, S. K., Lee, S. W., & Alagar, M. (2011). Biomimetic sequestration of CO<sub>2</sub> and reformation to CaCO<sub>3</sub> using bovine carbonic anhydrase immobilized on SBA-15. *Energy and Fuels*, 25(1), 438-445.
- Viti, C., & Hirose, T. (2010). Thermal decomposition of serpentine during coseismic faulting: Nanostructures and mineral reactions. *Journal of Structural Geology*, 32(10), 1476–1484.
- Wang, J., & Becker, U. (2009). Structure and carbonate orientation of vaterite (CaCO<sub>3</sub>). *American Mineralogist*, 94, 380-386.
- Wang, T., Park, A. H. A., Shi, Y., & Gadikota, G. (2019). *Carbon Dioxide Capture and Utilization—Closing the Carbon Cycle*, ACS Publications.
- Wang, Y., Liu, J., Shi, T., Yang, B., Li, C., Xu, H., & Yin, W. (2020). Preparation, properties and phase transition of mesoporous hydromagnesite with various morphologies from natural magnesite. *Powder Technology*, 364, 822-830.
- Werner, M., Hariharan, S., & Mazzotti, M. (2014). Flue gas CO<sub>2</sub> mineralization using thermally activated serpentine: from single-to double-step carbonation. *Physical Chemistry and Chemical Physics*, 16(45), 24978–24993.
- Weyl, P. K. (1959). The change in solubility of calcium carbonate with temperature and carbon dioxide content. *Geochimica et Cosmochimica Acta*, 17(3–4), 214–225.
- White, W. (2016). Chemistry and karst. *Acta Carsologica*, 44(3).
- Wilcox, J. (2012). *Carbon capture*. Springer Science & Business Media.
- Williams, N. J., Seipp, C. A., Brethomé, F. M., Ma, Y. Z., Ivanov, A. S., Bryantsev, V. S., Kidder, M. K., Martin, H. J., Holguin, E., Garrabrant, K. A., & Custelcean, R. (2019). CO<sub>2</sub> Capture via Crystalline Hydrogen-Bonded Bicarbonate Dimers. *Chem*, 5(3), 719-730.
- Wilson, S. A., Raudsepp, M., & Dipple, G. M. (2006). Verifying and quantifying carbon fixation in minerals from serpentine-rich mine tailings using the Rietveld method with X-ray powder diffraction data. *American Mineralogist*, 91(8–9), 1331–1341.
- Wogelius, R. A., & Walther, J. V. (1992). Olivine dissolution kinetics at near-surface conditions. *Chemical Geology*, 97, 101-102.
- Xue, W., Liu, X., Zheng, X., & Ding, C. (2005). Dissolution and mineralization of plasma-sprayed wollastonite coatings with different crystallinity. *Surface and Coatings Technology*, 200(7), 2420-2427.
- Yadav, V. S., Prasad, M., Khan, J., Amritphale, S. S., Singh, M., & Raju, C. B. (2010). Sequestration of carbon dioxide (CO<sub>2</sub>) using red mud. *Journal of Hazardous Materials*, 176, 1044-1050.
- Yin, W., Wang, Y., Ji, Q., Yao, J., Hou, Y., Wang, L., & Zhong, W. (2014). Synthesis and formation mechanism of micro/nano flower-like MgCO<sub>3</sub>·5H<sub>2</sub>O. *International Journal of Minerals, Metallurgy, and Materials*, 21(3), 304–310.
- Yu, B., Yu, H., Li, K., Ji, L., Yang, Q., Chen, Z., & Megharaj, M. (2019). Integration of a diamine solvent based absorption and coal fly ash based mineralisation for CO<sub>2</sub> sequestration. *Fuel Processing Technology*, 192, 220-226.

- Yu, J., & Chuang, S. S. C. (2016). The structure of adsorbed species on immobilized amines in CO<sub>2</sub> capture: An in situ IR study. *Energy and Fuels*, 30(9), 7579-7587.
- Zhang, P., Shi, Y., Wei, J., Zhao, W., & Ye, Q. (2008). Regeneration of 2-amino-2-methyl-1-propanol used for carbon dioxide absorption. *Journal of Environmental Sciences*, 20(1), 39-44.
- Zhang, Y., Yu, P., & Luo, Y. (2013). Absorption of CO<sub>2</sub> by amino acid-functionalized and traditional dicationic ionic liquids: Properties, Henry's law constants and mechanisms. *Chemical Engineering Journal*, 214, 355-363.
- Zhao, H., Park, Y., Lee, D. H., & Park, A. H. A. (2013). Tuning the dissolution kinetics of wollastonite via chelating agents for CO<sub>2</sub> sequestration with integrated synthesis of precipitated calcium carbonates. *Physical Chemistry Chemical Physics*, 15(36), 15185–15192.
- Zhao, Q., Li, J., You, K., & Liu, C. (2020). Recovery of calcium and magnesium bearing phases from iron- and steelmaking slag for CO<sub>2</sub> sequestration. *Process Safety and Environmental Protection*, 135, 81-90.
- Zhao, Q., Liu, C., Gao, T., Gao, L., Saxén, H., & Zevenhoven, R. (2019). Remediation of stainless steel slag with MnO for CO<sub>2</sub> mineralization. *Process Safety and Environmental Protection*, 127, 1-8.
- Zhao, Q., Liu, K., Sun, L., Liu, C., Jiang, M., Saxén, H., & Zevenhoven, R. (2020). Towards carbon sequestration using stainless steel slag via phase modification and co-extraction of calcium and magnesium. *Process Safety and Environmental Protection*, 133, 73-81.